

# Searching for weakly produced supersymmetric particles using the ATLAS detector at the LHC

Sarah Williams  
of  
King's College

CERN-THESIS-2013-335  
03/12/2013



A dissertation submitted to the University of Cambridge  
for the degree of Doctor of Philosophy  
October 2013

# Searching for weakly produced supersymmetric particles using the ATLAS detector at the LHC

Sarah Williams

## Abstract

The Large Hadron Collider (LHC) at CERN is the world's largest and highest energy particle accelerator to date, with the capability to produce proton-proton collisions at a centre-of-mass energy ( $\sqrt{s}$ ) of 14 TeV. The ATLAS experiment at the LHC is a multi-purpose detector designed to cover a wide range of physics programmes. It took its first data in November 2009, when collisions at  $\sqrt{s} = 900$  GeV were recorded. This thesis presents results based on two datasets: the  $4.7 \text{ fb}^{-1}$  of integrated luminosity at  $\sqrt{s} = 7$  TeV collected by ATLAS during 2011 running, and  $20.3 \text{ fb}^{-1}$  of data at  $\sqrt{s} = 8$  TeV, which was recorded in 2012. The first analysis on 2011 data targets weakly produced supersymmetric particles in events with exactly two leptons and missing transverse energy. This was the first dedicated search in ATLAS in this channel for electroweak production. No excess events were observed above the Standard Model expectation and the results are therefore presented as exclusion limits for several electroweak production processes. These were the first limits published from the LHC on direct slepton production. The first search for electroweak production using the 2012 dataset, is then presented. This specifically targeted two electroweak processes: direct slepton pair production, and chargino-pair production in the case that the charginos decay through intermediate sleptons. Again no excesses over the Standard Model were observed, and the previous limits were extended. The increased sensitivity of the 2012 analysis also allowed left-handed and right-handed sleptons to be considered separately.

## Declaration

This dissertation is the result of my own work, except where explicit reference is made to the work of others, and has not been submitted for another qualification to this or any other university. This dissertation does not exceed the word limit for the respective Degree Committee.

Sarah Williams

## Acknowledgements

To begin, I would like to thank the United Kingdom’s Science and Technology Facilities Council (STFC) for the studentship that has enabled me to do this degree, and also King’s College, which has been my home for the seven years I have been in Cambridge, and has contributed to making my time here a truly enjoyable and unforgettable experience.

I would not have been able to begin this degree without the support and encouragement of those who guided me through my undergraduate studies in Cambridge. For this I am indebted to David Munday for his guidance and support, and Andy Blake, whose contribution to my academic studies consistently went beyond the call of duty. I would also like to thank William Bell, who supervised my summer studentship at CERN, which gave me the enthusiasm and confidence to continue in high energy physics. Finally, I am grateful to Nicole Atack and Alethea Peters, with whom I shared some of my most memorable experiences of my undergraduate days, and who have continued to provide support and friendship ever since.

Moving on to the last three years, I would like to thank my supervisor, Chris Lester, for his guidance throughout this degree, and the entire Cambridge high energy physics group, for all the friendly advice I have received over the years. For her constant support during my time in the group, both as a colleague and a friend, I would also like to express my gratitude to Sky French. In addition, for their time spent over the last three years, giving general advice and also helping me solve my (not infrequent) computing issues, I would like to thank Teng Jian Khoo and Will Buttinger. I am also grateful to John Hill, who for the last three years has patiently dealt with the consequences that my computational work “occasionally” had on the group’s computer resources.

As for my time at CERN, I would like to thank all members of the 2-lepton analysis group that I was able to meet and collaborate with whilst there. I am particularly grateful to Brokk Toggerson and Serhan Mete, who not only provided help and support within the group, but were also valuable friends during my time there.

My time at CERN was an incredible experience that would not have been the same without the entire LTA community with whom I shared the year. In particular I would like to express my gratitude to Kara Lynch, who lived with me during the highs and lows of my time there, for her constant friendship and support, and the good times we've shared since we met as summer students at CERN. I would also like to thank Becky Chislett for her friendship since our LTA began; for the 11am coffees, the trips to Charlys, and everything else that came with it.

For his help in the closing stages of this degree, I am grateful to Krishna Kumar, without whom this thesis would have (for a still unknown reason) had several duplicated appendices. The period of writing was also made so much better (and even enjoyable at times), by Anna Bachmann and Alison Edwards, who I thank for their company in our "study sessions".

I would like to end by thanking all of my friends who have made the last three years such an enjoyable time, for all their guidance and support along the way, and the great times we have shared, and by giving special thanks to my family, who I am indebted to for their constant support and encouragement throughout the duration of my academic career.

## Preface

This thesis summarises the work undertaken by the author, as part of the ATLAS collaboration, throughout a three year period from October 2010 to October 2013. The studies on ATLAS data focus on the data taken throughout the 2011 and 2012 runs. After first providing an overview of the ATLAS experiment at the LHC, and a theoretical discussion of the Standard Model of particle physics, supersymmetry is motivated as a solution to some of the current problems in the Standard Model, particularly the hierarchy problem. This is followed by a chapter outlining the statistical procedure for searching for new physics scenarios in ATLAS, within the frequentist framework.

The experimental work in this thesis is then divided into three chapters, all focussed on searches for weakly produced supersymmetric particles at the LHC in events with exactly two leptons and missing transverse momentum. Chapter 5 firstly motivates searching for electroweak production and provides an overview of possible weak production processes. An optimisation study for a signal region targeting direct slepton production is presented, which is based on the  $m_{T2}$  variable. This study was performed entirely by the author, but the author would like to thank Christopher Lester and Christophe Clement for their discussion throughout the process. This study used a Monte Carlo signal grid designed by Christophe Clement, and all Monte Carlo samples used were produced centrally from ATLAS simulation by the ATLAS supersymmetry working group.

The signal region chosen from Chapter 5 then became one of four signal regions included in the ATLAS search for weak production in 2-lepton events using  $4.7 \text{ fb}^{-1}$  of data at  $\sqrt{s} = 7 \text{ TeV}$  collected during 2011, which was published in [1]. The author is very grateful to have had the opportunity to play an active role in producing the results for this publication, which is discussed in Chapter 6. Unless otherwise stated, all plots demonstrating agreement between data and Monte Carlo, and numerical results in tables, were produced by the author using the ROOT framework [2], including the plots labelled “ATLAS” that are included in the the publication. As well as designing the  $m_{T2}$ -based signal region, and producing plots showing comparisons between data and Monte Carlo for the publication, the author also produced the exclusion limits across the signal grids considered in the analysis. This involved computing  $\text{CL}_s$  [3] values for

---

all of the signal points for each of the signal regions considered. This was done using the `HistFitter` package which was developed by members of the ATLAS supersymmetry working group, and provides useful interfaces to the `RooStats` package [4]. The author was responsible for providing the data-counts in the signal region, Monte Carlo estimates of background contributions to the signal regions, the associated systematic uncertainties (though these were only used for comparison), and for evaluating the Monte Carlo estimates (with systematic uncertainties) for all signal models considered. The data-driven estimates for all signal regions, that were used for the final results, were provided by other analysers in the collaboration, and the model independent limits presented were also calculated by other members of the group. Again all Monte Carlo samples used in the analysis were produced centrally from ATLAS simulation by the ATLAS supersymmetry working group. The author would like to thank the rest of the 2-lepton analysis group for their support and cooperation, and particularly the editors of the paper, Sky French and Christophe Clement who coordinated the group effort.

Chapter 7 then focusses on studies based on the 2012 dataset, which amounted to an integrated luminosity of  $20.3 \text{ fb}^{-1}$  at  $\sqrt{s} = 8 \text{ TeV}$ . This includes a discussion of part of the first public ATLAS result for electroweak production in 2-lepton events in the 2012 dataset. It was made public in May 2013 and released in an ATLAS “Conference Note” [5]. Again the author was privileged to be able to play an active role in generating these public results. This analysis only used two signal regions, both based on the  $m_{T2}$  variable. The author performed the re-optimisation studies for these signal regions, again using Monte Carlo produced by the ATLAS supersymmetry working group. It should be noted that these signal regions also included an improved jet veto definition, which was designed by Brokk Toggerson, and then incorporated by the author into the re-optimisation of the signal regions. The author again performed the statistical interpretation of the results using the `HistFitter` package, with important cross-checks being provided by Serhan Mete. As an improvement from the 2011 analysis, the results of the 2012 analysis were obtained by constraining some of the background contributions using a simultaneous fit across all signal regions and control regions in the analysis. The author produced all the exclusion plots and the model independent limits. The inputs required for the statistical interpretation of the results (including Monte Carlo samples for signal and background, and the data), were provided by Serhan Mete. The author was involved in determining the final configuration used in the fit (i.e. which control regions to include and what backgrounds to fit) along with the other members of the analysis group. The data-driven cross-checks of the background estimates and the final control region definitions were provided by other analysers in the group, but the tables

containing the comparisons between these results and those from the simultaneous fit were made by the author. The author would again like to thank the other members of the analysis group, including Anyes Taffard and Christophe Clement, who coordinated the effort. The shape-fitting study in Chapter 7, which did not go into ATLAS public results, was performed independently by the author, but again using centrally produced Monte Carlo samples.

As part of the PhD programme, the author spent an extended period, from October 2011 to December 2012, based at CERN. During this time, in addition to the analysis work detailed in this thesis, the author was able to get involved in other aspects of the experiment. This included performing calibration work for the Level 1 Calorimeter Trigger, where the author continued work started by Will Buttinger. The author was also privileged to be able to take shifts on the trigger desk in the ATLAS control room during data-taking periods. This involved checking the trigger configuration in preparation for a data-taking run and monitoring the online trigger performance during data-taking.

# Contents

<b>1</b>	<b>Introduction</b>	<b>1</b>
<b>2</b>	<b>The ATLAS experiment at the Large Hadron Collider</b>	<b>3</b>
2.1	The LHC . . . . .	3
2.2	The ATLAS detector . . . . .	7
2.2.1	Introduction . . . . .	7
2.2.2	The Inner Detector . . . . .	9
2.2.3	The ATLAS calorimeters . . . . .	17
2.2.4	The Muon Spectrometer . . . . .	20
2.2.5	The ATLAS magnet system . . . . .	23
2.2.6	The ATLAS trigger system . . . . .	26
2.3	Analysing ATLAS data . . . . .	29
2.3.1	Introduction . . . . .	29
2.3.2	The ATLAS event data model . . . . .	29
2.3.3	The ATLAS computing model . . . . .	31
2.3.4	The Athena framework . . . . .	31
2.3.5	Reconstructing physics objects . . . . .	32
2.3.6	Simulating ATLAS data . . . . .	33
2.4	Conclusion . . . . .	35

---

<b>3</b>	<b>Theoretical background- the Standard Model and beyond</b>	<b>36</b>
3.1	The Standard Model . . . . .	36
3.1.1	Introduction . . . . .	36
3.1.2	The Standard Model as a quantum field theory . . . . .	37
3.1.3	Particles and interactions in the Standard Model . . . . .	39
3.1.4	Electroweak symmetry breaking through the Higgs mechanism . .	42
3.1.5	Summary of the Standard Model . . . . .	45
3.1.6	Limitations of the Standard Model . . . . .	45
3.2	Supersymmetry . . . . .	48
3.2.1	Overview of supersymmetry . . . . .	48
3.2.2	Searching for supersymmetry at colliders . . . . .	52
<b>4</b>	<b>Statistical techniques for searching for new physics</b>	<b>54</b>
4.1	Introduction . . . . .	54
4.2	Establishing discoveries or exclusions in the cut-and-count scenario . . .	55
4.2.1	Introduction . . . . .	55
4.2.2	p-values and likelihoods . . . . .	55
4.2.3	Frequentist hypothesis testing . . . . .	57
4.2.4	The $CL_s$ technique . . . . .	59
4.2.5	Systematic errors as nuisance parameters and profiling . . . . .	60
4.2.6	Calculating expected limits . . . . .	62
4.3	Extending the simple cut-and-count scenario . . . . .	63
4.3.1	Introduction . . . . .	63
4.3.2	Simultaneous fitting in signal and control regions . . . . .	63
4.3.3	Statistical combinations . . . . .	64

---

4.3.4	Shape-fitting . . . . .	65
4.4	Conclusions . . . . .	66
<b>5</b>	<b>Searching for weakly produced supersymmetric particles at the LHC</b>	<b>67</b>
5.1	Introduction and motivation . . . . .	67
5.2	Weak production processes . . . . .	70
5.3	Limits on weakly produced supersymmetry prior to the LHC . . . . .	71
5.4	Optimising a search for direct slepton production using the $m_{T2}$ variable	75
5.4.1	Introduction to the $m_{T2}$ variable . . . . .	75
5.4.2	The direct slepton signal grid . . . . .	77
5.4.3	Choosing the signal region . . . . .	78
5.5	Conclusions . . . . .	85
<b>6</b>	<b>The search for weakly produced supersymmetric particles with <math>4.7 \text{ fb}^{-1}</math> of data at <math>\sqrt{s} = 7 \text{ TeV}</math></b>	<b>86</b>
6.1	Introduction . . . . .	86
6.2	Data and Monte Carlo samples . . . . .	88
6.2.1	Data samples . . . . .	88
6.2.2	Background samples . . . . .	89
6.2.3	Signal grids . . . . .	89
6.3	Event selection . . . . .	90
6.4	Summary of the Signal Regions . . . . .	104
6.5	Outline of background estimation techniques . . . . .	108
6.6	Systematic uncertainties . . . . .	118
6.7	Comparisons of kinematic distributions in the top and $Z + X$ control regions	120
6.8	Results and statistical interpretation . . . . .	128

---

6.8.1	Interpretation in the chargino-pair production grid . . . . .	131
6.8.2	Interpretation in the chargino-neutralino pair production grid . . . . .	135
6.8.3	Interpretation in the direct slepton grid . . . . .	140
6.8.4	Interpretation in the weak production pMSSM grids . . . . .	144
6.9	Conclusions . . . . .	158
<b>7</b>	<b>Extending the reach with 2012 data</b>	<b>160</b>
7.1	Introduction . . . . .	160
7.2	Key developments in 2012 . . . . .	161
7.2.1	Higher centre-of-mass energy . . . . .	161
7.2.2	Higher luminosity . . . . .	161
7.2.3	Higher pile-up . . . . .	164
7.3	Extending the sensitivity of the $m_{T2}$ -based search . . . . .	166
7.3.1	Introduction . . . . .	166
7.3.2	Re-optimisation . . . . .	167
7.3.3	Background estimation techniques . . . . .	172
7.3.4	Results of the background estimation . . . . .	189
7.3.5	Performing the simultaneous fit . . . . .	192
7.3.6	Results . . . . .	193
7.3.7	Interpretation of results . . . . .	197
7.4	The potential of shape fitting . . . . .	204
7.5	The status of ATLAS searches for supersymmetry after the 2012 run . . . . .	207
<b>8</b>	<b>Concluding Comments</b>	<b>210</b>
<b>A</b>	<b>Constructing the <math>m_{T2}</math> variable</b>	<b>212</b>

---

B	$m_{T2}$ optimisation plots for chargino-pair production	215
C	Top-tagging using the $m_{CT}$ variable	219
D	Systematics in the 2011 analysis	221
E	Fit configuration used for the analysis on 2012 data	234
F	Fit configuration used for the shape fit investigation	249
	Colophon	255
	Bibliography	256
	List of Figures	270
	List of Tables	276

# Chapter 1

## Introduction

The Large Hadron Collider (LHC) at CERN, Switzerland, is the world’s highest energy particle experiment. By creating proton-proton collisions at a centre-of-mass energy of up to 14 TeV (at design running), it enables physicists on the ATLAS experiment (and the other LHC experiments) to probe the fundamental interactions in the universe to very high energies, close to the conditions of the Big Bang. ATLAS is a collaboration of around 3000 physicists at 175 universities in 38 different countries. Its incredible success over the first few years of running is a credit to the gains that can be made in science through large collaborative efforts.

Our current understanding of the fundamental particles in the universe and the interactions between them is encapsulated in the Standard Model. It was built throughout the second half of the 20th Century and has been remarkably successful at explaining (nearly all) experimental observations in high energy physics to high precision. Despite this, physicists are aware that the Standard Model on its own cannot provide a complete “theory of everything”. More recently, discrepancies between the Standard Model and experimental observations have begun to emerge, an example being the observation of neutrino oscillations which imply that neutrinos have a small but finite mass. The Standard Model is also incomplete, in that it doesn’t explain gravity, and there are theoretical issues with the Standard Model at high energies related to the stability of the mass of the Higgs boson (the so-called “hierarchy problem” [6–9]).

This thesis will firstly provide an overview of the ATLAS experiment, and then a theoretical introduction to the Standard Model. To address the current problems with the Standard Model, a large number of “Beyond-the-Standard-Model” (BSM) theories

have been postulated by theorists over the years. One popular BSM theory (possibly due to its ability to provide an elegant solution to the hierarchy problem) is supersymmetry. An overview of supersymmetry will also be provided.

The experimental chapters of this thesis focus on searches for weakly produced supersymmetric particles at the LHC, in events with exactly two leptons and missing transverse momentum. The motivation for such searches is presented, as well as an optimisation study for a cut-and-count search based on the “stransverse mass variable” ( $m_{T2}$ ) [10–12]. Two ATLAS analyses are then described, which searched for electroweak production using the 2011 and 2012 datasets. The chapter on the 2012 dataset also considers how the sensitivity to new physics could be improved by incorporating information on the shape of  $m_{T2}$  distributions into the likelihood function used when setting limits. This could be implemented in subsequent analyses, either on existing data, or on the data that will be collected after the first long shutdown of the LHC, which began after the 2012 run and is scheduled to last until the end of 2014.

# Chapter 2

## The ATLAS experiment at the Large Hadron Collider

### 2.1 The LHC

The Large Hadron Collider (LHC) [13] is the world's largest and highest energy particle accelerator. It is 27 km in circumference and lies beneath the Swiss-French border near Geneva. At design energy, the LHC will collide protons together at a centre-of-mass energy of  $\sqrt{s} = 14$  TeV. The protons circulate around the rings in up to 2808 bunches. Interactions between bunches therefore take place at discrete intervals (never less than 25 ns apart). To quantify the intensity of the beams, the instantaneous luminosity,  $\mathcal{L}$  is used. It is related to the number of events of a given type that would be expected in unit time through

$$\frac{dN_{\text{ev}}}{dt} = \sigma \mathcal{L}, \quad (2.1)$$

where  $\sigma$  is the cross-section for the process. The design instantaneous luminosity of the LHC is  $10^{34} \text{ cm}^{-2}\text{s}^{-1}$ , which corresponds to bunches of up to  $10^{11}$  protons colliding 40 million times per second at a centre of mass energy of 14 TeV.

Accelerating beams of particles to energies of 7 TeV is an incredible technological challenge. The LHC is actually the last in the succession of machines that make up the CERN accelerator complex, which is depicted in Figure 2.1. The complex utilises previous particle accelerators to achieve the required acceleration through a chain of

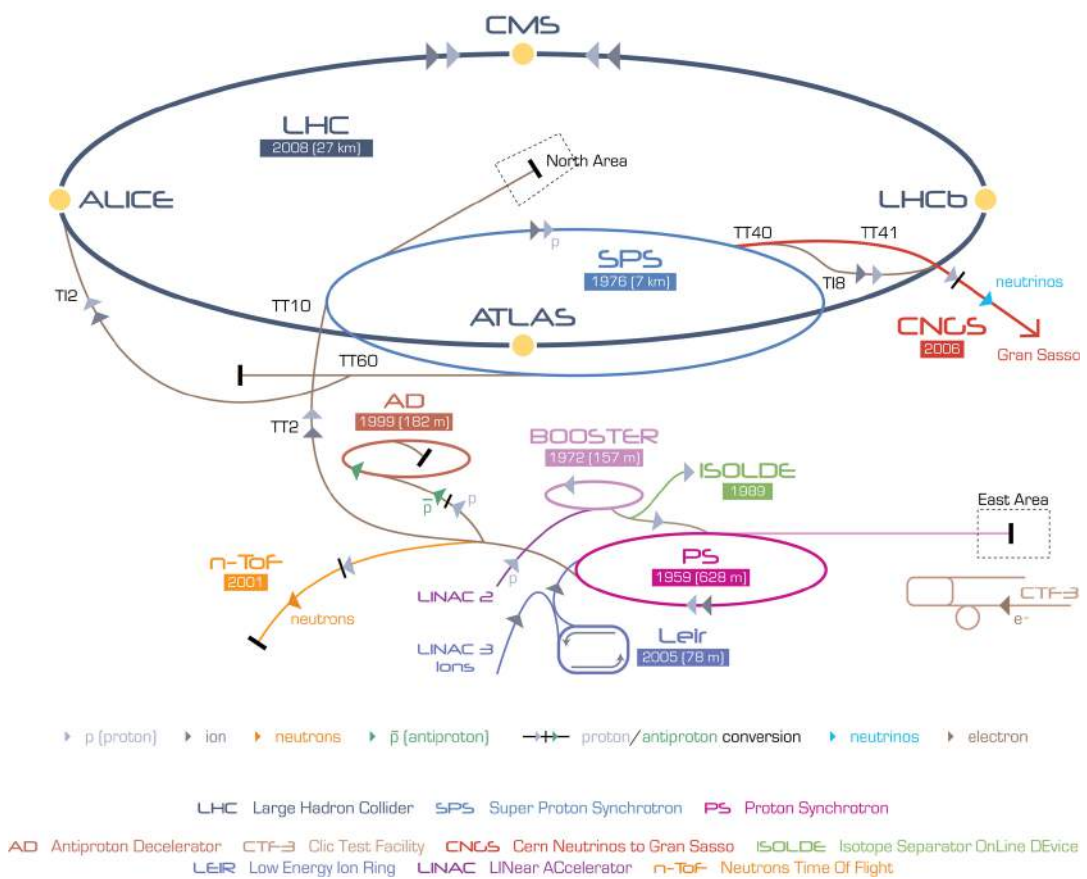


Figure 2.1: The CERN accelerator complex [14].

successive acceleration phases.

In the first step of the accelerator chain, an electric field is used to strip electrons from hydrogen atoms, which are stored in a simple bottle of hydrogen gas. The protons are then accelerated to an energy of 50 MeV by the first accelerator in the chain, Linac 2. The beam of protons is then successively injected into three circular accelerators: the Proton Synchrotron Booster (PSB), the Proton Synchrotron (PS) and the Super Proton Synchrotron (SPS), which accelerate the beam of protons to 1.4 GeV, 25 GeV and 450 GeV respectively. Once the beams are at 450 GeV they are ready for injection into the two beam pipes of the LHC (one clockwise and one anticlockwise). Bunches are injected until both rings are filled and then accelerated to their maximal energy, which was 3.5 TeV for the 2011 run and 4 TeV for the 2012 run.

There are six detectors installed around the LHC ring, in large caverns at the LHC's intersection points where beams can be brought together. The locations of the four main experiments: ATLAS, CMS, LHCb and Alice, are shown in Figure 2.2. ATLAS (A Toroidal LHC ApparatuS) and CMS (Compact Muon Solenoid) are the two multi-purpose detectors and have wide physics programmes, covering precision measurements of the Standard Model and searches for many BSM scenarios. ALICE (A Large Ion Collider Experiment) focuses on heavy-ion collisions, which occur for around one month each year. ALICE is aiming to study and make measurements of the quark-gluon plasma, which is a state of matter expected to have existed shortly after the Big Bang. LHCb is the only forward-backward asymmetric detector at the LHC, and is focussed on the physics of b-quarks. Amongst other things, it aims to measure CP violation in the interactions of B-hadrons. CP violation in nature is required to explain the excess of matter over anti-matter in the universe. CP violation can be included in the Standard Model as a complex phase in the CKM matrix [15] (which will be mentioned in Chapter 3), however the observed CP violation in the Standard Model is insufficient (by several orders of magnitude) to explain the observed matter anti-matter asymmetry [16] in the universe. This provides another motivation for searching for BSM physics.

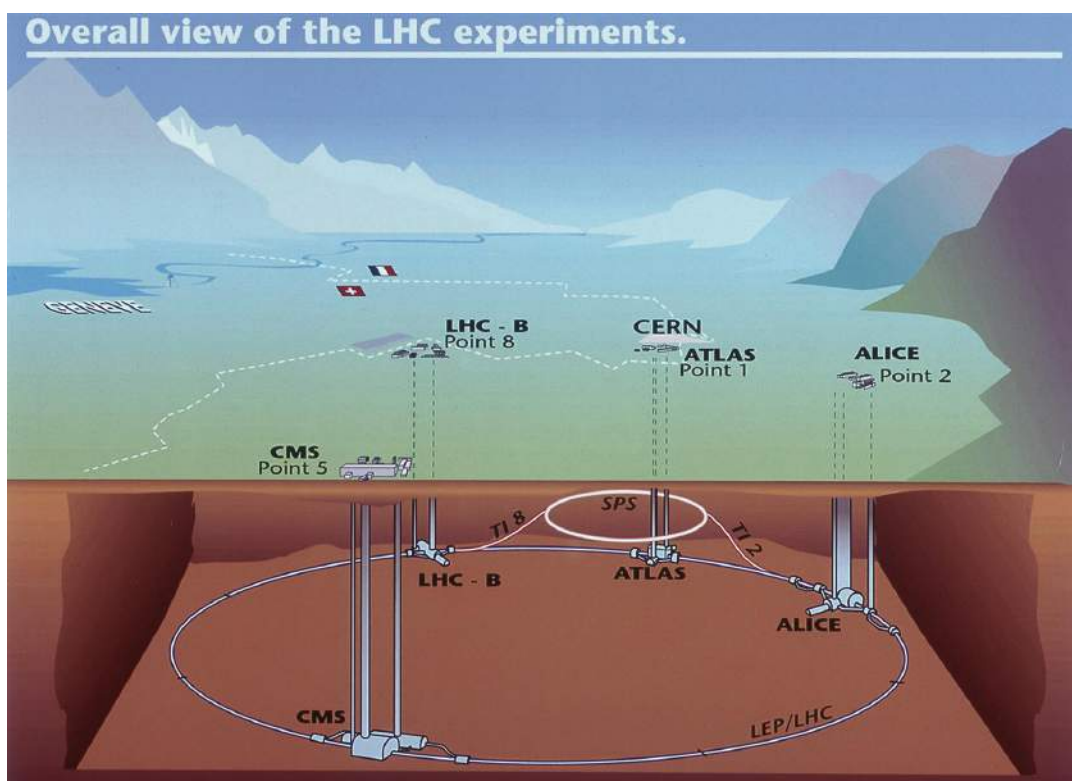


Figure 2.2: The locations of the four main LHC experiments around the LHC ring: ATLAS, CMS, Alice and LHCb [17].

## 2.2 The ATLAS detector

### 2.2.1 Introduction

The ATLAS detector is one of two multi-purpose detectors at the LHC, designed to study all areas of physics. About 45 m long and more than 25 m high, and weighing about 7000 tons, it is about half as big as Notre Dame Cathedral in Paris, and about the same weight as the Eiffel tower. The detector is made up of a number of sub-detectors, as shown in Figure 2.3. The Inner Detector (ID) is the closest part of the detector to the interaction point, and is primarily concerned with tracking charged particles. The electromagnetic and hadronic calorimeters surround the ID and measure energy deposited in the calorimeters from electromagnetic and hadronic particle showers respectively. The Muon Spectrometer (MS) is the outer most part of the detector, and was designed to provide good standalone momentum measurement of high  $p_T$  muons up to energies of 1 TeV. Within ATLAS there is also a complex magnetic field, required for the momentum measurement of charged particles. The read-out of data from the detector is controlled by the trigger and data acquisition system. Triggering selectively reduces the rate of data coming from the detector to a rate that can be stored on disk. These systems will each be discussed in this section. Detailed descriptions of the different components of the ATLAS detector can be found in the “Technical Design Reports” [18, 19].

The coordinate system used in ATLAS will firstly be introduced. The beam direction defines the z-axis, with the x-y plane transverse to the beam direction. The positive x-axis is defined as pointing from the nominal interaction point, which is taken to be the centre of the coordinate system, to the centre of the LHC ring, and the positive y-axis points upwards. The transverse energy  $E_T$  and, transverse momentum  $p_T$ , are defined in the x-y plane. The azimuthal angle  $\phi$  is measured around the beam axis and the polar angle  $\theta$  is the angle from the beam axis.  $\theta$  is usually described in terms of the pseudorapidity  $\eta$ , which is given by

$$\eta = -\ln \left[ \tan \left( \frac{\theta}{2} \right) \right]. \quad (2.2)$$

In the massless limit the pseudorapidity is equivalent to the rapidity:

$$y = \frac{1}{2} \ln \left( \frac{E + p_z}{E - p_z} \right). \quad (2.3)$$

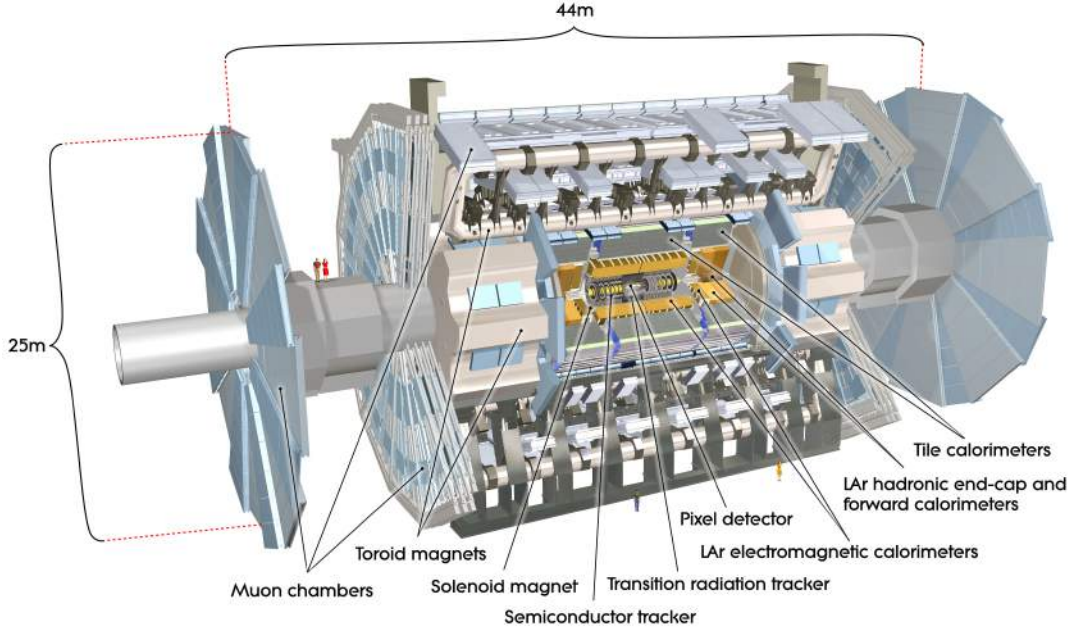


Figure 2.3: Computer generated image of the ATLAS detector, with people included for scale [17].

Rapidity is a useful quantity in hadron colliders as rapidity differences are invariant under boosts along the  $z$ -direction. Pseudorapidity is often used instead as an approximation as it is easier to measure. When quantifying the separation between reconstructed objects, the variable  $\Delta R$  is used, which is defined as

$$\Delta R = \sqrt{(\Delta\eta)^2 + (\Delta\phi)^2}. \quad (2.4)$$

The design requirements for the ATLAS detector will now be summarised. The high luminosity at the LHC posed new experimental challenges in designing the detectors, which had to be designed to cope with high particle multiplicities as well as high levels of radiation. Also, at design running of the LHC, every candidate event for new physics will be accompanied on average by 23 inelastic interactions. Detectors had to be designed to cope with this high level of “pile-up”.

When designing the ATLAS detector, a set of benchmark physics processes (including the Higgs, SUSY and other possible BSM theories including  $Z'$ ,  $W'$  and extra dimensional models) that could be targeted at LHC energies were used to define a set of performance goals for the experiment [20]. Detectors required fast electronics and

radiation hard sensors, in order to cope with the harsh running conditions at the LHC. Another requirement was efficient triggering on low  $p_T$  objects with good background rejection, to attain acceptable trigger rates for physics processes of interest. To identify rare signals over the overwhelming QCD backgrounds inherent in hadron collisions, accurate reconstruction of experimental signatures was essential. This meant being able to accurately reconstruct jets, muons and electrons, as well as detect secondary vertices arising from  $\tau$  leptons and  $b$ -jets. The missing transverse momentum two-vector ( $\mathbf{p}_T^{\text{miss}}$ ) is reconstructed from the transverse momenta of (ideally) all objects coming from the primary event, to represent the momentum imbalance in the transverse plane. Significant missing transverse momentum can represent invisible particles escaping undetected, so it is an important signature in BSM searches. For historical reasons, the missing transverse momentum is usually referred to as  $E_T^{\text{miss}}$ , and this nomenclature will be used throughout this thesis. To enable accurate reconstruction of  $E_T^{\text{miss}}$  in events, the detector was required to have a large acceptance in pseudorapidity as well as almost full azimuthal coverage. These requirements for the reconstruction of physics objects translated into resolution performance goals for the different sub-detectors of ATLAS, which are summarised in Table 2.1. A more detailed discussion of the individual sub-detectors will now be provided.

Detector component	Required resolution	$\eta$ coverage	
		Measurement	Trigger
Tracking	$\sigma_{p_T}/p_T = 0.05\%p_T \oplus 1\%$	$\pm 2.5$	
EM calorimetry	$\sigma_E/E = 10\%/\sqrt{E} \oplus 0.7\%$	$\pm 3.2$	$\pm 2.5$
Hadronic calorimetry (jets)			
Barrel and end-cap	$\sigma_E/E = 50\%/\sqrt{E} \oplus 3\%$	$\pm 3.2$	$\pm 3.2$
Forward	$\sigma_E/E = 100\%/\sqrt{E} \oplus 10\%$	$3.1 <  \eta  < 4.9$	$3.1 <  \eta  < 4.9$
Muon spectrometer	$\sigma_{p_T}/p_T = 10\%$ at $p_T = 1$ TeV	$\pm 2.7$	$\pm 2.4$

Table 2.1: General performance requirements of the ATLAS detector [20]. The units of energy and  $p_T$  are both in GeV.

## 2.2.2 The Inner Detector

The ID [21, 22] provides accurate measurements of the transverse momenta ( $p_T$ ) of charged particles, as well as allowing the observation of secondary vertices close to the

interaction point, which are used in the offline tagging of  $\tau$  leptons and  $b$ -jets. Close to the interaction point, high detector granularity is required to cope with the high particle multiplicities and to meet the resolution requirements for the momentum and vertexing measurements. The ID is contained within a cylindrical envelope of length  $\pm 3512$  mm and radius 1150 mm, and is immersed in a 2 T solenoidal magnetic field.

The ID is comprised of three complementary detector systems. The silicon pixel detector is closest to the interaction point, and mainly contributes to the accurate detection of secondary vertices. The SemiConductor Tracker (SCT) is outside the pixel detector, and gives high resolution measurements using discrete space-points. The Transition Radiation Tracker (TRT) is at a larger radius from the interaction point and comprises many layers of gaseous straw tube elements interleaved with transition radiation material. It provides continual tracking and so enhances the pattern recognition.

The sub-detectors are arranged so that a track from the interaction point will typically cross three pixel layers (each of which provides one space point for the track with  $\sigma_{r\phi} = 14 \mu\text{m}$  and  $\sigma_z = 87 \mu\text{m}$ ), four SCT layers (that each provides one space point with  $\sigma_{\text{strip}} = 22 \mu\text{m}$ ), and will have an average of 36 hits in the TRT. These TRT hits do not provide space points as there is no measurement of  $z$  or  $R$  in the barrel or end-cap respectively. The resolution in the TRT barrel is  $\sigma_{r\phi}=130 \mu\text{m}$ . A cross-section of these layers, with their relative distances from the beam pipe is shown in Figure 2.4, and a diagram of the ID as a whole is shown in Figure 2.5. A brief description of the three components of the ID will now be provided, and followed by a discussion of track reconstruction in the ID.

### The pixel detector

The pixel detector [23] is the innermost part of the ID. With approximately 80 million read-out channels in total, it provides the pattern recognition capability to meet the track reconstruction requirements of ATLAS at the full luminosity. It provides the spatial resolution for reconstructing primary vertices coming from the interaction region, even in the presence of high pile-up, and is also the most important detector used in the identification and reconstruction of secondary vertices.

Figure 2.6 shows a schematic view of the active region of the pixel detector. It consists of three barrel layers, with layer-0 often being referred to as the b-layer, and two identical end-cap regions, each of which has three disk layers. The active parts of the

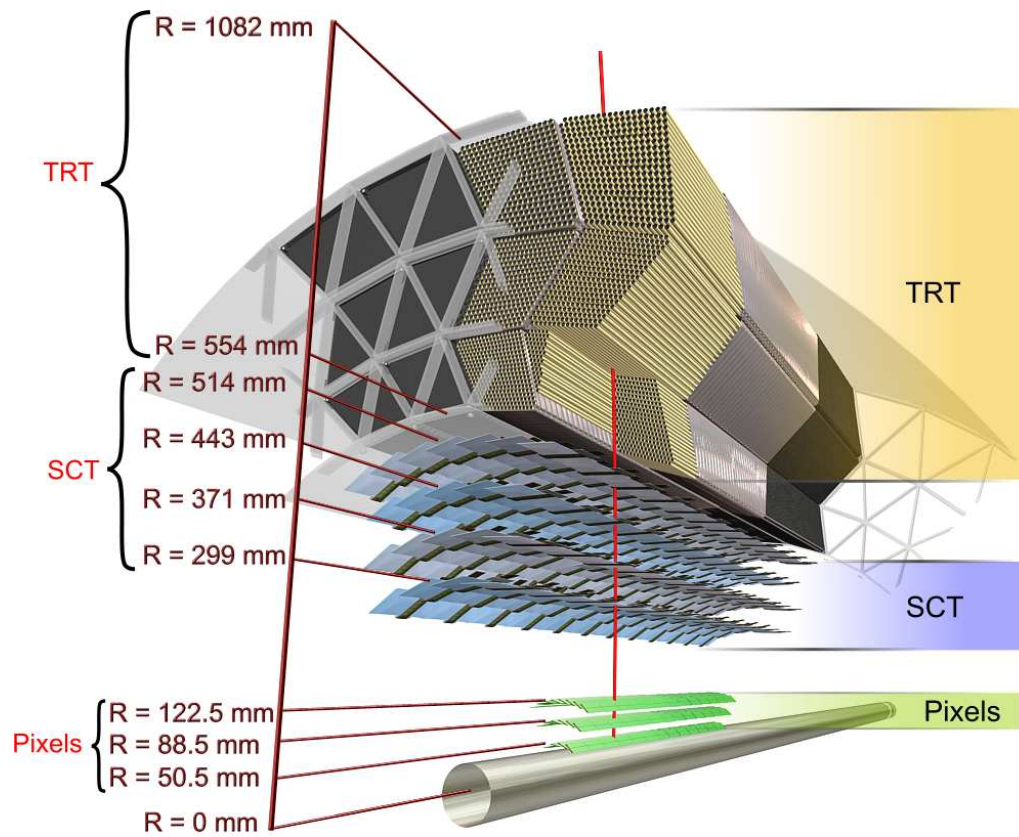


Figure 2.4: Diagram showing the sensors and structural elements traversed by a charged track of 10 GeV in  $p_T$  in the barrel ID ( $\eta = 0.3$ ) [20]. The distances of the three subsystems of the ID from the interaction point are also shown.

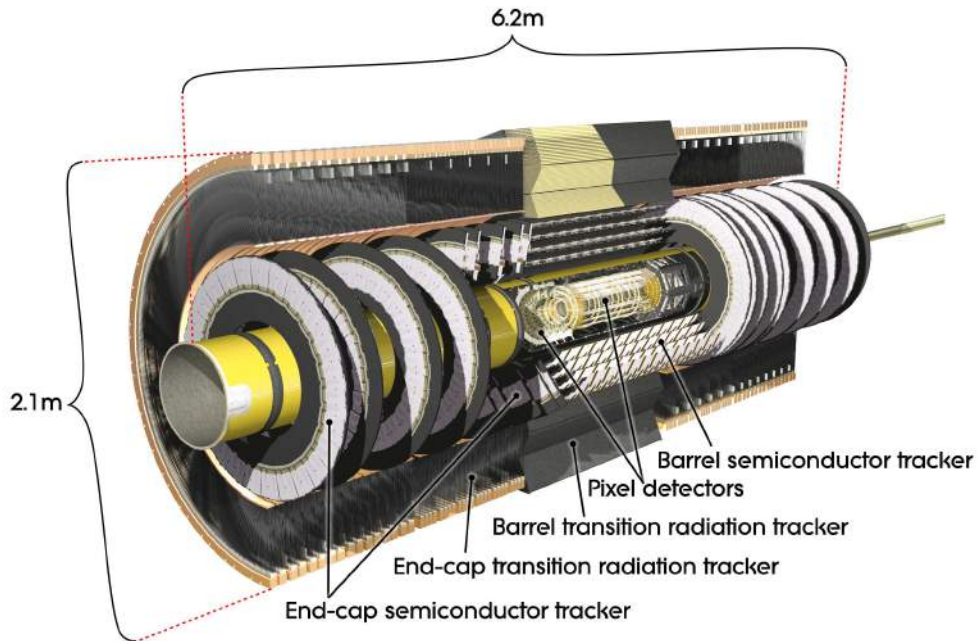


Figure 2.5: Computer generated image of ATLAS ID and its three sub-detectors [20].

detector are composed of pixel modules, which are made of the pixel sensors connected to front end electronics. A pixel sensor is a  $16.4 \times 60.8$  mm wafer of silicon with 46,080 pixel channels, with dimensions of  $50 \mu\text{m}$  in the  $\phi$  direction and  $400 \mu\text{m}$  in the  $z$  and  $r$  directions for the barrel and end-cap regions respectively. The three pixel layers are made of staves which cool the modules. Each staff holds 13 pixel modules, that are inclined with an azimuthal angle of  $20^\circ$ . In the end-cap regions modules are mounted on disk sectors for cooling and support, with eight identical sectors making up each disk. The disks lie at average positions of  $z = \pm 495$  mm,  $z = \pm 580$  mm and  $z = \pm 650$  mm.

Being closest to the interaction point the pixel layers were designed to cope with high doses of radiation. It was initially estimated that the inner pixel layer would have to be replaced after just three years of running at design luminosity. The radiation that the other layers had to withstand was calculated [20], and in order to maintain adequate noise performance after radiation damage, the silicon sensors must be kept at low temperatures ( $-5^\circ\text{C}$  to  $-10^\circ\text{C}$ ), which requires coolant temperatures of  $-25^\circ\text{C}$ .

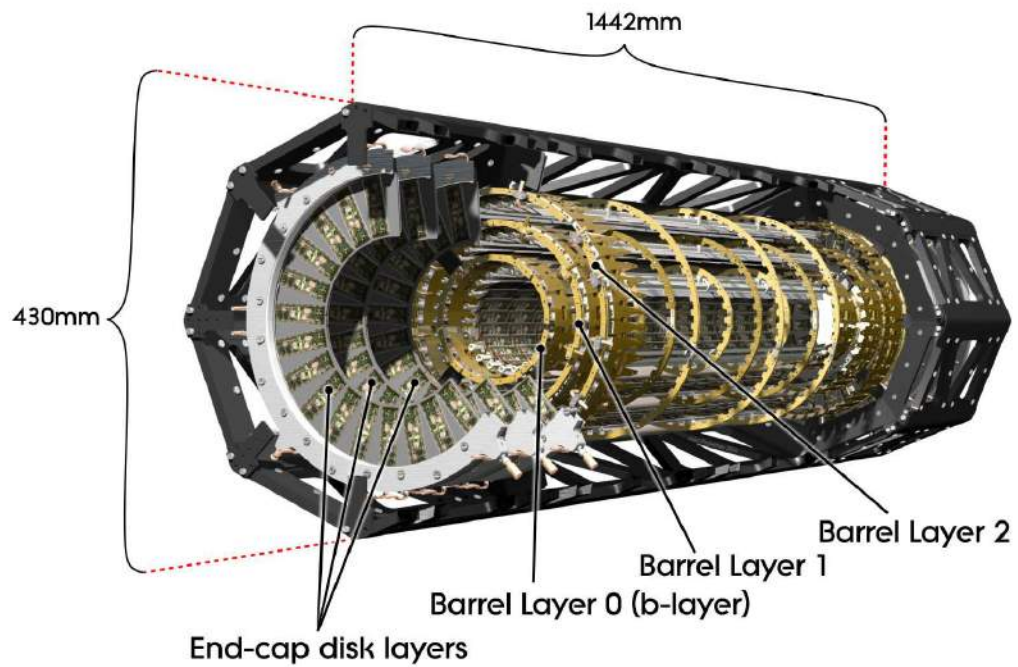


Figure 2.6: A schematic view of the active region of the pixel detector, consisting of barrel and end-cap layers [24].

## The SCT

The ATLAS SCT, shown in Figure 2.7, uses the same detector technology as the pixel detector. The SCT is at a larger radius from the interaction point, leading to a greater area ( $63 \text{ m}^2$  compared to  $1.7 \text{ m}^2$ ). This, along with read-out requirements, would make the use of pixel detectors unfeasible. In the SCT, eight layers of silicon micro-strip detectors are used to provide precision measurements in the  $r$ - $\phi$  and  $z$  directions.

Each silicon detector is made of four  $63.6 \text{ mm} \times 64 \text{ mm}$  wafers with 780 read-out strips of  $80 \mu\text{m}$  pitch, with two pairs of wafers being connected end-to-end, thus doubling the effective length. The two pairs of wafers are then placed back-to-back with a small stereo angle of  $40 \text{ mrad}$  between them which enables measurements of  $z$  and  $r$  in the barrel and end-cap respectively. In the barrel region one pair of strips is aligned parallel to the beam direction, whereas in the end-cap region one set of strips runs radially.

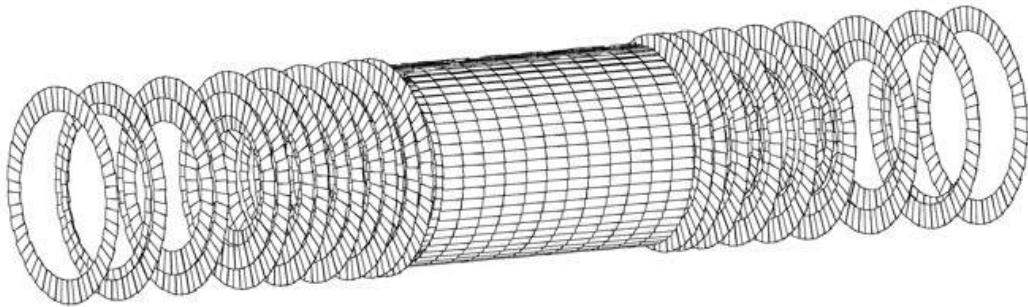


Figure 2.7: Layout of the ATLAS SCT [25].

The SCT has four barrels covering  $|\eta| < 1.1$  and nine disks in each end-cap region, which extend the coverage out to  $|\eta| < 2.5$ . The total number of read-out channels in the SCT is 6.3 million.

## The TRT

The TRT is the furthest away of the ID components from the interaction point, and makes up most of the ID volume. The TRT complements the precision tracking measurements from the pixel and SCT layers by providing a large number of hits which enhances pattern recognition.

The TRT enables track following up to  $|\eta|=2.0$ . It uses  $4 \text{ mm}$  diameter straw tube

detectors, with a central gold-plated tungsten wire of 31  $\mu\text{m}$  diameter as the anode. The inside of the straw is coated with aluminium to act as the cathode. In the barrel region the straws are parallel to the beam axis and up to 144 cm long. The wires are divided in two, approximately at  $\eta = 0$ , with read-out at both ends to reduce the occupancy. In the end-cap region the straws are 37 cm long and arranged radially in wheels, with read-out at the edge of the wheels.

The straws are filled with a non-flammable mix of gases comprising Xe (70%), CO<sub>2</sub> (27%) and O<sub>2</sub> (3%). As ionising particles pass through the gas, liberated charge is collected by the anode wire, providing a signal. The inclusion of Xenon adds electron identification capability through detecting transition radiation photons created in a polypropylene/polyethylene fibre radiator between the straws. Due to a varying refractive index in the radiator, ionising particles with a high Lorentz gamma factor (i.e. electrons) will emit X-ray radiation along their track (unlike pions, which have low Lorentz factors). Each channel gives a drift time measurement that gives a spatial accuracy of 170  $\mu\text{m}$  per straw, and provides information on two independent thresholds. These provide discrimination between tracking hits, which pass the lower threshold, and transition radiation hits, which pass the higher one.

### Track reconstruction in the Inner Detector

The space-points from the pixel and SCT detectors, and hits in the TRT are fed through the ID track reconstruction software. Track reconstruction in ATLAS is performed by the New Tracking algorithm [26]. Tracks are parametrised by five tracking parameters: the inverse transverse momentum ( $q/p_T$ ) which infers both the momentum and charge, the azimuthal angle ( $\phi$ ), the polar angle ( $\theta$ ), transverse impact parameter ( $d_0$ ) and longitudinal impact parameter ( $z_0$ ). In the ID the perigee representation is used to express the the closest approach to the nominal interaction point. The track parameters at the perigee are shown in Figure 2.8.

The resolution of a track parameter  $X$  as a function of transverse momentum  $p_T$  can be expressed as

$$\sigma_X(p_T) = \sigma_X(\infty)(1 \oplus p_X/p_T), \quad (2.5)$$

where  $\sigma_X(\infty)$  is the asymptotic resolution of the parameter at infinity and  $p_X$  is a constant. Specific values for these parameters are given elsewhere [27]. As an example,

for muons the inverse transverse momentum parameter  $\sigma_X(\infty)$  has values of  $0.34 \text{ TeV}^{-1}$  and  $0.41 \text{ TeV}^{-1}$  for the pseudorapidity ranges  $0.25 < |\eta| < 0.5$  and  $1.5 < |\eta| < 1.75$  and  $p_X$  values of  $44 \text{ GeV}$  and  $80 \text{ GeV}$ . The difference between these values is due to different material budgets in the different regions (in general there is more material in the end-cap region).

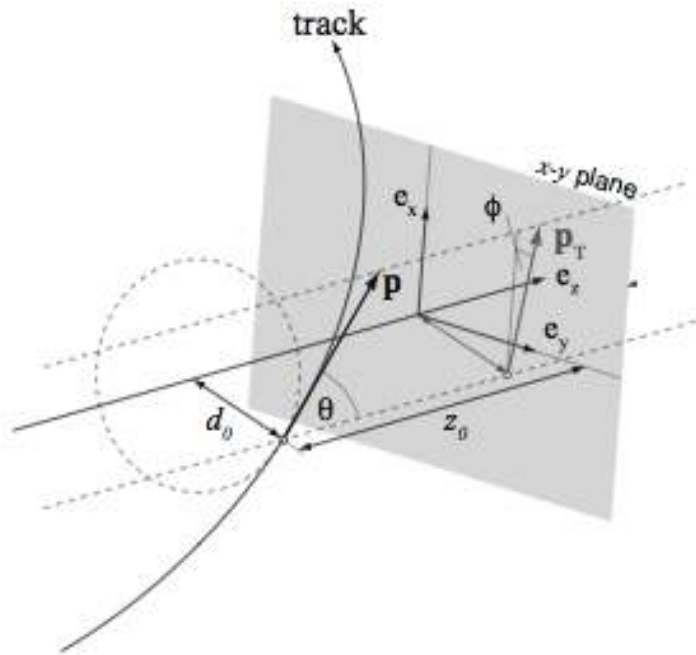


Figure 2.8: Track parameter definitions with respect to the perigee [28].

### 2.2.3 The ATLAS calorimeters

Calorimetry is concerned with measuring the energies of particles. A particle entering the calorimeter produces a particle shower, which deposits energy in the calorimeter, allowing measurement of the particle's energy. Transverse segmentation of calorimeters can provide information about the direction of the particle, and longitudinal segmentation can be used for particle identification by differentiating between the shapes of the particle showers. ATLAS uses sampling calorimeters, where the material producing the shower is distinct from the material measuring the deposited energy.

The calorimetry in the ATLAS detector consists of electromagnetic calorimeters, that are used in the identification and measurements of electrons and photons, and hadronic calorimeters, that are used for reconstructing jets. High granularity Liquid Argon sampling calorimeters (LAr) are used for the electromagnetic calorimetry in the range  $|\eta| < 3.2$ , which provide good energy and momentum resolution. For  $|\eta| < 1.7$  a scintillator-tile calorimeter is used for hadronic calorimetry. This is divided into one central barrel and two smaller extended barrel cylinders either side of the central barrel. For the end-cap regions  $|\eta| > 1.5$  LAr technology is also used for hadronic calorimetry and extends the coverage to the outer limits in  $|\eta|$  of the electromagnetic calorimeter. There are also forward LAr calorimeters to provide electromagnetic and hadronic measurements, which extend the pseudorapidity coverage out to  $|\eta| = 4.9$ .

A view of the ATLAS calorimeters is shown in Figure 2.9. A brief description of the components of the ATLAS calorimetry system will now be provided, followed by a description of the different clustering methods used for energy deposits in the calorimeters.

#### LAr electromagnetic calorimeter

The LAr electromagnetic calorimeter is split into a barrel ( $|\eta| < 1.475$ ) and two end-cap components ( $1.375 < |\eta| < 3.2$ ), each contained in their own cryostat. The LAr calorimeter is in the same vessel as the central solenoid to reduce the material budget in front of the calorimeter. The barrel calorimeter comprises two identical half barrels joined at  $z=0$ , and each end-cap calorimeter is divided into two coaxial wheels, covering the pseudorapidity ranges  $1.375 < |\eta| < 2.5$  and  $2.5 < |\eta| < 3.2$ .

The electromagnetic calorimeter is a lead LAr sampling detector. Over its full coverage the modules are made of accordion-shaped kapton electrodes and lead absorber

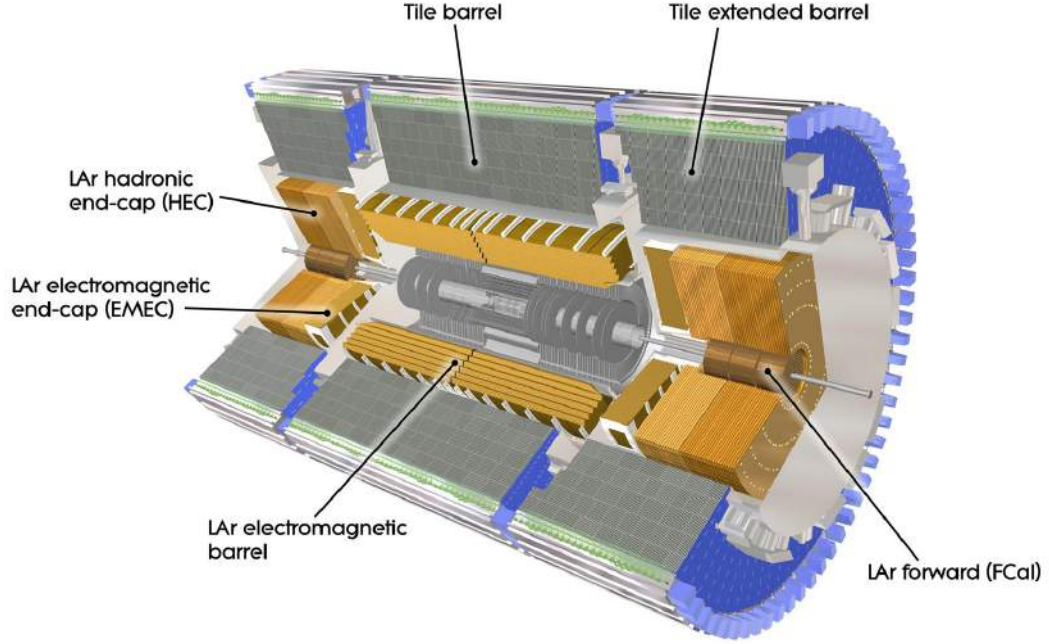


Figure 2.9: Computer generated view of the ATLAS calorimeters [17].

plates. This geometry, which is illustrated in Figure 2.10, was chosen to provide complete  $\phi$  symmetry without azimuthal cracks. For the  $\eta$  range mapped to the ID ( $|\eta| < 2.5$ ), fine granularity is required for precise measurements of electron and photon energies and the calorimeter is segmented into three sections in depth. In the region  $|\eta| < 1.8$  there is also a pre-sampler detector used to correct for energy lost by electrons and photons before reaching the calorimeter. The energy resolution of the electromagnetic calorimeter is often parametrised as

$$\frac{\sigma_E}{E} = \frac{a}{E} \oplus \frac{b}{\sqrt{E}} \oplus c, \quad (2.6)$$

where  $a$  is the noise term,  $b$  is the sampling term and  $c$  is a constant term. In the central region,  $b$  is around 10% whilst  $c$  is around 0.7% [27].

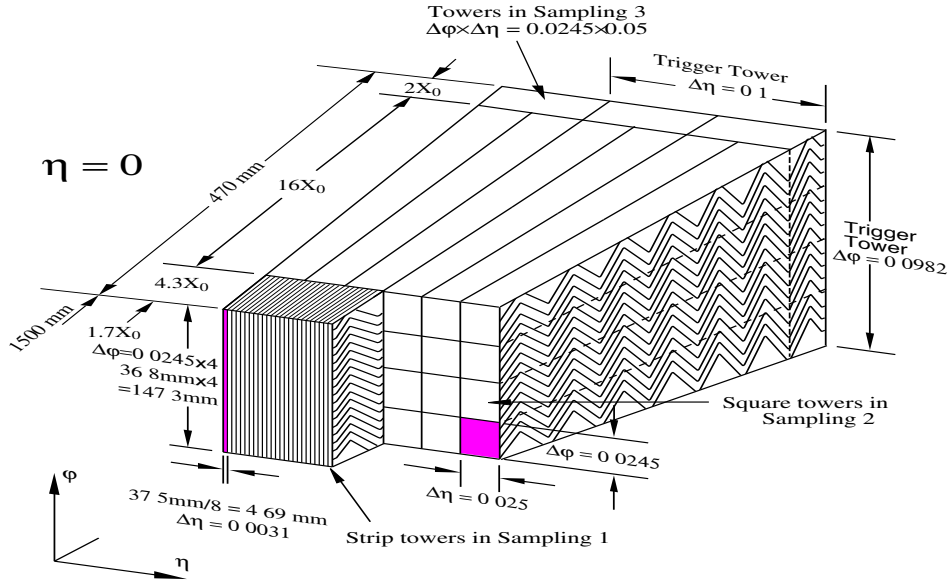


Figure 2.10: Sketch showing the accordion structure of the ATLAS electromagnetic calorimeter [20].

### Hadronic calorimeters

In the central region, hadronic measurements are provided by the scintillator tile calorimeter, which is placed directly outside the envelope of the electromagnetic calorimeter. It is a sampling calorimeter, but with steel as the absorber and scintillating tiles as the active material. The central barrel covers the range  $|\eta| < 1.0$  and two extended barrels cover the range  $0.8 < |\eta| < 1.7$ . All the barrels are divided azimuthally into 64 modules and radially the tile calorimeter extends from 2.28 m to 4.25 m. It is also segmented transversely into three layers.

The hadronic end-cap calorimeter (HEC) is formed from two wheels per end-cap, located behind the electromagnetic end-cap calorimeters and contained in the same cryostat. The HEC extends out to  $|\eta| = 3.2$ , thus overlapping with the forward calorimetry ( $|\eta| > 3.1$ ) in order to reduce the drop in material density at the transition between the two calorimetry elements. It also extends down to  $|\eta| = 1.5$  to overlap with the tile calorimetry. Each wheel comprises 32 wedge-shaped modules and is divided into two segments in depth. The wheels closest to the interaction point are built from 25 mm parallel copper plates, whilst those further away use 50 mm plates. The outer radius of

the copper plates is 2.03 m while the inner radius is 0.475 m. The plates are interleaved with 8.5 mm LAr gaps which provide the active medium for the calorimeter.

Finally, the LAr forward calorimeter (FCAL) is integrated into the end-cap cryostats, but with the front face recessed by 1.2 m with respect to the electromagnetic calorimeter front face to reduce the amount of neutron albedo in the ID. A high density design is required because of the limited depth. It is ten interaction lengths deep, with three modules in each end-cap. The first is optimised for electromagnetic measurements and uses copper, whereas the other two are mainly for hadronic measurements and use tungsten. Each module comprises a metal matrix, with longitudinal channels filled with the electrode structure, which consists of concentric rods and tubes parallel to the beam axis. LAr in the gap between the rod and tube provides the sensitive medium.

### Forming clusters in the ATLAS calorimeters

Two types of clustering algorithm are used for finding and reconstructing clusters in the ATLAS calorimeters. A detailed discussion of the reconstruction of objects in the calorimeters can be found in [27]. For electron and photon candidates the “sliding window” algorithm is used [29]. This forms seed clusters of longitudinal towers with total transverse energy above 2.5 GeV by sliding a window size of  $3 \times 5$  in units of  $0.025 \times 0.025$  in  $\eta \times \phi$  across the grid of the calorimeter.

For clusters used in the reconstruction of jets and  $E_T^{\text{miss}}$ , topological clusters are used [29]. Firstly, a seed cell is selected if it has a signal to noise ratio above a certain threshold. All directly neighbouring cells in all directions are then added, as well as neighbours of these neighbours if they exceed a secondary signal to noise threshold. A ring of guard cells with signal significances above a basic threshold is then added. These initial clusters are then analysed for local signal maxima using a splitting algorithm, and then split into separate clusters if these are found.

## 2.2.4 The Muon Spectrometer

The Muon Spectrometer (MS) [30] is the outer component of the ATLAS detector, and defines the overall dimensions of the detector. It detects and measures charged particles that pass through the barrel and end-cap calorimeters, in the range  $|\eta| < 2.7$ .

The air toroid system comprises a long barrel covering the range  $|\eta| < 1.4$ , and

two inserted end-cap magnets covering the range  $1.6 < |\eta| < 2.7$ . (The pseudorapidity range  $1.4 < |\eta| < 1.6$  is referred to as the transition region as deflection comes from a combination of the different magnet systems.) It generates a strong magnetic field, mostly orthogonal to the direction of the muon track. The target momentum resolution is then achieved through precision tracking detectors in three widely separated stations at increasing distances from the collision region. These can be seen clearly in Figure 2.11, which shows a quarter-section of the MS. The muon system also includes trigger chambers with timing resolutions of the order of 1.5-4 ns.

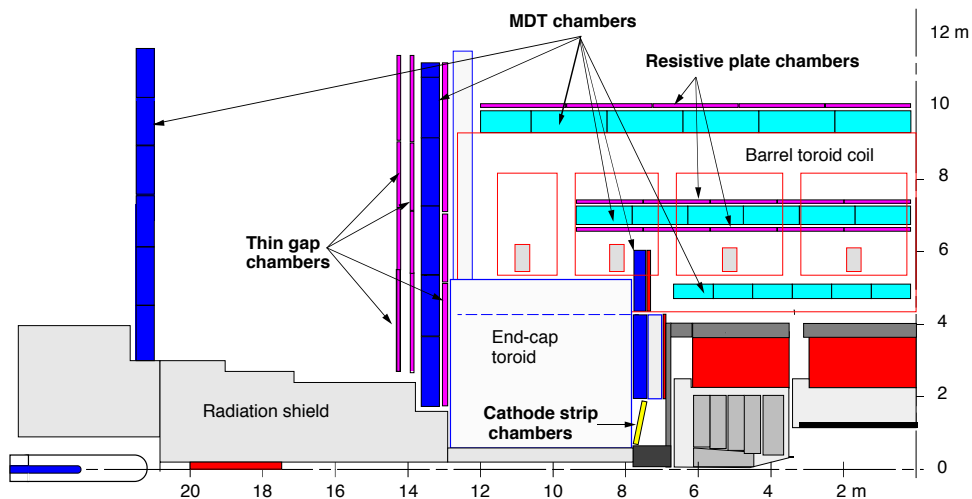


Figure 2.11: Diagram of a quarter-section of the ATLAS Muon Spectrometer [27].

A cut-away view of the ATLAS muon system is shown in Figure 2.12. In the barrel region, the tracking chambers are arranged in cylindrical layers around the beam axis, whereas in the transition and end-cap regions the chambers are arranged in planes perpendicular to the beam direction. The detector components of the muon system will now be explained briefly. The magnet system used in the MS will be discussed later in Section 2.2.5.

Monitored Drift Tubes (MDTs) are used to provide precision measurements of the track coordinates in the principle bending direction of the magnetic field over most of the  $\eta$  range considered. The coverage of the MDTs is  $|\eta| < 2.7$  (though only  $|\eta| < 2.0$  for the innermost layer), and comprises 1150 chambers with 354,000 read-out channels. At larger pseudorapidities ( $2.0 < |\eta| < 2.7$ ) Cathode Strip Chambers (CSCs), which are multi-wire proportion chambers with the cathodes segmented into strips are used in the innermost plane. These have higher granularity to withstand the demanding rate and

background conditions. There are 32 chambers in total, with 31,000 read-out channels.

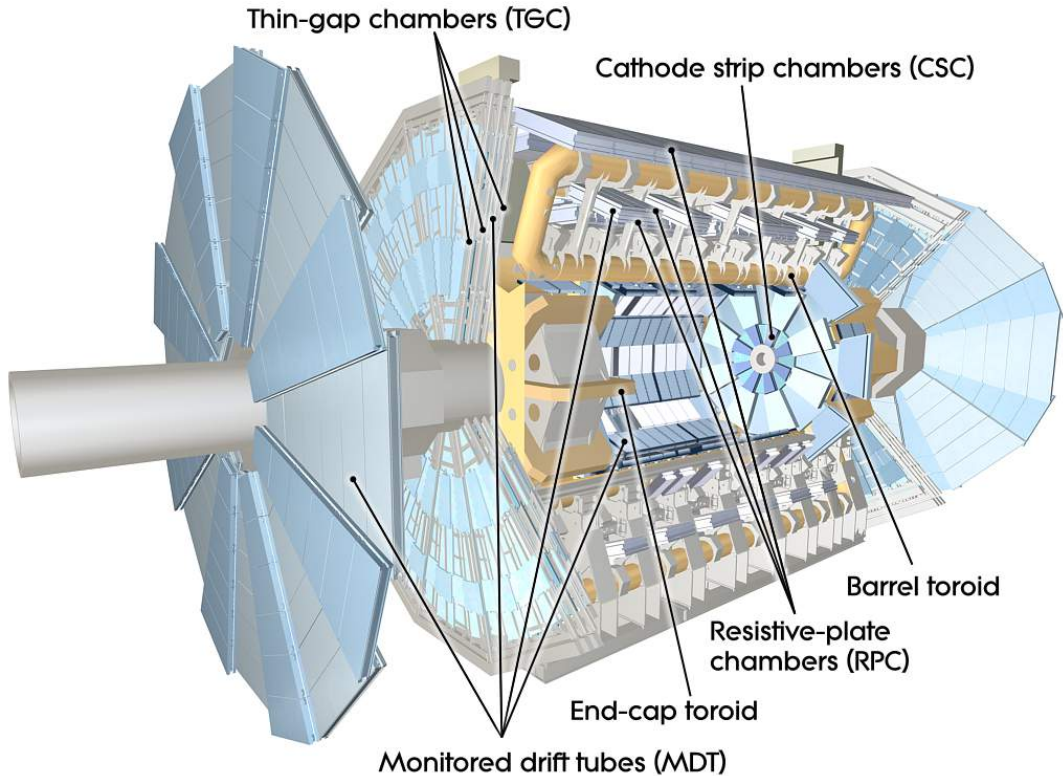


Figure 2.12: A cut-away view of the ATLAS Muon Spectrometer [20].

The muon trigger system covers the pseudorapidity range  $|\eta| < 2.4$ . Resistive Plate Chambers (RPCs) are used in the barrel and Thin Gap Chambers (TGCs) are used in the end-cap regions. These chambers have three purposes: to provide bunch crossing identification, provide well-defined  $p_T$  threshold for muons for triggering, and measure the muon coordinate in the direction orthogonal to that measured by the precision tracking chambers.

High  $p_T$  muons typically traverse all tracking stations in the MS. However, there are regions in  $\eta - \phi$  space where one, two or all of the stations cannot provide a precision measurement. This degrades the resolution and efficiency in these regions. Aside from these geometric constraints, Figure 2.13 shows how the contributions to the muon resolution vary as a function of muon  $p_T$  (as calculated based on simulation prior to data-taking [27]). At low  $p_T$  it is dominated by fluctuations in the energy loss of muons traversing the material in front of the MS. Multiple scattering is important in the intermediate momentum range and for  $p_T > 300$  GeV the single hit resolution dominates.

This is limited by detector characteristics, alignment and calibration. It should be noted that other subsystems of the ATLAS detector are also important for the final performance of muon identification and reconstruction. Energy measurements in the calorimeter can aid muon identification because of their characteristic minimum ionising signature, and can also provide a direct measure of the energy lost by muons crossing the calorimeter [27]. Information on tracks in the ID that are matched to MS tracks is also important. This will be explained further when discussing the offline reconstruction of muon candidates in Section 2.3.5.

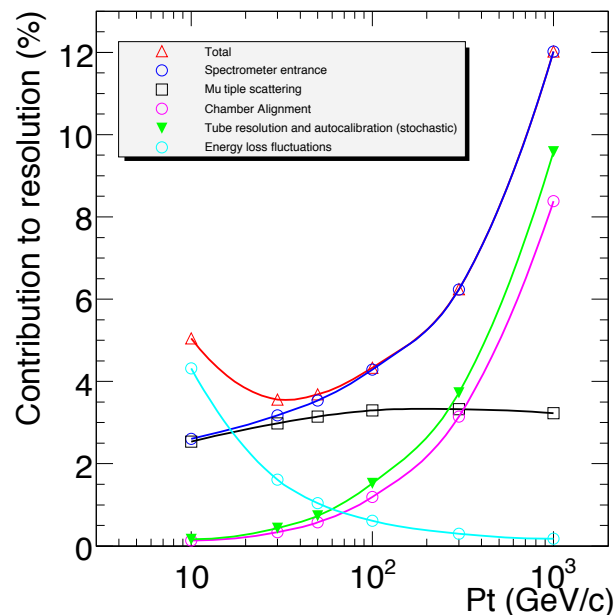


Figure 2.13: Expected contributions to the muon momentum resolution as a function of  $p_T$  for  $|\eta| < 1.5$  [27]. The alignment curve is for an uncertainty of  $30 \mu\text{m}$  in the chamber positions.

## 2.2.5 The ATLAS magnet system

Reconstructing the tracks of charged particles in ATLAS relies on the ATLAS magnet system [20, 31] to force the particles to travel in curved trajectories, thus allowing charge identification and the reconstruction of the momentum component perpendicular to the field direction. The ATLAS magnet system was designed to provide an optimised field configuration for particle bending around the various tracking detectors (namely the ID

and MS), in a light and open structure, thus minimising scattering effects (which could limit reconstruction).

The ATLAS detector includes four large superconducting magnets, the geometries of which are shown in Figure 2.14. There is one central solenoid, serving the ID, then one barrel and two end-cap toroids to provide the magnetic field for the MS.

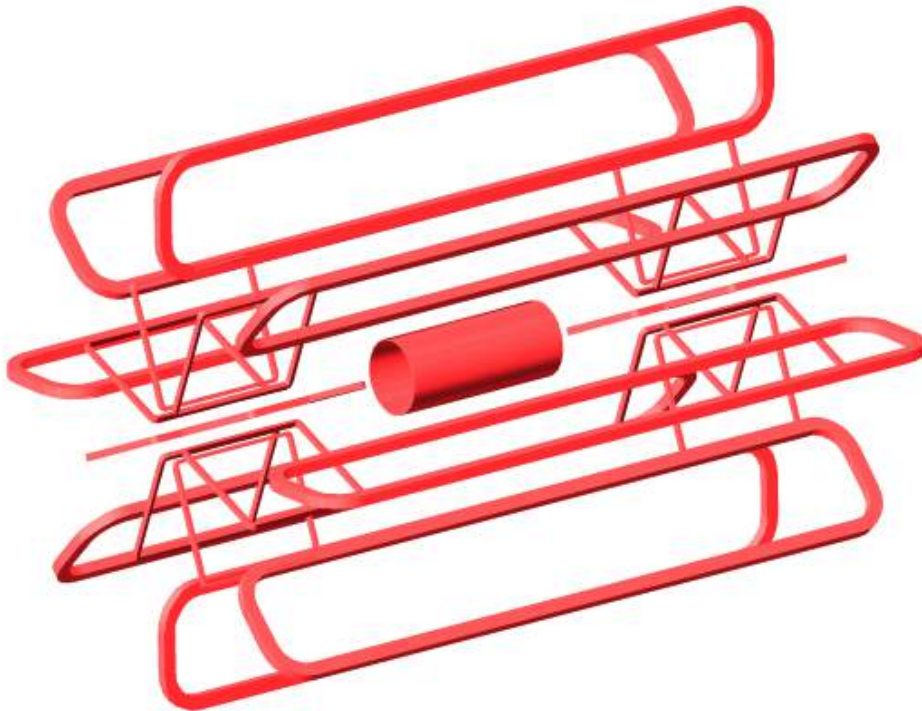


Figure 2.14: Geometry of the windings in the ATLAS magnet system [32].

The central solenoid, which is shown in Figure 2.15, was designed to provide a 2 T axial magnetic field in the ID. It is a conduction-cooled superconducting solenoid with minimal radial thickness (to avoid compromising calorimeter performance).

The barrel toroid, shown in Figure 2.16, is used to produce a toroidal magnetic field of around 0.5 T in the central region of the MS. The cylindrical volume surrounding the calorimeters and both end-cap toroids is filled by the magnetic field of the barrel toroid. It consists of eight flat superconducting race track coils, which are each 25 m long and 8 m wide. The eight coils are held in place by sixteen supporting rings (eight smaller rings at the inner radius of the toroid and eight larger rings at the outer radius). These can be seen in Figure 2.16.



Figure 2.15: Photo of the ATLAS central solenoid [32].

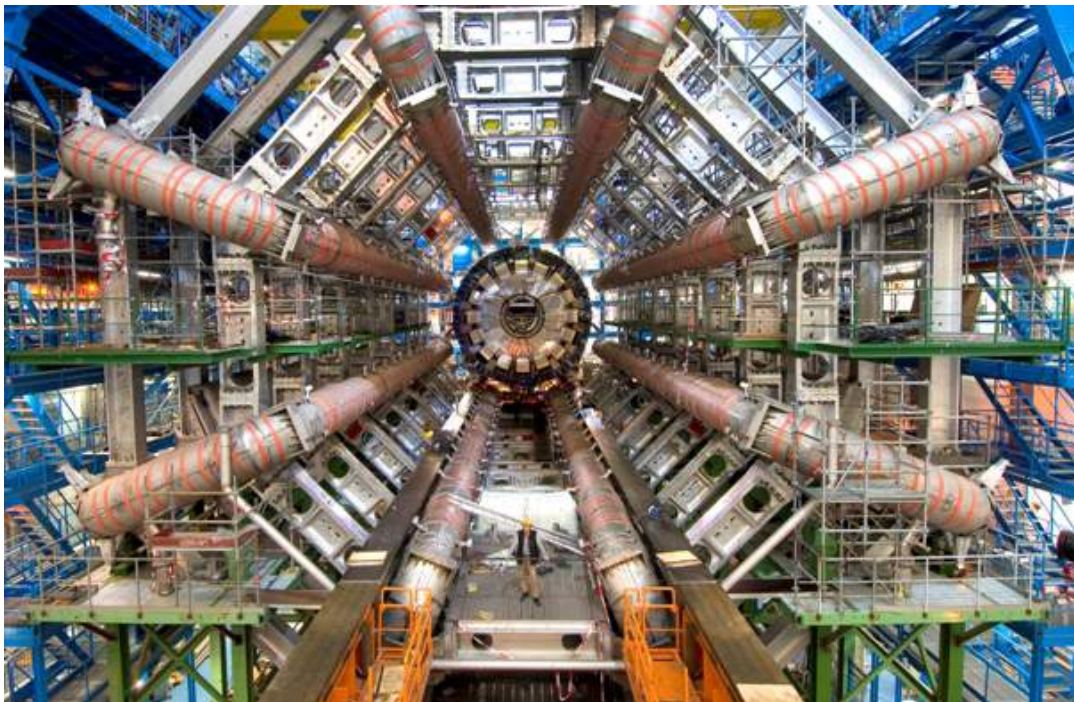


Figure 2.16: Photo of the ATLAS barrel toroid [32].

The two end-cap toroids, shown in Figure 2.17, are positioned at both ends of the central toroid and generate the magnetic fields required for optimising the bending power in the end-cap regions of the MS. They are supported on, and can slide along the central rails, which allows the opening of the detector for access and maintenance.



Figure 2.17: Photo of the ATLAS end-cap toroids [32].

## 2.2.6 The ATLAS trigger system

The ATLAS Trigger and Data Acquisition systems [20, 27], collectively termed TDAQ, are responsible for the collection and storage of data from the ATLAS detector. The proton-proton interaction rate at the design luminosity is approximately 1 GHz. The ATLAS trigger system reduces the rate of data read off the detector to a manageable event data recording rate, which is limited by the technology and resources available to around 200 Hz. This requires an overall rejection factor of  $5 \times 10^6$  against minimum bias processes whilst maintaining the maximum possible efficiency for new physics processes.

The ATLAS trigger is divided into three levels: The Level 1 (L1) trigger, the Level 2 (L2) trigger, and the Event Filter. The L1 trigger uses reduced-granularity information from a subset of detectors (the RPCs and TGCs for high  $p_T$  muons, and all of the

calorimeter subsystems for electromagnetic clusters and jets) to search for signatures from high  $p_T$  muons, electrons/photons, jets and hadronically decaying  $\tau$  leptons, as well as events with large  $E_T^{\text{miss}}$  or total transverse energy. A block diagram for the L1 trigger is shown in Figure 2.18. Results from the L1 muon and calorimeter triggers are processed by the central trigger processor (CTP) which implements a “menu” of trigger selections. It is possible to “pre-scale” trigger items (only accept events fulfilling a given trigger selection for a given fraction of occurrences). This allows optimal use of the available bandwidth as running conditions change. Events passing the L1 trigger selection are then transferred to the detector specific electronics and subsequently to the DAQ system via point-to-point links. The maximum L1 accept rate that can be handled by the detector read-out systems is 75 kHz, and the decision must reach the front-end electronics within  $2.5 \mu\text{s}$  after the bunch crossing with which it is associated.

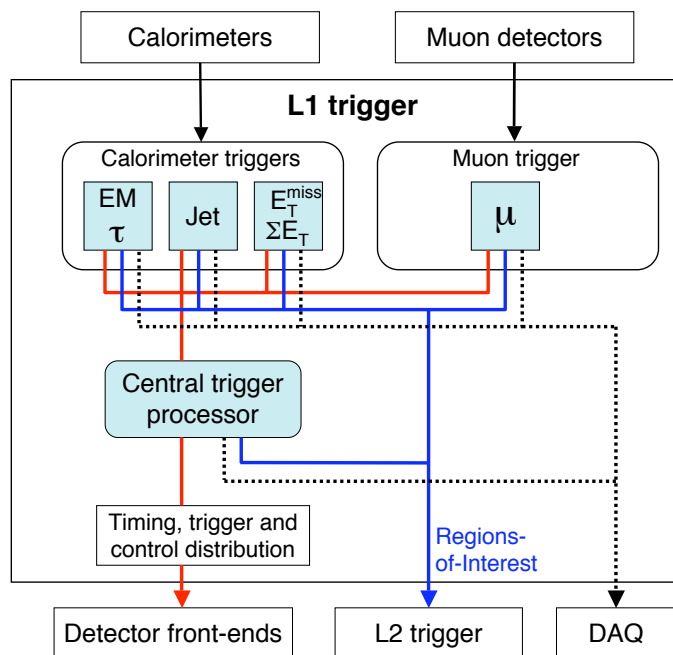


Figure 2.18: Block diagram of the ATLAS Level 1 (L1) trigger [20]. The paths to the detector front-ends, L2 trigger, and data acquisition system are shown from left to right in red, blue and black, respectively.

For a given event, the L1 trigger will identify one or more regions of interest (ROIs), which give the coordinates in  $\eta$  and  $\phi$  of the regions in the detector where its algorithms have identified interesting features. This includes information on the types of feature identified and the criteria passed, which are often thresholds and/or multiplicities. The

ROIs then seed the Level 2 (L2) trigger. This uses ROI information on the coordinates, energy and signature type to limit the amount of data that is transferred from the detector read-out. The L2 trigger has an average processing time of approximately 40 ms and reduces the event rate to below 3.5 kHz.

The final level in the trigger is the Event Filter (EF), which combined with the L2 trigger forms the High Level Trigger (HLT). In the Event Filter, offline analysis procedures are used on fully reconstructed events to further reject events down to a level that can be recorded for offline analysis. It reduces the rate down below 200 Hz, with an average event processing time of the order of four seconds. In the HLT algorithms the trigger selections are refined by using the full granularity and precision from the calorimeters and muon chambers. Track reconstruction from ID information enhances the particle identification, allowing, for example, electrons and photons to be distinguished.

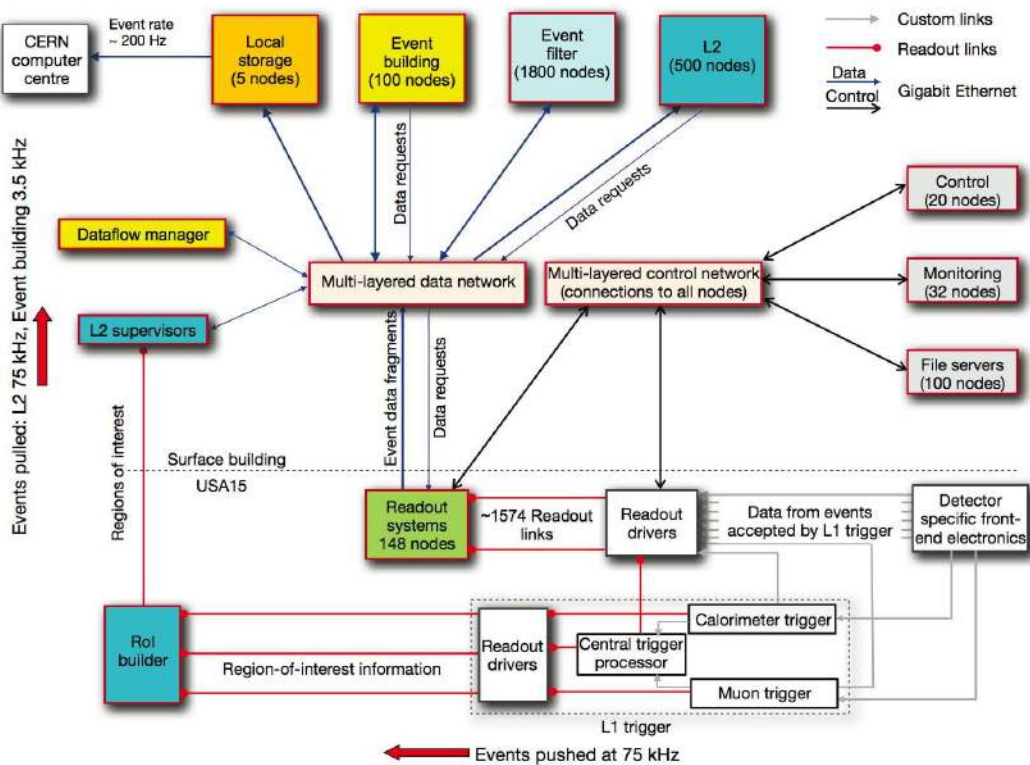


Figure 2.19: Block diagram of the ATLAS TDAQ system [20].

A block diagram showing the full ATLAS TDAQ system is shown in Figure 2.19. The Data Acquisition System (DAQ) receives and buffers the event data at the L1 accept rate

from the detector specific read-out electronics. It transmits to the L2 trigger any data requested by the trigger (usually corresponding to ROIs) and performs event building for events fulfilling the L2 event selection criteria. Assembled events are then moved to the Event Filter, and then those selected are moved to permanent event storage. As well as controlling event movement down the ATLAS trigger chain, the DAQ system also provides for the configuration, control and monitoring of the ATLAS detector during data taking. The Detector Control System (DCS) provides supervision of the detector hardware.

## 2.3 Analysing ATLAS data

### 2.3.1 Introduction

This section discusses the flow of ATLAS data after it has left the ATLAS trigger system, and the reconstruction steps required to convert the data into a form that can be used in physics analyses. Figure 2.20 shows the flow of data selected from the trigger, through the various tiers of the ATLAS computing model [33, 34]. The data read off the detector is organised into data streams, based on the trigger chains used to select the event. These streams are inclusive (so events can appear in more than one) and are broadly categorised into physics streams and calibration streams. For the 2011 and 2012 data-runs, the physics streams were the MinBias, Egamma, Muons, JetTauEtMiss and Cosmic Calo streams. Data is reconstructed using the **Athena** framework [33], and is stored in several data formats, according to the ATLAS event data model (EDM) [33]. To compare observed data with the predictions of the Standard Model, which is essential in all BSM searches, accurate Monte Carlo simulations for different physics processes are also essential. This is handled by the ATLAS simulation framework [35], which is also discussed in this section.

### 2.3.2 The ATLAS event data model

One major challenge for a large collaboration like ATLAS is to ensure easy maintenance and coherence of the experiment's software platform over long periods of time. The ATLAS EDM [33] was designed to give commonality between the data formats used across the different detector subsystems (such as the trigger, ID, and MS), and also to

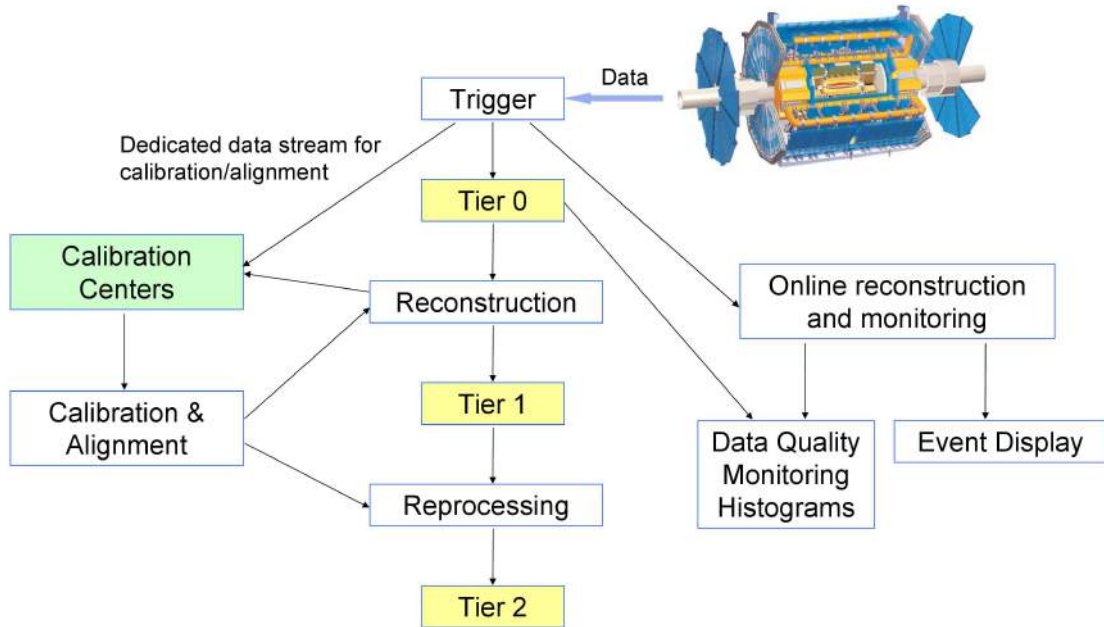


Figure 2.20: Flowchart of ATLAS data through the trigger system, then through the three “tiers” of the ATLAS computing model [36].

allow the use of common software for both online and offline reconstruction. It also had to be consistent with the constraints of the three tier ATLAS computing model, and the **Athena** software framework, both of which will be detailed later.

The EDM defines a number of different data formats: “RAW” data, which is in “byte-stream” format, is the form in which data is read off the detector, and corresponds to about 1.6 MB/event. “ESDs”, or event summary data, contain the full output of reconstruction in object format, where the objects include tracks (and their hits), calo clusters and calo cells. ESDs store (at time of writing) around 1 MB/event. “AODs”, or analysis object data, store the summary of event reconstruction in terms of the “physics” objects, such as electrons, muons and jets, with a nominal size of 100 kB/event. There are also “DPDs”, or derived physics objects. These are collections of skimmed or slimmed events and other useful user-specific data derived from AODs (or ESDs). More specifically, all the analyses discussed in this thesis were performed on “D3PDs”, which are ROOT files centrally produced by the ATLAS supersymmetry working group containing event data necessary for performing physics analyses. Finally, the “TAG” format is a database (or ROOT file) used to quickly select events in AODs or ESDs.

### 2.3.3 The ATLAS computing model

The ATLAS computing model [33], arranges the computing resources for the simulation, reconstruction and analysis of ATLAS data into a hierarchical structure, made of 3 “tiers”. Events passing the Event Filter selection in the HLT are sent to Tier-0 for initial processing by the offline reconstruction software. Tier-0 is a large farm of computers at CERN. This is responsible for copying RAW data to CERN Castor (storage disks) for archiving, and to Tier-1’s for storage and reprocessing. A first pass at calibration and alignment of the detector components is performed at Tier-0 within 24 hours using dedicated data-streams. A first round of reconstruction is also performed at Tier-0, within 48 hours, using the latest calibration and alignment information, and the results of this reconstruction (in the form of ESDs, AODs, DPDs and TAGS) are then transferred to Tier-1’s and Tier-2’s via the CERN computing grid [33].

There are several Tier-1 centres around the world (typically major national computing centres) and many more Tier-2 centres, which are organised into “clouds” around the Tier-1 centres. The Tier-1 centres store a fraction of the RAW data permanently, and are responsible for data reprocessing. This involves re-running the reconstruction software with better alignment and calibration information, and/or improved algorithms. This output is then distributed to Tier-2s. Tier-1 centres are also used to run large scale event selection and analysis jobs for physics and detector groups. The Tier-2 centres are intended for the majority of end-user analysis jobs, but are also used alongside Tier-1 centres for the simulation of ATLAS data, which is discussed further in Section 2.3.6.

### 2.3.4 The Athena framework

Athena is the software framework used in ATLAS for a variety of purposes, including high-level triggering, reconstruction, monitoring, and analysis. It uses `python` as an object oriented scripting and interpreter language to configure and load C++ algorithms and objects. It is based on the Gaudi framework [37], which was originally developed by LHCb. Specific applications, such as reconstruction or simulation, are built from Athena algorithms, that are configured through `jobOptions` files. These are `python` scripts used to control an Athena application configuration at run-time.

### 2.3.5 Reconstructing physics objects

The output of running reconstruction algorithms in *Athena* are physics objects which can then be used in data analysis. This section will summarise some of the algorithms used for reconstructing the physics objects used in subsequent sections, namely electrons, muons and jets. Further discussions can be found in [27].

For electrons, the standard *egamma* reconstruction algorithm [38] used for reconstructing isolated high- $p_T$  electrons is seeded by clusters reconstructed in the electromagnetic calorimeter using the sliding window algorithm (as discussed in Section 2.2.3). Shower shape variables are then calculated around the centre of mass for these clusters and finally track matching is performed, where the best match of the cluster to a track is found.

For muons, tracks are first reconstructed independently in the ID and the MS. The MS tracks are back-extrapolated to the interaction point, and ID track selection can be performed. For identifying muons, there are various possible strategies corresponding to different ways of combining data from the different sub-detectors, and this gives several possible collections of muon objects that can be used in physics analyses. The three which comprise the “StacoMuonCollection” [39], which is used throughout thesis, are “combined”, “segment-tagged” and “stand-alone” muons. Combined muons use ID tracks combined with MS tracks for identification and momentum reconstruction, whereas segment-tagged muons use ID tracks extrapolated to the MS and combined with segments reconstructed in MS stations. Stand-alone muons use only MS tracks which are extrapolated back to the interaction point, however they are not included in the analyses in this thesis.

Of the many jet-finding algorithms available, the default algorithm used in ATLAS to construct jets from calorimeter clusters is the anti- $k_T$  algorithm [40]. Jet-finding is a complicated subject and will not be detailed further here. A discussion of the expected performance of the ATLAS detector for various possible jet algorithms can be found elsewhere [27]. Once jets have been reconstructed, there are additional algorithms available for identifying jets arising from the hadronisation of  $b$ -quarks. These are referred to as “ $b$ -tagging” algorithms, and further information on the algorithms used in ATLAS can be found in [27, 41]. For a specific algorithm, “working points” are defined that correspond to a specified average efficiency of the algorithm.

### 2.3.6 Simulating ATLAS data

A schematic representation of the full Monte Carlo production chain required to produce AODs that can be used in analysis is shown in Figure 2.21. All simulations are performed in `Athena` framework, which provides interfaces to the Monte Carlo event generators where required. The splitting of the chain into distinct steps uses resources (particularly CPU time) more efficiently than a single step simulation, and also simplifies the validation of the software.

The generation step refers to the production of final state primary particles for specified physics processes. Events are produced in the standard HepMC format [42], which is a C++ event record for Monte Carlo event generators, and can be filtered at generation so that only events with a certain property (e.g. lepton multiplicity) are kept. This is often necessary to gain sufficient Monte Carlo statistics for a given signature. The generator is responsible for any prompt decays (of, say,  $W$  or  $Z$  bosons), but stores any “stable” particle expected to propagate through the detector.

In the simulation step, the generated events are passed through a GEANT4 [43] simulation of the ATLAS detector to produce “hits”. These provide a record of where each particle traversed the detector and how much energy was deposited at different points. The configuration of the detector and any misalignments can be specified at run-time.

In the digitisation step, the GEANT4 hits are subjected to the detector response, to give digits (i.e. times and voltages), as in the RAW data from real events in the ATLAS detector. At digitisation, hit outputs from different types of simulated event, including hard scattering signal, minimum bias, and other backgrounds such as beam halo and cavern background, can be overlaid at a user-defined rate before the detector signal is generated. Performing the overlay of pile-up during digitisation rather than at the simulation step reduces the CPU time required by the simulation (which is very CPU intensive). The output of the digitisation is a raw data object (RDO), on which the ATLAS HLT and reconstruction algorithms can then be run, as with data recorded by the detector.

In both the generation and simulation steps of the chain, “truth” information is recorded for each event. For generation, this is a history of the interactions from the generator, including the incoming and outgoing particles at every vertex. In the simulation jobs, the truth information contains truth tracks and decays for certain particles, includ-

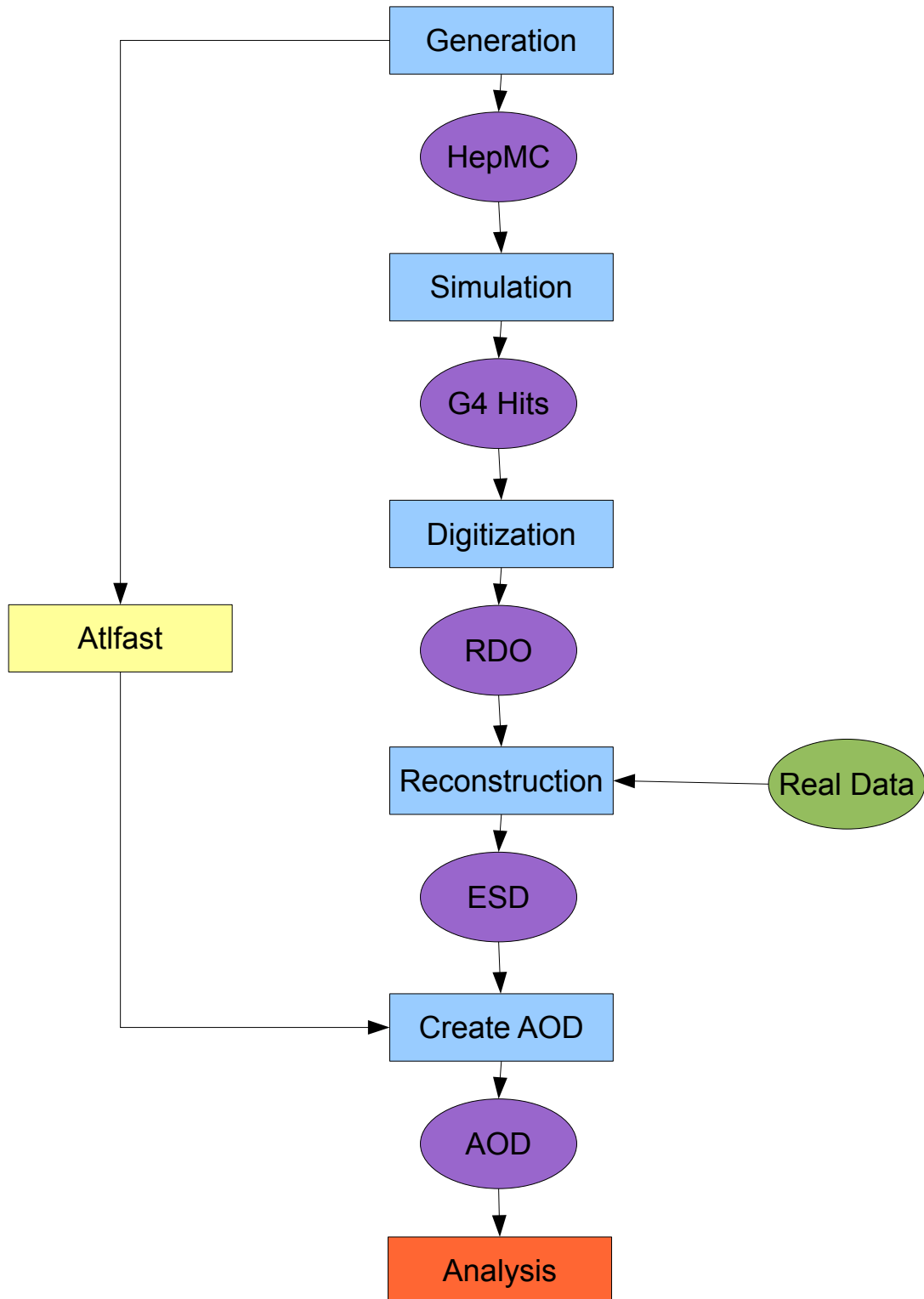


Figure 2.21: Diagram showing the full chain for Monte Carlo production in ATLAS.

ing, for example, the conversions of photons within the ID into electron and positron tracks. In the digitisation step, the truth information is used to create simulated data objects (SDOs), which are maps from the GEANT4 hits in the sensitive regions of the detector to the particles in the simulation truth record that deposited the hit's energy. The truth information is further processed in the reconstruction jobs, and can then be used in physics analyses to match reconstructed objects to particles in the Monte Carlo truth information. This “truth-matching” technique is implemented at various points in this thesis. The presence of truth information is the only difference between simulation and data in reconstruction.

It is possible to avoid performing the full chain by using fast simulation software such as Atfast II [44, 45]. This software essentially replaces the full detector simulation and reconstruction phases of the Monte Carlo reconstruction chains by smearing Monte Carlo truth information directly with resolutions measured in studies using full simulation. It is particularly useful to reduce the CPU time required to simulate large signal grids required in searches for BSM physics.

## 2.4 Conclusion

This section has provided an overview of the ATLAS detector. Brief discussions of the hardware used in the different sub-detectors has been provided, as well as an overview of the software used to simulate and reconstruct ATLAS data. The analyses presented in this thesis use the results of ATLAS data-taking during 2011 and 2012. At this point the author would like to thank all of those involved in the design and installation of the ATLAS detector which occurred prior to the start of the work detailed in this thesis, as well as those involved in designing and implementing all aspects of the ATLAS computing model. The results obtained by ATLAS throughout the first run of the LHC are a credit to the excellent performance of the detector hardware and the ATLAS offline software during its first few years of running.

# Chapter 3

## Theoretical background- the Standard Model and beyond

### 3.1 The Standard Model

#### 3.1.1 Introduction

Our current understanding of particle physics, that is to say the fundamental particles in the universe and the interactions between them, is encapsulated in the Standard Model, which describes the electroweak and strong forces of nature in terms of gauge theories. With very few exceptions (neutrino oscillations being an important example), the Standard Model has performed exceptionally well at describing all experimental data collected in high energy physics throughout the latter half of the 20th Century. Although it does have limitations, which will be discussed in Section 3.1.6, no significant deviations from the predictions of the Standard Model have yet been observed up to the electroweak scale.

This section will proceed as follows: firstly, in Section 3.1.2 an introduction to the Standard Model in the context of quantum field theory will be provided. To simplify the mathematics, analogies to classical mechanics will be drawn and used to explain the underlying concepts. This discussion aims to provide an overview of the mathematical structure of the Standard Model, but will then be followed in Section 3.1.3 by a description of the Standard Model in terms of the elementary particle content, and the interactions between them. Section 3.1.4 will provide a brief overview of the Higgs

mechanism which is used in the Standard Model to invoke the spontaneous breaking of the electroweak symmetry. The Standard Model in its current state will then be summarised in Section 3.1.5, and its limitations discussed in Section 3.1.6. Supersymmetry is a popular extension to the Standard Model, which addresses some of these limitations. An overview of supersymmetry will be provided in Section 3.2.1 and an introductory discussion of standard techniques used to search for supersymmetry at collider experiments will be given in Section 3.2.2.

### 3.1.2 The Standard Model as a quantum field theory

The mathematical formulation of the Standard Model [46, 47] is built by imposing local gauge symmetries on a Lorentz invariant Lagrangian density. Symmetries play an important role, and in fact define the gauge sector of the Standard Model. Before discussing the quantum field theory formulation of the Standard Model, the concepts of the Lagrangian and the principle of least action will be discussed. Noether's theorem, which concerns global symmetries, will be introduced, before proceeding to a discussion of the Standard Model as a fully relativistic quantum field theory.

Returning briefly to the Lagrangian formulation of classical mechanics [47], a kinematic system can be described by a Lagrangian  $L(q_i, \dot{q}_i) = T - V$ , where  $T$  is the total kinetic energy,  $V$  is the potential energy, and  $q_i$  are the set of generalised coordinates that uniquely describe the configuration of the system. The action  $S$  of the system is defined as the time integral of the Lagrangian:

$$S = \int_{t_0}^{t_1} L dt. \quad (3.1)$$

The ‘‘Principle of Least Action’’ then states that the trajectory of the system between times  $t_0$  and  $t_1$  is such that the action is stationary, i.e.  $\delta S = 0$ . This implies that the system obeys the Euler-Lagrange equations of motion, given by

$$\frac{d}{dt} \left( \frac{\partial L}{\partial \dot{q}_i} \right) = \frac{\partial L}{\partial q_i}. \quad (3.2)$$

Classical mechanics deals with systems with a finite number of degrees of freedom. Field theories deal with systems defined by an infinite number of degrees of freedom (the value of the field at all points in space and time). This requires the introduction of the

concept of the Lagrangian density  $\mathcal{L}$  such that

$$S = \int d^4x \mathcal{L}(\phi, \partial_\mu \phi). \quad (3.3)$$

The action is an integral over all space-time of the Lagrangian density, which is a functional involving the field and its derivatives (with respect to the space-time coordinates  $\mu = 0\dots 3$ ) at that point. The Euler-Lagrange equations for the field  $\phi$  then become

$$\partial_\mu \left( \frac{\partial \mathcal{L}}{\partial(\partial_\mu \phi)} \right) = \frac{\partial \mathcal{L}}{\partial \phi}. \quad (3.4)$$

A powerful example of the importance of symmetries in field theories is Noether's theorem [48]. This states that every continuous global symmetry of the Lagrangian gives rise to a conserved current  $j^\mu(x)$  such that the equations of motion imply

$$\partial_\mu j^\mu = 0. \quad (3.5)$$

The existence of a conserved current also implies a conserved charge:

$$Q = \int_{\mathbf{R}^3} d^3x j^0. \quad (3.6)$$

Noether's theorem refers only to global symmetries of the Lagrangian density. When promoting global symmetries to local symmetries, as in the Standard Model, in order to make the Lagrangian density invariant under local transformations generated by a chosen symmetry group, it is necessary to introduce gauge fields, which transform in such a way as to leave the Lagrangian unchanged (they undergo "gauge transformations"). These gauge fields mediate interactions between fields carrying the charges associated with that symmetry. In the Standard Model, after electroweak symmetry breaking, these charges are electric charge for the electromagnetic interaction, colour charge for QCD, and weak isospin for the weak interaction. All Standard Model interactions must conserve these quantities.

In quantum field theories, particles are treated as excited states of underlying physical fields. Distinctions are made between fermionic (half-integer) and bosonic (integer) fields. The quarks and leptons are fermionic fields. Interactions between particles are represented by interaction terms of the underlying fields that appear in the Lagrangian density of the theory. These interaction terms include the gauge fields (which are bosonic fields) that are introduced into the Lagrangian density to make it invariant under local

symmetry transformations.

A gauge theory [47] is a field theory in which the Lagrangian is invariant under a continuous group of local transformations. To give a full mathematical description of the Standard Model, the language of group theory is required. For a given gauge transformation defining a theory, all possible transformations of that type form a Lie group referred to as the symmetry group of that theory. Associated with the Lie group is the Lie algebra of group generators. For each generator of the symmetry under question, there arises a vector field, or gauge field, that must be included in the Lagrangian in order to guarantee invariance of the Lagrangian under the local group transformations. When the theory is then quantised the quanta of these fields are the gauge bosons which mediate interactions between particles.

The Standard Model is a non-abelian (non-abelian refers to non-commutative symmetry groups) gauge theory with the symmetry group  $U(1)_Y \times SU(2)_L \times SU(3)$ , leading to a total of twelve physical gauge bosons (after electroweak symmetry breaking): the photon, three weak gauge bosons and eight gluons. Before electroweak symmetry breaking all the gauge bosons are massless, however the Higgs mechanism, which will be discussed in Section 3.1.4, is invoked to break electroweak symmetry (leading to 3 massive gauge bosons for the weak force and a massless photon for the electromagnetic force). It also enables the inclusion of fermion mass terms in the Lagrangian via Yukawa interactions. The Higgs field is the only scalar field in the Standard Model.

A mathematical discussion of the Standard Model will not be pursued further in this section, but can be found in most standard textbooks on quantum field theory (for example [46, 47]). The next section will introduce the elementary particles in the theory and their interactions. Important experimental observations relevant to the development of the Standard Model will also be included as part of the discussion.

### 3.1.3 Particles and interactions in the Standard Model

Particles in the Standard Model [46, 49] are divided into fermions (which constitute matter) and bosons (which mediate interactions). The fermions can be further divided into quarks (which feel the strong interaction) and leptons (which do not). There are three generations of fermions, which have identical quantum numbers but increasing mass. These are shown in Table 3.1.

Fermion Generations			
<b>Leptons</b>	e	$\mu$	$\tau$
	$\nu_e$	$\nu_\mu$	$\nu_\tau$
<b>Quarks</b>	u	c	t
	d	s	b

Table 3.1: The three generations of Standard Model fermions.

The electroweak quantum numbers for the first generation of fermions are shown in Table 3.2 (it should be noted that all quarks possess an extra degree of freedom, colour). For all quarks and leptons, it is useful to work in the representation where the “left-handed” and “right-handed” chiral components are treated as separate fields. Chirality is an abstract concept that arises when considering possible “representations” (in a group theory sense) of the Lorentz group. The distinction is necessary because experimental observations showed that the weak interaction couples only to left-handed particles. The left-handed components of quarks and leptons appear in the Standard Model as “isospin doublets” (they couple to the SU(2) gauge fields), whereas the right-handed components are “singlets” (they don’t couple to the SU(2) gauge fields). Neutrinos were originally assumed massless in the Standard Model (right-handed neutrinos would have no Standard Model charges). The interactions of the Standard Model will now be discussed further, with references to the charges that they couple to.

The  $U(1)_Y \times SU(2)_L$  symmetry group in the Standard Model generates the electroweak interactions. This unifies the electromagnetic and weak interactions above the unification energy, which is of the order of 100 GeV. The unification of the two forces was proposed by Glashow in 1960 [50] and it acquired its modern form in 1967 when Steven Weinberg [51] and Abdus Salam [52] added the Higgs mechanism [53, 54] to provide a mechanism for electroweak symmetry breaking. Before electroweak symmetry breaking, the gauge bosons are the three  $W$  bosons (often numbered  $W^1$ ,  $W^2$ ,  $W^3$ ) of weak isospin corresponding to  $SU(2)_L$  and the  $B$  boson of weak hypercharge from  $U(1)_Y$ , which are all massless. By invoking spontaneous symmetry breaking through the Higgs mechanism, (see Section 3.1.4) the  $U(1)_Y \times SU(2)_L$  symmetry is broken to  $U(1)_{em}$ . The generator of  $U(1)_{em}$  is given by  $Q = Y/2 + I_3$ , where  $I_3$  is one of the SU(2) generators. Mixing occurs between the neutral  $W^3$  and  $B$  bosons to give the massless

Fermion	Weak Hypercharge	Isospin	Weak Isospin	Electric Charge	
	Y	I	$I_3$	$Q=Y/2+I_3$	
Leptons	$e_R^-$	-2	0	0	-1
	$\begin{pmatrix} \nu_e \\ e^- \end{pmatrix}_L$	-1	$-\frac{1}{2}$	$\frac{1}{2}$ $-\frac{1}{2}$	0 -1
Quarks	$u_R$	$\frac{4}{3}$	0	0	$\frac{2}{3}$
	$d_R$	$-\frac{2}{3}$	0	0	$-\frac{1}{3}$
	$\begin{pmatrix} u \\ d \end{pmatrix}_L$	-1	$-\frac{1}{2}$	$\frac{1}{2}$ $-\frac{1}{2}$	0 $-\frac{1}{3}$

Table 3.2: Electroweak quantum numbers of the Standard Model fermions.

photon, which mediates the electromagnetic force, and the massive neutral  $Z^0$  boson, which causes weak neutral current interactions. This was confirmed experimentally at CERN in 1973 through the observation of neutral current interactions in the Gargamelle bubble chamber [55], and provided strong evidence for the model. The two remaining gauge bosons after electroweak symmetry breaking are the  $W^+$  and  $W^-$  gauge bosons of the weak interaction that couple to weak isospin. They have electric charge, so also couple to the electromagnetic interaction.

Another subtlety of the weak interaction that has been observed experimentally is that for quarks, the eigenstates of the weak interaction (those that couple to the  $W$  and  $Z$  bosons) are different to the mass eigenstates of the Standard Model. This provides a mechanism for the weak interaction to couple different generations of quarks. If this were not the case, for example, the only way for a charm quark to decay weakly would be into a  $W^+$  boson and a strange quark. However, due to off diagonal elements in the CKM matrix [56, 57] (named after Nicola Cabibbo, Makoto Kobayashi and Toshihide Maskawa), which represents the transformation between the two sets of states; decays of a charm quark into, for example, a down quark, are possible.

Quantum Chromodynamics (QCD) is the gauge theory of the strong interaction, and is described by the  $SU(3)$  gauge group. The charge associated with the interaction is referred to as colour charge. There are three colours; red, green and blue. The 1950's saw the invention of spark and bubble chambers, and experimental physicists started to discover a wealth of new particles called hadrons (which we now understand to be

bound states of quarks). Assuming that not all of these new particles were fundamental, attempts were made to classify the hadrons. The proposal by Gell-Mann [58] and Zweig [59] that hadrons were formed of fractionally charged quarks was supported when the predicted  $\Omega^-$  hyperon (which has strangeness -3) was observed experimentally [60]. In 1965 it was realised that an additional quantum number was needed for quarks in order to explain observations, which was later called colour charge [61]. It was also postulated by Moo-Young Han and Yoichiro Nambu that quarks may interact through an octet of vector gauge bosons: the gluons [62]. Although this “quark model”, as it was known, described the experimental observations, no quarks had been observed as free particles, and it was not until 1973, with the formulation of QCD as a SU(3) gauge theory [63], that quarks were accepted as elemental particles. The non-observation of quarks was then consistent with the hypothesised property of confinement.

In QCD there are eight coloured gluons which mediate interactions between quarks, which are the only fermions which feel the strong interaction. As the gluons also carry colour charge they can interact with themselves. These gluon “self interactions” lead to two interesting properties of QCD that are not seen in any of the other interactions: confinement and asymptotic freedom. Colour confinement is the requirement that observed states must have zero colour charge. This means that gluons cannot be observed on their own, since they carry colour charge. Also bare quarks cannot be observed, and must instead form bound states of either three quarks, i.e. baryons, or a quark anti-quark pair (from a colour anti-colour pair), i.e. mesons. An experimental consequence of confinement is that quarks and gluons are not observed as single particles in detectors, but as hadronic jets. Asymptotic freedom is the property that at very high energies, the strong coupling between quarks and gluons actually becomes weaker. This allows perturbative calculations to be performed at high energies.

### 3.1.4 Electroweak symmetry breaking through the Higgs mechanism

The Standard Model breaks the electroweak symmetry (giving masses to the  $Z$  and  $W^\pm$  bosons whilst leaving the photon massless) through spontaneous symmetry breaking with the Higgs mechanism [53, 54]. In this section the concept of spontaneous symmetry breaking will first be introduced, and an example of the spontaneous breaking of a global symmetry will be shown, to demonstrate “Goldstone’s theorem” [64, 65]. The Higgs mechanism, which enables spontaneous breaking of the local electroweak symme-

try in the Standard Model, will then be described, but without a detailed mathematical derivation.

Spontaneous symmetry breaking occurs when the vacuum state of the system does not obey the symmetry of the Lagrangian. As an example, consider a complex Klein-Gordon field, but with an extra interaction term added:

$$\mathcal{L} = \partial_\mu \phi \partial^\mu \phi^* - m^2 |\phi|^2 - \lambda |\phi|^4. \quad (3.7)$$

This extra term does not violate Lorentz invariance and the Lagrangian is still invariant under the global symmetry transformation  $\phi \rightarrow e^{i\alpha} \phi$ . In order to consider the structure of the vacuum, the terms in the Lagrangian which do not involve derivatives (these give the kinetic terms) can be thought of as the potential of the field:

$$V(\phi) = m^2 |\phi|^2 + \lambda |\phi|^4. \quad (3.8)$$

When  $m^2 > 0$  (as is expected for Klein-Gordon fields) the potential has a minimum at  $\phi = 0$  (this is the point about which canonical quantisation of the field is then performed), however in the case that  $m^2 < 0$  the global minimum actually occurs at

$$|\phi| = \frac{\sqrt{-m^2}}{2\lambda} = \frac{v}{\sqrt{2}}, \quad (3.9)$$

where  $v$  is the “vacuum expectation value” of the field. The shape of this potential in the complex plane is the famous “mexican hat” potential often associated with the Higgs field. It should be noted that equation 3.9 does not describe a single point, but a circle of points in the complex  $\phi$  plane that are all degenerate in potential energy. Spontaneous symmetry breaking occurs because for whatever point the theory chooses for the vacuum state, the global symmetry  $\phi \rightarrow e^{i\alpha} \phi$  will then be broken. When quantising the theory, fluctuations about the minimum are considered and interpreted as particles. In this case, when considering fluctuations about the chosen minimum point, there will be a direction (the direction around the circle of degenerate points) where fluctuations have no associated potential energy, which means for sufficiently long wave length fluctuations the energy cost of the fluctuation will be small. This effect is formalised in Goldstone’s theorem [64, 65], which states that for every spontaneously broken global symmetry there will be a corresponding massless boson in the spectrum of possible excited states when the theory is quantised.

When the global symmetry is promoted to a local gauge symmetry, the effect of spontaneous symmetry breaking is that the gauge boson acquires mass. A common explanation is that the Goldstone boson is “eaten” by the gauge field, to become an additional longitudinal polarisation state for the gauge boson, thus making it massive. (Massless gauge bosons only have two transverse polarisation states.)

In the case of the Standard Model electroweak symmetry breaking, the  $U(1) \times SU(2)_L$  symmetry is broken to  $U(1)_{em}$ . A scalar Higgs field is introduced such that it transforms as an  $SU(2)$  doublet with hypercharge  $Y=1/2$ . The three Goldstone bosons that arise from the spontaneous symmetry breaking of the  $SU(2)$  symmetry give mass to the  $W^\pm$  and  $Z$  bosons, whereas the photon, which is the gauge boson corresponding to the  $U(1)_{em}$  symmetry that remains unbroken, remains massless. This mechanism predicts the ratio of the  $W$  and  $Z$  masses to be given by the cosine of the weak mixing angle,  $\cos \theta_W$ .  $\theta_W$  defines the angle by which spontaneous symmetry breaking rotates the original  $W^3$  and  $B^0$  planes to give the photon and  $Z$  boson:

$$\begin{pmatrix} \gamma \\ Z^0 \end{pmatrix} = \begin{pmatrix} \cos \theta_W & \sin \theta_W \\ -\sin \theta_W & \cos \theta_W \end{pmatrix} \begin{pmatrix} B^0 \\ W^0 \end{pmatrix}. \quad (3.10)$$

By construction, the mechanism also predicts the existence of a massive Higgs boson in the Standard Model. The mass of the Higgs boson is not however predicted by the theory and is instead a free parameter in the model. When the LHC began taking data in September 2010, although data from previous experiments (LEP and the Tevatron) had excluded the existence of a Standard Model Higgs boson in certain mass ranges, no direct experimental evidence for its existence had been observed. The observation of a “new particle” with properties consistent with those of the Standard Model Higgs boson, which was announced jointly by the spokespeople of ATLAS and CMS on 4th July 2012 [66, 67], was a huge milestone in particle physics.

The introduction of the Higgs field into the Standard Model Lagrangian also provides a mechanism to generate masses for the fermions. Having a hypercharge of  $Y=1/2$ , the quarks and leptons (but not neutrinos) can acquire masses through coupling to the Higgs field in Yukawa interaction terms. The strengths of the couplings to the Higgs field are proportional to the masses of the particles, which must also be inserted into the Lagrangian as free parameters.

### 3.1.5 Summary of the Standard Model

The Standard Model is a remarkable theory which effectively provides particle physicists with a recipe book for high energy physics. It describes what the fundamental particles in the universe are, what interactions between them are possible and what the probabilities of these interactions are. Although the Standard Model provides an excellent framework for making predictions that can then be tested, in its current form there are 18 free parameters in the Lagrangian which must be measured experimentally then included in the model. These include the masses of all of the quarks and charged leptons (the neutrinos are assumed massless), four parameters (three angles and one CP violating phase) defining the CKM matrix (which was mentioned in Section 3.1.3, and defines the transformation matrix between the quark eigenstates of the weak interaction and the mass eigenstates we observe), and the gauge couplings of the U(1), SU(2), and SU(3) groups. For the electroweak sector, the gauge couplings are usually inferred through measurements of observable quantities such as  $e$ ,  $\sin \theta_W$ , and  $m_W$ . The Higgs mass and Higgs vacuum expectation value must also be included. The requirement that there are so many free parameters that have to be measured experimentally is one limitation of the Standard Model.

### 3.1.6 Limitations of the Standard Model

Despite its enormous success at describing experimental data, the Standard Model cannot provide the complete picture. Firstly, although it explains three out of the four fundamental forces it does not include gravity, whereas ideally scientists would like to have a “theory of everything” which would describe all forces within the same framework. This theory of everything should also account for the large number of free parameters in the Standard Model in a more elegant way than inserting them by hand as measured in experiment. Furthermore the Standard Model with its current particle content does not provide a candidate particle for Dark Matter, which, from cosmological evidence, actually makes up most of the matter content in the universe. (Dark matter is estimated to make up around 25% of the total mass-energy in the universe, with baryonic matter constituting only around 5%. The rest is dark energy.)

Within the model itself, small discrepancies have emerged. For example, when the Standard Model was formulated neutrinos were thought to exist only in one helicity state (i.e. there were no right handed neutrinos) and therefore assumed to be mass-

less. However observations including the solar neutrino deficit [68] and the atmospheric neutrino anomaly [69, 70] provide strong evidence of neutrino flavour oscillations, which would require neutrinos to have a small but finite mass. The Standard Model can be modified to include neutrino masses, but then additional questions arise such as why the observed masses of the neutrinos [15], which are of the order of electron volts, are so much smaller than those of the quarks and charged leptons (which are at the MeV scale, or greater).

Another important problem with the Standard Model is the hierarchy problem [6–9], which effectively questions why the Higgs boson mass is so much lighter than the Planck mass (this is a typical gravitational mass scale where quantum effects become important and is around  $10^{19}$  GeV). A full discussion of the mathematics of the hierarchy problem requires a diversion into the issues of renormalisation in the Standard Model, which will not be taken here. Instead, the problem will be outlined, as a precursor to the discussion of supersymmetry in the next section, which provides an elegant solution to the hierarchy problem.

The “bare” Higgs boson mass, which appears in the Standard Model Lagrangian density, is different to the mass measured experimentally. This is due to radiative quantum corrections to the Higgs boson mass arising from loops with virtual fermions and bosons, such as the contribution from the top quark loop shown in Figure 3.1. When calculating the contribution of such a loop to the Higgs mass, the integral over possible loop momenta diverges, forcing the introduction of an ultra-violet momentum cut-off to regulate the loop integral. This cut-off is interpreted as the scale at which new physics must enter to alter the high energy behaviour of the theory. The contribution to the Higgs mass is then  $\delta m^2 \sim \Lambda^2$ , where  $\Lambda$  is the scale beyond which the low energy theory no longer applies. A more detailed treatment of this problem can be found in [71].

If the cut-off is set to the Planck scale  $M_P$ , the quantum corrections to the squared Higgs boson mass are around 30 orders of magnitude larger than the required value of  $m_H^2 \sim (100 \text{ GeV})^2$  [71]. Therefore, if there was no new physics beyond the Standard Model up to the Planck scale, an incredible amount of fine tuning would be required to cancel the various contributions to  $m_H^2$ . To prevent the Higgs self-coupling getting too strong without fine-tuning, this cut-off scale for new physics is required to be below around a few TeV.

So despite its experimental success over the last half-century, the Standard Model on its own cannot be the “theory of everything”. Some extension, or new physics, is required

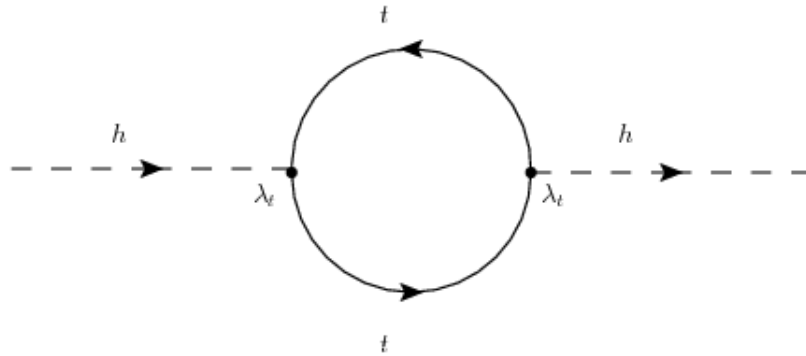


Figure 3.1: Diagram showing the contribution to the Higgs boson mass from a top quark loop [72].

to come into play at the TeV scale in order explain the physics at the Planck scale, and that at the electroweak scale in a coherent way, without large amounts of fine-tuning. There are many possible BSM theories that attempt to address the hierarchy problem. Supersymmetry, which will be discussed in the next section, is one such theory.

## 3.2 Supersymmetry

### 3.2.1 Overview of supersymmetry

Supersymmetry (SUSY) [73–81] is a very popular BSM theory as, if it exists at the TeV scale, it provides an elegant solution to the hierarchy problem. It can also allow the unification of the gauge couplings at high energies [82–90], whereas in the Standard Model the electroweak and strong couplings do not meet. Furthermore, there is a class of supersymmetric theories that can provide a natural candidate for Dark Matter [91, 92] (these are the R-parity conserving models with, for example, the lightest neutralino as the lightest supersymmetric particle). A detailed discussion of supersymmetry can be found in [71].

Supersymmetry relates fermionic and boson degrees of freedom. Essentially new fermion (boson) partners are postulated for all known Standard Model bosons (fermions), and such that their spins differ by a half. The supersymmetric particles have the same quantum numbers as their Standard Model counterparts, except for spin. The total number of bosonic and fermionic degrees of freedom must be equal, so, for example, for a given fermion there are two supersymmetric scalar “sfermions” for each of the left-handed and right-handed fermionic fields. The simplest possible supersymmetric model consistent with the Standard Model includes only the extra particles required to be the superpartners of all existing Standard Model particles. The spin-0 superpartners of the quarks, charged leptons and neutrinos are referred to as squarks, sleptons and sneutrinos respectively. The spin-1/2 superpartners of the gluons are called gluinos. Supersymmetry is invoked before electroweak symmetry breaking therefore the “gauginos”, which are the fermionic superpartners of the Standard Model electroweak gauge bosons, are formed from the supersymmetric partners of the  $W^{1,2,3}$  and  $B$  bosons of the unbroken electroweak symmetry. These are referred to as winos and the bino respectively.

In supersymmetric theories, two Higgs doublets are required in order to give mass to all of the Standard Model particles. After electroweak symmetry breaking this leads to five observable Higgs particles. The neutral scalar that corresponds to the Standard Model Higgs boson is a linear combination of the neutral components of the two doublets. Another complication is that the mass matrices for the supersymmetric particles can mix particles which carry the same values of conserved quantum numbers. In the gaugino sector, the term chargino refers to the superpartners of the charged  $W$  and Higgs bosons and the neutralinos correspond to linear combinations of the bino and neutral higgsinos.

Supersymmetry can solve the hierarchy problem by providing cancellations of the divergent amplitudes in the quantum corrections to the Higgs boson mass [83, 93–97]. This is because the signs of fermionic and bosonic corrections to the squared Higgs mass are opposite. In supersymmetric theories, the contribution to the quantum correction of a given particle is cancelled by that of its supersymmetric particle, thus giving zero contribution to the divergence. This is shown in Figure 3.2, and an explicit example of such a calculation is given in the appendix of [98].

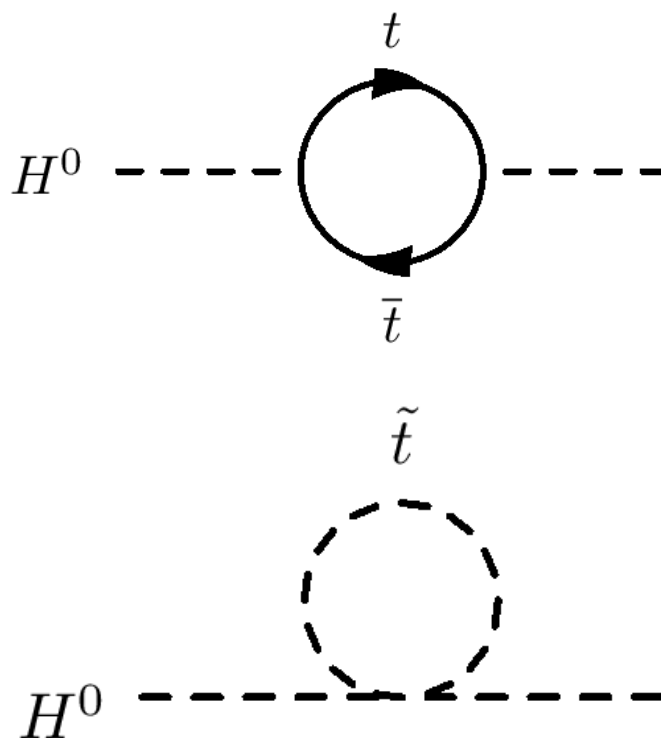


Figure 3.2: Diagrams showing how supersymmetry can offer a solution to the hierarchy problem, by providing a supersymmetric bosonic loop for every Standard model fermionic loop (and vice versa) such that contributions to the quadratic divergence in the squared Higgs mass vanish [99].

Since supersymmetric partners of the Standard Model particles have not been observed experimentally, supersymmetry must be a broken symmetry. This does not prevent it from solving the hierarchy problem as even with different masses, the one loop divergences will still cancel provided that the SUSY particles have masses at or below the Fermi scale (i.e.  $|M_F^2 - M_B^2| < 1 \text{ TeV}^2$ ).

In supersymmetric extensions of the Standard Model there are some couplings that

do not conserve lepton or baryon number. These symmetries have been tested to high precision in the Standard Model, so such couplings need to be very small in order not to conflict with existing experimental data (such as the lifetime of the proton). It is possible to define a quantity called R-parity [93, 100–103]:

$$R = (-1)^{2s+3B+L}, \quad (3.11)$$

where  $s$  is the spin,  $L$  the lepton number and  $B$  the baryon number. By requiring that R-parity be conserved in all interactions, lepton and baryon-number violating couplings are then suppressed. All Standard Model particles have an R-parity value of 1 while supersymmetric particles have an R-parity of -1. R-parity values combine multiplicatively, so conservation of R-parity means that supersymmetric particles must be produced in pairs. Each sparticle would then decay, in an R-parity conserving cascade or directly, to the lightest supersymmetric particle (LSP) which would be stable. R-parity conserving SUSY models are often favoured because the LSP can provide a natural candidate for Dark Matter.

This discussion has concentrated on the concepts involved in a minimal extension of the Standard Model. Formally, the Minimal Supersymmetric Standard Model (MSSM) is the minimal extension to the Standard Model, as described above, which invokes R-parity conservation to explain the stability of the proton (whose decay would violate lepton/baryon number) [93, 100–103]. To incorporate supersymmetry into a realistic theory, one requires that the underlying dynamics of the theory be supersymmetric but that this symmetry is not reflected in the ground state of the system because the symmetry is broken. The mechanism for SUSY breaking is unknown. SUSY breaking cannot be achieved in the MSSM alone, therefore there must be a new sector of the theory responsible for SUSY breaking, the only constraint being that it must break supersymmetry permanently and give the superpartners TeV scale masses. In the MSSM, to parametrise the relevant features, soft supersymmetry breaking operators are added into the Lagrangian to explicitly break SUSY, but which do not explain the mechanism of SUSY breaking. These terms mean that the MSSM contains 105 free parameters, in addition to the Standard Model free parameters.

With 105 free parameters in the theory, when no additional constraints are applied, the MSSM is too complex to study in detail. Because the nature of the mechanism that breaks supersymmetry is unknown, the number of free parameters can be reduced and hence the theory simplified by specifying a particular SUSY-breaking scenario. A pop-

ular example is minimal super-gravity mediated SUSY breaking (mSUGRA) [104, 105]. This has been widely studied as once supersymmetry breaking has been invoked only four input parameters and a sign are required to determine the low energy phenomenology from the scale of grand unification. The masses and couplings are described in terms of four parameters:  $m_0$ , the universal scalar mass,  $m_{\frac{1}{2}}$  the universal gaugino mass,  $A_0$  the trilinear coupling (a constant related to the Higgs sector of the theory) and  $\tan\beta = v_2/v_1$ , where  $v_1$  and  $v_2$  are the vacuum expectation values of the Higgs fields. There is also a parameter  $\text{sign}(\mu)$ , which is the sign of the Higgs mixing parameter. Other popular symmetry breaking scenarios include Gauge Mediated Supersymmetry Breaking (GMSB) [106, 107] and Anomaly Mediated Supersymmetry Breaking (AMSB) [108].

Each SUSY breaking mechanism strongly influences the mass spectra and decay patterns of the sparticles in the theory and so biases the signals that can be targeted. It also makes it difficult to make model-independent statements about the theory. Two approaches which can be used to look at SUSY in a more general way are the phenomenological Minimally Supersymmetric Standard Model (pMSSM) [109, 110], and the use of simplified models [111], both of which are used in this thesis.

The pMSSM arises from imposing a set of theoretically and experimentally motivated constraints on the general MSSM, whilst leaving the specific SUSY-breaking mechanism unspecified. This class of models is becoming increasingly relevant as exclusion limits in models such as mSUGRA are being pushed to higher masses. The pMSSM is based on the most general CP-conserving MSSM, with R-parity conservation, and minimal flavour violation. The first two generations of sfermions are also required to be degenerate and have negligible Yukawa couplings. This leaves 19 independent weak scale parameters to consider: there are the ten sfermion masses (five for the degenerate first two generations and five for the third generation), three tri-linear couplings  $A_{\tau,t,b}$  which give the couplings between the Higgs field and the third generation sfermions, the bino, wino and gluino mass parameters  $M_{1,2,3}$ , the higgsino mixing parameter  $\mu$ , the ratio of the vacuum expectation values of the Higgs fields  $\tan\beta$ , and the mass of the pseudoscalar Higgs boson  $m_A$ .

Another approach to make statements about supersymmetry whilst minimising the model dependence of the conclusions is the use of simplified models. These have been used extensively throughout the first run of the LHC. A simplified model is specifically designed to involve only a few new particles and interactions. In theories such as SUSY where a large number of new particles are predicted, this is usually achieved by setting the masses of the other particles heavy, so they are out of the reach of the experiment.

Simplified models can often be described by a small number of parameters, such as the masses of the particles involved. This simplifies the interpretation of results and also allows rare signatures to be targeted, independent of other possible new particles. The results of such searches can also then be interpreted in a wider context, for example to provide limits on other models that could give rise to the same topology.

To summarise, this sub-section has provided an overview of supersymmetry as a theory. Due to its theoretical advantages, in solving the hierarchy problem, and, in some cases, providing a natural candidate for Dark Matter, it has been searched for extensively at collider experiments. The next section will discuss techniques for searching for supersymmetry at colliders such as the LHC.

### 3.2.2 Searching for supersymmetry at colliders

Different supersymmetric models will typically give different signatures. In R-parity conserving supersymmetric models, sparticles must be pair produced, and each then decays in a chain that must end in the lightest supersymmetric particle (LSP), which is usually the neutralino or gravitino. The LSPs then escape undetected, so a typical signature involves missing transverse energy,  $E_T^{\text{miss}}$ , and then other objects produced in the decay chains such as leptons and jets. In R-parity violating models, single sparticle production can occur, or in the case that the R-parity violating couplings are weak, sparticle pair production can still dominate, and interesting signatures can arise from the subsequent decay of the LSP. Some supersymmetric models also predict long-lived particles, which then decay in-flight in the detector. Examples include AMSB, which often leads to a small mass splitting between the lightest chargino and the LSP. The long-lived chargino can then be observed in the detector [112].

All of the models tested in this thesis concern searches for R-parity conserving supersymmetric models with a neutralino LSP. The pair production of different sparticles will give different characteristic signatures in the detector, which can then be searched for. The sensitivity of a given search will depend on the cross-section for SUSY production, and the background processes to the signatures being targeted. Figure 3.3 shows cross-sections for supersymmetric pair production for various pair production processes at centre-of-mass energies of 7 TeV and 8 TeV, as calculated to next-to-leading (NLO) order in the strong coupling constant by PROSPINO [113].

If they were light, it was expected that the LHC would be a “squark and gluino”

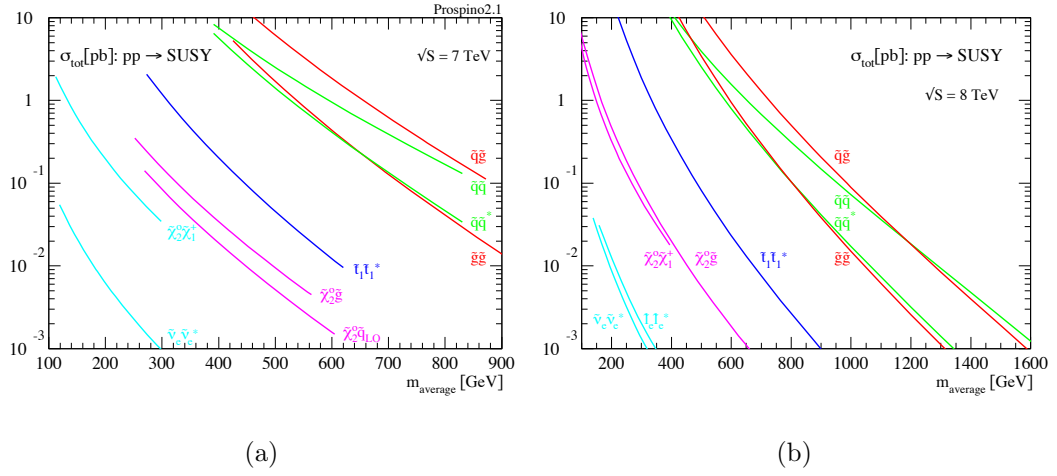


Figure 3.3: Cross-sections for supersymmetric particle production calculated using PROSPINO [113], for centre-of-mass energies of 7 TeV (a) and 8 TeV (b).

factory, as, they can be produced by the strong interaction so have higher cross-sections. Pair production of squarks and gluinos were therefore the first processes targeted at the LHC. For a given signature, typical SUSY searches involve identifying a signal region, where we would expect to see a significant excess of signal over the background, and then comparing the Standard Model expectation with the observed data. The statistical methods used to quantify the level of agreement between the data and the background expectation are discussed in the next chapter.

# Chapter 4

## Statistical techniques for searching for new physics

### 4.1 Introduction

In high energy physics, searches for new physics rely on being able to quantify the level of agreement of the observed data with a given hypothesis. In simple “cut-and-count” experiments, this equates to computing the level of agreement of the observed data count in a given signal region, with the Standard Model expectation value, taking into account both statistical and systematic uncertainties on the signal region estimate. This chapter will explain the important concepts and techniques used in the statistical interpretation of searches for new physics in ATLAS.

Section 4.2 provides an introduction to the underlying concepts of frequentist hypothesis testing, and the  $CL_s$  technique, which is used to calculate all exclusion limits in this thesis. Section 4.3 then contains a discussion of standard ways to extend the simple cut-and-count scenario to increase the sensitivity of searches. This includes determining background normalisation parameters by including control regions in the likelihood function, and using binned fits to exploit shape information. All of these techniques were implemented in the 2012 data analysis discussed in Chapter 7. For performing the statistical interpretation of results in this thesis, a package called `HistFitter` was used, which is based on the `RooStats` framework [4].

## 4.2 Establishing discoveries or exclusions in the cut-and-count scenario

### 4.2.1 Introduction

This section will discuss the concepts and techniques used for establishing either a discovery or exclusion in a simple cut-and-count scenario. It is assumed that the observation against which the hypothesis is tested corresponds to the data count in one single signal region. The extension of this scenario will be discussed later in Section 4.3. Firstly, the concepts of p-values and test statistics will be introduced, with a focus on the profile log-likelihood ratio, which is the test statistic used in all searches in this thesis. Frequentist hypothesis testing will be discussed and finally, the  $CL_s$  technique [3, 114] will be introduced. This is often referred to as a modified frequentist technique, and is the standard technique used in both ATLAS and CMS for calculating exclusion limits in searches for new physics.

### 4.2.2 p-values and likelihoods

An important building block for frequentist hypothesis testing is the concept of a p-value. The p-value of a hypothesis is the probability, under the assumption of that hypothesis, of obtaining data with equal or lesser compatibility with the hypothesis compared to the level of compatibility found with the observed data. Computing the p-value for a hypothesis is the usual way to quantify the level of compatibility of the hypothesis with the observed data.

The significance of a p-value is the number of standard deviations  $Z$  at which a Gaussian random variable of zero mean would give a one-sided tail area equal to the p-value. The two values are thus related by

$$p = \int_Z^{\infty} \frac{1}{\sqrt{2\pi}} e^{-x^2/2} dx = 1 - \Phi(Z), \quad (4.1)$$

where  $\Phi$  is the cumulative distribution function for the standard Gaussian. Alternatively, inverting this equation gives

$$Z = \Phi^{-1}(1 - p). \quad (4.2)$$

In high energy physics, a significance of three is often referred to as “evidence” whereas a significance of five is usually required to claim a discovery. These correspond to p-values of  $1.35 \times 10^{-3}$  and  $2.87 \times 10^{-7}$  respectively.

Frequentist hypothesis testing is based around constructing “test statistics” to provide an estimate of the p-value for a given hypothesis, that can then be used to either claim discovery or exclusion of a given model. An important ingredient in constructing test statistics is the likelihood function. The likelihood of a hypothesis based on parameters  $\boldsymbol{\theta}$ , assuming the outcome  $x$ , is defined as

$$\mathcal{L}(\boldsymbol{\theta}|x) = P(x|\boldsymbol{\theta}). \quad (4.3)$$

The likelihood quantifies the probability of the observed data, under the assumption of a given hypothesis. For a BSM theory such as SUSY, the hypothesis in its theoretical form comprises a quantum field theory Lagrangian density. The parameters of the theory can be used to make predictions for the probability of specific outcomes of experiments. This prediction could be the cross-section for the pair production of a certain type of particle, which, once the event selection of an analysis had been performed, would correspond to a quantifiable excess in a given signal region. In the simple cut and count case, where  $n$  events are observed in the signal region, the likelihood can be written as

$$\mathcal{L}(n, \boldsymbol{\theta}^0 | \mu, \boldsymbol{\theta}) = P_{\text{SR}} \times P_{\text{SYST}} = P(n|\lambda(\mu, \boldsymbol{\theta})) \times P_{\text{SYST}}(\boldsymbol{\theta}^0, \boldsymbol{\theta}). \quad (4.4)$$

The first number reflects the Poisson probability of measuring  $n$  events in the signal region.  $\lambda$  is the Poisson expectation for the signal region and depends the signal strength  $\mu$ , and the set of nuisance parameters  $\boldsymbol{\theta}$  that parametrise the systematic uncertainties in the analysis.  $\mu = 1$  corresponds to the nominal value of the signal expectation for the model under question, and for  $\mu = 0$  the signal is turned off. This assumes that the background normalisation is fixed (the possibility of including background normalisations as free parameters will be revisited in Section 4.3.2). The probability density function  $P_{\text{SYST}}$  handles the systematic uncertainties.  $\boldsymbol{\theta}^0$  are the nominal values around which the systematic uncertainties can be varied. A common implementation of systematic uncertainties is to model them as unit Gaussians such that  $\theta_i^0 = 0$  and  $\theta_i = \pm 1$  correspond to one sigma deviations about the nominal value. For independent nuisance parameters (i.e. un-correlated systematics)  $P_{\text{SYST}}$  is then the product of the unit Gaussians for each systematic uncertainty.

### 4.2.3 Frequentist hypothesis testing

The frequentist formalism for statistical interpretation of results will now be summarised, though a more detailed discussion can be found in [115]. When testing for discovery or exclusion it is necessary to distinguish between the “background-only” hypothesis, which contains only known processes (i.e. the Standard Model) and the “signal-plus-background” hypothesis, where for all analyses in this thesis the signal is a supersymmetric process of interest. When testing a discovery, the p-value for the background-only hypothesis is required to be below a given threshold, whereas for exclusion limits, signal-plus-background hypothesis must be rejected to a certain confidence level.

Likelihood ratios can be used to quantify the agreement of the measurement  $n$  with one prediction  $\lambda(\mu, \boldsymbol{\theta})$  relative to the agreement with another prediction  $\lambda(\mu', \boldsymbol{\theta}')$ . A typical likelihood ratio (LR) can be written as

$$\text{LR} = \frac{\mathcal{L}(n|\mu, \boldsymbol{\theta})}{\mathcal{L}(n|\mu', \boldsymbol{\theta}')} \quad (4.5)$$

The Neyman-Pearson lemma [116] states that when comparing two point hypotheses  $H_0$  and  $H_1$ , defined by parameters  $\theta_0$  and  $\theta_1$ , the likelihood ratio test for an observation  $x$  defined by

$$\Lambda(x) = \frac{\mathcal{L}(\theta_0|x)}{\mathcal{L}(\theta_1|x)} \leq \eta, \quad (4.6)$$

where  $P(\Lambda(x) \leq \eta|H_0) = \alpha$ , is the most powerful test of size  $\alpha$ , that rejects  $H_0$  in favour of  $H_1$ . This only holds for hypotheses with no unknown parameters, however likelihood ratios are also used to construct the test statistics used in searches for new physics. The construction of test statistics using likelihood ratios is discussed extensively in the literature [115]. The version of the likelihood ratio used in ATLAS is the lower bound one-sided profile log likelihood ratio, defined by:

$$q_\mu(n) = \begin{cases} -2 \log \frac{\mathcal{L}(n|\mu, \hat{\boldsymbol{\theta}}_\mu)}{\mathcal{L}(n|\hat{\mu}, \hat{\boldsymbol{\theta}}_{\hat{\mu}})} & \mu \geq \hat{\mu} \geq 0 \\ 0 & \text{otherwise} \end{cases} \quad (4.7)$$

The nuisance parameters  $\boldsymbol{\theta}$  are chosen such that the likelihood of the observation is maximised. The  $\hat{\boldsymbol{\theta}}_\mu$  are obtained by performing a constrained maximum likelihood fit as a function of  $\mu$  (i.e. the parameters are chosen such that  $\mathcal{L}(n|\mu, \hat{\boldsymbol{\theta}}_\mu) \geq \mathcal{L}(n|\mu, \boldsymbol{\theta})$  for all

$\theta$ ). The values  $\hat{\mu}$  and  $\hat{\theta}_{\hat{\mu}}$  correspond to the global maximum of the likelihood (i.e.  $\hat{\mu}$  and  $\hat{\theta}_{\hat{\mu}}$  are chosen such that:  $\mathcal{L}(n|\hat{\mu}, \hat{\theta}_{\hat{\mu}}) \geq \mathcal{L}(n|\mu, \theta)$  for all  $\mu, \theta$ ). The profile log-likelihood ratio is a positive quantity, and the larger it is the more the observation  $n$  disagrees with the prediction of  $\lambda(\mu, \hat{\theta}_{\mu})$  compared to  $\lambda(\hat{\mu}, \hat{\theta}_{\hat{\mu}})$ .  $\hat{\mu}$  is constrained to be non negative so that only positively scaled cross-sections are considered (this assumes that the signal can only enhance the total count in the signal region).

The observation  $n$  is subject to statistical fluctuations, so  $q_{\mu}(n)$  will have different values in independent measurements. Assuming that the expectation value of the measurement can be described by the (Poisson) prediction  $\lambda(\mu, \hat{\theta}_{\mu})$ , the distribution of the test statistic can then be described by a probability distribution  $f(q_{\mu}|\mu)$ . From this distribution, the p-value for a hypothesised value of  $\mu$  can be calculated by assuming that values of  $q_{\mu}$  higher than that observed correspond to measurements of greater disagreement with the data. This gives

$$p_{\mu} = \int_{q_{\mu, obs}}^{\infty} f(q_{\mu}|\mu) dq_{\mu}. \quad (4.8)$$

Since analytic evaluation of  $f(q_{\mu}|\mu)$  is generally not possible, it must be approximated. There are typically two approaches used for the approximation of  $f(q_{\mu}|\mu)$ . The first involves using a large number of simulated Monte Carlo toy measurements and replicas to sample the distribution of  $f(q_{\mu}|\mu)$ . In principle this method could be used to determine the distribution with arbitrary precision, but in practise the computational costs increase with the number of toys. A computationally less intensive approach uses an approximate analytic expression often referred to as the asymptotic formula [115, 117] (derivations of the formulae for general likelihood based test statistics can be found in [117]). The formula uses the result from [118] that for a large number of samples  $N$  in the measurement  $n$  the test statistic can be approximated as

$$q_{\mu}(n) \sim \left( \frac{\mu - \hat{\mu}}{\sigma} \right)^2 + \mathcal{O} \left( \frac{1}{\sqrt{N}} \right). \quad (4.9)$$

This assumes  $\hat{\mu}$  is Gaussian distributed about its true mean  $\mu_0$  with a standard deviation  $\sigma$ , which can be estimated through

$$\sigma^2 \approx \frac{(\mu - \mu_0)^2}{q_{\mu}(n^A)}. \quad (4.10)$$

In this equation  $q_{\mu}(n^A)$  is the test statistic evaluated for the ‘‘Azimov data set’’ [115].

This is defined as a set with infinite statistics corresponding to the prediction  $\lambda(\mu, \hat{\theta}_\mu)$ . Observables evaluated using the Azimov data set will have their true values, i.e.  $\hat{\mu} = \mu_0$ . The Azimov set can either be calculated using the expected values of the hypothesis exactly, or by approximating it by performing a sufficiently high statistics Monte Carlo simulation of the prediction. Under these assumptions, the distribution  $f(q_\mu|\mu)$  for the test statistic in Equation (4.7) is given by Equation (57) in [117].

#### 4.2.4 The $CL_s$ technique

Instead of directly calculating a p-value, the  $CL_s$  method uses a “modified frequentist” technique to set upper limits on cross-sections and constrain model parameter values. This technique was developed at LEP for placing exclusion limits on the mass of the Standard Model Higgs boson. Detailed discussions can be found in the literature [3, 114], but a summary will be provided here. The  $CL_s$  value for a given hypothesis is constructed from the ratio of the p-values for the signal-plus-background and background-only hypotheses. To provide a measure of the statistical significance of the observation, that is to say, the likelihood it could have arisen by chance,  $CL_{s+b}$  is defined as the p-value for the signal-plus-background hypothesis, which is given by

$$CL_{s+b}(\mu) = \int_{q_{\mu,obs}}^{\infty} f(q_\mu|\mu) dq_\mu. \quad (4.11)$$

As a reminder, this p-value corresponds to the cumulative probability of observing a measurement that yields a higher value of the test statistic than that observed, assuming that the Poisson probability distribution  $\lambda(\mu, \hat{\theta}_\mu)$  correctly models the outcome of the observation. Large values of  $CL_{s+b}$  thus imply high compatibility with  $\lambda(\mu, \hat{\theta}_\mu)$  (because there is a large probability of observing data with equal or worse probability with your hypothesis). When constructing the  $CL_s$  value, this p-value is normalised by dividing by the probability of observing a larger test statistic than the observed one, under the assumption of the background-only hypothesis. This p-value is denoted  $1 - CL_b$ :

$$CL_s(\mu) = \frac{CL_{s+b}}{1 - CL_b}. \quad (4.12)$$

The quantity  $1 - \text{CL}_b$  is defined as

$$1 - \text{CL}_b = \int_{q_{\mu,obs}}^{\infty} f(q_{\mu}|0) dq_{\mu}. \quad (4.13)$$

The distribution  $f(q_{\mu}|0)$  can be derived using the same methods as for  $f(q_{\mu}|\mu)$ , either by generating toy replicas or using the asymptotic formula. This quantity provides a measure of the disagreement of the observation with the background-only hypothesis. It is intended to quantify how frequently a measurement suggesting a higher signal contribution than that observed would occur due to background fluctuations.

Figure 4.1 shows probability distribution functions for the test statistic used in final combination of searches for the Standard Model Higgs boson from the four experiments at LEP [119], for the signal-plus-background and background only hypothesis, assuming that the signal corresponded to a Standard Model Higgs boson at  $m_H = 115.6$  GeV. LEP used a different test statistic to the profile log-likelihood defined in Equation (4.7), which was defined as  $Q = \mathcal{L}_{s+b}/\mathcal{L}_b$ . The values of  $\text{CL}_{s+b}$  and  $1 - \text{CL}_b$  correspond to the dark (green) and light (yellow) shaded regions respectively.

$\text{CL}_s$  provides a measure of how well the predictions of  $\lambda(\mu, \hat{\theta}_{\mu})$  can be distinguished from  $\lambda(\hat{\mu}, \hat{\theta}_{\hat{\mu}})$  based on the observed measurement. Normalising to  $1 - \text{CL}_b$  is aimed at regulating the behaviour of  $\text{CL}_{s+b}$  for models where sensitivity would not be expected. Without it, statistical downward fluctuations in the background expectation could lead to deficits in observed events which are inconsistent with the expected background. This could cause the signal-plus-background hypothesis to be excluded even if the expected signal contribution is so small there should be little or no experimental sensitivity. This would be especially important in searches involving low background expectations. Small values of  $\text{CL}_s(\mu)$  imply that a signal strength of  $\mu$  is strongly disfavoured compared to  $\lambda(\hat{\mu}, \hat{\theta}_{\hat{\mu}})$ . A signal hypothesis is considered excluded at 95% confidence level if it has  $\text{CL}_s < 0.05$ .

#### 4.2.5 Systematic errors as nuisance parameters and profiling

As discussed in Section 4.2, systematic uncertainties on the Poisson expectation for the event count in a signal region are included in the likelihood as nuisance parameters. The test statistic used in ATLAS uses a profile likelihood ratio, where, for a given value of the parameter of interest (the signal strength in this discussion), the nuisance parameters

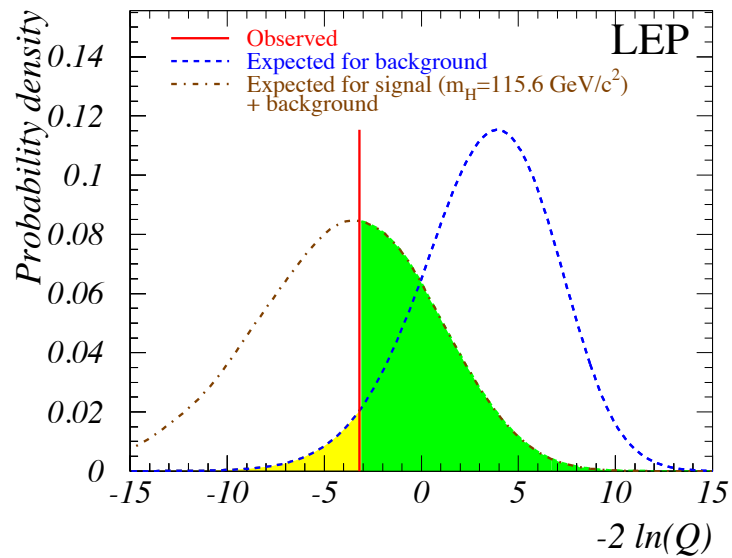


Figure 4.1: Probability density functions taken from the LEP Higgs combination [119] corresponding to a test-mass  $m_H = 115.6$  GeV, for the background and signal-plus-background hypotheses. The observed value of  $-2 \ln Q$  (where  $Q = \mathcal{L}_{s+b}/\mathcal{L}_b$ ) which corresponds to the data is indicated by the vertical line. The light shaded region is a measure of the compatibility with the background-only hypothesis,  $1 - \text{CL}_b$ , and the dark shaded region is a measure of compatibility with the signal-plus-background hypothesis,  $\text{CL}_{s+b}$ .

are determined using a constrained maximum likelihood fit (see Equation 4.7). After performing the fit, the Poisson expectation for the signal region is then a function of  $\mu$  with the nuisance parameters set to their optimal values  $\hat{\theta}_\mu$ . This maximises the agreement with the observation for a given value of  $\mu$ , which in turn reduces the sensitivity. This can be easily visualised in the case of exclusion: in allowing the profiling of nuisance parameters, for a given value of  $\mu$ , the nuisance parameters will be fixed at the value that maximises the agreement of the data with the hypothesis, therefore the likelihood of exclusion is reduced. Within this framework, it is important to ensure that nuisance parameters are not being over-profiled, that is to say, constrained by the fit to have unphysically small values. In all analyses in this thesis, the outputs of the fits used in calculating  $\text{CL}_s$  were checked to ensure that no significant over-profiling was observed.

#### 4.2.6 Calculating expected limits

As well as computing  $\text{CL}_s$  values, for a given observation, it is also useful to be able to quantify the expected  $\text{CL}_s$  value for a given hypothesis. This is useful when assessing the potential sensitivity of an experiment to a given scenario. Focussing for now on exclusions, the expected exclusion sensitivity for a given signal hypothesis ( $\mu = 1$ ) is taken from the median  $\text{CL}_s$  value for that hypothesis, assuming that the data was generated by the  $\mu=0$  hypothesis. Essentially the lower limits in Equations (4.11) and (4.13) are replaced by the median value of the distribution  $f(q_\mu|0)$  (which must then be evaluated). Methods for calculating expected p-values using the Azimov dataset are detailed in [115] but will not be discussed further here. All of the exclusion plots presented in this thesis display the expected exclusion contours as well as the observed ones. When limits are calculated with data compatible with the background-only hypothesis, the observed contour is equally likely to fall above or below the expected one. If the observed limit is stronger than expected, this implies an under-fluctuation of the observed data, and vice versa.

## 4.3 Extending the simple cut-and-count scenario

### 4.3.1 Introduction

This section will introduce some common ways to extend the sensitivity of the simple cut-and-count analysis described in the previous section. Firstly, the simultaneous fitting of background normalisation factors by including them as nuisance parameters in the likelihood is discussed in Section 4.3.2. Secondly, when trying to extend the reach of a search, incorporating additional information into the likelihood can enhance the sensitivity if this information increases the discrimination between the signal and background. Two such ways of achieving this: statistically combining signal regions, and performing binned fits to exploit shape information, are then introduced in Section 4.3.3 and Section 4.3.4 respectively.

### 4.3.2 Simultaneous fitting in signal and control regions

The discussion in Section 4.2 assumed that the background normalisation was fixed in the likelihood function. This could either be through relying only on the Monte Carlo prediction, or by performing data driven calculations for the signal region estimates. If using data driven methods any additional uncertainties from these methods, for example due to limited statistics in control regions, would need to be included as nuisance parameters in the fit. Control regions are designed to be enriched in a given background component, the normalisation of which can then be measured in that control region (examples of these methods are given in Section 6.5 of Chapter 6).

Assuming the control regions are orthogonal to the signal regions, they can be included as channels in the likelihood:

$$\mathcal{L}(\mathbf{n}, \boldsymbol{\theta}^0 | \mu, \boldsymbol{\theta}) = P(n_s | \lambda_s(\mu, \mathbf{b}, \boldsymbol{\theta})) \times \prod_{i \in CR} P(n_i | \lambda_i(\mu, \mathbf{b}, \boldsymbol{\theta})) \times P_{\text{SYST}}(\boldsymbol{\theta}^0, \boldsymbol{\theta}). \quad (4.14)$$

In this treatment, the background normalisation factors  $\mathbf{b}$  are nuisance parameters in the fit and can be extracted from the fit. They are profiled in the same way as the nuisance parameters defining the systematic uncertainties. The vector  $\mathbf{n}$  now refers to the set of observations in the signal regions and the control regions defined for determining background normalisation. The subscript  $s$  refers to the signal region and  $i$  refers to the

control regions. The test statistic is then

$$q_\mu(n) = \begin{cases} -2 \log \frac{\mathcal{L}(\mathbf{n}|\mu, \hat{\mathbf{b}}_\mu, \hat{\boldsymbol{\theta}}_\mu)}{\mathcal{L}(\mathbf{n}|\hat{\mu}, \hat{\mathbf{b}}_{\hat{\mu}}, \hat{\boldsymbol{\theta}}_{\hat{\mu}})} & \mu \geq \hat{\mu} \geq 0 \\ 0 & \text{otherwise} \end{cases}. \quad (4.15)$$

This test statistic can then be used in the same way as in Section 4.2 to calculate  $CL_s$  values. Although this does not enhance the sensitivity in the sense that the control region channels provide any significant discrimination between the signal and background (as they should be designed to be dominant in a chosen background process), it provides a more sophisticated way to extract the background normalisation rather than explicitly performing data driven calculations. It ensures that contamination due to other background contributions and correlations between systematic uncertainties in control regions are handled correctly. It also allows signal contamination in control regions to be taken into account when performing exclusion limits. The use of simultaneous fitting is discussed in more detail in Section 7.3.5, as it was used in the 2012 analysis described in Chapter 7.

### 4.3.3 Statistical combinations

This subsection discusses the possibility of including additional signal channels in the likelihood, which allows the statistical combination of signal regions. Only the combination of statistically independent, or orthogonal, signal regions, in the likelihood, will be considered. When multiple channels are included, providing they are orthogonal, the likelihood is then the product of the likelihoods of the individual channels. Equation (4.14) then extends to

$$\mathcal{L}(\mathbf{n}, \boldsymbol{\theta}^0 | \mu, \boldsymbol{\theta}) = \prod_{s \in SR} P(n_s | \lambda_s(\mu, \mathbf{b}, \boldsymbol{\theta})) \times \prod_{i \in CR} P(n_i | \lambda_i(\mu, \mathbf{b}, \boldsymbol{\theta})) \times P_{\text{SYST}}(\boldsymbol{\theta}^0, \boldsymbol{\theta}). \quad (4.16)$$

This can enhance the sensitivity of a search by improving the discrimination between signal and background. As a simple example, consider the statistical combination of two signal regions, each of which, before combination, disfavoured the signal hypothesis but not enough to exclude the scenario. The combined likelihood, which is the product of the individual likelihoods (that each give the probability of observing the data in that region given the hypothesis) will be pushed down relative to the maximum likelihood since both data observations are incompatible with the hypothesis. In turn this means the

test statistic (the profile log likelihood ratio) will be larger, corresponding to decreasing compatibility of the data with the hypothesis. Although the propagation of this through to the final  $CL_s$  value is not trivial, referring to the equation for  $CL_{s+b}$  (Equation (4.12)), since the observed test statistic appears as the lower limit in the integral, this could give some contribution to a decrease in  $CL_{s+b}$  value (the change in the probability distribution function of the test statistic would also be important). This is not a rigorous explanation though, as the  $1 - CL_b$  term in the denominator of  $CL_s$  could also be important.

Another advantage of combining signal regions in SUSY analyses is that often exclusions are presented across signal grids for a given model or process. It is often the case that different signal regions have more sensitivity across different regions of parameter space on the grid. By combining the results of different signal regions, the best exclusion across the whole of the signal grid can be obtained.

In both the analyses detailed in Chapters 6 and 7, the signal regions are not orthogonal so cannot be included in a single likelihood. For all signal points  $CL_s$  values were computed separately for all signal regions considered, then the  $CL_s$  value used for the final exclusion was taken to be the one with the best expected sensitivity (so as to avoid bias). For the 2012 analysis in Chapter 7, the statistical combination of the different lepton flavour channels was performed for each signal region, but the results for each signal region were still combined by selecting the signal region with the best expected sensitivity.

#### 4.3.4 Shape-fitting

Additional discrimination between signal and background can also be achieved for a single signal region by exploiting shape information in a chosen kinematic variable rather than just using the overall data count as the observation. For example, if the “measurement” in an experiment is actually a binned histogram containing all events in a signal region, each bin constitutes an independent channel in the likelihood. The likelihood then looks like Equation (4.16), but with one channel for every bin in the histogram. When deciding whether to use shape information, it is important to assess if there are sufficient statistics in all of the bins. Otherwise the statistical errors on the individual bins could limit the sensitivity. This is discussed in more detail Section 7.4, which investigates the possibility of using a shape-fit to increase the sensitivity of the analysis on 2012 data.

## 4.4 Conclusions

This chapter has provided an overview of the frequentist techniques used in ATLAS for quantifying the level of agreement between observed data and a given hypothesis, either for discovery or exclusion. These will be used extensively in subsequent chapters. The author would like to thank the developers of `HistFitter` and the `RooStats` package, who have developed tools that allow the implementation of these methods in user friendly frameworks.

# Chapter 5

## Searching for weakly produced supersymmetric particles at the LHC

### 5.1 Introduction and motivation

Strategies for early LHC searches for supersymmetry were dictated by cross-sections and luminosity. They focussed on the strong production of squarks and gluinos, mainly in the context of mSUGRA and the Constrained Minimal Supersymmetric Standard Model (CMSSM) [120, 121]. The CMSSM works in the framework of the MSSM (usually in mSUGRA) but adds experimental constraints such as the anomalous magnetic moment of the muon and the amount of dark matter in the universe. The theory is then restricted to an allowed region of parameter space.

Figure 5.1 summarises the best ATLAS exclusions on the masses of the SUSY particles as of July 2011. Inclusive searches for squarks and gluinos had already pushed limits out towards 1 TeV. The strong exclusions in the squark and gluino mass planes, along with more data (thus increasing the sensitivity to more challenging models) encouraged physicists to start searching for SUSY in new channels, one of which was electroweak production. The term electroweak production refers to the production of SUSY particles which do not feel the strong force (i.e. the gauginos and sleptons). In models with heavy squarks and gluinos, if the gauginos and/or sleptons were light, their direct production could be a potential discovery mode for SUSY, as their low masses could (partly) counteract their lower production cross-sections.

This section will provide an introduction to searches for weakly produced super-

symmetric particles at the LHC. Possible weak production processes are considered in Section 5.2, and existing limits prior to the LHC, that are relevant to the searches in this thesis, will be presented in Section 5.3. Section 5.4 presents a detailed optimisation of a search strategy for weak production in events with two-leptons. This aimed at finding a signal region to search for direct slepton production with the  $4.7 \text{ fb}^{-1}$  of 2011 data at  $\sqrt{s} = 7 \text{ TeV}$ , using events with 2-leptons, missing transverse energy ( $E_{\text{T}}^{\text{miss}}$ ), and the “stransverse mass variable” ( $m_{\text{T}2}$ ) [10–12].

The signal region resulting from this study was then used to search for weakly produced SUSY in ATLAS using the full 2011 dataset. The search is described in Chapter 6, and has been published in [1]. This analysis, and the subsequent analysis on 2012 data that will be discussed in Chapter 7, only considered electroweak production in R-parity conserving SUSY models where the lightest neutralino is the LSP, so the discussions in this chapter will do the same. In many models where the SUSY breaking mechanism is explicitly given (including mSUGRA), the mass differences between coloured and non coloured sparticles are not enough to give significantly lighter sleptons and/or gauginos, which means weak production would never be expected to be a discovery channel. In this chapter no particular SUSY-breaking scenario will be assumed and instead the discussion will remain in the more general framework of the pMSSM.

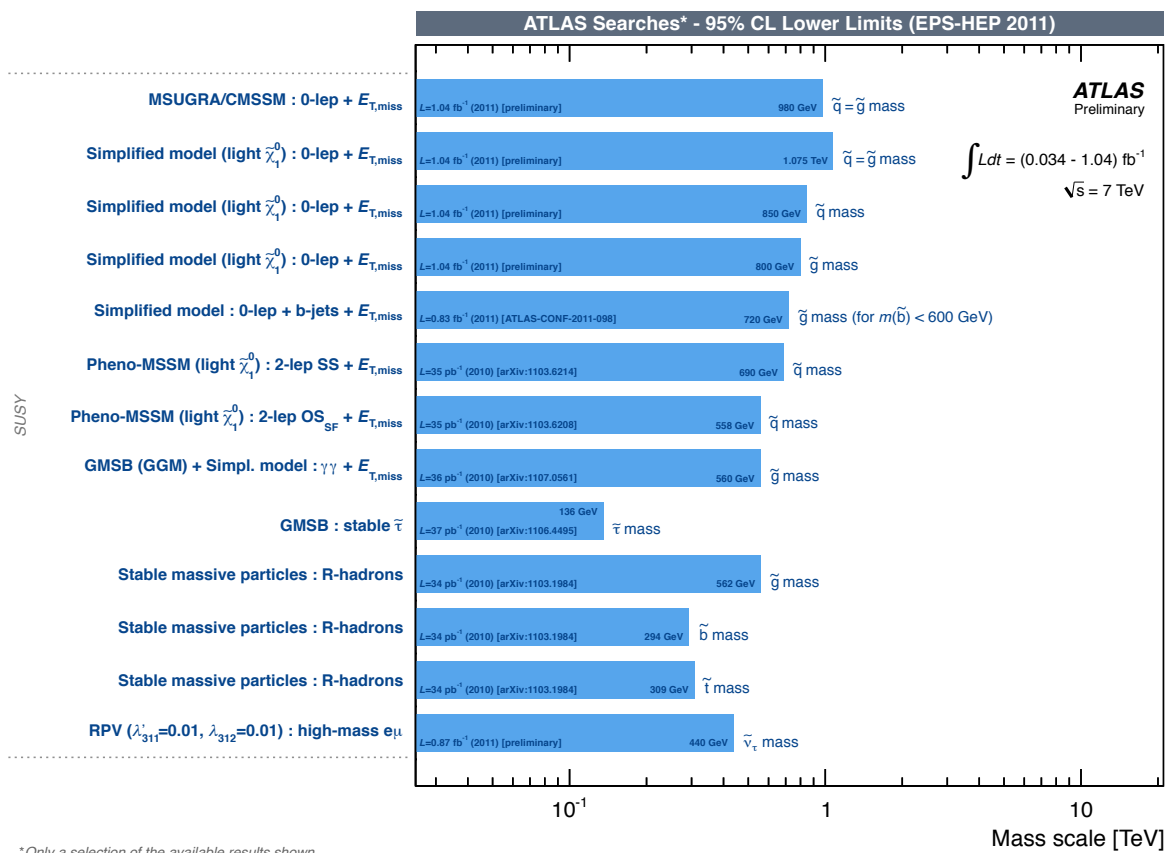


Figure 5.1: Summary of the best ATLAS exclusions on the masses of the SUSY particles as of July 2011 [122].

## 5.2 Weak production processes

Electroweak gauginos and sleptons can be pair-produced at hadron colliders by intermediate  $W^*$  and Drell-Yan processes. Feynman diagrams for three such processes are shown in Figure 5.2. The dominant processes depend on the exact SUSY mass hierarchy. If the gauginos are light then  $\tilde{\chi}_1^\pm \tilde{\chi}_2^0$  associated production and  $\tilde{\chi}_1^\pm \tilde{\chi}_1^\mp$  pair production would be dominant channels, with their cross-sections dependent on the gaugino masses, as well as the parameters  $M_1, M_2, \tan \beta$  and  $\mu$  (as defined in Section 3.2.1) that enter the chargino and neutralino mixing matrices. Depending on the masses, other processes involving heavier charginos and/or neutralinos could also be important.

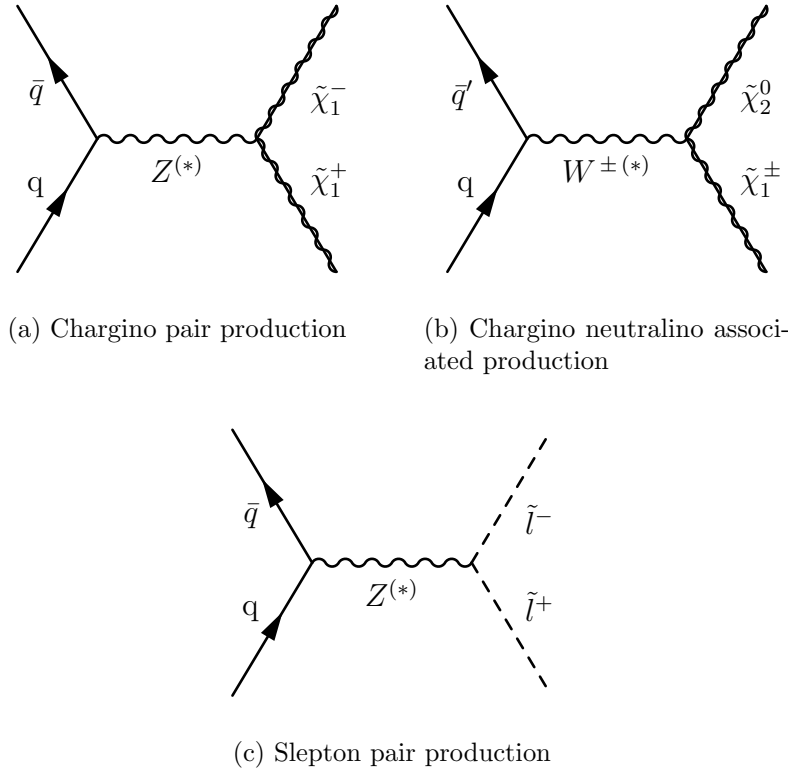


Figure 5.2: Feynman diagrams for three possible weak production processes at the LHC.

At the time of writing, all ATLAS searches for weakly produced SUSY particles in models with R-parity conservation and a neutralino LSP, have relied on leptonic final states in order to extract the rare signals from large Standard Model backgrounds. After production, charginos decay through  $W$  bosons or sleptons, and neutralinos can decay through  $Z$  or Higgs bosons (depending on the neutralino mixing parameters), or sleptons. Decays through sleptons are only accessible if the sleptons are also light.

In models where the sleptons are lighter than the gauginos, the only possible decay of the sleptons is into a lepton and the LSP. In this thesis the term “slepton” is actually usually referring only to the supersymmetric partners of the charged leptons. Sneutrinos are considered separately, though in all models considered in this thesis they are taken to be degenerate with the sleptons. Direct sneutrino production is almost impossible to search for at the LHC (there are no visible particles in the final state and it has a very low cross-section) so will not be considered further here.

A selection of Feynman diagrams showing possible decays of pair-produced electroweak gauginos and sleptons is shown in Figure 5.3. Such a wealth of signals could not be covered in a single analysis. Early ATLAS searches for electroweak production were divided by lepton multiplicity, as the main background components are different in each channel. However, at time of writing, analyses are starting to probe more challenging signatures, which require dedicated searches within these channels, that often target just one process in a given analysis.

Finally, when considering final states involving leptons, a distinction is usually made between light leptons (electrons and muons), and taus. Taus are harder to reconstruct as they decay before they can be directly detected. In ATLAS, searches involving taus rely on reconstructing hadronically decaying taus. This has a very challenging background from other Standard Model processes that can lead to “fake” taus being reconstructed. Searches for electroweak SUSY involving taus in the final state have been performed [124], but this thesis focuses only on final states involving light leptons.

### 5.3 Limits on weakly produced supersymmetry prior to the LHC

This section will summarise three existing constraints from LEP, the predecessor to the LHC, on the masses of electroweak gauginos and sleptons, that are relevant to the signals targeted in this thesis. Being an electron-positron collider, LEP had a much cleaner collision environment, making reconstruction easier. Searches for new physics did not have to overcome the overwhelming QCD background inherent in hadron colliders, and also the centre-of-mass energy of the collisions was precisely known, though considerably lower than that at the LHC. Further details on all results discussed in this section can be found in [125].

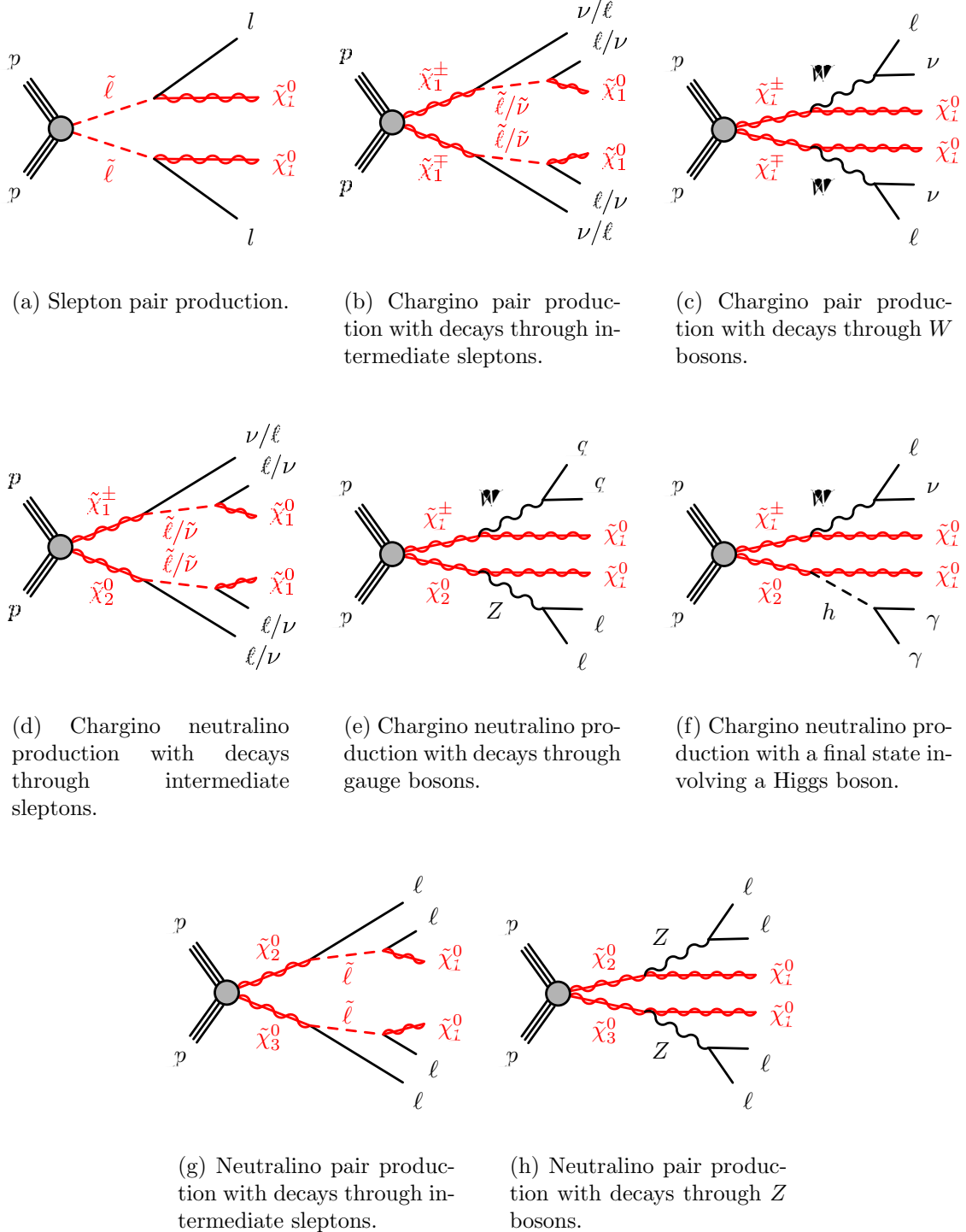


Figure 5.3: Feynman diagrams for possible decays of pair-produced electroweak sparticles at the LHC [123].

Firstly, limits on direct slepton production were calculated, through the statistical combination of results from the four LEP experiments: ALEPH, DELPHI, L3 and OPAL, using data taken at centre-of-mass energies ranging between 183 and 208 GeV. A summary of the results shown in Figure 5.4. These limits were calculated within the framework of the MSSM under the assumption of the unification of gaugino masses at the GUT scale (the GUT scale is the scale above which the electroweak and strong forces unify into one force and become equal in strength). Since the cross-section for right-handed sleptons is often predicted to be lower than for left-handed sleptons, limits were set on  $\tilde{\ell}_R^+ \tilde{\ell}_R^-$  only, as by setting a limit on the smallest slepton contribution, it is then independent of any model assumption on the hierarchy of left-handed and right-handed sleptons. Limits were calculated separately for each slepton flavour. For a massless neutralino the 95% upper limit on the mass is 99.9 GeV for selectrons and 94.9 GeV for smuons whereas in the case of a 40 GeV neutralino, which is closer to the limit on the LSP mass which will be discussed later in this section, the selectron limit is still 99.9 GeV whereas the smuon limit is 96.6 GeV [125–129].

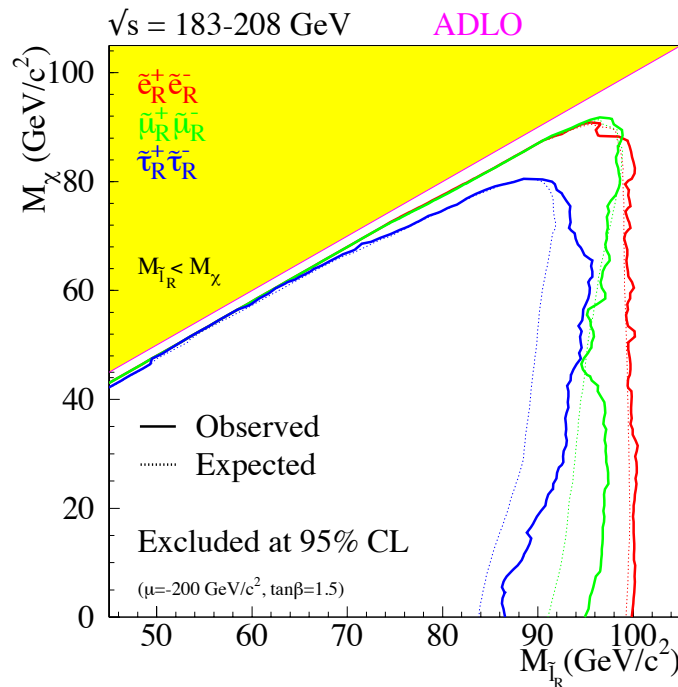


Figure 5.4: Previous limits on direct slepton production from LEP [125].

Secondly, limits were also calculated for the mass of the lightest chargino in the same MSSM scenario as the slepton search. The results of searches for chargino pair production, with subsequent decay into leptons, leptons plus jets and jets were combined,

assuming the charginos decayed through  $W$  bosons. The 95% CL lower limit on the mass of the lightest chargino was 103.5 GeV [125, 127, 130–132].

LEP also published a combined lower bound on the mass of the lightest neutralino in a constrained MSSM model, where lowest order gaugino and sfermion mass unification was assumed at the GUT scale. The result was a combination of the LEP combined slepton result, which was mentioned previously in this section, the ALEPH searches for chargino pair production [130] (which was included in the the chargino combination) and the combined LEP result on Higgs searches in the  $HZ$  channel [119]. The result in the plane of  $\tan\beta$  vs  $m_{\tilde{\chi}_1^0}$  is shown in Figure 5.5. At large  $\tan\beta$ , where the result is driven by the slepton search, the lower limit on  $m_{\tilde{\chi}_1^0}$  is 47 GeV.

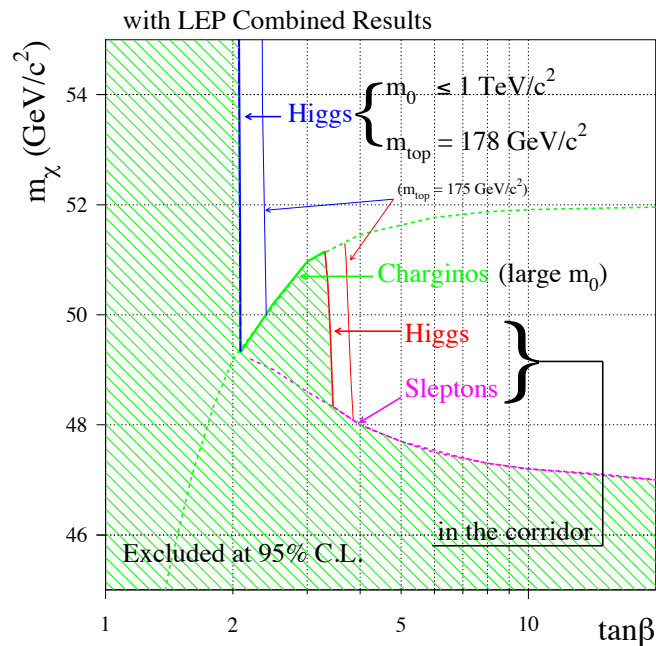


Figure 5.5: LEP limit on the mass of the lightest neutralino in a constrained MSSM, as a function of  $\tan\beta$  [125].

## 5.4 Optimising a search for direct slepton production using the $m_{T2}$ variable

### 5.4.1 Introduction to the $m_{T2}$ variable

The “stransverse mass” variable,  $m_{T2}$  [10–12], is an extension of the transverse mass variable  $m_T$ , which was first used by the UA1 and UA2 experiments at CERN to measure the  $W$  boson mass [133, 134]. The formulation of  $m_{T2}$ , and its relation to the transverse mass, is explained in Appendix A.  $m_{T2}$  was constructed to obtain bounds on the masses of pair produced heavy particles, each of which decays to one visible and one invisible particle that then escapes undetected, giving missing transverse momentum in the event. Direct slepton production, shown in Figure 5.6, is a good example of such a process.

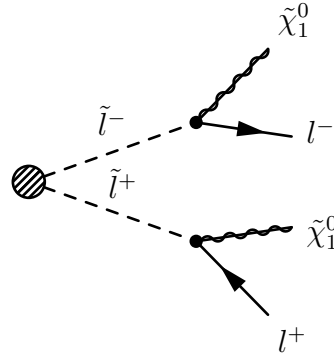


Figure 5.6: Feynman diagram for direct slepton production at the LHC.

$m_{T2}$  can be calculated from the 4-momenta of any two “objects” (e.g. jets, leptons or even combinations of jets and/or leptons) in the event, and the missing transverse energy. In all analyses in this thesis  $m_{T2}$  is calculated using the reconstructed lepton momenta. For two objects with transverse momentum vectors  $\mathbf{p}_T^a$  and  $\mathbf{p}_T^b$ ,  $m_{T2}$  is defined as:

$$m_{T2}^2 = \min_{\mathbf{p}_T^{\text{miss}} = \mathbf{q}_T + \mathbf{r}_T} [\max\{m_T^2(\mathbf{p}_T^a, \mathbf{q}_T), m_T^2(\mathbf{p}_T^b, \mathbf{r}_T)\}], \quad (5.1)$$

where  $\mathbf{p}_T^{\text{miss}}$  is the missing transverse momentum in the event and  $\mathbf{q}_T$  and  $\mathbf{r}_T$  are possible transverse momentum vectors of the invisible particles, which are constrained to equal the missing transverse momentum. (Note that the true momentum vectors are unknown). The minimisation is performed by trying all possible decompositions of  $\mathbf{p}_T^{\text{miss}}$ .

The transverse mass is defined as:

$$m_{\text{T}}(\mathbf{p}_{\text{T}}^a, \mathbf{q}_{\text{T}}) = \sqrt{m_a^2 + m_{\chi}^2 + 2(E_{\text{T},\text{p}}^a E_{\text{T},\text{q}} - \mathbf{p}_{\text{T}}^a \cdot \mathbf{q}_{\text{T}})}, \quad (5.2)$$

where  $E_{\text{T}}$  is the transverse energy of a particle ( $E_{\text{T}} = \sqrt{m^2 + |\mathbf{p}_{\text{T}}|^2}$ , where  $m$  is the mass of the particle and  $\mathbf{p}_{\text{T}}$  is its transverse momentum) and  $m_{\chi}$  is the hypothesised mass of the invisible particles.

By construction  $m_{\text{T}2}$  is a function of the hypothesised mass of the invisible particles, which, in searches for SUSY, are not known. For all the analyses detailed in this thesis, instead of trying to measure masses, properties of  $m_{\text{T}2}$  were exploited in the construction of signal regions targetting discovery. Extensive discussions of the properties of  $m_{\text{T}2}$  can be found in the literature [10–12]. The feature of  $m_{\text{T}2}$  that is exploited in the 2-lepton analyses in this thesis, is that for a given value of the hypothesised invisible mass, the  $m_{\text{T}2}$  distribution for events having the topology shown in Figure 5.6, has an endpoint which is a function of the mass of the heavy pair produced particles (the sleptons in our case). The full expression is given in Equation 88 of [12]. As the invisible mass is unknown it is usually set to 0 (this is the case throughout this thesis), in which case the equation reduces to

$$m_{\text{T}2}^{\text{max}} = \sqrt{\left(m_{\tilde{l}}^2 - m_{\tilde{\chi}_1^0}^2\right) \left(1 - \frac{m_{\tilde{\chi}_1^0}^2}{2m_{\tilde{l}}^2}\right)}, \quad (5.3)$$

where  $m_{\tilde{\chi}_1^0}$  and  $m_{\tilde{l}}$  are the masses of the neutralino and chargino respectively. The dependence of the  $m_{\text{T}2}$  endpoint on the mass-splitting between the slepton and neutralino can be explicitly seen. Analogously, the  $m_{\text{T}2}$  distributions of well reconstructed fully leptonic  $WW$  and  $t\bar{t}$  events (shown in Figure 5.7) would (in the absence of a finite  $W$  width) fall off rapidly at values above the  $W$  boson mass (around 80.3 GeV). The finite width, together with reconstruction effects, smears this endpoint, allowing events at higher values of  $m_{\text{T}2}$ , however events significantly beyond the  $W$  mass are highly suppressed. The aim in the optimisation study detailed in the next section was that, by selecting events with a hard cut on  $m_{\text{T}2}$ , the backgrounds would be heavily suppressed, thus providing sensitivity to models where the  $m_{\text{T}2}$  distribution extends beyond the cut value.

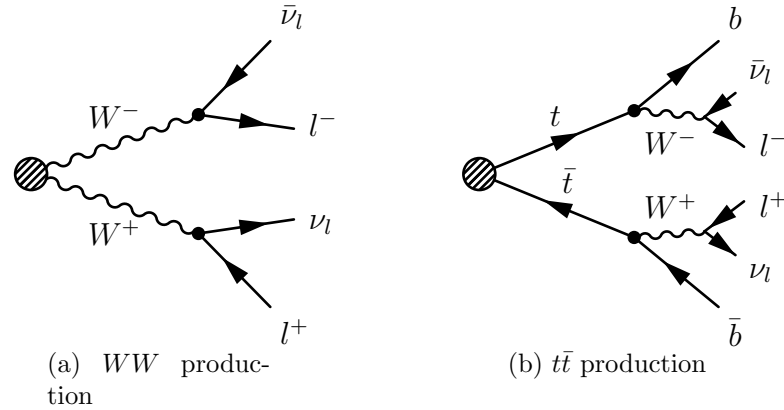


Figure 5.7: Feynman diagram for  $WW$  (a) and  $t\bar{t}$  (b) production at the LHC, with subsequent decays into final states containing two leptons.

## 5.4.2 The direct slepton signal grid

As discussed in Section 5.3, existing limits on slepton-pair production prior to the LHC came from LEP. The 2011 dataset available for analysis from ATLAS corresponded to  $4.7 \text{ fb}^{-1}$  of data. As more data would be needed to do better than the LEP results in the scenarios they considered, it was decided instead that by removing the constraints at the GUT scale ATLAS would have sensitivity.

Since direct slepton production is one of the processes with the smallest production cross-sections at the LHC (see Figure 3a), the grid focussed on relatively low slepton masses. The pMSSM was used to generate simplified models where the first and second generation sleptons (selectrons and smuons) and the  $\tilde{\chi}_1^0$  (which is the LSP) are light. Staus were not included in the grid because their exact position in the mass hierarchy with respect to the first and second generation sleptons would have added further model dependence into the grid.

The models generated were based on those described in [135]. The masses of the gluinos, squarks, third generation sfermions and gauginos (apart from the  $\tilde{\chi}_1^0$ ) were set out of reach at 2.5 TeV. In this simplified case, the left-handed and right-handed production cross-sections depend only on the slepton mass and the kinematics of the event are dictated by the masses of the sleptons and the  $\tilde{\chi}_1^0$ . The mass of the (bino-like)  $\tilde{\chi}_1^0$  was varied by scanning the value of the gaugino mass parameter  $M_1$  in steps of 20 GeV in the range 20-160 GeV, and the selectron and smuon mass was scanned using the constraint  $m_{\tilde{l}} > m_{\tilde{\chi}_1^0} + 30 \text{ GeV}$ . The signal points were generated using the HERWIG event

generator [136], and the cross-sections calculated to next-to-leading order in the strong coupling constant (NLO) using PROSPINO [113]. The cross-section dependence across the grid can be seen in Figure 5.8. The produced grid contained charged-slepton pairs, sneutrino pairs and sneutrino charged-slepton pairs (with the selectrons and sneutrinos assumed degenerate), but only the charged slepton pairs are of interest in this study (and the subsequent analysis that followed).

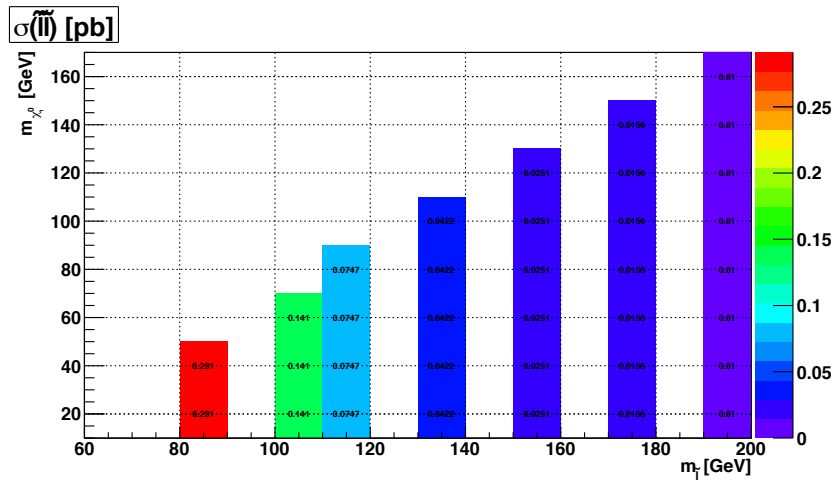


Figure 5.8: Grid showing the cross-sections for all points in the direct slepton signal grid at  $\sqrt{s} = 7$  TeV, calculated using PROSPINO [113].

In the signal grid left-handed and right-handed sleptons were assumed to be degenerate. Although in reality this may not be reflected in any true theory, left-handed and right-handed sleptons could be considered separately using Monte Carlo truth filtering (this was not done for the 2011 analysis in Chapter 6, but was performed for the later analysis on the 2012 dataset, which is discussed in Chapter 7). The LEP constraint of gauge unification was also removed, allowing low-mass neutralinos to be considered.

In this simplified scenario, as all other sparticle masses are set to be out-of-reach, the sleptons decay exclusively through  $\tilde{l}^{\pm} \rightarrow l\tilde{\chi}_1^0$ , as in the Feynman diagram in Figure 5.6. The next section will discuss the optimisation of a  $m_{T2}$ -based search for direct slepton production using this grid.

### 5.4.3 Choosing the signal region

The Feynman diagram for direct slepton production shown in Figure 5.6 has a distinct event topology: two isolated opposite-sign same-flavour leptons, no jets except for ini-

tial state radiation (ISR), and missing transverse energy,  $E_T^{\text{miss}}$ , due to the undetected neutralinos. Before considering possible  $m_{T2}$  selection criteria, this information can be used to achieve a large suppression of the Standard Model backgrounds. The  $Z/\gamma^* \rightarrow ll$  component is suppressed by veto-ing events with a di-lepton invariant mass within 10 GeV of the  $Z$ -mass (which is taken to be 91.2 GeV), referred to in this thesis as the  $Z$ -mass window. In addition a veto on jets in the event is applied to reduce the  $t\bar{t}$  background, leaving only the irreducible  $WW$  contribution. All object definitions used in this section will be discussed further in Section 6.3.

- Two isolated same-flavour opposite-sign leptons
- Jet veto- veto all events containing at least one signal jet (as defined in Section 6.3).
- $|m_{ll} - m_Z| > 10$  GeV (with  $m_Z = 91.2$  GeV)

Instead of cutting on  $E_T^{\text{miss}}$  to suppress the backgrounds, a variation on this variable is used. The variable  $E_T^{\text{miss,rel}}$  is constructed such that

$$E_T^{\text{miss,rel}} = \begin{cases} E_T^{\text{miss}} & \text{if } \Delta\phi_{\ell,j} \geq \pi/2 \\ E_T^{\text{miss}} \times \sin \Delta\phi_{\ell,j} & \text{if } \Delta\phi_{\ell,j} < \pi/2 \end{cases}, \quad (5.4)$$

where  $\Delta\phi_{\ell,j}$  is the azimuthal angle between the direction of the  $E_T^{\text{miss}}$  and that of the nearest electron, muon or jet. By construction, in situations where the direction of the  $E_T^{\text{miss}}$  is aligned with one of the jets or leptons, which could happen as a result of that object being badly reconstructed, only the component of the  $E_T^{\text{miss}}$  perpendicular to that object is considered. This can reduce the  $E_T^{\text{miss}}$  resolution in processes with only real  $E_T^{\text{miss}}$ , however it reduces significantly the instrumental  $E_T^{\text{miss}}$  in processes such as  $Z/\gamma^* \rightarrow e^+e^-, \mu^+\mu^-$  [137]. It also helps to reduce the process  $Z/\gamma^* \rightarrow \tau\tau \rightarrow ee, e\mu, \mu\mu$  where the  $E_T^{\text{miss}}$  tends to be aligned with the direction of the leptons.

In optimising the signal region, different combinations of cuts on  $E_T^{\text{miss,rel}}$  and  $m_{T2}$  were considered, with  $m_{T2}$  defined as in Section 5.4.1. In order to quantify the significance and compare different sets of cuts, a variable denoted  $Z_N$  was used:

$$Z_n = \sqrt{2}\text{erf}^{-1}(1 - 2p), \quad (5.5)$$

where “ $\text{erf}^{-1}$ ” is the inverse error function. It essentially transforms a probability  $p$  into the equivalent number of standard deviations of a normal distribution from the mean.

The probability  $p$  satisfies

$$p \propto \int_0^\infty db G(b; N_b, \delta b) \sum_{i=N_{data}}^\infty \frac{e^{-b} b^i}{i!}. \quad (5.6)$$

This is the probability that the background count  $N_b$  with uncertainty  $\delta b$  fluctuates to  $N_{data}$  or above. Uncertainties on the background are incorporated into the significance by convolving the Poisson probability that the background fluctuates to the observed probability with a Gaussian probability distribution function  $G(N_b, \delta b)$  with mean  $N_b$  and deviation  $\delta b$ . In the optimisation study `RooStats` [4] functions were used to calculate a value for  $Z_N$  in the case that  $N_{data} = N_s + N_b$ . Since  $N_s + N_b$  is in general non-integer the value for  $Z_n$  obtained does not correspond to the equation above, but is a good approximation to the significance.

In optimising the signal region a scan over possible values of the  $m_{T2}$  and  $E_T^{\text{miss,rel}}$  cuts was performed. The  $Z_N$  value and expected exclusion contours for a range of  $m_{T2}$  cuts is shown in Figure 5.9 for  $E_T^{\text{miss,rel}} > 40$  GeV, in Figure 5.10 for  $E_T^{\text{miss,rel}} > 60$  GeV and Figure 5.11 for  $E_T^{\text{miss,rel}} > 80$  GeV. The background estimation was taken entirely from Monte Carlo, using the same samples as will be outlined in Section 6.2, and a uniform systematic uncertainty of 20% was assumed for the background expectation. The solid contours on the plots indicate the expected 95% CL exclusion, which correspond to  $Z_N = 1.64$ .

The signal region was chosen to be that which gave the best exclusion across the grid. The cuts chosen were  $E_T^{\text{miss,rel}} > 40$  GeV and  $m_{T2} > 90$  GeV. By examining Figures 5.9–5.11, extra sensitivity could be gained at higher slepton masses with harder  $m_{T2}$  cuts, since this gave further background rejection whilst still retaining signal events for these models. Furthermore sensitivity closer to the diagonal was better with moderate cuts on  $m_{T2}$  but harder  $E_T^{\text{miss,rel}}$  cuts. For such models the  $m_{T2}$  endpoints for the signal are lower but high  $E_T^{\text{miss}}$  events could be generated if an ISR jet were emitted (that did not satisfy the signal jet criteria). Apart from close to the diagonal, the sensitivity for moderate and high  $m_{T2}$  cuts does not seem to depend on the value of the  $E_T^{\text{miss,rel}}$  cut chosen, thus implying most of the sensitivity comes from background rejection due to  $m_{T2}$ .

It is useful to compare expected exclusion contour for the chosen signal region with the distribution of theoretical  $m_{T2}$  endpoints, calculated using Equation (5.3), in the direct slepton grid, which is shown in Figure 5.12. For lower slepton masses, where the production cross-section is higher, the expected exclusion contour for the signal

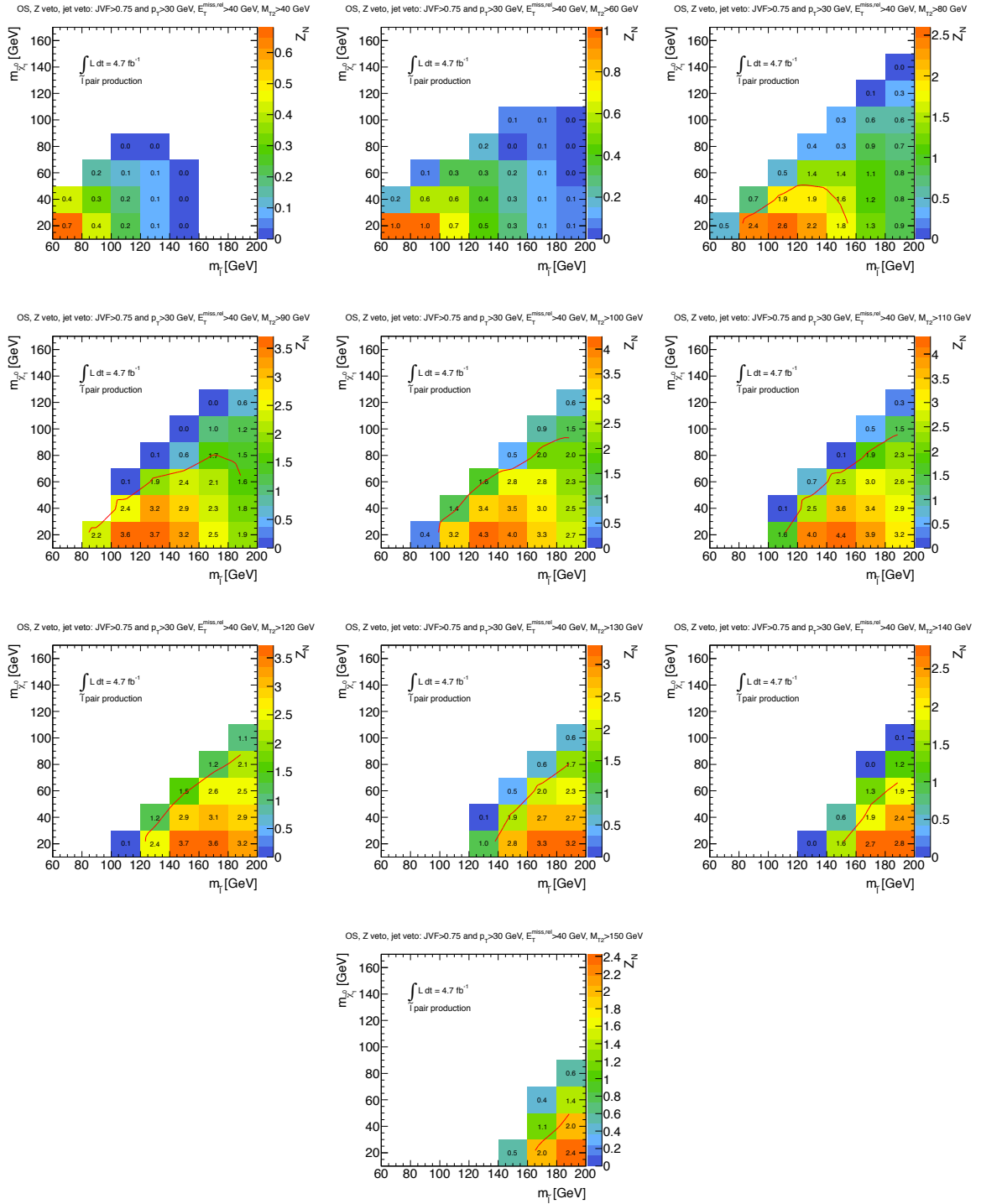


Figure 5.9: Optimisation plots for possible  $m_{T2}$ -based signal regions to target direct slepton production with  $4.7 \text{ fb}^{-1}$  of data at  $\sqrt{s} = 7 \text{ TeV}$ . All signal regions considered have a  $E_T^{\text{miss,rel}}$  cut at 40 GeV. The solid contours indicate the expected 95% CL exclusion, which corresponds to  $Z_N = 1.64$ .

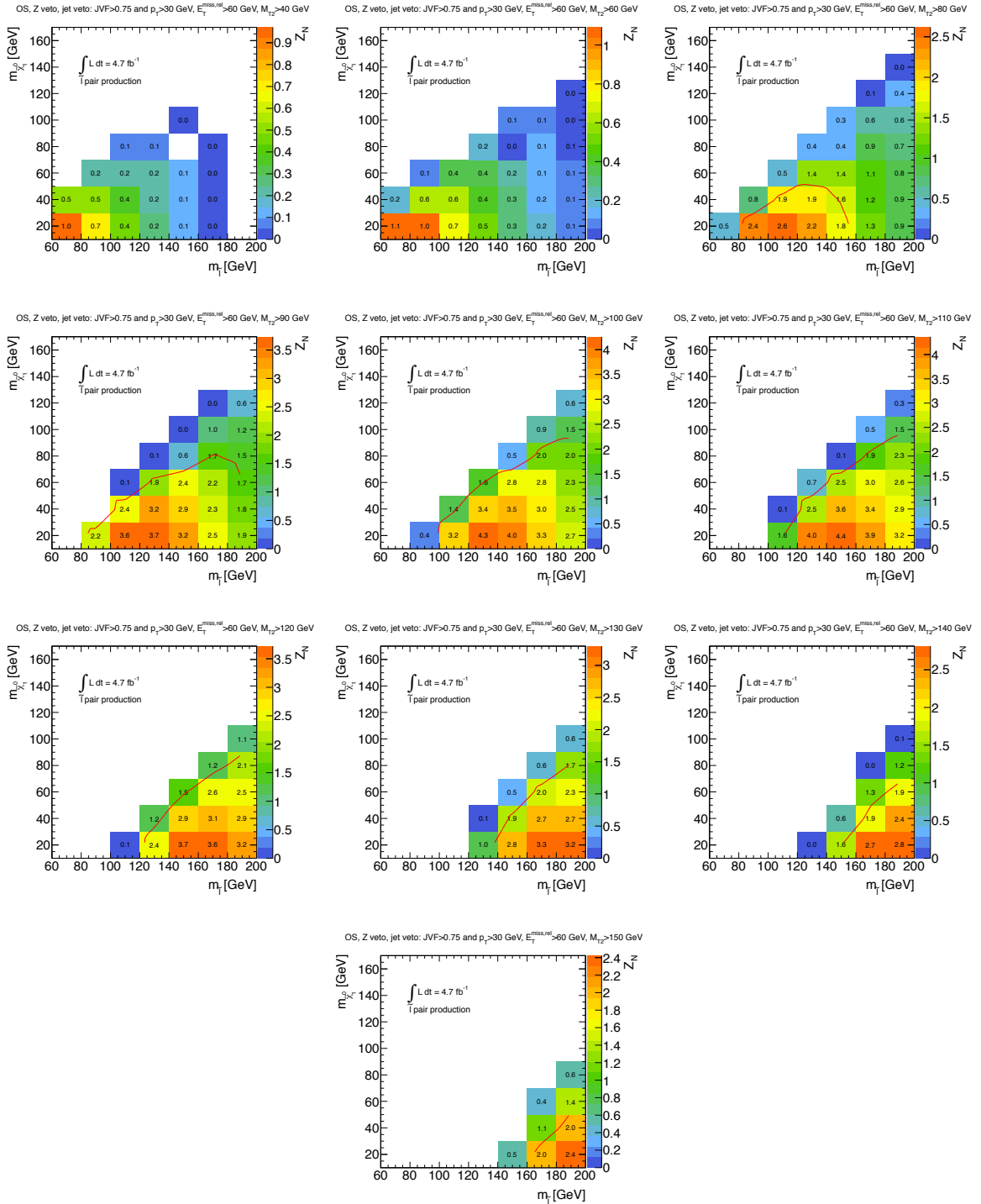


Figure 5.10: Optimisation plots for possible  $m_{T2}$ -based signal regions to target direct slepton production with  $4.7 \text{ fb}^{-1}$  of data at  $\sqrt{s} = 7 \text{ TeV}$ . All signal regions considered have a  $E_T^{\text{miss,rel}}$  cut at 60 GeV. The solid contours indicate the expected 95% CL exclusion, which corresponds to  $Z_N = 1.64$ .

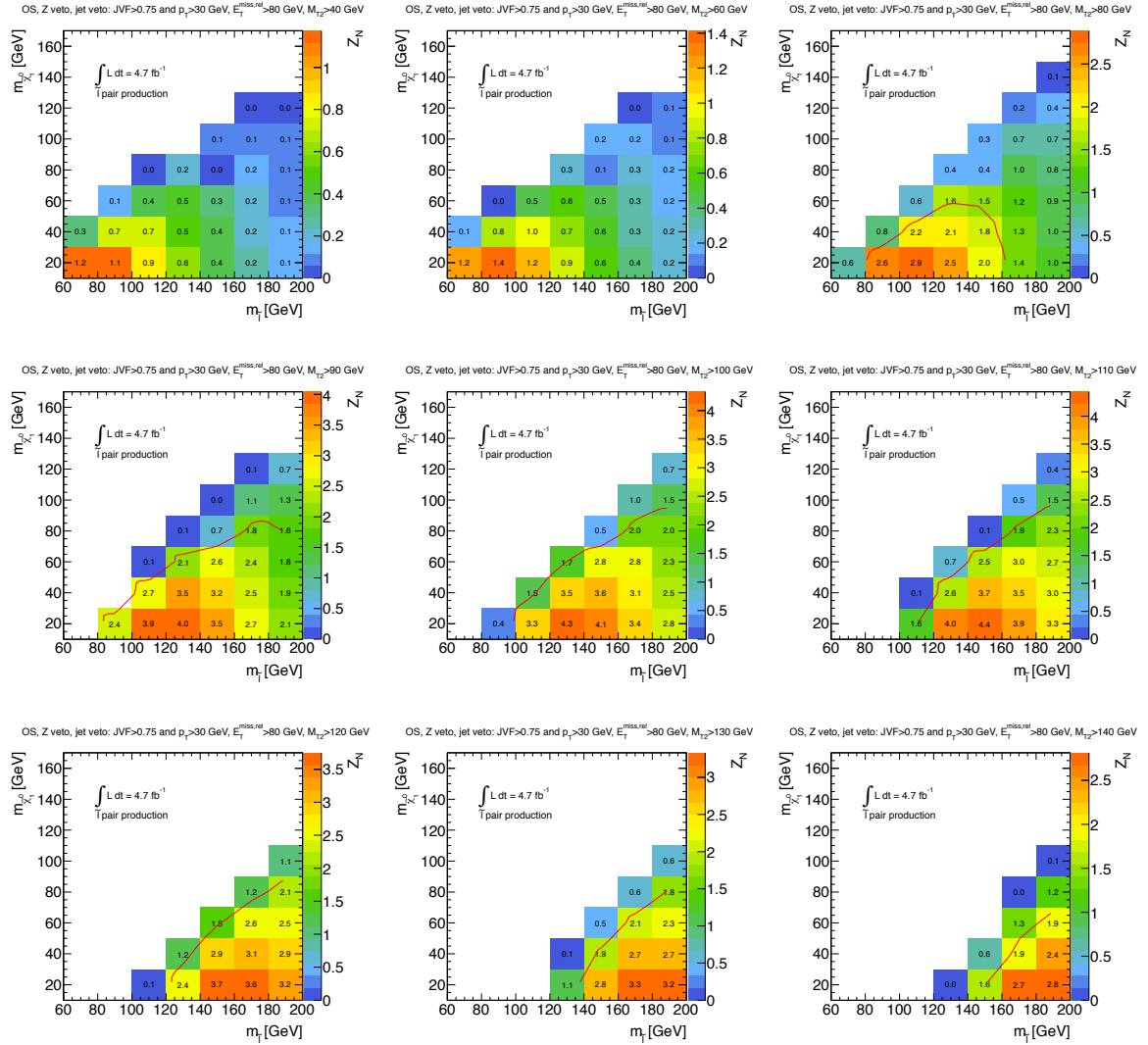


Figure 5.11: Optimisation plots for possible  $m_{T2}$ -based signal regions to target direct slepton production with  $4.7 \text{ fb}^{-1}$  of data at  $\sqrt{s} = 7 \text{ TeV}$ . All signal regions considered have a  $E_T^{\text{miss,rel}}$  cut at 80 GeV. The solid contours indicate the expected 95% CL exclusion, which corresponds to  $Z_N = 1.64$ . The plot for  $m_{T2} > 150 \text{ GeV}$  is not included here as no signal points passed the cuts.

region with  $E_T^{\text{miss,rel}} > 40$  GeV,  $m_{T2} > 90$  GeV is consistent with the contour at 90 GeV in Figure 5.12, though it should be noted that detector and reconstruction effects will smear the endpoints of the distributions. As the slepton masses increase, except for the region of phases space close to the diagonal most model points have expected endpoints above 90 GeV. Here the decreasing cross-sections starts to dominate the shape of the expected exclusion.

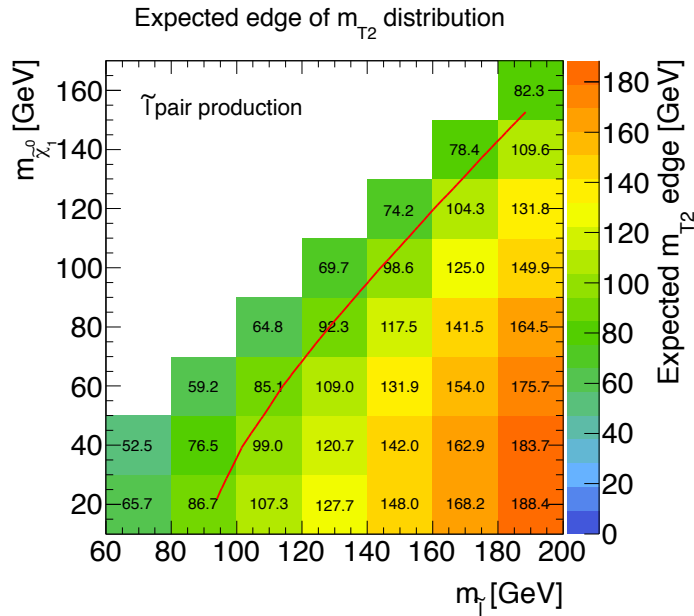


Figure 5.12: Grid showing the theoretically expected endpoints of the  $m_{T2}$  distributions, calculated using Equation (5.3), for all points in the direct slepton signal grid used for the 2011 data analysis. The contour drawn on the plot corresponds to expected end-points of 90 GeV.

As will be seen in Chapter 6, the signal region using  $m_{T2}$  was also the most sensitive signal region in the search for chargino-pair production, with decays through intermediate sleptons (the Feynman diagram is shown in Figure 5.3). In the case that both charginos decay as  $\tilde{\chi}_1^\pm \rightarrow l^\pm \tilde{\nu}$ , with subsequent decay of the sneutrinos into a neutrino and a neutralino, the event is the same as the direct slepton case in terms of the observable kinematics, even though there are additional massless particles in the final state. The nature of the endpoint in this case is as in Equation 5.3. For the other two topologies, i.e. for the case where both charginos decay as  $\tilde{\chi}_1^\pm \rightarrow \tilde{l}^\pm \nu$  or where each chargino decays differently (i.e. one decays as  $\tilde{\chi}_1^\pm \rightarrow l^\pm \tilde{\nu}$  and one as  $\tilde{\chi}_1^\pm \rightarrow \tilde{l}^\pm \nu$ ), the dynamics and kinematics are different to the slepton case. Furthermore, in the third topology the

decay is no longer symmetric. In these cases the behaviour of  $m_{T2}$  will be different. Nevertheless, even if there is no endpoint for a class of events, as long as the  $m_{T2}$  distribution extends beyond the  $m_{T2}$  cut the signal region could be sensitive. As this signal can also give electron-muon events, the opposite flavour electron-muon channel was also included in the signal region. The optimisation plots for possible signal regions using the simplified model grid for chargino-pair production are given in Appendix B.

## 5.5 Conclusions

This chapter has presented an optimisation study for a signal region targeting direct slepton production in ATLAS using the 2011 dataset. This study showed that despite the small cross-sections and large Standard Model backgrounds, sensitivity could be achieved by exploiting kinematic and topological features of the signal. This region was used in the analysis that will be presented in the next chapter, which searched for direct slepton pair production and other electroweak production processes using the full 2011 ATLAS dataset.

# Chapter 6

## The search for weakly produced supersymmetric particles with $4.7 \text{ fb}^{-1}$ of data at $\sqrt{s} = 7 \text{ TeV}$

### 6.1 Introduction

This chapter presents the search for direct gaugino and slepton-pair production that was performed with  $4.7 \text{ fb}^{-1}$  of data at  $\sqrt{s} = 7 \text{ TeV}$  that was collected by ATLAS during the 2011 run, using events with exactly two light leptons (electrons  $e$  or muons  $\mu$ ) and missing transverse energy in the final state [1]. This was the first search for direct slepton production at the LHC and was also the first 2-lepton search in ATLAS specifically targeting direct gaugino production. Previous 2-lepton analyses had been optimised to target signatures where leptons are produced in the cascade decays of strongly produced squarks and gluinos [138–140].

The author was lucky to have the opportunity to make significant contributions to the published results [1]. In addition to optimising the  $m_{T2}$ -based signal region, this included making plots of kinematic distributions showing comparisons between data and Monte Carlo that were included in the paper, and producing the exclusion limits across relevant signal grids. Unless otherwise stated all plots in this chapter, including those labelled “ATLAS”, were produced by the author. Additionally the author was responsible for producing Monte Carlo estimates for all background (these were needed to compare with the data driven estimates) and signal (these were needed to compute the exclusion  $\text{CL}_s$

values) samples in each of the signal regions. This also included evaluating the impact of all systematic uncertainties on these estimates. When calculating the  $\text{CL}_s$  values for the signal points, the author used data-driven estimates for various background components, that were provided by other analysers.

In a particular SUSY scenario, if the sleptons are sufficiently light, they can be present in the decay chains of  $\tilde{\chi}_i^0$  or  $\tilde{\chi}_i^\pm$ . On-shell sleptons in decay chains maximise the branching ratio to leptonic final states, which means the sensitivity to models with intermediate sleptons is usually higher. All models considered in this chapter are such that gaugino decays through intermediate sleptons are kinematically accessible.

Table 6.1 details the possible final states arising from the direct pair production of weak gauginos. Allowing for the possibility of leptons being out of the detector acceptance or failing lepton identification (denoted  $\ell_{miss}$  in the table), a particular signal process could give events in more than one lepton multiplicity channel. For example chargino-neutralino pair production with intermediate sleptons leads to a 3-lepton signal. However if one lepton is misidentified it could also give a 2-lepton signal. The bold labels in the description column for the 2-lepton signals refer to the signal region in the 2-lepton analysis that targets that signal. These signal regions will be described in Section 6.4.

Decay	Signal Region
$\tilde{\chi}_2^0 \tilde{\chi}_1^\pm \rightarrow (\ell^+ \ell^- \tilde{\chi}_1^0) + (\ell^\pm \nu \tilde{\chi}_1^0)$	3-lepton
$\tilde{\chi}_2^0 \tilde{\chi}_1^\pm \rightarrow (\ell^+ \ell^- \tilde{\chi}_1^0) + (\ell_{miss}^\pm \nu \tilde{\chi}_1^0)$	<b>SR-OSjveto</b>
$\tilde{\chi}_2^0 \tilde{\chi}_1^\pm \rightarrow (\ell^+ \ell_{miss}^- \tilde{\chi}_1^0) + (\ell^\pm \nu \tilde{\chi}_1^0)$	<b>SR-SSjetveto</b>
$\tilde{\chi}_2^0 \tilde{\chi}_1^\pm \rightarrow (\ell_{miss}^+ \ell^- \tilde{\chi}_1^0) + (\ell^\pm \nu \tilde{\chi}_1^0)$	<b>SR-SSjetveto</b>
$\tilde{\chi}_2^0 \tilde{\chi}_1^\pm \rightarrow (\ell^+ \ell^- \tilde{\chi}_1^0) + (q\bar{q}' \tilde{\chi}_1^0)$	<b>SR-2jets</b>
$\tilde{\chi}_1^\pm \tilde{\chi}_1^\pm \rightarrow (\ell^\pm \nu \tilde{\chi}_1^0) + (\ell^\mp \nu \tilde{\chi}_1^0)$	<b>SR-OSjveto</b>
$\tilde{\chi}_2^0 \tilde{\chi}_2^0 \rightarrow (\ell^\pm \ell^\mp \tilde{\chi}_1^0) + (\ell^\pm \ell^\mp \tilde{\chi}_1^0)$	4-lepton
$\tilde{\chi}_2^0 \tilde{\chi}_2^0 \rightarrow (\ell^\pm \ell^\mp \tilde{\chi}_1^0) + (q\bar{q} \tilde{\chi}_1^0)$	<b>SR-2jets</b>

Table 6.1: Possible final states arising various electroweak production processes. The symbol  $\ell_{miss}$  refers to a lepton that failed lepton identification. The bold labels in the description column refer to the signal region in the 2-lepton analysis that targets that signal.

Searches for weakly produced supersymmetric particles using the 2011 dataset were also performed in ATLAS in a dedicated 3-lepton analysis [141]. The search for direct gaugino production is best performed by statistically combining dedicated searches

(providing the object definitions are consistent, the 2-lepton and 3-lepton channels are orthogonal so can be statistically combined as described in Section 4.3.3). A statistical combination of the 2-lepton and 3-lepton analyses for the pMSSM grid was performed and is published along with the results of the 3-lepton analysis [141]. The author contributed to the statistical combination by providing the signal yields in the 2-lepton signal regions for the pMSSM grids. The direct slepton signal is exceptional in that only the 2-lepton analysis had sensitivity.

The structure of this chapter is as follows. Section 6.2 summarises the data and Monte Carlo event samples used in the analysis. The basic event selection for 2-lepton events, including the trigger strategy and lepton selection criteria, is discussed in Section 6.3. The signal regions chosen for the analysis are presented in Section 6.4, together with a discussion of the dominant background processes for each signal region. Although these were not performed by the author, Section 6.5 contains a brief description of the background estimation techniques used for the various Standard Model background components. A discussion of the systematic uncertainties considered in the analysis is provided in Section 6.6. Section 6.7 presents a validation of the some of the background estimation techniques by presenting data-Monte Carlo comparison plots for important kinematic distributions in the control regions.

No significant excess was observed over the Standard Model expectation in any of the signal or control regions considered in the analysis. Section 6.8 presents the statistical interpretation of the results, through both model independent limits and exclusion contours across relevant signal grids. Conclusions from the analysis are given in Section 6.9.

## 6.2 Data and Monte Carlo samples

### 6.2.1 Data samples

The analysis used data events at  $\sqrt{s} = 7 \text{ TeV}$  recorded in ATLAS in both the Egamma and Muon streams, between March and the end of October 2011. After applying data quality requirements this corresponded to an integrated luminosity of  $4.7 \text{ fb}^{-1}$ .

## 6.2.2 Background samples

Simulated Monte Carlo samples for the Standard Model background components were required for the optimisation of the signal regions for the analysis. They were also used to evaluate the Standard Model backgrounds in the signal regions, either directly or as part of the data-driven background estimates (despite being data driven all the methods described in Section 6.5 had some dependence on Monte Carlo simulation).

Samples for  $t\bar{t}$  production were simulated using POWHEG [142] (assuming a top mass of 172.5 GeV), and MC@NLO [143–145] was used to model single top production. The ALPGEN event generator [146] was used for the  $W$ +jets and  $Z$ +jets samples. The diboson background (comprising  $WW$ ,  $WZ$  and  $ZZ$ ) was modelled using samples from two different generators. HERWIG [136] was used as the default generator, however samples generated using the Sherpa event generator [147] were used for signal regions requiring jets. For the ALPGEN and MC@NLO samples, fragmentation and hadronisation were performed by HERWIG, using JIMMY [148] to model the underlying event, whilst for the POWHEG  $t\bar{t}$  samples PYTHIA [149] was used.

When calculating signal region estimates it was necessary to renormalise expected Monte Carlo yields using the sample cross-section and the required luminosity. The top quark contributions were normalised using cross-sections calculations at approximately next-to-next-to-leading order (NNLO) [150]. The diboson cross-sections were calculated using next-to-leading order (NLO) QCD predictions using MCFM [151, 152], and cross-sections for inclusive  $W$ +jets and  $Z/\gamma^*$ +jets were calculated at NNLO using FEWZ [153].

## 6.2.3 Signal grids

In addition to the direct slepton signal grid, introduced in Section 5.4.2, the analysis considered two further simplified model grids for gaugino pair production, and three weak production pMSSM grids.

The first simplified model grid targeted chargino-pair production, with decays through (left-handed) intermediate sleptons, with a 50% branching ratio to both charged sleptons and sneutrinos (including  $\tilde{\tau}_L$  and  $\tilde{\nu}_\tau$ ). This was used to set limits on the chargino mass in the pMSSM, independently of the  $\tilde{\chi}_2^0$  mass. The second simplified model grid targeted  $\tilde{\chi}_2^0\tilde{\chi}_1^\pm$  production, again with decays through intermediate sleptons. In each of the simplified models the masses of the relevant particles are the only free parameters.

The  $\tilde{\chi}_2^0$  and  $\tilde{\chi}_1^\pm$  were assumed to be wino-like whilst the  $\tilde{\chi}_1^0$  was assumed to be bino-like, and the masses of the sleptons were fixed by:  $m_{\tilde{L}} = m_{\tilde{\nu}} = (m_{\tilde{\chi}_1^\pm} + m_{\tilde{\chi}_1^0})/2$ . For these grids the masses of the squarks, gluinos and third generation sfermions were set at 2 TeV. These grids were generated in the pMSSM framework using `Herwig++` [154], and the cross-sections calculated to next-to-leading order in the strong coupling constant (NLO) using `PROSPINO` [113].

The direct gaugino pMSSM grids contain 32 possible weak production processes. The squarks and gluinos were again assumed heavy (set at 2 TeV) so the production of supersymmetric particles is dominated by direct weak production of neutralinos, charginos and/or sleptons. The right-handed sleptons, with a common mass for all three generations were inserted between the two lightest neutralino masses, with the left-handed sleptons set out of reach. In the pMSSM the specific mixing of the underlying gauginos and higgsinos that make up the chargino and neutralino mass eigenstates are determined by  $M_1$  (neutralinos only),  $M_2$  and  $\mu$  (and to a lesser extent  $\tan\beta$ ). In general the phenomenology associated with the neutralino-chargino sector is very sensitive to the underlying gaugino/higgsino structure of the mass eigenstates. It first impacts their pair-production cross-sections and affects the branching patterns.

Two dimensional grids in  $(\mu, M_2)$  were generated for three values of  $M_1$ : 100 GeV, 140 GeV and 250 GeV, with  $\tan\beta = 6$  and  $m_A = 500 \text{ GeV}$ .  $\tan\beta$  controls the branching fractions into the various slepton flavours for many values of  $M_1$ ,  $M_2$ , and  $\mu$ , with higher values favouring staus. The value chosen for this grid allows a good proportion of decays to selectrons and smuons. The trilinear couplings were set to zero for staus and sbottoms, and to maximal mixing for stops. Signal points in these grids were generated using `HERWIG`, and again the cross-sections calculated using `PROSPINO`.

### 6.3 Event selection

All the signal regions in the analysis under discussion in this chapter require “exactly two signal leptons”. The discussion of event selection will be done in two parts. This section discusses the baseline 2-lepton event selection, including a definition of what is meant by “signal leptons”. Once this was established, the signal regions were defined by placing additional requirements on jet multiplicity, the di-lepton invariant mass, the  $E_T^{\text{miss,rel}}$  variable (which was introduced in Section 5.4), and other relevant kinematic event variables. The signal region definitions are given in Section 6.4.

A summary of the definitions used in the 2011 analysis for “baseline” and “signal” objects for electrons, muons and jets is given in Table 6.2. These definitions were used to be consistent with recommendations from performance groups within the ATLAS collaboration and with other analyses in the ATLAS SUSY working group at the time the analysis was performed.

<b>Muons</b>		
	Baseline	Signal
Cut	Value/Description	Value/Description
Algorithm	<b>STACO</b> (combined and segment-tagged)	<b>STACO</b> (combined and segment-tagged)
$p_T$	$p_T > 10 \text{ GeV}$	$p_T > 10 \text{ GeV}$
$\eta$ -Acceptance	$ \eta  < 2.4$	$ \eta  < 2.4$
isolation	-	$p_{T\text{cone}20} < 1.8 \text{ GeV}$
tracking cuts	various	various
<b>Electrons</b>		
	Baseline	Signal
Cut	Value/Description	Value/Description
Algorithm	<b>egamma</b>	<b>egamma</b>
$p_T$	$p_T > 10 \text{ GeV}$	$p_T > 10 \text{ GeV}$
$\eta$ -Acceptance	$ \eta  < 2.47$	$ \eta  < 2.47$
quality	<b>mediumPP</b>	<b>tightPP</b>
isolation	-	$p_{T\text{cone}20}/p_T < 0.1$
<b>Jets</b>		
	Baseline	Signal
Cut	Value/Description	Value/Description
Algorithm	anti- $k_t$ ( $\Delta R = 0.4$ )	anti- $k_t$ ( $\Delta R = 0.4$ )
$p_T$	$p_T > 20 \text{ GeV}$	$p_T > 30 \text{ GeV}$
$\eta$ -Acceptance	$ \eta  < 4.9$	$ \eta  < 2.5$
JVF	-	JVF $> 0.75$
<b>b-Jets</b> (additional requirements to jets)		
tag	<b>JetFitterCombNN</b> $> -1.25$	<b>JetFitterCombNN</b> $> -1.25$

Table 6.2: A summary of all baseline and signal object selection criteria used in the analysis of the 2011 dataset.

All jets in the analysis were reconstructed from topological clusters using the anti- $k_T$  algorithm [40] with  $R=0.4$  as the distance parameter. After the selection of baseline

jets as in Table 6.2, and after overlap-removal (which will be described later), additional requirements were placed on jets for the signal regions and control regions used in the analysis. The “signal jet” definition was used to define the signal regions (either to veto or require a certain multiplicity) and requires transverse momentum  $p_T > 30 \text{ GeV}$  and  $|\eta| < 2.5$ . The “jet vertex fraction” (JVF) of signal jets must also satisfy  $\text{JVF} > 0.75$ . The jet vertex fraction is defined as the total track momentum associated with the jet and coming from the primary vertex divided by the total transverse momentum in the jet. This requirement was added to remove jets originating from other collisions (such as pile-up) and without reconstructed tracks. In signal regions defined by a jet veto, this reduces the risk of vetoing signal events due to the presence of pile-up jets in the event.

For  $b$ -jets the 80% working point of the `JetFitterCombNN` algorithm [41] was used. The algorithm uses the long lifetime of  $b$ - and  $c$ - hadrons to identify jets containing a  $b$ -hadron decay. The nominal  $b$ -tagging efficiency required was higher than the typical working point used for ATLAS supersymmetry analyses of 60%, but was necessary in order to sufficiently suppress the  $t\bar{t}$  background in the signal regions defined by a  $b$ -jet veto. For events in Monte Carlo, when requiring either  $b$ -tagged jets or vetoing them, events were assigned multiplicative weights, calculated based on the jets in that event, to account for the differences in  $b$ -tagging efficiencies between data and Monte Carlo.

For electrons in the analysis, the `egamma` algorithm [38] was used. Baseline electrons were required to have  $p_T > 10 \text{ GeV}$ ,  $|\eta| < 2.47$  and satisfy the “medium” selection in [155]. When selecting signal electrons, additional isolation criteria were applied. The  $p_T$  sum of tracks above 1 GeV within a cone of  $\Delta R < 0.2$  ( $\Delta R = \sqrt{(\Delta\eta)^2 + (\Delta\phi)^2}$ ) around each electron candidate (denoted  $p_{T\text{cone}20}$  in Table 6.2) was required to be less than 10% of the electron’s  $p_T$ . The `tightPP` selection included cuts on  $E/p$  (where  $E$  is the shower energy in the calorimeter and  $p$  is the track momentum from the ID) and TRT cuts which provided extra rejection against fakes from conversions and hadrons. (This is the “tight” requirement in [155]). When running over all Monte Carlo samples, multiplicative weights were applied to the Monte Carlo event weight for every selected signal lepton, to correct for differences in efficiency between the data and simulation. This correction included both the identification efficiency of the `tightPP` selection and the reconstruction and track quality efficiency.

This analysis used “segment tagged” and “combined” muons reconstructed using the STACO algorithm [39] that combines a track reconstructed in the MS with its corresponding track in the ID. In addition to the baseline selection ( $p_T > 10 \text{ GeV}$ ,  $|\eta| < 2.4$ ) signal muons were required to be isolated: the  $p_T$  sum of tracks in a cone

$\Delta R < 0.2$  of the muon track had to be less than 1.8 GeV, excluding the muon track. As with electrons, a smearing correction was applied to the muon momenta in Monte Carlo events to correct for differences in the scale and resolution of the muon energy between data and Monte Carlo, and multiplicative event weights were applied to Monte Carlo to correct for the difference in muon reconstruction efficiency observed between data and the simulation. Events were vetoed if they contain any “bad” or “cosmic” muons. Cosmic muons were defined as having  $|z_0| > 1 \text{ mm}$  or  $|d_0| > 0.2 \text{ mm}$  where  $z_0$  and  $d_0$  are the longitudinal and transverse impact parameters with respect to the primary vertex respectively. The “bad muon” requirement was designed to veto badly measured non-isolated muons; bad muons were defined as having  $\sigma_{q/p}/|q/p| \geq 0.2$ , where  $q$  and  $p$  are the charge and momentum respectively and  $\sigma_{q/p}$  is the square root of the covariance of  $q/p$ . This requirement was applied before overlap-removal whereas cosmic muons were only vetoed after overlap-removal.

All the 2011 signal regions used in the analysis included a cut on the  $E_T^{\text{miss,rel}}$  variable (see Equation (5.4)), which is built from the  $E_T^{\text{miss}}$ . The  $E_T^{\text{miss}}$  used in the analysis was constructed from jets with  $p_T > 20 \text{ GeV}$ , all electron and muon candidates, and topological calorimeter clusters not belonging to pre-cited objects (this is referred to as the “CellOut” term).

Overlap-removal on the selected baseline objects in an event was necessary to avoid the duplication of a given object in more than one particle collection. There were five steps to this procedure: firstly, if any two baseline electrons lay within a distance  $\Delta R < 0.1$  of each other, the electron with the lowest cluster transverse energy ( $E_T$ ) was removed. Secondly, if the distance between any baseline jet and any baseline electron passing the first overlap-removal step was less than 0.2 the jet was removed. If, for any of the jets surviving this step, the distance between that jet and any baseline electron (which survived the first step) was less than 0.4, the baseline electron was removed. The same procedure was then applied to all baseline muons. Finally, if any surviving baseline electrons or surviving baseline muon were within  $\Delta R < 0.1$  of each other, both the electron and muon were removed.

Events were only considered if they passed certain “event quality criteria”. The full set of cuts is provided in Table 6.3. These criteria were designed to reject events where the event reconstruction could be unreliable. The “Good Runs List” criteria ensured that events were only used for analysis if they corresponded to data-taking during stable beam that satisfied the data-quality requirements (essentially all sub-detectors should be functioning correctly, enabling accurate reconstruction of events), and the “LArError”

Cut	Detail
Good Runs List	Events in data must pass requirements on data quality
LArError	Events must report no error after LAr quality assessment
Jet Cleaning	Events must not contain a jet failing the jet quality criteria
Good Vertex	Events must have one primary vertex associated with at least 5 tracks
Cosmic Veto	Reject events with at least one muon failing the cosmic rejection cuts
Bad Muon Veto	Reject events with at least one muons failing the bad muon criteria

Table 6.3: Event quality criteria used for the analysis on 2011 data. These are additional cuts applied at the event selection level before applying the signal/control region selections.

cut rejected any events reporting an error after the LAr quality assessment (this was needed to remove noise events with noise bursts in the calorimeter). The “Jet Cleaning” cut rejected events containing bad quality jets, which were likely to have arisen from detector noise or cosmic rays [156], and also any jets pointing towards dead regions of the LAr calorimeter (so energy measurements could not be trusted). Once these criteria were satisfied, events in all the signal regions and control regions were required to have exactly two signal leptons, after overlap-removal, with a di-lepton invariant mass greater than 20 GeV.

The trigger strategy for the analysis will now be discussed. The analysis took data events from both the “Egamma” and “Muon” data streams. A combination of several single- and di-lepton triggers were used to maximise the efficiency for signal events. The 2011 data run was divided into different data-taking periods. For each period the lowest un-prescaled triggers were used. The triggers used for the di-electron and di-muon channel are listed in Tables 6.4 and 6.5 respectively. For the electron-muon channel the single-electron or single-muon triggers shown in Tables 6.4 and 6.5 were used alongside the electron-muon trigger given in Table 6.6. To explain the nomenclature, as an example, the “e22\_medium” selection required one identified electron in the HLT satisfying the “medium” selection with a  $p_T$  greater than 20 GeV. The extra letters in the “e22vh\_medium1”, “e22vh\_medium1”, “2e12T\_medium” and “2e12vh\_medium” decisions refer to additional isolation criteria applied at the HLT. This was necessary to avoid pre-scaling as the instantaneous luminosity delivered by the LHC increased throughout the year.

The trigger strategy for Monte Carlo events was designed to remove the reliance of the analysis on the trigger simulation. Instead of requiring an event to pass a given trigger in Monte Carlo, the events were assigned a multiplicative weight, derived from data, which reflected the efficiency of that trigger for that event (full details are given in [157]). To ensure consistency between the approaches for data and Monte Carlo, for data events a “trigger matching” requirement was applied, that required that one or both of the reconstructed signal leptons must match onto the trigger objects in the event. This was done by testing if the reconstructed lepton was within a certain distance  $\Delta R$  of the trigger object.

The trigger strategy imposed additional offline cuts on the  $p_T$  of the leptons considered, which are detailed in Tables 6.4 to 6.6. They were necessary in order to only select leptons in the plateau region of the triggers in question and so avoid the turn-on region where the efficiencies depend on the lepton  $p_T$ . These are detailed in Tables 6.4 to 6.6. The plateau trigger efficiencies were dependent on both  $\eta$  and  $\phi$ . For the muon triggers the maximum plateau efficiencies in the barrel and end-cap regions were around 90% and 70% respectively. For the electron triggers, the efficiencies reached a maximum of  $> 95\%$  (degrading to efficiencies  $\sim 90\%$  for electrons with  $|\eta| > 2.37$ ).

Period	Single		Double	
	Trigger	Offline $p_T$ cut	Trigger	Offline $p_T$ cut
A-J	e20_medium	25 GeV	2e12_medium	17 GeV
K	e22_medium	25 GeV	2e12T_medium	17 GeV
L-M	e22vh_medium1	25 GeV	2e12Tvh_medium	17 GeV

Table 6.4: Single-electron and double-electron triggers used in 2011 for each period of data analysed.

Period	Single		Double	
	Trigger	Offline $p_T$ cut	Trigger	Offline $p_T$ cut
A-I	mu18	20 GeV	2mu10_loose	12 GeV
J-M	mu18_medium	20 GeV	2mu10_loose	12 GeV

Table 6.5: Single-muon and double-muon triggers used in 2011 for each period of data analysed.

For a given channel, the maximal trigger efficiency would have been achieved by requiring events to pass either the single-lepton or the di-lepton triggers. However, to propagate this strategy to Monte Carlo would have required calculating conditional trigger probabilities, which increased the complexity, especially since the triggers being used changed with time. Instead, for each lepton flavour channel, the 2D parameter space defined by the  $p_T$ s of the two signal leptons was divided into disjoint regions, and in each region the most efficient trigger was used. These regions are shown in Figure 6.1. In general single-lepton triggers were used in areas with one high  $p_T$  lepton and di-lepton triggers were used in areas with two intermediate momenta leptons. The only exception to this is in the di-muon channel. The single-muon triggers only reached a plateau efficiency around 80%. This is much lower than the single-electron trigger, which was used in Regions A and B (with leading electron  $p_T > 25 \text{ GeV}$ ) of Figure 6.1, and had a very high efficiency of around 95% on the plateau. Consequently in the di-muon channel in events in Region A were required to pass either the di-muon or single-muon triggers. This did require the calculation of the conditional single-muon to di-muon trigger probability, however it brought the trigger efficiency in region A up to around 90% therefore the additional steps in the calculation were justified. The triggers used in each region are summarised in Table 6.7.

It was also necessary to re-weight Monte Carlo events on an event-by-event basis to correct for differences in the amount of pile-up between data and the simulation. As the Monte Carlo samples had to be launched before the data was taken, they did not have the same distribution of the average number of interactions per bunch crossing ( $\langle \mu \rangle$ ), as the data. As the range of  $\langle \mu \rangle$  in data and simulation was similar, it was possible to reweight the Monte Carlo samples to model the distribution of  $\langle \mu \rangle$  observed in data.

In summary, events with exactly two signal leptons were selected in data and Monte

Period	Single	
	Trigger	Offline $p_T$ cuts
A-M	e10_medium_mu6	$p_T(e) > 15 \text{ GeV}, p_T(\mu) > 8 \text{ GeV}$

Table 6.6: Details of the electron-muon trigger used in 2011 for each period of data analysed. This was combined with the single electron and single muon triggers given in Tables 6.4 and 6.6.

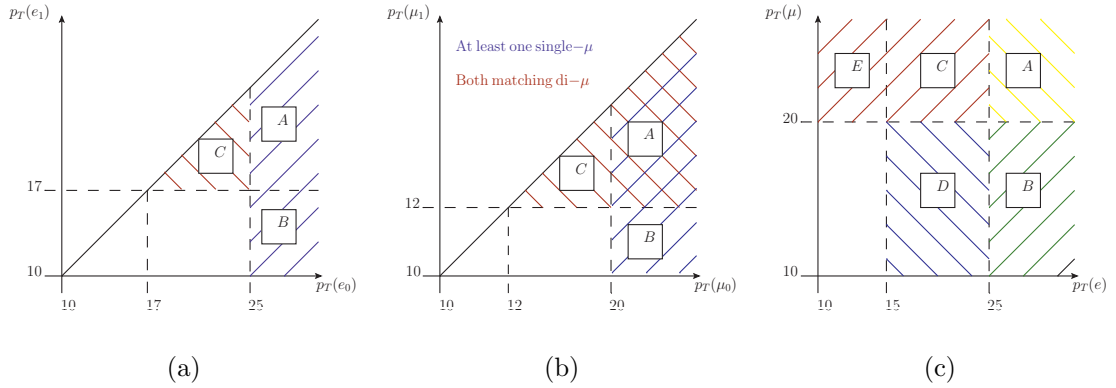


Figure 6.1: Illustrations of the 2D parameter space defined by the transverse momenta of the two signal leptons in di-lepton events for the three lepton flavour channels,  $e^\pm e^\mp$  (a),  $\mu^\pm \mu^\mp$  (b) and  $e\mu$  (c), and the labels of the different regions [157].

Region	ee	$\mu\mu$	$e\mu$
A	single electron	single muon or dimuon	single electron or single muon
B	single electron	single muon	single electron
C	di-electron	dimuon	single muon
D	-	-	electron-muon
E	-	-	single muon

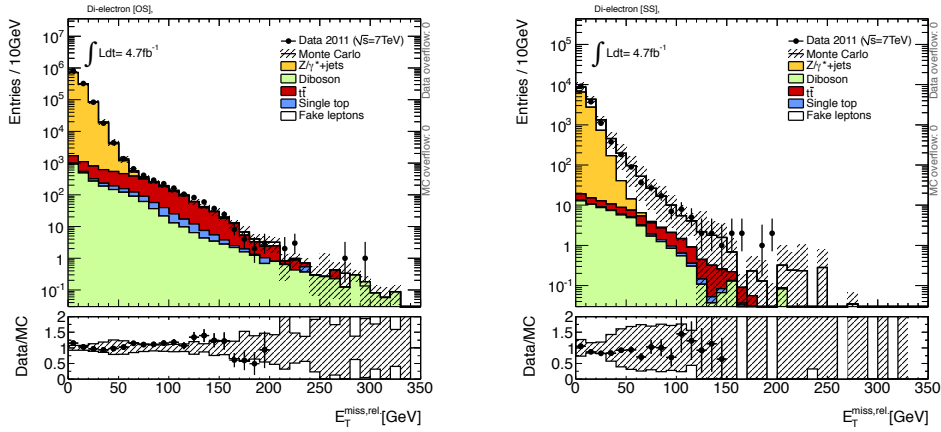
Table 6.7: Summary of the trigger strategy for the different areas of phase space depicted in Figure 6.1.

Carlo events if they satisfied the event quality criteria summarised in Table 6.3, contained exactly two signal leptons, after overlap-removal, with a di-lepton invariant mass  $m_{ll} > 20 \text{ GeV}$ , and the  $p_T$  s of the leptons corresponded to one of the trigger regions shown in Figure 6.1. Data events were then required to pass the trigger requirement for that region, with the reconstructed lepton(s) being matched to the corresponding trigger objects in the event, whereas for Monte Carlo trigger weights were applied. Additionally, multiplicative event weights were applied to Monte Carlo events to correct for differences in lepton identification and b-tagging efficiency, and to correct for differences in the  $\langle \mu \rangle$  distribution between data and Monte Carlo.

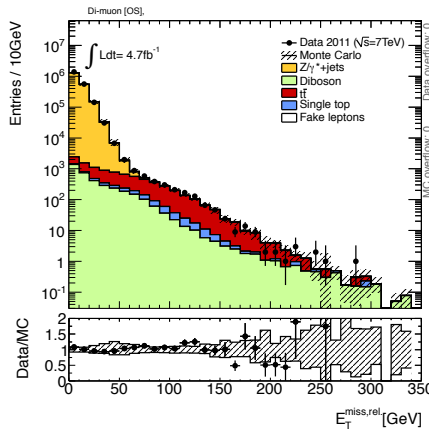
Before proceeding to the signal region definitions, comparisons between data and Monte Carlo for selected events containing exactly two signal leptons will be presented. Distributions for events containing opposite-sign and same-sign lepton pairs will be shown separately. The fake-lepton background was evaluated using the matrix method and for the distributions of same-sign events the data driven “charge-flip” estimate is included. Both of these methods will be introduced in Section 6.5. Figures 6.2 and 6.3 show the  $E_T^{\text{miss,rel}}$  distributions in the di-electron, di-muon and electron-muon channels for the opposite-sign and same-sign channels respectively. The same-flavour opposite-sign channels are dominated by  $Z/\gamma^* + \text{jets}$  at low  $E_T^{\text{miss,rel}}$ , with  $t\bar{t}$  becoming more significant at higher  $E_T^{\text{miss,rel}}$  values. The same-sign distributions across all channels are dominated by the fake background (which was evaluated using the matrix method). The larger uncertainty bands in the same-sign distributions correspond to the uncertainty on the fake estimate from the matrix method. The data agrees with the background predictions, within to the uncertainty band, except for the low  $E_T^{\text{miss,rel}}$  regions of the di-muon same-sign, electron-muon same-sign and the electron-muon opposite-sign distributions. These are the regions dominated by the fake background. After further investigation it was concluded that the implementation of the matrix method for the analysis was only reliable in the region  $E_T^{\text{miss,rel}} > 40 \text{ GeV}$ .

Figures 6.4 and 6.5 show distributions of the di-lepton invariant mass and the signal jet multiplicity respectively, for opposite-sign events, after placing a requirement on  $E_T^{\text{miss,rel}} > 40 \text{ GeV}$ . In the di-electron and di-muon channels the peak around the  $Z$ -mass in the invariant mass distribution is clearly visible, justifying the implementation of vetos on the  $Z$ -mass window in signal region definitions. In the electron-muon channel, apart from at low  $m_{ll}$  where the fake background is important, the  $t\bar{t}$  background dominates. The multiplicity of signal jets is well-modelled up to high jet multiplicities in all lepton flavour channels. Finally, Figure 6.6 shows distributions of the leading lepton  $p_T$  for

events with  $E_T^{\text{miss,rel}} > 40 \text{ GeV}$ . At low  $p_T$  the same flavour channels are dominated by  $Z$ +jets, with  $t\bar{t}$  also becoming important at higher  $p_T$ , whereas the electron-muon channel is dominated by the fake lepton background at low  $p_T$  and  $t\bar{t}$  at high  $p_T$ .

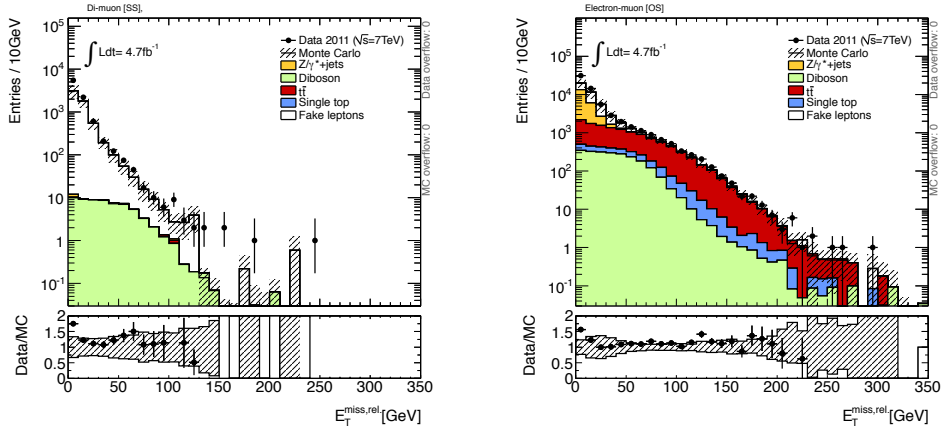


(a) Di-electron opposite-sign  $E_T^{\text{miss,rel}}$ . (b) Di-electron same-sign  $E_T^{\text{miss,rel}}$ .



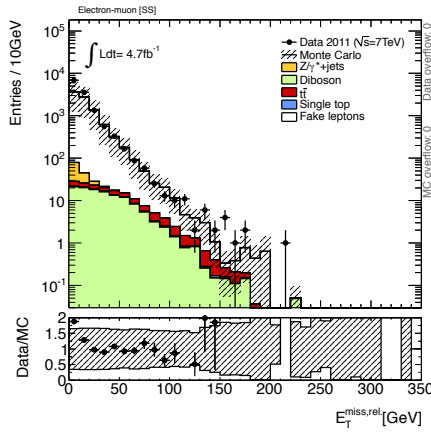
(c) Di-muon opposite-sign  $E_T^{\text{miss,rel}}$ .

Figure 6.2: Comparisons between data and Monte Carlo for the  $E_T^{\text{miss,rel}}$  distributions in opposite-sign events for the di-electron (a), di-muon (b) and electron-muon (c) channels, for  $4.7 \text{ fb}^{-1}$  of data at  $\sqrt{s} = 7 \text{ TeV}$ .



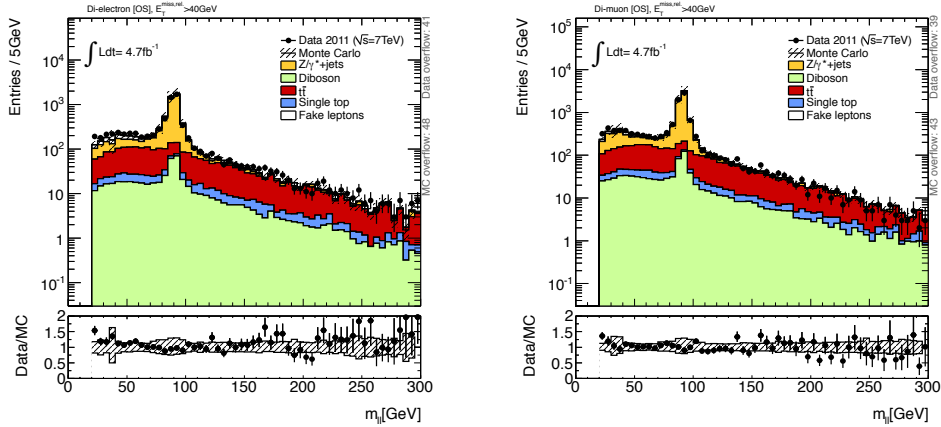
(a) Di-muon same-sign  $E_T^{\text{miss,rel}}$ .

(b) Electron-muon opposite-sign  $E_T^{\text{miss,rel}}$ .



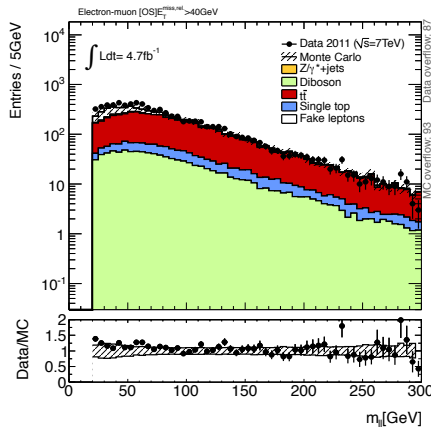
(c) Electron-muon same-sign  $E_T^{\text{miss,rel}}$ .

Figure 6.3: Comparisons between data and Monte Carlo for the  $E_T^{\text{miss,rel}}$  distributions in same-sign events for the di-electron (a), di-muon (b) and electron-muon (c) channels, for  $4.7 \text{ fb}^{-1}$  of data at  $\sqrt{s} = 7 \text{ TeV}$ .



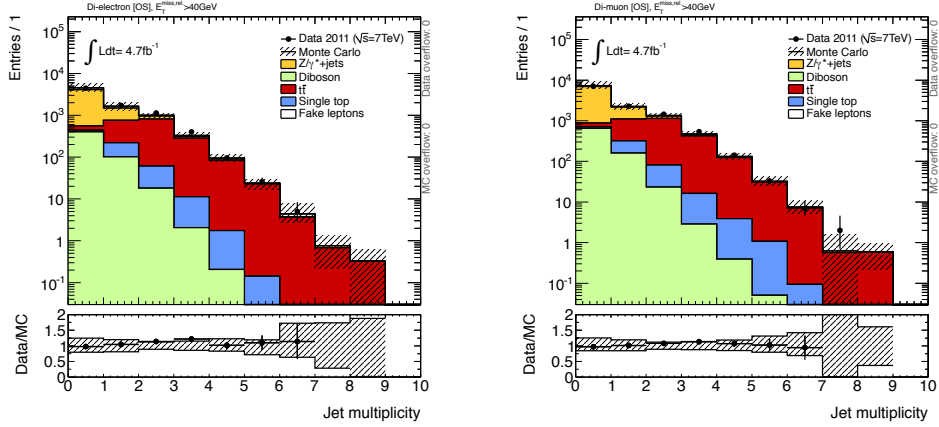
(a) Di-electron opposite-sign  $m_{ll}$ .

(b) Di-muon opposite-sign  $m_{ll}$ .



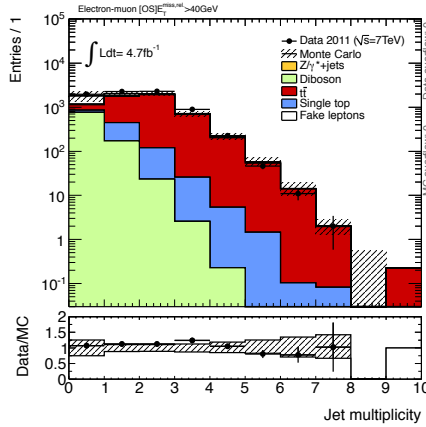
(c) Electron-muon opposite-sign  $m_{ll}$ .

Figure 6.4: Comparisons between data and Monte Carlo for distributions of the di-lepton invariant mass in opposite-sign di-electron (a), di-muon (b) and electron-muon (c) events with  $E_T^{\text{miss,rel}} > 40 \text{ GeV}$ , for  $4.7 \text{ fb}^{-1}$  of data at  $\sqrt{s} = 7 \text{ TeV}$ .



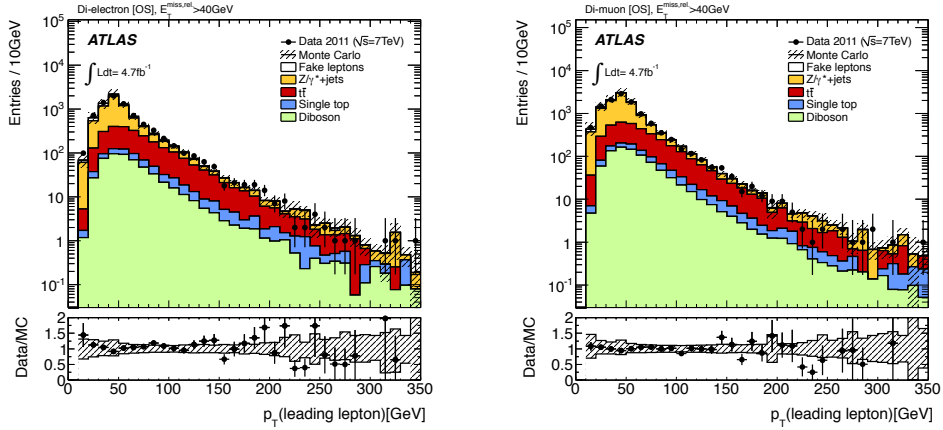
(a) Di-electron opposite-sign signal jet multiplicity.

(b) Di-muon opposite-sign signal jet multiplicity.



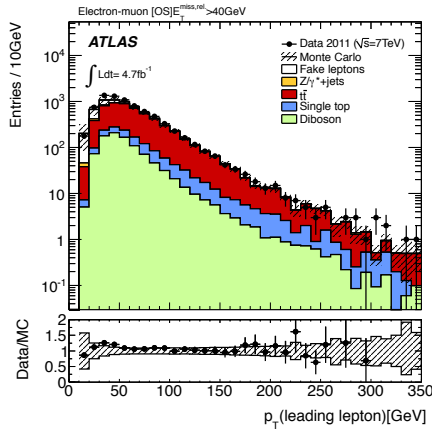
(c) Electron-muon opposite-sign signal jet multiplicity.

Figure 6.5: Comparisons between data and Monte Carlo for distributions of the signal jet multiplicity in opposite-sign di-electron (a), di-muon (b) and electron-muon (c) events with  $E_T^{\text{miss,rel}} > 40 \text{ GeV}$ , for  $4.7 \text{ fb}^{-1}$  of data at  $\sqrt{s} = 7 \text{ TeV}$ .



(a) Di-electron opposite-sign leading lepton  $p_T$ .

(b) Di-muon opposite-sign leading lepton  $p_T$ .



(c) Electron-muon opposite-sign leading lepton  $p_T$ .

Figure 6.6: Comparisons between data and Monte Carlo for distributions of the leading lepton  $p_T$  in opposite-sign di-electron (a), di-muon (b) and electron-muon (c) events with  $E_T^{\text{miss,rel}} > 40 \text{ GeV}$ , for  $4.7 \text{ fb}^{-1}$  of data at  $\sqrt{s} = 7 \text{ TeV}$ .

## 6.4 Summary of the Signal Regions

The analysis published in [1] used four signal regions, each of which were optimised to target different signal processes. The signal region based on the  $m_{T2}$  variable, that was introduced in Section 5.4, will be referred to in this chapter as “SR- $m_{T2}$ ”. In addition to this, there were three further signal regions: “SR-OSjveto” (opposite-sign leptons with a jet veto), “SR-SSjveto” (same-sign leptons with a jet veto), “SR-2jets” (opposite-sign leptons with a requirement of at least two signal jets). These were designed to provide sensitivity to the pair production of electroweak gauginos (but not sleptons). The cuts defining all of the signal regions are summarised in Table 6.8.

Shorthand	Description	Cuts
SR-OSjveto	OS jet-veto	jet-veto $E_T^{\text{miss,rel.}} > 100 \text{ GeV}$ $ m_Z - m_u  > 10 \text{ GeV}$
SR-SSjveto	SS jet-veto	jet-veto $E_T^{\text{miss,rel.}} > 100 \text{ GeV}$
SR-2jets	OSSF with jets	$\geq 2$ -jets $b$ -jet veto $m_{CT}$ top-tag veto $ m_Z - m_u  > 10 \text{ GeV}$ $E_T^{\text{miss,rel.}} > 50 \text{ GeV}$
SR- $m_{T2}$	OS(SF) $m_{T2}$	jet-veto $ m_Z - m_u  > 10 \text{ GeV}$ $E_T^{\text{miss,rel.}} > 40 \text{ GeV}$ $m_{T2} > 90 \text{ GeV}$

Table 6.8: Signal region definitions for the search for gaugino and slepton-pair production in the analysis on 2011 data. The label “OS” refers to an opposite sign lepton pair, “SS” refers to a pair of same sign leptons and “OSSF” refers to an opposite sign same flavour lepton pair. For SR- $m_{T2}$  the same flavour requirement is only applied for the direct slepton grid. The  $Z$  boson mass  $m_Z$  was taken to be 91.2 GeV.

When requiring either a jet veto or a certain jet multiplicity, signal jets were used. In this analysis  $m_Z$  was taken to be 91.2 GeV. The top-tagging veto used in the definition of SR-2jets used the “contransverse mass”  $m_{CT}$ . More detailed discussions of the variable

can be found in [158, 159] and an outline of the top-tagging technique is provided in Appendix C.

SR-OSjveto, SR-SSjveto and SR-2jets were primarily aimed at  $\tilde{\chi}_1^\pm \tilde{\chi}_1^\mp$  pair production and  $\tilde{\chi}_2^0 \tilde{\chi}_1^\pm$  associated production. The cross-sections for these processes, assuming equal masses of the  $\tilde{\chi}_1^\pm$  and  $\tilde{\chi}_2^0$ , are shown in Figure 6.7, along with the cross-sections for  $\tilde{\chi}_2^0 \tilde{\chi}_2^0$  production which was not targeted by the analysis but could be in the future. The processes of  $\tilde{\chi}_2^0 \tilde{\chi}_1^\pm$ ,  $\tilde{\chi}_1^\pm \tilde{\chi}_1^\mp$  and  $\tilde{\chi}_2^0 \tilde{\chi}_2^0$  production are labelled “Mode A”, “Mode C” and “Mode D” respectively. The cross-sections displayed are for the “pure wino” scenario, where the  $\tilde{\chi}_1^\pm$  has no higgsino component and the  $\tilde{\chi}_2^0$  has no higgsino or bino component. The optimisation of the signal regions used the two direct gaugino simplified model grids

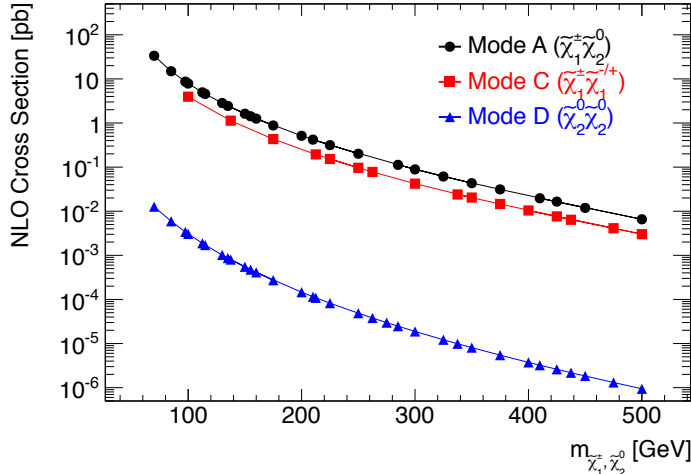


Figure 6.7: Cross-sections for different direct gaugino production modes in the “pure wino” scenario, where the  $\tilde{\chi}_1^\pm$  has no higgsino component and the  $\tilde{\chi}_2^0$  has no higgsino nor bino component [157].

and the weak production pMSSM signal grids that were introduced in Section 6.4, and in all cases the  $Z_N$  variable (as used in Section 5.4.3) was used as a measure of the significance.

SR-OSjveto targeted chargino-pair production. The two possible decay topologies giving rise to two leptons are shown in Figure 6.8. Both topologies give two opposite-sign leptons, uncorrelated in flavour, no jets and  $E_T^{\text{miss}}$  due to the undetected neutralinos, however this analysis was only sensitive to the case with intermediate sleptons in the decay chains. Optimisation was performed using the chargino-pair production simplified model grid. After requiring a jet veto and a veto on the  $Z$ -mass window, to suppress dominant  $t\bar{t}$  and  $Z/\gamma^* \rightarrow ll + \text{jets}$  backgrounds, a cut on  $E_T^{\text{miss,rel}}$  rather than  $E_T^{\text{miss}}$  alone

was chosen to reduce the impact of contributions to the  $E_T^{\text{miss}}$  from mis-measured objects, particularly jets. A scan over possible  $E_T^{\text{miss,rel}}$  cuts was performed and the final cut was fixed at 100 GeV.

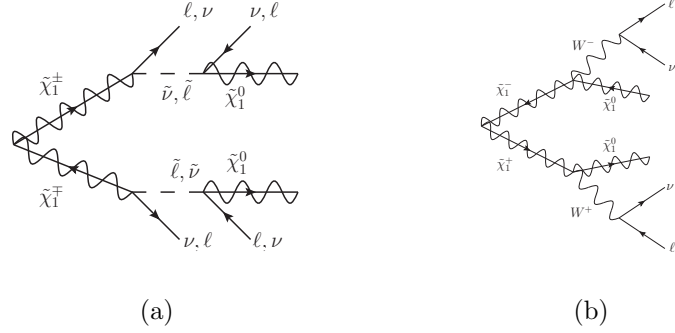


Figure 6.8: Feynman diagrams for  $\tilde{\chi}_1^+ \tilde{\chi}_1^-$  pair production with, (a), and without, (b), intermediate sleptons. The intermediate slepton can be either a charged slepton or a sneutrino.

SR-SSjveto targeted di-lepton signatures arising from  $\tilde{\chi}_2^0 \tilde{\chi}_1^\pm$  associated production, which are tri-lepton events at truth level but only two leptons are reconstructed. The 3-lepton analysis [141] had more sensitivity to this process but SR-SSjveto was optimised with a view to improving the 3-lepton sensitivity through a statistical combination. Diagrams showing the case that one of the leptons from the decay of the  $\tilde{\chi}_2^0$  is not reconstructed are given in Figure 6.9 and equations for the decays are given in Equations (6.1) and (6.2):

$$\tilde{\chi}_2^0 \tilde{\chi}_1^\pm \rightarrow (\ell_{rec}^+ \ell^- \tilde{\chi}_1^0) + (\ell_{rec}^\pm \nu \tilde{\chi}_1^0) \quad (6.1)$$

$$\tilde{\chi}_2^0 \tilde{\chi}_1^\pm \rightarrow (\ell^+ \ell_{rec}^- \tilde{\chi}_1^0) + (\ell_{rec}^\pm \nu \tilde{\chi}_1^0) \quad (6.2)$$

Optimisation was performed on the simplified model grid for  $\tilde{\chi}_2^0 \tilde{\chi}_1^\pm$  production with intermediate sleptons. The same jet veto was used as in SR-OSjveto (for simplicity) and a scan was performed over possible values of the  $E_T^{\text{miss,rel}}$  cut, with the final value being chosen to be 100 GeV.

SR-2jets targeted  $\tilde{\chi}_2^0 \tilde{\chi}_1^\pm$  associated production but in topologies with jets in the final

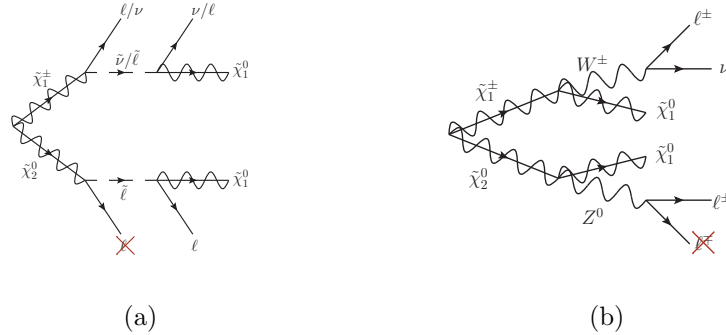


Figure 6.9: Feynman diagrams showing  $\tilde{\chi}_2^0 \tilde{\chi}_1^\pm$  pair production with (a) and without (b) intermediate sleptons, that lead to a same sign di-lepton signature through the failure to reconstruct one of the leptons from the  $\tilde{\chi}_2^0$  leg of the decay.

state. Possible diagrams, both with and without intermediate sleptons, are shown in Figure 6.10. These give signatures involving two opposite-sign same-flavour leptons, two jets and  $E_T^{\text{miss}}$  due to the undetected LSPs. The dominant backgrounds are  $t\bar{t}$  and  $Z/\gamma^* + \text{jets}$ . The  $Z/\gamma^* + \text{jets}$  background was suppressed by veto-ing the  $Z$  mass window and a  $b$ -jet veto was used to suppress the  $t\bar{t}$  background as well as the top-tag veto discussed in Appendix C. The final cut defining the signal region is  $E_T^{\text{miss,rel}} > 50 \text{ GeV}$ . This was optimised using the weak production pMSSM grid by scanning over possible cut values.

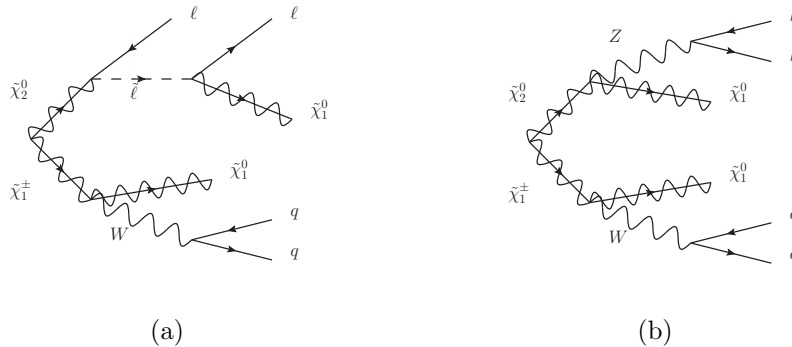


Figure 6.10: Feynman diagrams for  $\tilde{\chi}_2^0 \tilde{\chi}_1^\pm$  pair production with (a), and without (b) intermediate sleptons. The quarks from the hadronic  $W$  decay lead to jets in the final state.

## 6.5 Outline of background estimation techniques

The methods for estimating the Standard Model background contributions in the analysis were chosen so that, where possible, dominant background contributions to each of the signal regions were evaluated using data-driven technique. This minimised the reliance on Monte Carlo predictions (which could potentially have mis-modelled the normalisation and/or kinematic distributions of the a given background component).

To illustrate the background compositions of the signal regions, Tables 6.9, 6.10, and 6.11, give the sample compositions, as approximated by Monte Carlo, in all of the signal regions for the di-electron channel, di-muon channel and electron-muon channel respectively. The counts were taken directly from the Monte Carlo prediction except for the fake lepton component, which was estimated using the data-driven technique (to be described later). In these tables the “diboson” component refers to the  $WW$ ,  $WZ$  and  $ZZ$  backgrounds combined and all other components are shown separately. Also “single top” refers only to  $Wt$ -channel single top production as the  $s$ - and  $t$ -channels were included in the fake lepton background.

SR-OSjveto, SR-2jets and SR- $m_{T2}$  all require opposite-sign leptons and high  $E_T^{\text{miss,rel}}$  so are dominated by real lepton backgrounds. The fully leptonic  $t\bar{t}$  and  $WW$  backgrounds are significant as they give true  $E_T^{\text{miss}}$  in events. Although  $Z/\gamma^* + \text{jets}$  has no real  $E_T^{\text{miss}}$ , high  $E_T^{\text{miss}}$  events can arise from mis-measurement, particularly of jets, and detector imperfections, and these effects may not be well-modelled in Monte Carlo.

Across all channels SR-OSjveto is dominated by  $t\bar{t}$  and diboson contributions, which are approximately equal in the di-electron and di-muon channels, whereas  $t\bar{t}$  contributes more in the electron-muon channel. The counts in SR- $m_{T2}$  are dominated by the diboson backgrounds. These are principally from the  $WW$  background which is kinematically similar to the signal. The cut on  $m_{T2}$  at 90 GeV is successful at reducing the  $t\bar{t}$  background. The  $Z$ -veto applied to all opposite-sign signal region leads to low contributions of  $Z/\gamma^* + \text{jets}$ .

SR-SSjveto has a very low Standard Model background, with both the di-electron and electron-muon channels being dominated by the fake-lepton contribution. There were also contributions from processes with multiple real isolated leptons, but where one is out of acceptance (e.g. diboson  $WZ$  events). For the  $e^+e^+$  and  $e^+\mu^+$  channels, there are also contributions from Standard Model processes that originate as opposite-sign events but one electron undergoes a “charge-flip” (see later).

ee	SR-OSjveto	SR-SSjveto	SR-2jets	SR- $m_{T2}$
$Z/\gamma^* + \text{jets}$	$0.121 \pm 0.122 \pm 0.121$	-	$3.21 \pm 1.56 \pm 0.781$	$0.422 \pm 0.196 \pm 0.212$
Diboson	$11.9 \pm 7.29 \pm 0.655$	$1.26 \pm 0.306 \pm 0.152$	$7.4 \pm 4.31 \pm 0.5$	$5.18 \pm 1.53 \pm 0.339$
$t\bar{t}$	$14.6 \pm 2.62 \pm 1.73$	$0.516 \pm 0.0668 \pm 0.298$	$13.1 \pm 3.07 \pm 1.62$	$1.44 \pm 0.637 \pm 0.55$
Single top	$4.61 \pm 0.94 \pm 0.75$	$0.302 \pm 0.116 \pm 0.225$	$1.21 \pm 0.432 \pm 0.375$	$0.668 \pm 0.245 \pm 0.255$
fakes	$2.91 \pm 1.17 \pm 1.19$	$3.2 \pm 1.69 \pm 0.923$	$2.5 \pm 1.48 \pm 1.22$	$1.03 \pm 0.586 \pm 0.626$
Total SM	$34.2 \pm 7.96 \pm 2.33$	$5.27 \pm 1.73 \pm 1.01$	$27.4 \pm 6.63 \pm 2.26$	$8.75 \pm 1.88 \pm 0.959$

Table 6.9: Composition of the signal regions in the 2011 analysis as approximated by Monte Carlo only, in the di-electron channel. These event yields do not include the data-driven estimates, apart from the fake contribution which is calculated using the matrix method. The first quoted uncertainty is the systematic uncertainty, without Monte Carlo generator systematics, and the second is statistical, arising from limited Monte Carlo statistics.  $Z/\gamma^* + \text{jets}$  is omitted for SR-SSjveto as the contribution is negligible.

$\mu\mu$	SR-OSjveto	SR-SSjveto	SR-2jets	SR- $m_{T2}$
$Z/\gamma^* + \text{jets}$	$0.543 \pm 0.0435 \pm 0.431$	$0.0872 \pm 0.00744 \pm 0.0872$	$5.45 \pm 1.86 \pm 1.14$	$0.903 \pm 0.324 \pm 0.376$
Diboson	$17 \pm 10.5 \pm 0.74$	$0.9 \pm 0.253 \pm 0.137$	$9.68 \pm 5.76 \pm 0.55$	$6.36 \pm 1.46 \pm 0.388$
$t\bar{t}$	$21.5 \pm 4.56 \pm 2.04$	$0.393 \pm 0.0457 \pm 0.28$	$20.1 \pm 5.48 \pm 1.96$	$3.27 \pm 1.42 \pm 0.823$
Single top	$4.9 \pm 0.699 \pm 0.716$	$0.0812 \pm 0.0739 \pm 0.0734$	$1.49 \pm 0.505 \pm 0.445$	$0.677 \pm 0.35 \pm 0.243$
fakes	$0.424 \pm 0.323 \pm 0.647$	$0.562 \pm 0.289 \pm 0.607$	$1.68 \pm 0.828 \pm 1.32$	$-0.017 \pm 0.045 \pm 0.008$
Total SM	$44.4 \pm 11.8 \pm 2.42$	$2.02 \pm 0.397 \pm 0.692$	$38.4 \pm 9.01 \pm 2.72$	$11.2 \pm 2.37 \pm 1.01$

Table 6.10: Composition of the signal regions in the 2011 analysis as approximated by Monte Carlo only, in the di-muon channel. These event yields do not include the data-driven estimates, apart from the fake contribution which is calculated using the matrix method. The first quoted uncertainty is the total systematic uncertainty, without Monte Carlo generator systematics, and the second is statistical, arising from limited Monte Carlo statistics.

$e\mu$	SR-OSjveto	SR-SSjveto	SR- $m_{T2}$
$Z/\gamma^* + \text{jets}$	$0.168 \pm 0.0115 \pm 0.168$	-	-
Diboson	$21.2 \pm 15.7 \pm 0.94$	$1.95 \pm 0.373 \pm 0.198$	$5.14 \pm 0.737 \pm 0.467$
$t\bar{t}$	$34.1 \pm 5.29 \pm 2.65$	$0.137 \pm 0.138 \pm 0.137$	$4.12 \pm 1.14 \pm 0.951$
Single top	$8.54 \pm 1.4 \pm 0.987$	$0.556 \pm 0.305 \pm 0.314$	$0.684 \pm 0.479 \pm 0.289$
fakes	$6.92 \pm 2.62 \pm 1.79$	$2.88 \pm 1.85 \pm 0.935$	$1.14 \pm 0.812 \pm 0.614$
Total SM	$70.9 \pm 17.3 \pm 3.48$	$5.53 \pm 1.89 \pm 1.02$	$11.1 \pm 2.03 \pm 1.26$

Table 6.11: Composition of the signal regions in the 2011 analysis as approximated by Monte Carlo only, in the electron-muon channel. These event yields do not include the data-driven estimates, apart from the fake contribution which is calculated using the matrix method. The first quoted uncertainty is the total systematic uncertainty, without Monte Carlo generator systematics, and the second is statistical, arising from limited Monte Carlo statistics.  $Z/\gamma^* + \text{jets}$  is omitted for SR-SSjveto and SR- $m_{T2}$  as the contributions are negligible.

For computing the final estimates in the opposite-sign signal regions, the Standard Model background processes were grouped into four different backgrounds, which are summarised in Table 6.12. For SR-SSjveto the  $Z + X$  background was split up into  $Z/\gamma^*$ +jets and diboson contributions to ensure the charge-flipped contribution could be handled correctly. Whilst  $Z + X$  technically includes  $Z/\gamma^* \rightarrow \tau\tau$ , this was instead evaluated from Monte Carlo and not included in  $Z + X$  background as the di-lepton invariant mass for this process does not necessarily peak in the  $Z$ -mass window.

Name	Processes included
Top	$t\bar{t}$ , $Wt$ -channel single top
WW	WW only
Z+X	$Z/\gamma^*$ +jets, WZ, ZZ
Fake	Non-prompt lepton backgrounds (e.g W+jets, QCD, $s$ - and $t$ - channel single top)

Table 6.12: Details of the groupings of the Standard Model background processes for the opposite-sign signal regions for the analysis on 2011 data.

Table 6.13 summarises the background estimation techniques used for each background component. With the exception of the fake estimate, all of the data-driven methods used for the opposite-sign signal regions used a control region that was chosen to be dominated by the background process in question but as kinematically close to the signal region as possible. A comparison between the data and Monte Carlo in this region was used to renormalise the Monte Carlo expectation in the signal region. The number of events for a component  $X$  (where  $X$  is either  $Z + X$ , top or  $WW$ ) in a given signal region  $(N_X^{SR})_{est}$  was extracted from the data count in the control region  $(N_{data}^{CR})$ , with the “non- $X$ ” contamination  $(N_{non-X}^{CR})$  subtracted (this was evaluated either from Monte Carlo or using data-driven techniques), using a transfer factor  $\mathcal{T}$  given by

$$(N_X^{SR})_{est} = (N_{data}^{CR} - N_{non-X}^{CR}) \times \mathcal{T}. \quad (6.3)$$

The transfer factor was defined as

$$\mathcal{T} = \left( \frac{N_X^{SR}}{N_X^{CR}} \right)_{MC}, \quad (6.4)$$

where  $(N_X^{SR})_{MC}$  and  $(N_X^{CR})_{MC}$  were the Monte Carlo estimates for the background  $X$  in the signal region and control region respectively. These methods relied on the Monte

Carlo correctly modelling the shape of distributions such as  $E_T^{\text{miss,rel}}$ , as they only changed the normalisation. For SR- $m_{T2}$ , the hard cut on  $m_{T2} > 90 \text{ GeV}$  meant that including the cut in control region definitions would not give enough statistics in the control regions. The data-driven methods were instead used to extract the count in the signal region before the  $m_{T2}$  cut, referred to as “SR-pre- $m_{T2}$ ”, and the  $m_{T2}$  efficiency measured from Monte Carlo was applied to give the signal region yield. This then assumed the Monte Carlo correctly modelled the  $m_{T2}$  efficiency.

The top control regions for the opposite-sign signal regions were defined by requiring two signal jets, one of which must be b-tagged, and a  $E_T^{\text{miss,rel}}$  cut at the same value as the signal region under consideration. The method was therefore applied three times to get estimates for SR-2jets, SR-OSjveto and SR-pre- $m_{T2}$  separately. The three control regions used are summarised in Table 6.14.

For the top background, Equation (6.3) included an additional multiplicative scale factor  $SF_{\mathcal{T}}$  which was derived from data to correct for discrepancies between the jet veto efficiency in data and Monte Carlo. This was studied by the analyser performing the background estimate and found to be consistent with 1. It was taken to be 1 with an uncertainty of 6%.

The data-driven method for the  $Z + X$  background in the  $e^\pm e^\mp$  and  $\mu^\pm \mu^\mp$  channels used data events at high  $E_T^{\text{miss,rel}}$  inside the  $Z$ -mass window to renormalise the Monte Carlo in the signal region. This meant that the extrapolation from low to high  $E_T^{\text{miss,rel}}$  was not performed using Monte Carlo, which could have modelled it incorrectly.

The  $Z + X$  control regions had the same event selection as their corresponding signal region but with the  $Z$ -veto reversed. The control region definitions are shown in Table 6.15 along with their corresponding signal region definition for comparison.

For the  $Z + X$  estimate the contamination from processes including  $t\bar{t}$ ,  $WW$  and  $Z/\gamma^* \rightarrow \tau\tau$  was extracted from electron-muon events in data inside the  $Z$ -window, with corrections applied for the differences between electron and muon reconstruction efficiencies.

$Z + X$  contributions to all opposite-sign signal regions in the electron-muon channel were taken directly from Monte Carlo predictions. This was necessary as the data-driven method used a control region based on the  $Z$ -mass window, assuming both leptons came from the one  $Z$ -boson, and hence was only applicable to the di-electron and di-

SR $\downarrow$ BG $\rightarrow$	$t\bar{t}$ /single top	WW	Z $\rightarrow$ ll+jets	WZ	ZZ	fakes
SR-OSjveto	Data driven	Data driven	Data driven for ee/ $\mu\mu$ (Z+x estimate) MC for $e\mu$			Data/MC driven
SR-SSjveto	MC- OS using charge-flip	MC only	MC- OS using charge-flip for ee/ $e\mu$	Mixture of SS MC and charge-flipped OS		Data/MC driven
SR-2jets	Data driven	MC only	Data driven	Data driven for ee/ $\mu\mu$ (Z+x estimate) MC for $e\mu$		Data/MC driven
SR- $m_{T2}$	Data driven	MC only	Data driven	Data driven for ee/ $\mu\mu$ (Z+x estimate) MC for $e\mu$		Data/MC driven

Table 6.13: Summary of background estimation techniques used in the 2011 analysis [157].

	$N_{\text{jets}}$	$N_{\text{jets}}^b$	$E_{\text{T}}^{\text{miss,rel}}$ cut
	$p_{\text{T}} > 30 \text{ GeV}$	$p_{\text{T}} > 30 \text{ GeV}$	GeV
	$JVF > 0.75$	$JVF > 0.75$	
	CombNN > -1.25		
SR-jveto	=0	=0	100
SR-jveto CR	$\geq 2$	$\geq 1$	100
SR-2jets	$\geq 2$	=0	50
SR-2jets CR	$\geq 2$	$\geq 1$	50
SR-mT2	=0	=0	40
SR-pre-mT2 CR	$\geq 2$	$\geq 1$	40

Table 6.14: Selections defining the  $t\bar{t}$  and single top control region for each signal region in the 2011 analysis. Each region is defined by its selection on the number of signal jets  $N_{\text{jets}}$ , on the number of tagged signal jets  $N_{\text{jets}}^b$ , and on  $E_{\text{T}}^{\text{miss,rel}}$ . The control region associated to SR- $m_{\text{T}2}$  is SR-pre- $m_{\text{T}2}$  CR where the  $m_{\text{T}2} > 90 \text{ GeV}$  selection has been removed [157].

SR-OSjveto	jet-veto & $E_{\text{T}}^{\text{miss,rel}} > 100 \text{ GeV}$ & $Z$ -veto
$Z + X$ CR for SR-OSjveto	jet-veto & $E_{\text{T}}^{\text{miss,rel}} > 100 \text{ GeV}$ & $Z$ -window
SR-2jets	2 signal jets & b- and top-veto & $E_{\text{T}}^{\text{miss,rel}} > 50 \text{ GeV}$ & $Z$ -veto
$Z + X$ CR for SR-2jets	2 signal jets & b- and top-veto & $E_{\text{T}}^{\text{miss,rel}} > 50 \text{ GeV}$ & $Z$ -window
SR- $m_{\text{T}2}$	jet-veto & $E_{\text{T}}^{\text{miss,rel}} > 40 \text{ GeV}$ & $m_{\text{T}2} > 90 \text{ GeV}$ & $Z$ -veto
$Z + X$ CR for SR- $m_{\text{T}2}$	jet-veto & $E_{\text{T}}^{\text{miss,rel}} > 40 \text{ GeV}$ & $Z$ -window

Table 6.15: Definition of the  $Z + X$  control regions for the data-driven  $Z + X$  background calculations in the 2011 analysis, along with their corresponding signal region definitions. All selections were applied to events with exactly two opposite-sign signal leptons [157].

muon channels, and not the electron-muon channel. The  $Z/\gamma^* + \text{jets}$  contribution to the electron-muon channel is negligible in all opposite-sign signal regions as shown in Table 6.11, but the diboson ( $WZ, ZZ$ ) contribution is actually the largest background to SR- $m_{\text{T}2}$  in the electron-muon channel. Although relying on Monte Carlo for the most significant background was not ideal, there was no evidence of mis-modelling of this background by the Monte Carlo.

The  $WW$  background in SR-OSjveto used a data-driven method. The control region chosen had the same selection as SR-OSjveto up to the  $E_{\text{T}}^{\text{miss,rel}}$  cut, but it required 70

$\text{GeV} < E_{\text{T}}^{\text{miss,rel}} < 100 \text{ GeV}$  and had an additional veto on  $b$ -jets with  $p_{\text{T}} > 20 \text{ GeV}$ . This additional cut reduced the contamination by the top background in the control region. For the other opposite-sign signal regions, i.e. SR-2jets and SR- $m_{\text{T}2}$ , the expectation in the signal region was taken from Monte Carlo. Although a data-driven method would have been preferable it proved too difficult to find suitable control regions, with intermediate  $E_{\text{T}}^{\text{miss,rel}}$  cuts, that were not too contaminated by the top background.

The fake lepton background refers to any process which could be mis-reconstructed as having two real isolated signal leptons. In the 2011 analysis the main sources of fake leptons were from photon conversions, or leptons produced inside jets of heavy or light flavour, that were mis-reconstructed and passed the isolation and signal lepton criteria. Processes contributing to the fake lepton background include QCD multi-jets,  $W$ +jets, semi-leptonic  $t\bar{t}$  and  $s$ - and  $t$ -channel single top production.

The fake lepton background was evaluated using the matrix method technique. The method is based around considering two different lepton selections: tight (T), which is the usual signal lepton selection and loose (l) which has no isolation requirement (and also for electrons the `mediumPP` flag is used instead of `tightPP`). Fake and the real isolated leptons can then be differentiated according to their different probabilities to pass from the loose to the tight category. A real isolated lepton that already fulfils the loose requirement has a high probability to pass the tight selection, whereas a fake lepton has a much lower probability. The probability for loose real or fake leptons to pass the tight requirements is measured in designated control regions or taken from Monte Carlo, to give the real-efficiency ( $r$ ) and fake-efficiency ( $f$ ). Once the real and fake efficiencies are known, by counting the number of events with loose and tight leptons in a given region the fraction of real and fake leptons can be derived.

In the presence of two leptons this is formalised through a system of four equations with four unknowns, where each equation expresses the composition of one of the regions with loose or tight leptons as a function of the unknown number of real or fake leptons and the real and fake efficiencies. In matrix form this can be expressed as

$$\begin{bmatrix} N_{TT} \\ N_{Tl} \\ N_{lT} \\ N_{ll} \end{bmatrix} = \begin{bmatrix} r_1 r_2 & r_1 f_2 & f_1 r_2 & f_1 f_2 \\ r_1(1-r_2) & r_1(1-f_2) & f_1(1-r_2) & f_1(1-f_2) \\ (1-r_1)r_2 & (1-r_1)f_2 & (1-f_1)r_2 & (1-f_1)f_2 \\ (1-r_1)(1-r_2) & (1-r_1)(1-f_2) & (1-f_1)(1-r_2) & (1-f_1)(1-f_2) \end{bmatrix} \begin{bmatrix} N_{LL}^{RR} \\ N_{LL}^{RF} \\ N_{LL}^{FR} \\ N_{LL}^{FF} \end{bmatrix}. \quad (6.5)$$

To get the signal region counts, the different lepton-pair combinations  $N_{ll}$ ,  $N_{lT}$ ,  $N_{Tl}$  and  $N_{TT}$  (T=tight, l = non-tight) in signal regions are counted and then the matrix is inverted with the measured  $r$ ,  $f$ ,  $N_{ll}$ ,  $N_{lT}$ ,  $N_{Tl}$  and  $N_{TT}$  values to get the estimated amount of real ( $R$ ) and fake ( $F$ ) leptons pairs,  $N_{FF}$ ,  $N_{FR}$ ,  $N_{RF}$  and  $N_{RR}$ . The fake contribution in the signal region is then  $N_{FF} + N_{FR} + N_{RF}$ . A full discussion of this is given in [1]. In this analysis a combination of data and Monte Carlo driven fake efficiencies were used, with the conversion fake efficiency for electrons taken from data, but the QCD fake efficiencies taken from Monte Carlo.

A data-driven estimate for the ‘‘charge misidentification’’ rate was needed to correctly model the Standard Model background in SR-SSjveto. As this region was defined by same-sign lepton pairs with a jet veto and a high  $E_T^{\text{miss,rel}}$  cut, the Standard Model backgrounds were low. However an important background in the di-electron and electron-muon channels came from Standard Model events with charge-misidentification, or with a charge-flip due to a hard bremsstrahlung followed by asymmetric pair production, i.e.  $(e_{\text{hard}}^{\mp} \rightarrow \gamma_{\text{hard}} e_{\text{soft}}^{\mp} \rightarrow e_{\text{soft}}^{\mp} e_{\text{soft}}^{\mp} e_{\text{hard}}^{\pm})$ . A previous analysis [140] calculated the rate of charge flip in data to be 81.3% of that in the Monte Carlo, presumably due to the differences in material budget between the simulation and data.

To reduce the dependence on simulation, the charge-flip rate as a function of  $\eta$  was measured in data using a likelihood minimisation technique with  $Z$ - bosons. The  $p_T$  dependence was taken from Monte Carlo as the effect was a factor of ten smaller and was also better modelled by Monte Carlo. For backgrounds where no true same-sign events would be expected, namely  $t\bar{t}$  and  $Z/\gamma^* + \text{jets}$ , the estimates in SR-SSjveto were calculated by applying weights to opposite-sign Monte Carlo events, calculated using the data-driven probabilities for the electrons to undergo a charge-flip. There were some processes that were also expected to contribute true same-sign events, such as  $WZ$  production, where both the  $W$  and  $Z$  decay leptonically but one lepton is out of

acceptance and two same-sign leptons pass the signal lepton selection. For such processes truth matching in the Monte Carlo was required and the signal region counts taken as the sum of the true same-sign events (where both reconstructed leptons are matched to the hard process) and opposite-sign events re-weighted using the data-driven charge-flip estimate. When applying the data-driven charge-flip rate to opposite-sign Monte Carlo events a  $p_T$  correction was also applied to account for the energy lost when an electron undergoes a charge-flip. Propagating this to the  $E_T^{\text{miss,rel}}$  and di-lepton invariant mass distributions was essential to ensure good agreement between data and the predictions.

## 6.6 Systematic uncertainties

This section describes the uncertainties that had to be taken into account for the analysis. These can be divided into two categories. Firstly there were statistical uncertainties, which arose from limited statistics of Monte Carlo samples in signal regions and control regions. For purely Monte Carlo-based estimates the only source of statistical error was the statistical uncertainty on the number of Monte Carlo events in a given signal region. For the data-driven estimates there were statistical errors due to limited Monte Carlo statistics in the signal and control regions. Furthermore there were statistical errors associated with the estimated contaminations from other processes that were subtracted from the control region counts. All of these sources contributed to the statistical uncertainties quoted for data-driven estimates.

The set of systematic uncertainties considered in the analysis will now be presented. The following systematic uncertainties were evaluated by applying the variation to Monte Carlo (by varying the appropriate scale, resolution, or event weight), and then taking the change in the signal region estimate as a measure of the impact of the systematic. For the data-driven background techniques, the variations were applied to all Monte Carlo samples involved in the estimate, then propagated through the method to give the change in the signal region estimates. The difference between the new evaluation of the background, and the nominal estimate quantified the impact of the systematic.

Firstly, all Monte Carlo samples used in the analysis were normalised to the correct luminosity using the luminosity measured in data and the cross-section calculated for the sample. Both of these numbers had associated uncertainties. The luminosity uncertainty for the 2011 dataset was taken to be 3.9% [160, 161].

The systematics that had the largest impacts on the signal region estimates were the jet energy scale (JES) [156] and jet energy resolution (JER) uncertainties [162, 163]. The JES refers to the calibration applied to observed jets reconstructed using the anti- $k_T$  algorithm [40] so that on average the jet energy corresponds to that of the associated stable particles in the detector. The JES uncertainty was applied as a function of the  $p_T$  and  $\eta$  of the jets. The JER uncertainty considers the impact of additional jet energy resolution. When applying this uncertainty jets were smeared using a gaussian distribution with unit mean and a width given by a  $p_T$  dependent resolution function.

Uncertainties on the b-tagging weights that were introduced in Section 6.3 were also considered (for more details see [41, 164]). There were three uncertainties, due to uncertainties in b-tagging weights for  $b$ -jets, light jets and charm jets. These affected all opposite-sign signal regions as the top control regions required at least one b-jet.

Uncertainties in the trigger weights (introduced in Section 6.3) applied to Monte Carlo samples were accounted for by applying a 1.5% systematic to the trigger weights for each of an electron and a muon trigger. This was conservative for most  $p_T$  and  $\eta$  combinations.

The impact of uncertainties in the lepton energy scale/resolution, and reconstruction efficiency, as estimated in [38, 165, 166] were also evaluated, though these had smaller impacts on the signal region estimates.

When investigating any uncertainty that affected the momenta and energies of objects in the events (i.e. jet and lepton energy scales and resolutions), the impact of the systematics were also propagated to the  $E_T^{\text{miss}}$  of the event. The nominally scaled/smeared objects were vectorially removed from the  $E_T^{\text{miss}}$  and then re-added using the momentum components scaled/smeared with the relevant uncertainty applied. The impact of uncertainties in the `CellOut` term and the effect of pile-up on the  $E_T^{\text{miss}}$  were also investigated.

There were also additional uncertainties that were relevant to specific background components. For example, for the  $t\bar{t}$  theoretical uncertainties in the amount of ISR/FSR were investigated along with the uncertainty due to the choice of generator, according to the prescription in [167]. The generator uncertainty was also significant for diboson backgrounds, and were evaluated by comparing the predictions from three different generators: `HERWIG`, `Sherpa` and `Alpgen`. Finally, for the  $Z/\gamma$ +jets background, the impact of theoretical uncertainties on the cross-section due to varying the PDF and renormalisation scale in the calculation were evaluated.

A quantitative indication of the relative impacts of the different systematic uncertainties on the Monte Carlo predictions for the signal regions in the analyses can be found in Appendix D. The impacts of the systematic uncertainties on the final background estimates will be presented in Section 6.8. All systematic uncertainties discussed in this section were incorporated into the statistical interpretation of the results as nuisance parameters (as discussed in Chapter 4).

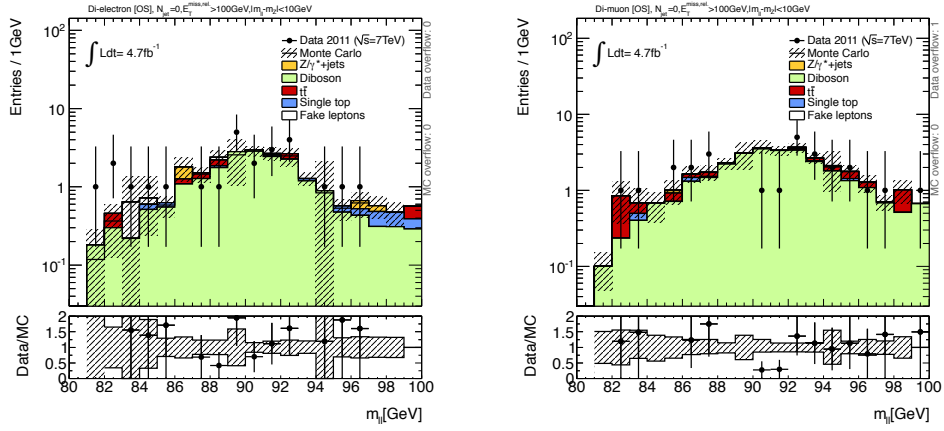
## 6.7 Comparisons of kinematic distributions in the top and $Z + X$ control regions

The data driven methods for the top,  $Z + X$  and  $WW$  backgrounds in the opposite-sign signal regions, that were introduced in the previous section, used data counts in control regions to renormalise Monte Carlo predictions in the signal regions. These methods relied on the assumption that the Monte Carlo correctly modelled the shape of the distributions, just not necessarily the normalisation. This section presents distributions in the  $Z + X$  and top control regions that were made by the author to demonstrate good Monte Carlo modelling of relevant kinematic variables. Distributions in the  $WW$  control region for SR-OSjveto will not be included as these were made by other analysers.

In all of the figures, the error bars on the data points are statistical Poisson errors while the error band on Monte Carlo represents the statistical uncertainties and the dominant systematic uncertainties, namely the JES, JER, b-tagging and missing transverse energy uncertainties, as well as the luminosity uncertainty and the theory uncertainty on the Monte Carlo cross-sections. In the bottom histogram the data points and uncertainty band have been divided by the total Monte Carlo distribution to show whether the fractional deviation of the data from the Monte Carlo expectation lies within the uncertainty band. The component labelled “Fakes” is derived from data using the matrix method, as outlined in 6.5, and the component labelled “Diboson” refers to the  $WW$ ,  $WZ$  and  $ZZ$  contributions combined.

The background estimation for the  $Z + X$  background for the opposite-sign signal regions relied on using the data inside the  $Z$ -window to normalise the Monte Carlo in the signal regions. Figures 6.11, 6.12 and 6.13 show distributions of  $m_{ll}$  for the  $Z + X$  control regions for SR-OSjveto, SR-2jets, and SR- $m_{T2}$  respectively, and Figures 6.14, 6.15 and 6.16 shows distributions of  $E_T^{\text{miss,rel}}$  for these regions. Good agreement is observed

for the shape of these distributions. It should be noted that the control regions for SR-OSjveto and SR- $m_{T2}$  are the same apart from the value of the  $E_T^{\text{miss,rel}}$  cut applied. The higher  $E_T^{\text{miss,rel}}$  cut in the control region for SR-OSjveto leads to the diboson contribution to  $Z + X$  ( $WZ$  and  $ZZ$ ) being more significant than the  $Z$ +jets component, whereas for the control region for SR- $m_{T2}$  the  $Z$ +jets contribution is greater, particularly at low  $E_T^{\text{miss,rel}}$ .



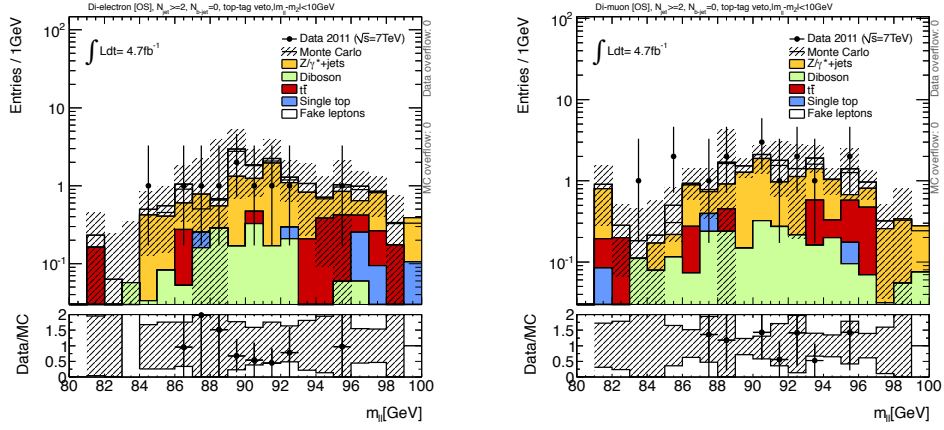
(a) Di-electron  $m_{ll}$  in the  $Z+X$  control region for SR-OSjveto.

(b) Di-muon  $m_{ll}$  in the  $Z+X$  control region for SR-OSjveto.

Figure 6.11: Comparisons between data and Monte Carlo for the di-lepton invariant mass distribution inside the  $Z$  peak ( $|m_{ll} - m_Z| < 10 \text{ GeV}$ ) in the  $Z+X$  control region for SR-OSjveto, for the di-electron (a) and di-muon (b) channels, for  $4.7 \text{ fb}^{-1}$  of data at  $\sqrt{s} = 7 \text{ TeV}$ .

The  $m_{T2}$  distributions in the  $e^\pm e^\mp$  and  $\mu^\pm \mu^\mp$  channel of the  $Z+X$  control region for SR- $m_{T2}$  are shown in Figures 6.17. The good agreement between data and Monte Carlo for the  $m_{T2}$  distribution inside the  $Z$  peak in Figure 6.17 justifies the assumption that the Monte Carlo correctly models the shape of the  $m_{T2}$  distribution for the  $Z+X$  background, which is dominated by  $Z/\gamma^*$ +jets at low  $m_{T2}$  and the diboson contribution at high  $m_{T2}$ .

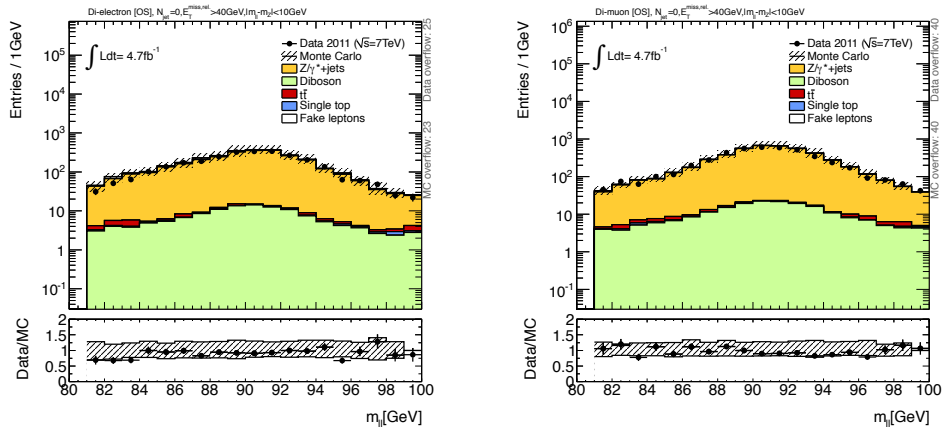
Figure 6.18 compares the  $E_T^{\text{miss,rel}}$  distribution in the top control region for SR- $m_{T2}$  for all three channels. The only difference between the control regions for the three opposite-sign signal regions is the value of the  $E_T^{\text{miss,rel}}$  cut. The top contribution ( $t\bar{t}$  and single top) dominates and good agreement between data and Monte Carlo is observed. Figure 6.19 shows the  $m_{T2}$  distribution in the top control region for SR- $m_{T2}$ . The plots



(a) Di-electron  $m_{ll}$  in the  $Z + X$  control region for SR-2jets.

(b) Di-muon  $m_{ll}$  in the  $Z + X$  control region for SR-2jets.

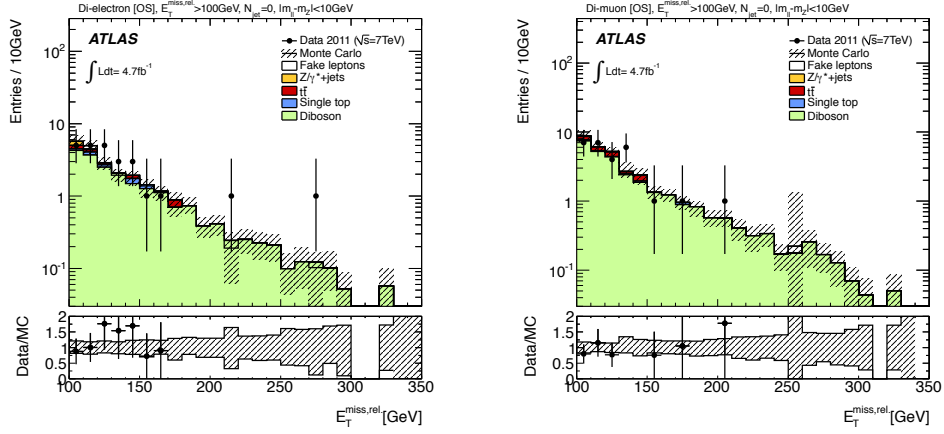
Figure 6.12: Comparisons between data and Monte Carlo for the di-lepton invariant mass distribution inside the  $Z$  peak ( $|m_{ll} - m_Z| < 10 \text{ GeV}$ ) in the  $Z + X$  control region for SR-2jets, for the di-electron (a) and di-muon (b) channels, for  $4.7 \text{ fb}^{-1}$  of data at  $\sqrt{s} = 7 \text{ TeV}$ .



(a) Di-electron  $m_{ll}$  in the  $Z + X$  control region for SR- $m_{T2}$ .

(b) Di-muon  $m_{ll}$  in the  $Z + X$  control region for SR- $m_{T2}$ .

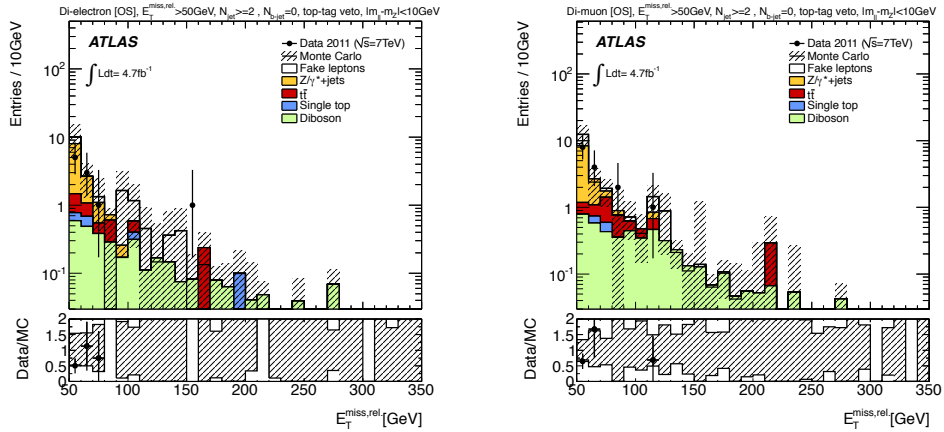
Figure 6.13: Comparisons between data and Monte Carlo for the di-lepton invariant mass distribution inside the  $Z$  peak ( $|m_{ll} - m_Z| < 10 \text{ GeV}$ ) in the  $Z + X$  control region for SR- $m_{T2}$ , for the di-electron (a) and di-muon (b) channels, for  $4.7 \text{ fb}^{-1}$  of data at  $\sqrt{s} = 7 \text{ TeV}$ .



(a) Di-electron  $E_T^{\text{miss,rel}}$  in the  $Z + X$  control region for SR-OSjveto.

(b) Di-muon  $E_T^{\text{miss,rel}}$  in the  $Z + X$  control region for SR-OSjveto.

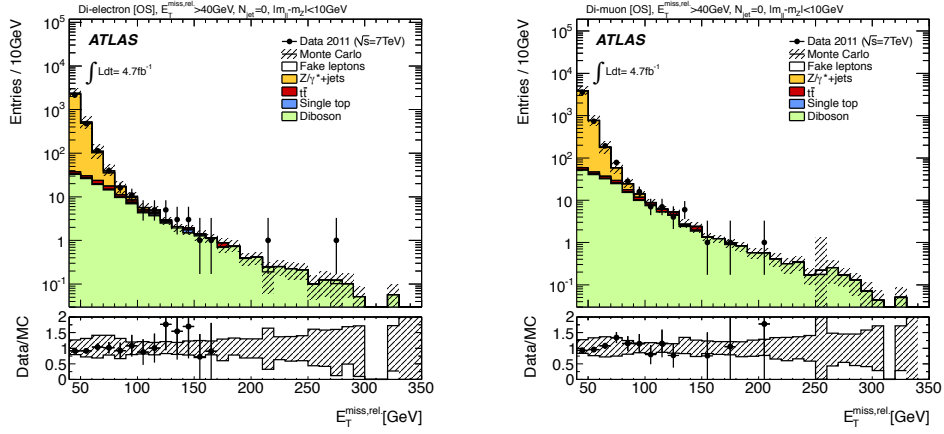
Figure 6.14: Comparisons between data and Monte Carlo for the  $E_T^{\text{miss,rel}}$  distribution inside the  $Z$  peak ( $|m_U - m_Z| < 10 \text{ GeV}$ ) in the  $Z + X$  control region for SR-OSjveto, for the di-electron (a) and di-muon (b) channels, for  $4.7 \text{ fb}^{-1}$  of data at  $\sqrt{s} = 7 \text{ TeV}$ .



(a) Di-electron  $E_T^{\text{miss,rel}}$  in the  $Z + X$  control region for SR-2jets.

(b) Di-muon  $E_T^{\text{miss,rel}}$  in the  $Z + X$  control region for SR-2jets.

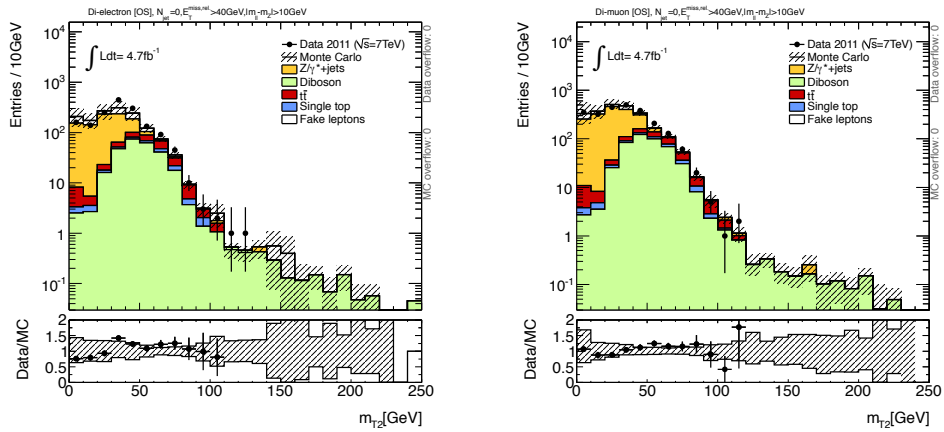
Figure 6.15: Comparisons between data and Monte Carlo for the  $E_T^{\text{miss,rel}}$  distribution inside the  $Z$  peak ( $|m_U - m_Z| < 10 \text{ GeV}$ ) in the  $Z + X$  control region for SR-2jets, for the di-electron (a) and di-muon (b) channels, for  $4.7 \text{ fb}^{-1}$  of data at  $\sqrt{s} = 7 \text{ TeV}$ .



(a) Di-electron  $E_T^{\text{miss,rel}}$  in the  $Z + X$  control region for  $\text{SR-}m_{T2}$ .

(b) Di-muon  $E_T^{\text{miss,rel}}$  in the  $Z + X$  control region for  $\text{SR-}m_{T2}$ .

Figure 6.16: Comparisons between data and Monte Carlo for the  $E_T^{\text{miss,rel}}$  distribution inside the  $Z$  peak ( $|m_{ll} - m_Z| < 10 \text{ GeV}$ ) in the  $Z + X$  control region for  $\text{SR-}m_{T2}$ , for the di-electron (a) and di-muon (b) channels, for  $4.7 \text{ fb}^{-1}$  of data at  $\sqrt{s} = 7 \text{ TeV}$ .

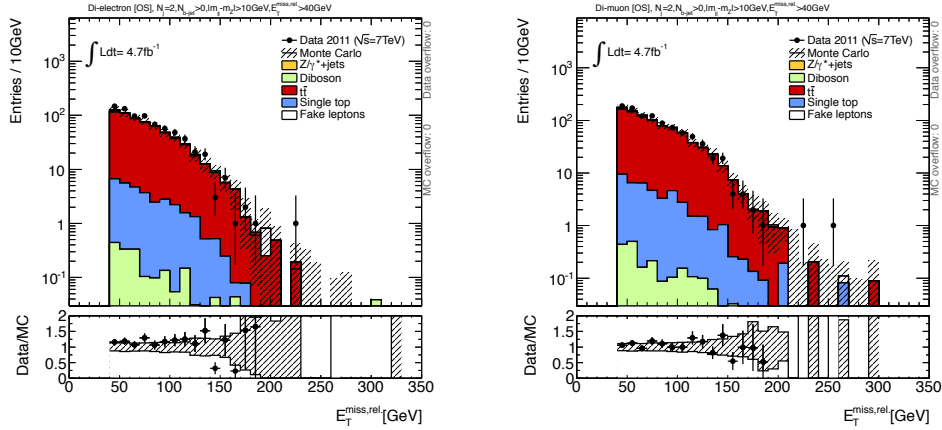


(a) Di-electron  $m_{T2}$  in  $|M_{ll} - M_Z| < 10 \text{ GeV}$ .

(b) Di-muon  $m_{T2}$  in  $|M_{ll} - M_Z| < 10 \text{ GeV}$ .

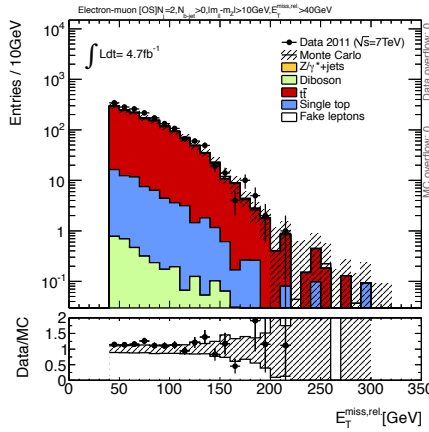
Figure 6.17: Distribution of  $m_{T2}$  inside the  $Z$  peak in the di-electron (a) and di-muon (b)  $Z + X$  control region for  $\text{SR-}m_{T2}$ , for  $4.7 \text{ fb}^{-1}$  of data at  $\sqrt{s} = 7 \text{ TeV}$ .

in Figure 6.19 were made by another analyser and included in [1] but are shown here to demonstrate the good modelling by Monte Carlo of the  $m_{T2}$  shape.



(a) Di-electron  $E_T^{\text{miss,rel}}$  in the top control region for SR- $m_{T2}$ .

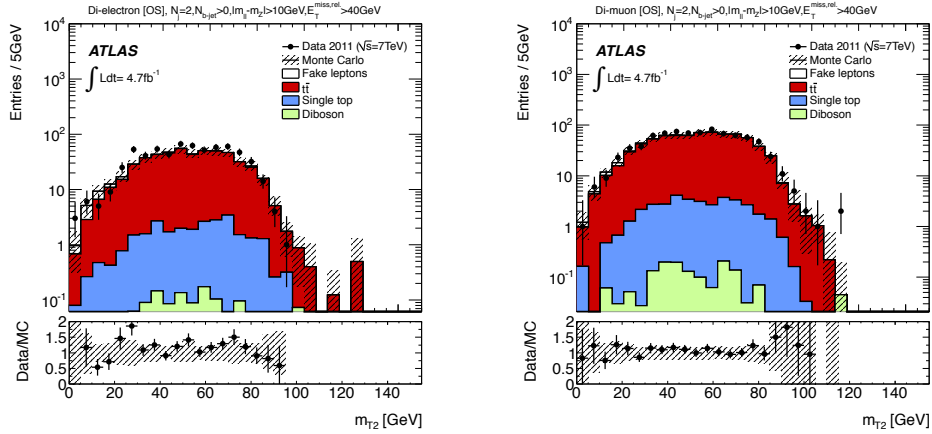
(b) Di-muon  $E_T^{\text{miss,rel}}$  in the top control region for SR- $m_{T2}$ .



(c) Electron-muon  $E_T^{\text{miss,rel}}$  in the top control region for SR- $m_{T2}$ .

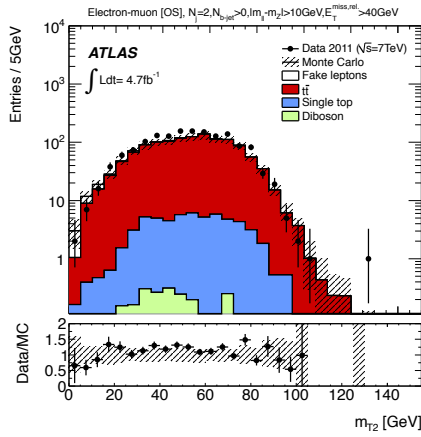
Figure 6.18: Comparisons between data and Monte Carlo for the  $E_T^{\text{miss,rel}}$  distribution in the top control region for SR- $m_{T2}$  in the di-electron (a), di-muon (b) and electron-muon channels (c), for  $4.7 \text{ fb}^{-1}$  of data at  $\sqrt{s} = 7 \text{ TeV}$ .

In summary, the comparisons between the data and Monte Carlo for distributions of kinematic variables such as  $E_T^{\text{miss,rel}}$  and  $m_{T2}$  in the  $Z + X$  and top control regions of the analysis showed good agreement. This validated the use of the data driven techniques



(a) Di-electron  $m_{T2}$  in the top control region for SR- $m_{T2}$ .

(b) Di-muon  $m_{T2}$  in the top control region for SR- $m_{T2}$ .



(c) Di-muon  $m_{T2}$  in the top control region for SR- $m_{T2}$ .

Figure 6.19: Comparisons between data and Monte Carlo for the  $m_{T2}$  distribution in the top control region for SR- $m_{T2}$  in the di-electron (a), di-muon (b) and electron-muon channels (c), for  $4.7 \text{ fb}^{-1}$  of data at  $\sqrt{s} = 7 \text{ TeV}$ .

used in the analysis, and the results of these methods will be presented in the next section.

## 6.8 Results and statistical interpretation

No significant excesses over the Standard Model background were observed in any of the signal regions in the 2011 analysis. This is demonstrated in Figure 6.20, where the level of agreement between data and Monte Carlo is shown prior to applying the final cut on  $E_T^{\text{miss,rel}}$  (for SR-OSjveto, SR-2jets and SR-SSjveto) or  $m_{T2}$  (for SR- $m_{T2}$ ). The distributions for relevant signal points for each signal region are also overlaid.

In the absence of any significant excess, model independent limits were set on the visible cross-section for new physics and exclusion contours calculated for the relevant signal grids. The results of the background estimates, the observed data counts and the model independent limits for each of the signal regions, including the results of each lepton flavour channel individually, are presented in Table 6.16. All limits are calculated using the  $\text{CL}_s$  technique, as discussed in Section 4.2, with the profile likelihood ratio as the test statistic (see Equation (4.4)). As the data driven background estimates were calculated explicitly the normalisations of the background components were not allowed to vary in the fit (they were assumed fixed). The systematic uncertainties and their correlations are taken into account using nuisance parameters (as discussed in Section 4.2.5). The model independent limits in Table 6.16 were not calculated by the author- but are included as they provide useful insight into the results.

The following subsections present the exclusion contours across the relevant weak production signal grids. All of the exclusion contours are presented in the same format: the expected and observed limits are shown by the bold red and dashed black lines respectively. These include all uncertainties except for the theoretical uncertainty on the signal cross-section. The yellow band around the expected limit shows the  $\pm 1\sigma$  result where all uncertainties are considered, except the signal cross-section uncertainty. The impact of the signal cross-section uncertainty is shown by the dashed red lines, which represent the observed limit when the nominal signal cross-section is moved up or down by the  $1\sigma$  theoretical uncertainty. These uncertainties are taken from an envelope of cross-section predictions obtained by using different PDF sets and factorisation and normalisation scales, as described in [168].

The exclusion contours for the di-chargino and chargino-neutralino simplified model grids are presented in Sections 6.8.1 and 6.8.2 respectively, and the results for direct slepton grid are discussed in Section 6.8.3. The limits in the weak production pMSSM grids are shown in Section 6.8.4 and are their consistency with the simplified model

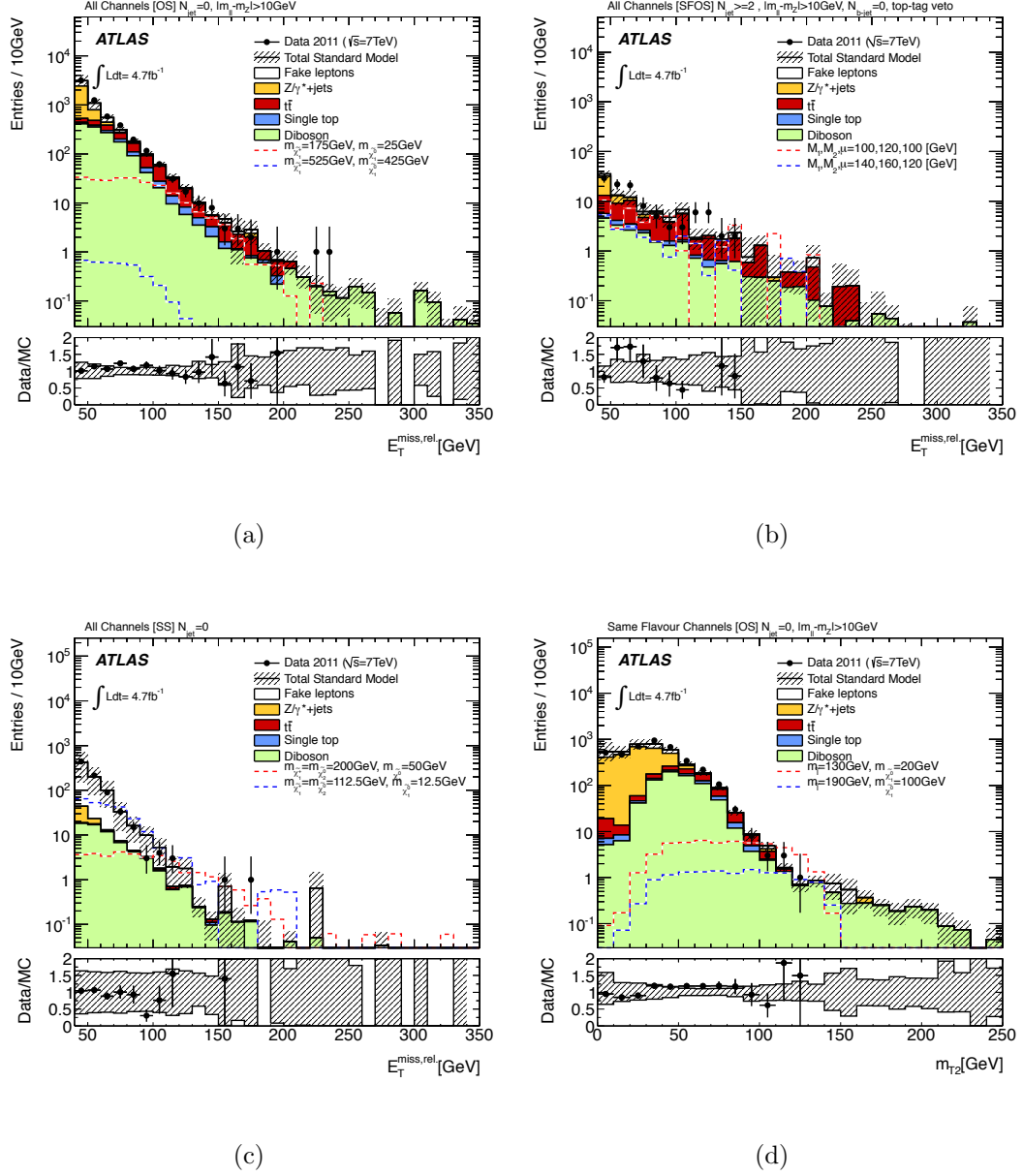


Figure 6.20: The  $E_T^{\text{miss,rel}}$  distributions for SR-OSjveto (a), SR-2jets (b) and SR-SSjveto (c) in the high-  $E_T^{\text{miss,rel}}$  ( $> 40 \text{ GeV}$ ) region, and  $m_{T2}$  in SR- $m_{T2}$ , prior to the application of the  $m_{T2}$  cut (d), for  $4.7 \text{ fb}^{-1}$  of data at  $\sqrt{s} = 7 \text{ TeV}$ . The hatched bands indicate the experimental uncertainties on the background expectations. All components were taken from Monte Carlo except the fake background (labelled “fakes”). The bottom panels show the ratio of the data to the expected background (points) and the systematic uncertainty on the background (shaded area). In each figure two signal points are illustrated. In (d) two points in the direct slepton grid are illustrated, with  $(\tilde{l}, \tilde{\chi}_1^0)$  masses of (130,20) and (190,100) GeV. In (a) the two points illustrated are from the simplified model grid for chargino-pair production with  $(\tilde{\chi}_1^\pm, \tilde{\chi}_1^0)$  masses of (97.5,27.5) and (425,525) GeV. In (c) there are two points from the simplified model grid for chargino-neutralino associated production, with  $(\tilde{\chi}_1^\pm, \tilde{\chi}_1^0)$  masses of (200,50) and (112.5,12.5) GeV. For (b) two pMSSM points are shown.

SR- $m_{T2}$					
	$e^+e^-$	$e^\pm\mu^\mp$	$\mu^+\mu^-$	all	SF
Z+X	$3.2 \pm 1.1 \pm 1.7$	$0.3 \pm 0.1 \pm 0.2$	$3.6 \pm 1.3 \pm 1.7$	$7.1 \pm 1.7 \pm 2.1$	$6.8 \pm 1.7 \pm 2.1$
WW	$2.3 \pm 0.3 \pm 0.4$	$4.8 \pm 0.4 \pm 0.7$	$3.5 \pm 0.3 \pm 0.5$	$10.6 \pm 0.6 \pm 1.5$	$5.8 \pm 0.4 \pm 0.9$
$t\bar{t}$ , single top	$2.6 \pm 1.2 \pm 1.3$	$6.2 \pm 1.6 \pm 2.9$	$4.1 \pm 1.3 \pm 1.6$	$12.9 \pm 2.4 \pm 4.6$	$6.8 \pm 1.8 \pm 2.3$
Fake leptons	$1.0 \pm 0.6 \pm 0.6$	$1.1 \pm 0.6 \pm 0.8$	$-0.02 \pm 0.01 \pm 0.05$	$2.2 \pm 0.9 \pm 1.4$	$1.0 \pm 0.6 \pm 0.6$
Total	$9.2 \pm 1.8 \pm 2.5$	$12.4 \pm 1.7 \pm 3.1$	$11.2 \pm 1.9 \pm 3.0$	$32.8 \pm 3.2 \pm 6.3$	$20.4 \pm 2.6 \pm 3.9$
Data	7	9	8	24	15
$\sigma_{\text{vis}}^{\text{obs(exp)}} \text{ (fb)}$	1.5 (1.8)	1.6 (2.0)	1.6 (1.9)	2.5 (3.3)	1.9 (2.5)
SR-OSjveto					
	$e^+e^-$	$e^\pm\mu^\mp$	$\mu^+\mu^-$	all	
Z+X	$4.5 \pm 1.2 \pm 1.2$	$3.0 \pm 0.9 \pm 0.5$	$4.7 \pm 1.1 \pm 1.2$	$12.2 \pm 1.8 \pm 1.8$	
WW	$8.8 \pm 1.8 \pm 4.4$	$20.9 \pm 2.6 \pm 6.2$	$13.3 \pm 1.9 \pm 3.5$	$43.0 \pm 3.7 \pm 12.2$	
$t\bar{t}$ , single top	$21.1 \pm 2.3 \pm 4.2$	$47.7 \pm 3.4 \pm 20.5$	$27.5 \pm 2.5 \pm 9.0$	$96.2 \pm 4.8 \pm 29.5$	
Fake leptons	$2.9 \pm 1.2 \pm 1.2$	$6.9 \pm 1.8 \pm 2.6$	$0.4 \pm 0.6 \pm 0.3$	$10.3 \pm 2.2 \pm 4.1$	
Total	$37.2 \pm 3.3 \pm 6.4$	$78.5 \pm 4.7 \pm 20.9$	$45.9 \pm 3.4 \pm 9.4$	$161.7 \pm 6.7 \pm 30.8$	
Data	33	66	40	139	
$\sigma_{\text{vis}}^{\text{obs(exp)}} \text{ (fb)}$	3.3 (3.8)	6.8 (7.8)	4.0 (4.6)	9.8 (11.9)	
SR-SSjveto					
	$e^\pm e^\pm$	$e^\pm\mu^\pm$	$\mu^\pm\mu^\pm$	all	
Charge flip	$0.49 \pm 0.03 \pm 0.17$	$0.34 \pm 0.02 \pm 0.11$	—	$0.83 \pm 0.04 \pm 0.18$	
Dibosons	$0.62 \pm 0.13 \pm 0.18$	$1.93 \pm 0.23 \pm 0.36$	$0.94 \pm 0.16 \pm 0.26$	$3.50 \pm 0.31 \pm 0.54$	
Fake leptons	$3.2 \pm 0.9 \pm 1.7$	$2.9 \pm 0.9 \pm 1.9$	$0.6 \pm 0.6 \pm 0.3$	$6.6 \pm 1.4 \pm 3.8$	
Total	$4.3 \pm 0.9 \pm 1.7$	$5.1 \pm 1.0 \pm 1.9$	$1.5 \pm 0.6 \pm 0.4$	$11.0 \pm 1.5 \pm 3.9$	
Data	1	5	3	9	
$\sigma_{\text{vis}}^{\text{obs(exp)}} \text{ (fb)}$	0.7 (1.1)	1.6 (1.6)	1.3 (0.9)	1.9 (2.1)	
SR-2jets					
	$e^+e^-$	$e^\pm\mu^\mp$	$\mu^+\mu^-$	SF	
Z+X	$3.8 \pm 1.3 \pm 2.7$	—	$5.8 \pm 1.6 \pm 3.9$	$9.6 \pm 2.0 \pm 5.1$	
WW	$6.4 \pm 0.5 \pm 4.3$	—	$8.4 \pm 0.6 \pm 5.7$	$14.8 \pm 0.7 \pm 9.9$	
$t\bar{t}$ , single top	$14.8 \pm 1.9 \pm 9.2$	—	$22.1 \pm 2.1 \pm 20.7$	$36.9 \pm 2.9 \pm 29.6$	
Fake leptons	$2.5 \pm 1.2 \pm 1.5$	—	$1.7 \pm 1.3 \pm 0.8$	$4.2 \pm 1.8 \pm 2.3$	
Total	$27.5 \pm 2.6 \pm 10.6$	—	$37.9 \pm 3.0 \pm 21.0$	$65.5 \pm 4.0 \pm 31.8$	
Data	39	—	39	78	
$\sigma_{\text{vis}}^{\text{obs(exp)}} \text{ (fb)}$	6.9 (5.3)	—	7.7 (7.6)	13.6 (12.5)	

Table 6.16: Evaluated Standard Model backgrounds in each signal region of the 2011 analysis separated by flavour ( $ee$ ,  $e\mu$ ,  $\mu\mu$ ) and combined in an “all” channel. In SR- $m_{T2}$  the evaluated background components in the same flavour ( $ee+\mu\mu$ ) channel are quoted separately as the  $e\mu$  channel is not appropriate for a direct slepton search. The first quoted error is statistical and the second is the total systematic uncertainty. The observed (expected) 95% confidence limits on the visible cross-section for non-SM events in each signal region,  $\sigma_{\text{vis}}^{\text{obs(exp)}}$  are also shown [1].

limits is discussed.

Where relevant comparisons with previous limits will be made, and in addition attempts will be made to explain the form of the exclusion contours. For the simplified model grids, this will be done by considering three quantities, that were calculable for all signal points in the grids: the efficiency-times-acceptance ( $A \times \epsilon$ ), the acceptance ( $A$ ), and the efficiency ( $\epsilon$ ). For a given signal model, the efficiency-times-acceptance is the full event selection efficiency at the detector level. The individual values for the efficiency and acceptance for a given point can also be defined. The acceptance is defined as

$$A = \frac{N_{\text{Fiducial}}}{N_{\text{Total}}}, \quad (6.6)$$

where  $N_{\text{Total}}$  refers to the total number of signal events in a sample and  $N_{\text{Fiducial}}$  is the number that pass the signal selection at truth level. When defining the fiducial cuts, truth level information from the event generator is used, including truth level electrons and muons, hadron level jets and for  $b$ -jets the  $b$ -quark should be matched to the jet. The analysis cuts are then applied to these objects. The efficiency is defined as

$$\epsilon = \frac{N_{\text{Fiducial-reco}}}{N_{\text{Fiducial}}}, \quad (6.7)$$

where  $N_{\text{Fiducial-reco}}$  refers to the nominal analysis cuts applied to reconstructed variables. The difference with respect to the acceptance are due to reconstruction efficiencies, particle identification cuts, resolution effects and trigger inefficiencies. In practise the efficiency is calculated by dividing the efficiency-times-acceptance by the acceptance, and can consequently take values smaller or greater than one.

### 6.8.1 Interpretation in the chargino-pair production grid

Exclusion contours are presented as a function of the chargino and neutralino masses in Figure 6.21. To maximise sensitivity, for every signal point the exclusion  $\text{CL}_s$  values were taken from the signal region with the best expected  $\text{CL}_s$  values. The numbers on the exclusion plot at every signal point indicate the signal region contributing to the exclusion at that point (a key is given at the top of the plot). For a 10 GeV neutralino, chargino masses between 110 and 340 GeV are excluded at 95% CL. This provided the first limit since LEP on the mass of the  $\chi_1^\pm$  independent of that of the  $\tilde{\chi}_2^0$  (previous limits on the  $\tilde{\chi}_1^\pm$  mass from the Tevatron and LHC had targeted  $\tilde{\chi}_1^\pm \tilde{\chi}_2^0$

associated production [140, 169–171] so the limits were dependent on the assumed mass of the  $\tilde{\chi}_2^0$ ). The limits presented here do however depend on the mass of the LSP and assume a specific mass hierarchy between the charginos and sleptons. For this signal grid all lepton flavour channels (i.e.  $e^\pm e^\mp, \mu^\pm \mu^\mp$  and  $e^\pm \mu^\mp$ ) were used for SR- $m_{T2}$ . As shown in Figure 6.21 SR- $m_{T2}$  provides most of the sensitivity across the grid except for a few points close to the diagonal.

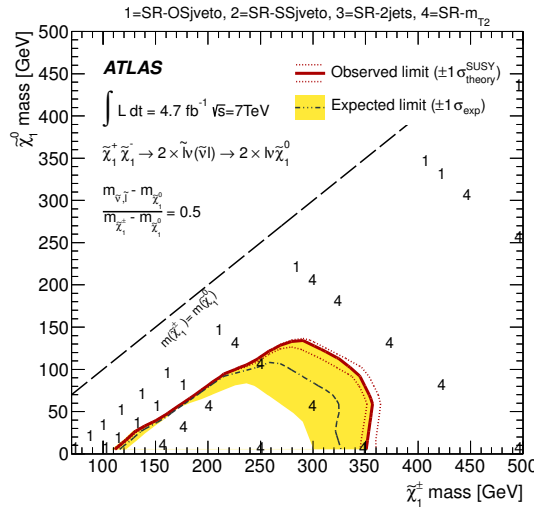


Figure 6.21: 95% CL exclusion limits for  $\tilde{\chi}_1^\pm \tilde{\chi}_1^\mp$  pair production in the simplified model grid with intermediate sleptons for the 2-lepton search using the 2011 dataset [1]. The dashed and solid lines show the 95% CL<sub>s</sub> expected and observed limits, respectively, including all uncertainties except for the theoretical signal cross-section uncertainty. The solid band around the expected limit shows the  $\pm 1\sigma$  result where all uncertainties, except those on the signal cross-sections, are considered. The  $\pm 1\sigma$  lines around the observed limit represent the results obtained when moving the nominal signal cross-section up or down by the  $\pm 1\sigma$  theoretical uncertainty.

The shape of the exclusion contour will now be examined. Figures 6.22 and 6.23 show the efficiency-times-acceptance, acceptance and efficiency for the chargino-pair production grid for SR- $m_{T2}$  and SR-OSjveto respectively. The other signal regions will not be considered here as they do not contribute to the exclusion at any points in the grid.

The cross-sections for the points in the grid are shown in Figure 6.24. Examining the contour in Figure 6.21, the point at 0 GeV in neutralino mass and 350 GeV in chargino mass lies marginally inside the observed exclusion contour. It has a cross-section of 0.0222 pb and an efficiency-times-acceptance of 10.9%. Multiplying the two numbers

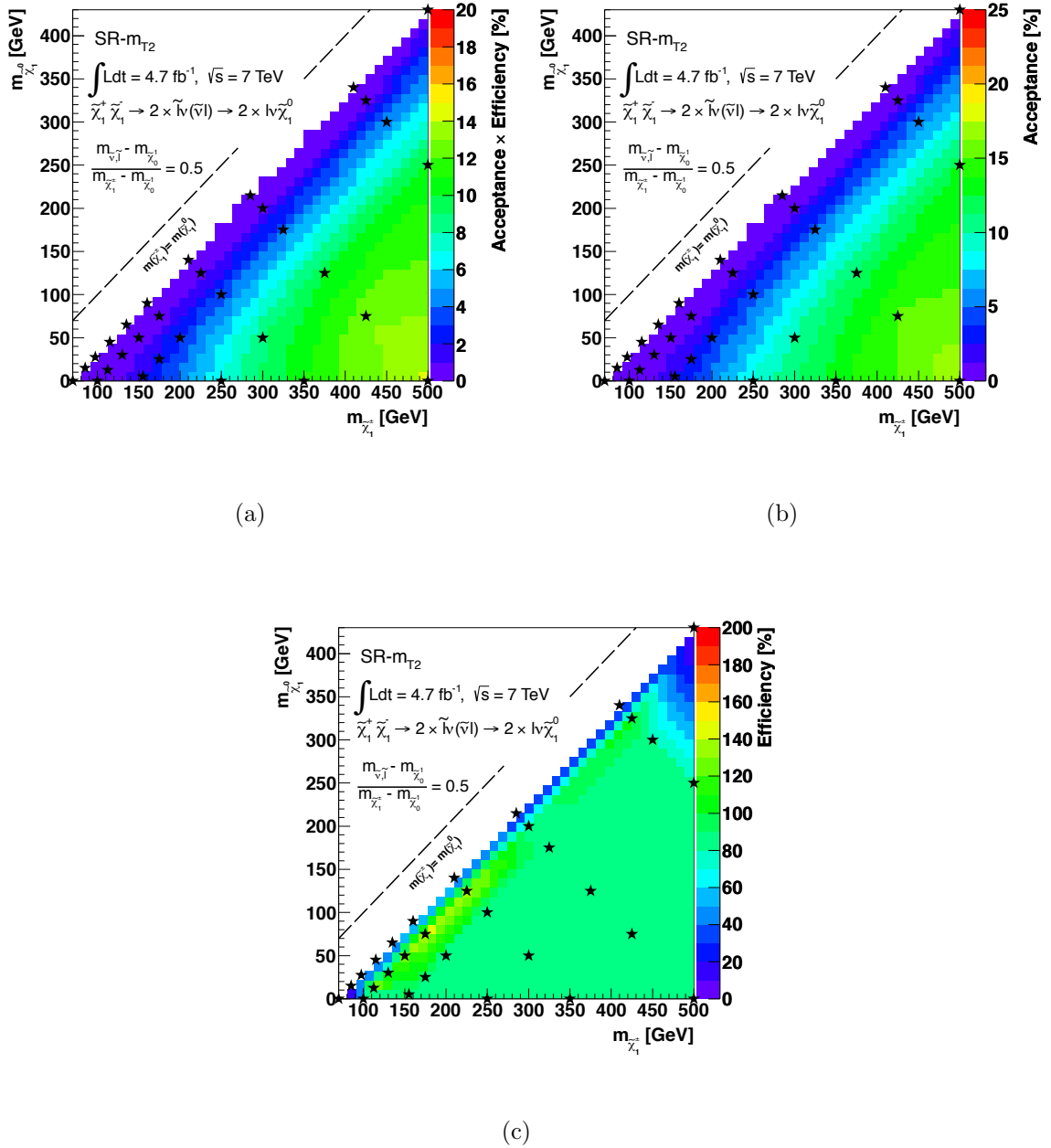


Figure 6.22: Distributions of the efficiency-times-acceptance  $A \times \epsilon$  (a), acceptance  $A$  (b) and efficiency  $\epsilon$  (c) for SR- $m_{T2}$  for  $\tilde{\chi}_1^\pm \tilde{\chi}_1^\mp$  pair production in the simplified model with intermediate sleptons. All lepton flavour channels ( $e^\pm e^\mp, \mu^\pm \mu^\mp$  and  $e^\pm \mu^\mp$ ) are included in SR- $m_{T2}$ . The stars indicate the positions of the simulated signal points.

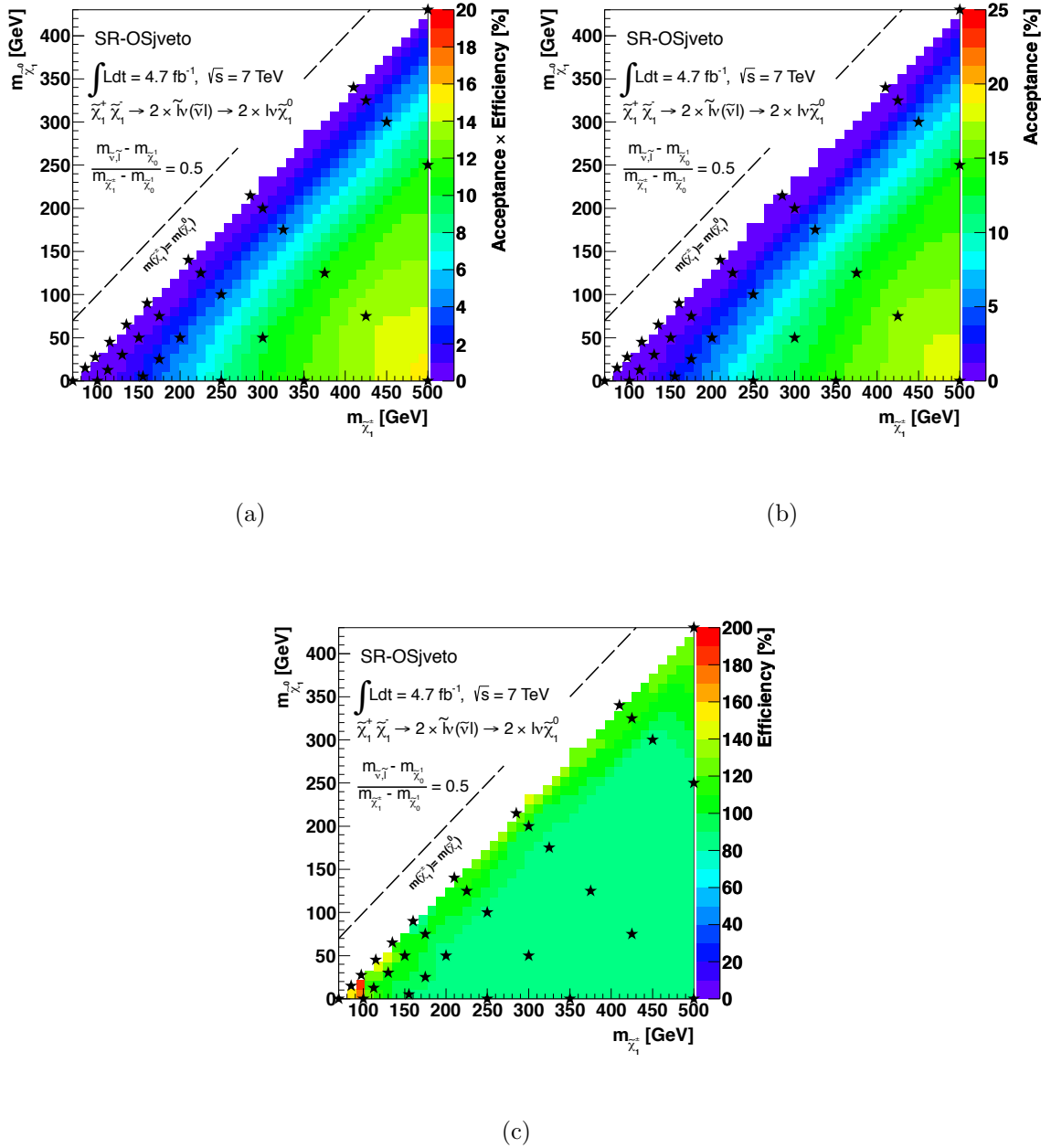


Figure 6.23: Distributions of the efficiency-times-acceptance  $A \times \epsilon$  (a), acceptance  $A$  (b) and efficiency  $\epsilon$  (c) for SR-OSjveto for  $\tilde{\chi}_1^\pm \tilde{\chi}_1^\mp$  pair production in the simplified model with intermediate sleptons. The stars indicate the positions of the simulated signal points.



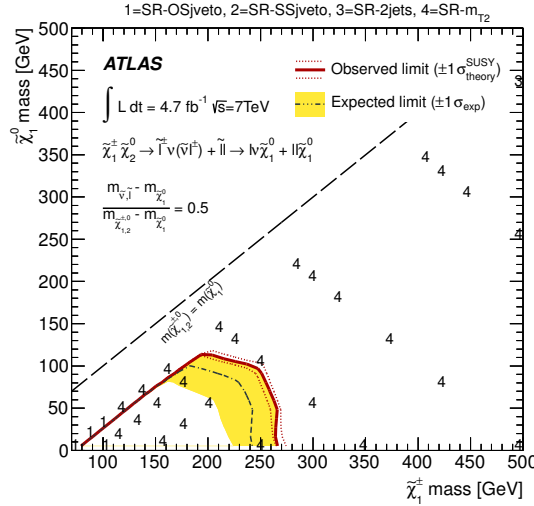


Figure 6.25: 95% CL exclusion limits for  $\tilde{\chi}_1^\pm \tilde{\chi}_2^0$  associated production in the simplified model grid with intermediate sleptons for 2-lepton search using the 2011 dataset [1]. The limits are presented in the same format as in Figure 6.21.

the efficiency-times-acceptance, acceptance and efficiency for the chargino-neutralino associated production grid for SR- $m_{T2}$  and SR-OSjveto respectively.

The efficiency-times-acceptance decreases sharply towards the diagonal for SR- $m_{T2}$ . The efficiency-times-acceptance values are much lower then for the chargino-pair production grid, which helps to explain the weaker exclusions across the grid. In the region of parameter space where SR-OSjveto contributes to the exclusion the efficiency-times-acceptance for SR- $m_{T2}$  is close to 0, whereas the values for SR-OSjveto they fall off less severely.

Although SR-SSjveto targeted this process, it didn't contribute to the exclusion for any points in the grid. Figure 6.28 shows the efficiency-times-acceptance, acceptance and efficiency for the chargino-neutralino associated production grid for SR-SSjveto. The efficiency-times-acceptance values are in general lower across the grid and the efficiency-times-acceptance again falls close to the diagonal. SR- $m_{T2}$  ended up outperforming SR-SSjveto across grid since both signal regions essentially targeted the same areas of parameter space, and SR- $m_{T2}$  was more sensitive. The need to avoid this redundancy of signal regions was identified as an area for improvement in future analyses.

As expected, the exclusion contours for this scenario in the 2-lepton analysis for  $4.7 \text{ fb}^{-1}$  were not as strong as those in the equivalent 3-lepton search [141], where

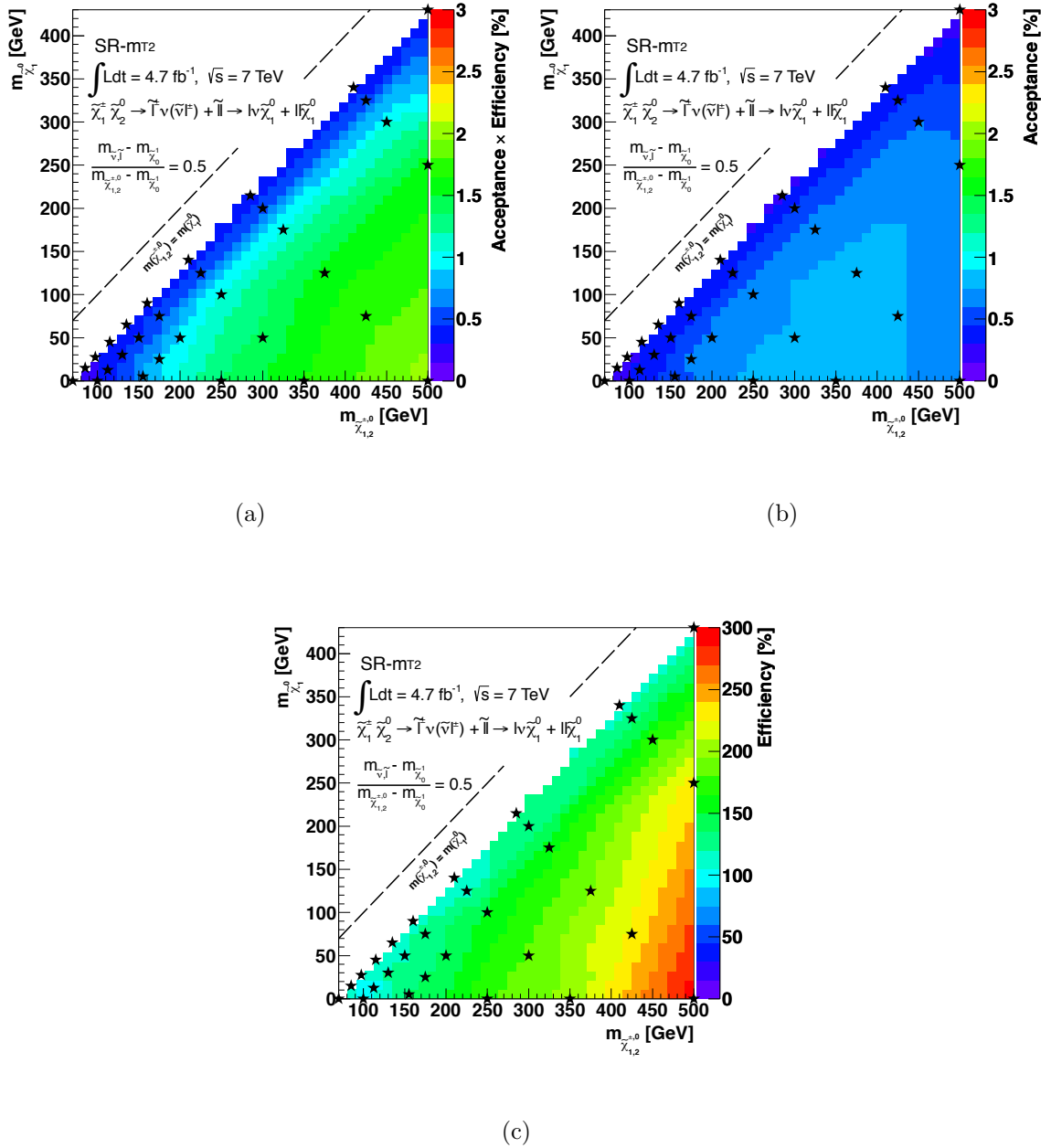


Figure 6.26: Distributions of the efficiency-times-acceptance  $A \times \epsilon$  (a), acceptance  $A$  (b) and efficiency  $\epsilon$  (c) for SR- $m_{T2}$  for  $\tilde{\chi}^{\pm} \tilde{\chi}_2^0$  associated production in the simplified model grid with intermediate sleptons. All lepton flavour channels are included in SR- $m_{T2}$ . The stars indicate the positions of the simulated signal points.

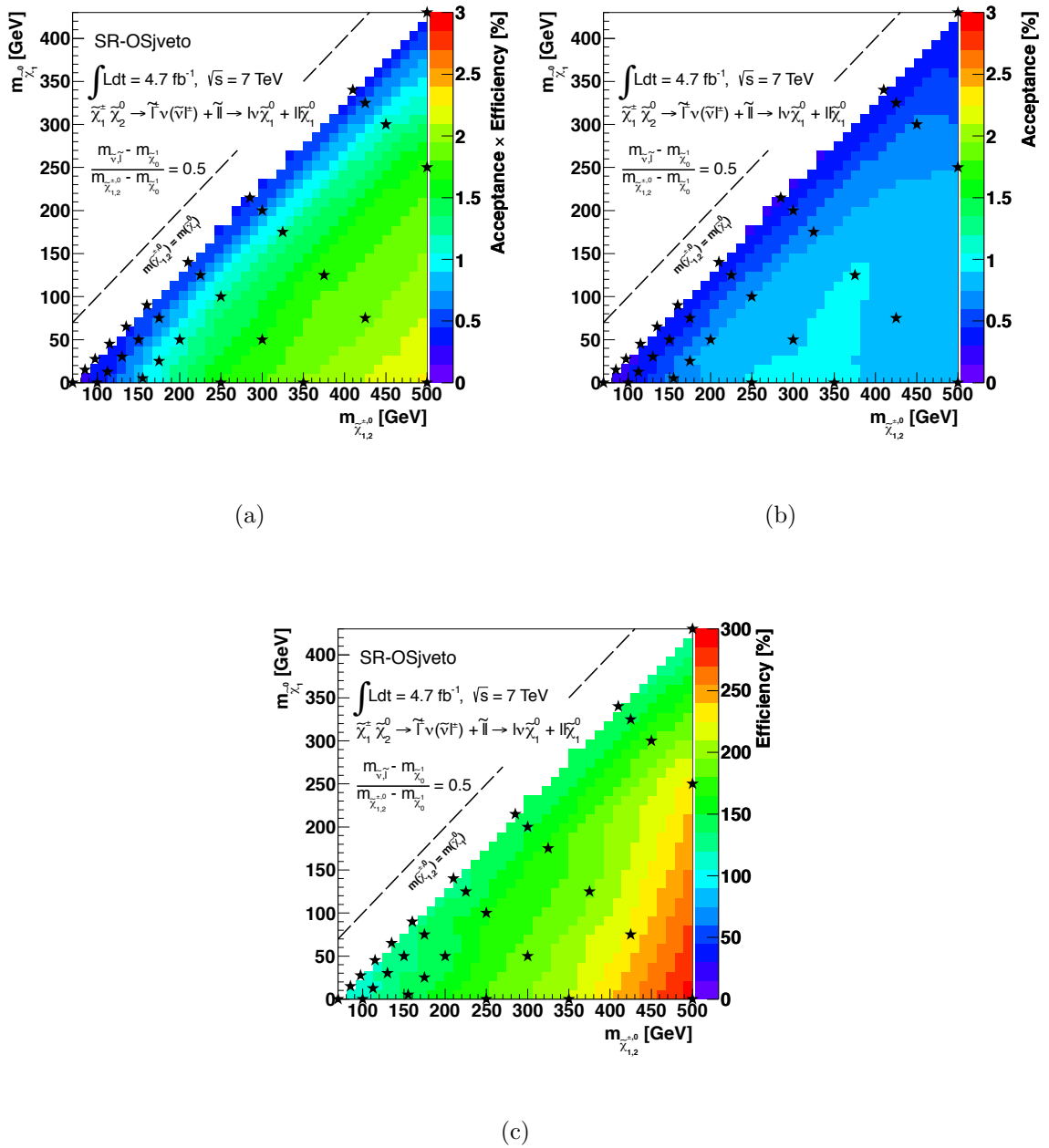


Figure 6.27: Distributions of the efficiency-times-acceptance  $A \times \epsilon$  (a), acceptance  $A$  (b) and efficiency  $\epsilon$  (c) for SR-OSjveto for  $\tilde{\chi}^\pm \tilde{\chi}_2^0$  associated production in the simplified model grid with intermediate sleptons. The stars indicate the positions of the simulated signal points.

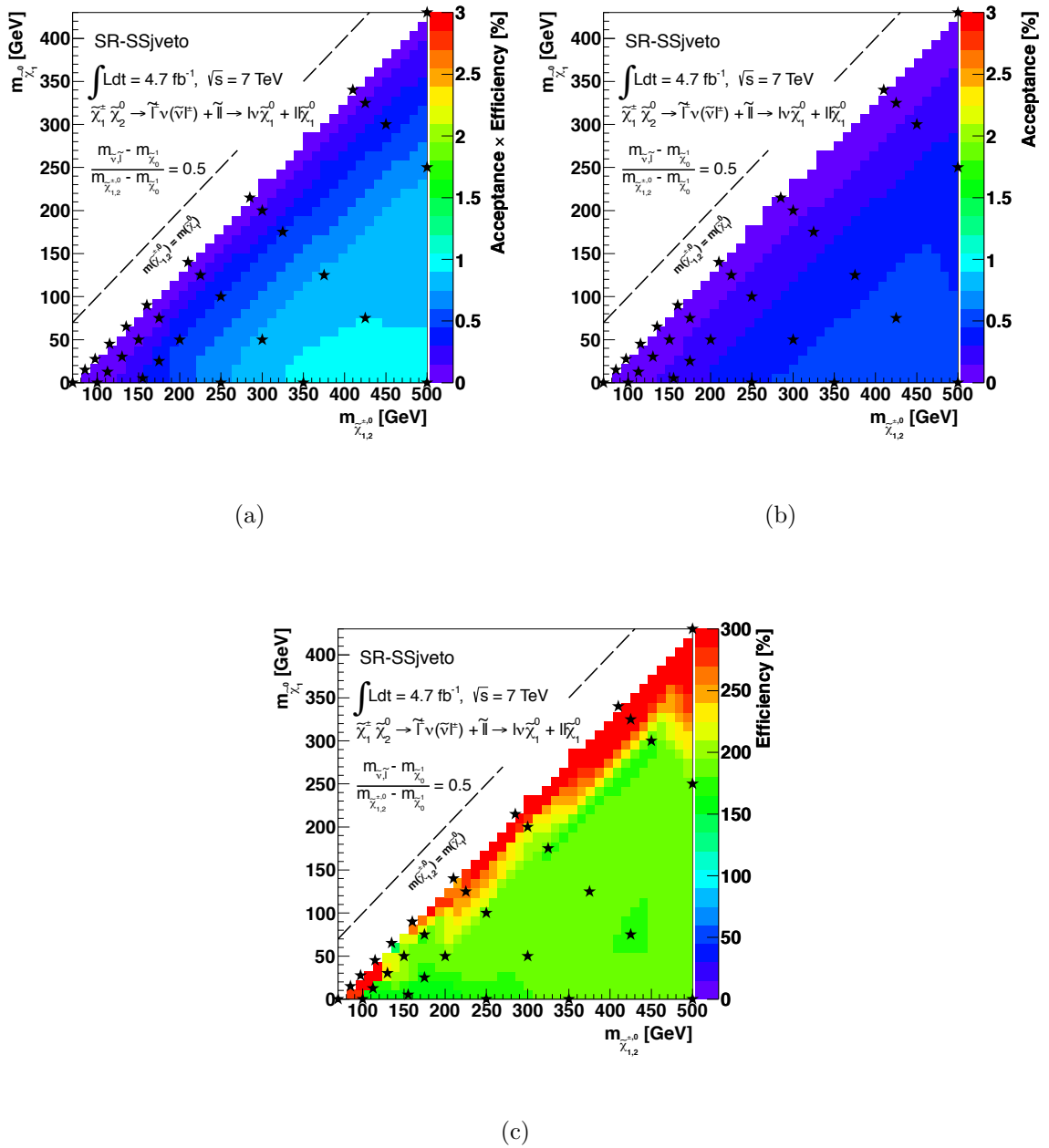


Figure 6.28: Distributions of the efficiency-times-acceptance  $A \times \epsilon$  (a), acceptance  $A$  (b) and efficiency  $\epsilon$  (c) for SR-SSjveto for  $\tilde{\chi}^\pm \tilde{\chi}_2^0$  associated production in the simplified model grid with intermediate sleptons. The stars indicate the positions of the simulated signal points.

degenerate  $\tilde{\chi}_1^\pm$  and  $\tilde{\chi}_2^0$  masses up to 500 GeV were excluded for large mass splittings from the  $\tilde{\chi}_1^0$  in the intermediate slepton scenario.

### 6.8.3 Interpretation in the direct slepton grid

The exclusion contour for direct slepton production that was included in [1] is shown in Figure 6.29. Unlike the scenario assumed for the optimisation in Section 5.4 (where both the first and second generation sleptons were to be degenerate), this exclusion corresponds to a flavour blind analysis; the signal region allowed both di-electron and di-muon events but searched for only a single slepton flavour. The signal cross-sections were effectively half those shown in Figure 5.8. This limit is weaker than the optimisation plot for SR- $m_{T2}$  shown in Figure 5.9 because the background expectation is effectively doubled with respect to the signal. These limits are more conservative but no longer relied on the assumption that both slepton flavours would show up simultaneously in the signal region. Although not directly comparable, (as the direct slepton grid contains both left handed and right handed sleptons), the orange shaded region indicates the limit from LEP on the right handed smuon mass (the smuon limit is displayed as it is the weaker of the selectron and smuon limits). For a neutralino mass of 20 GeV slepton masses between 85 GeV and 195 GeV are excluded at 95%. The sensitivity decreases as the mass-splitting  $m_{\tilde{\ell}} - m_{\tilde{\chi}_1^0}$  decreases as in these scenarios the endpoints in the  $m_{T2}$  distributions are lower. For a neutralino mass of 60 GeV slepton masses between 135 GeV and 185 GeV are excluded.

The corresponding efficiency-times-acceptance, acceptance and efficiency plots are shown in Figure 6.30. Both the acceptance and the efficiency-times-acceptance are close to 0 near to the diagonal, but increase as the mass splitting increases, with the efficiency-times-acceptance exceeding 20% for slepton masses of 190 GeV with a 20 GeV neutralino. The efficiency is also zero close to the diagonal, and is fairly uniform across most of the rest of the grid, however on the boundary of where the region has sensitivity there is a band of points with exceptionally high efficiency values (greater than 100%). These are just artefacts of calculating the efficiency by dividing the efficiency-times-acceptance by the acceptance value.

The exclusion contour that can be compared directly to the optimisation plots in Figure 5.9 in Section 5.4 is shown in Figure 6.31. The observed exclusion contour is consistent with the optimisation plot for SR- $m_{T2}$ . In trying to rationalise the shape of the contour it is interesting to refer back to the distribution of expected  $m_{T2}$  endpoints

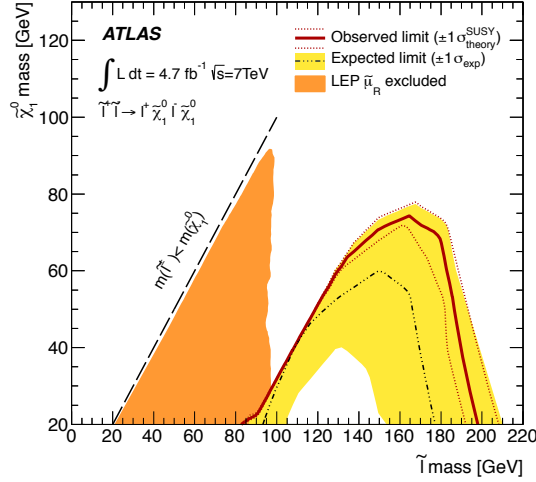
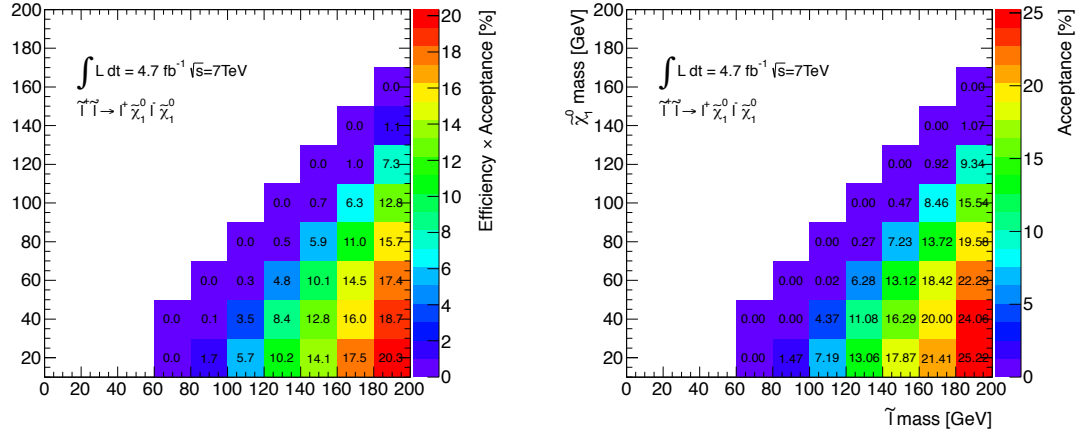


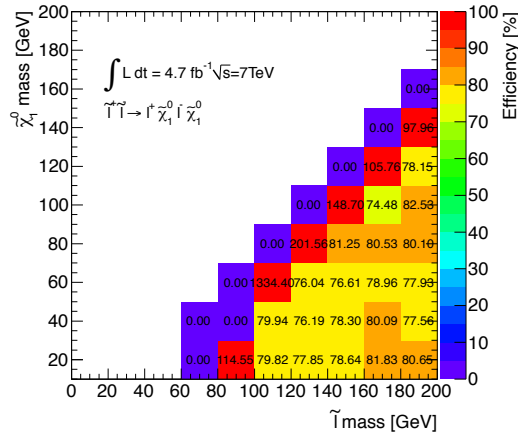
Figure 6.29: 95% CL exclusion limits for  $\tilde{\ell}^\pm$  pair production in the  $m_{\tilde{\ell}} - m_{\tilde{\chi}_1^0}$  mass plane of the direct slepton pMSSM for the 2-lepton search using the 2011 dataset, as published in [1]. The limits are presented in the same format as in Figure 6.21. The  $CL_s$  values for this grid use only the same flavour channels of SR- $m_{T2}$  but they correspond to a flavour blind analysis targeting only a single slepton flavour in the signal region.

shown in Figure 5.12. For lower slepton masses which have larger cross-sections for pair production, whether or not a point is excluded roughly depends on whether the model has an endpoint in the  $m_{T2}$  distribution greater to or less than 90 GeV (though detector effects can smear the endpoints of the distributions). As an example, for a slepton mass of 110 GeV, neutralino masses of 20 GeV and 40 GeV are excluded. These two models have calculated endpoints of 107.3 GeV and 99 GeV effectively. However the point with a 110 GeV slepton mass and a 60 GeV neutralino mass is not excluded even though the production cross-section is the same. The  $m_{T2}$  endpoint for this point is 85.1 GeV, which is below the 90 GeV threshold. The same argument can be used to explain why the efficiency-times-acceptance, and acceptance distributions in Figure 6.30 decrease sharply on approaching the diagonal.



(a)

(b)



(c)

Figure 6.30: Distributions of the efficiency-times-acceptance  $A \times \epsilon$  (a), acceptance  $A$  (b) and efficiency  $\epsilon$  (c) for the same-flavour channels of SR- $m_{T2}$  for  $\tilde{\ell}^{\pm}$  pair production in the  $m_{\tilde{\ell}} - m_{\tilde{\chi}_1^0}$  mass plane of the direct slepton pMSSM, assuming a flavour-blind analysis.

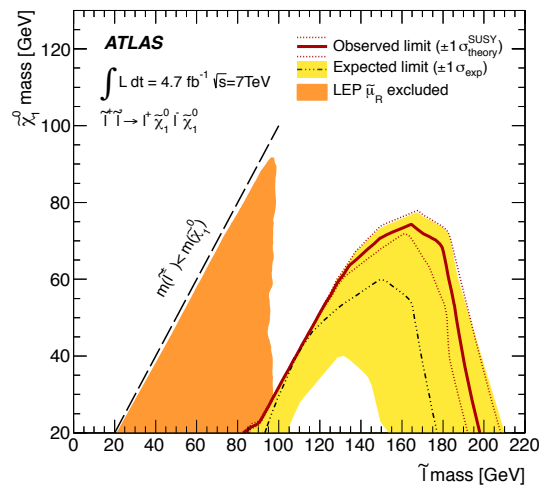


Figure 6.31: As in Figure 6.29 but with both slepton flavours assumed to be present in the signal region. The model cross-sections are then as in Figure 5.8 and the exclusions can be directly compared to the optimisation plots in Section 5.4.

### 6.8.4 Interpretation in the weak production pMSSM grids

The 95% confidence level exclusion contours for the pMSSM grids detailed above are shown in Figure 6.32 for  $M_1 = 100 \text{ GeV}$ , Figure 6.33 for  $M_1 = 140 \text{ GeV}$  and Figure 6.34 for  $M_1 = 250 \text{ GeV}$ . In each figure the exclusion limit is displayed on the left, and the numbers on the grid on the right indicate the signal region contributing to the exclusion limit. Across most of the grids the exclusion is driven by SR- $m_{T2}$ .

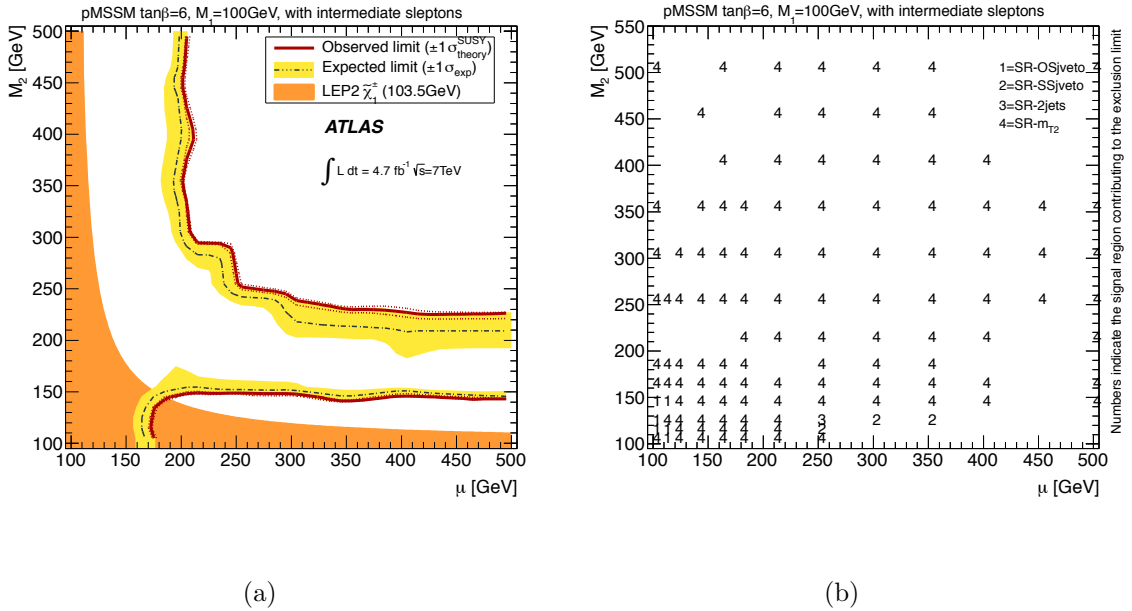


Figure 6.32: 95% exclusion limits in the  $\mu - M_2$  mass planes of the pMSSM for  $M_1 = 100 \text{ GeV}$  (a). The limits are presented in the same format as in Figure 6.21. For each signal point the  $CL_s$  is that corresponding to the signal region with the best expected sensitivity, which is indicated in (b).

Finding a simple interpretation for these exclusion contours is not trivial. Compared to the simplified model grids in previous sections the pMSSM grids under consideration are complicated because there are many subprocesses (32 in total) which contribute to the yields in the signal regions. To rationalise the shapes of the exclusion contours this section will continue by examining whether the pMSSM exclusions are consistent with those in the simplified model grids. Comparing the exclusion contours for the  $M_1 = 100 \text{ GeV}$  and  $M_1 = 140 \text{ GeV}$  grids, there is an island in the  $M_1 = 140 \text{ GeV}$  grid going from  $\mu = 180 \text{ GeV}$  to  $\mu = 300 \text{ GeV}$  where there are points not excluded, which are excluded in the  $M_1 = 100 \text{ GeV}$  grid. This is evident in Figure 6.35, where the points in the three

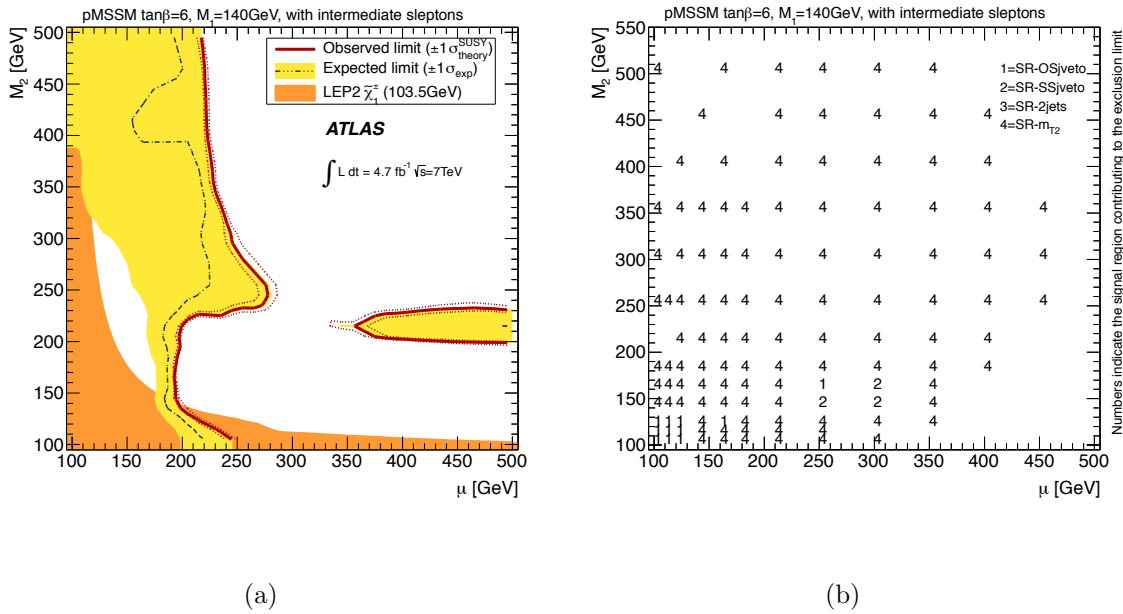


Figure 6.33: 95% exclusion limits in the  $\mu - M_2$  mass planes of the pMSSM for  $M_1 = 140 \text{ GeV}$  (a). The limits are presented in the same format as in Figure 6.21. For each signal point the  $CL_s$  is that corresponding to the signal region with the best expected sensitivity, which is indicated in (b).

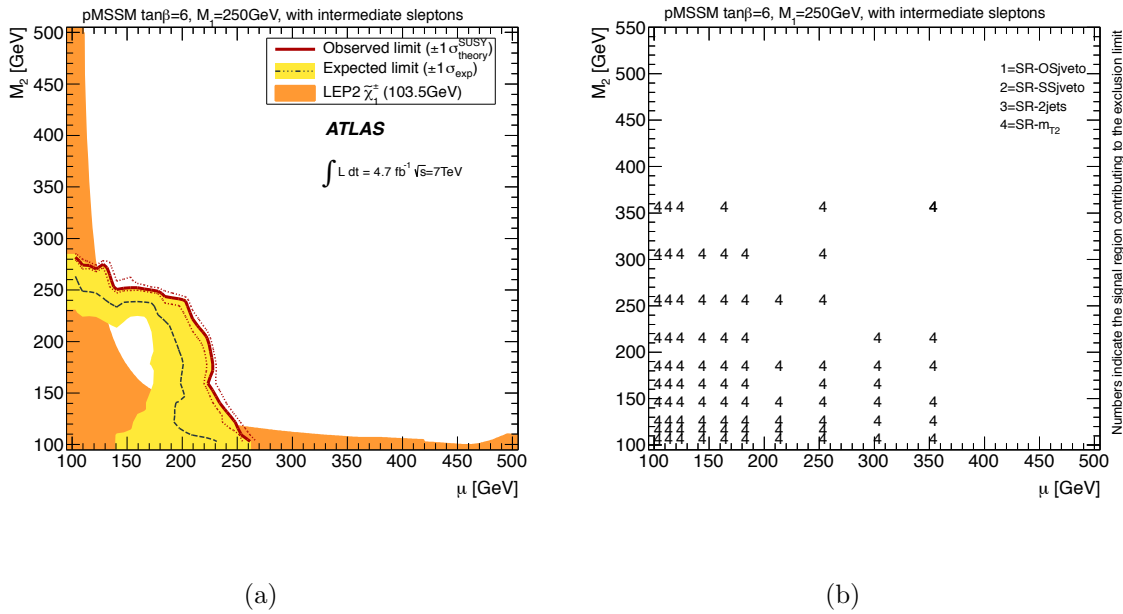
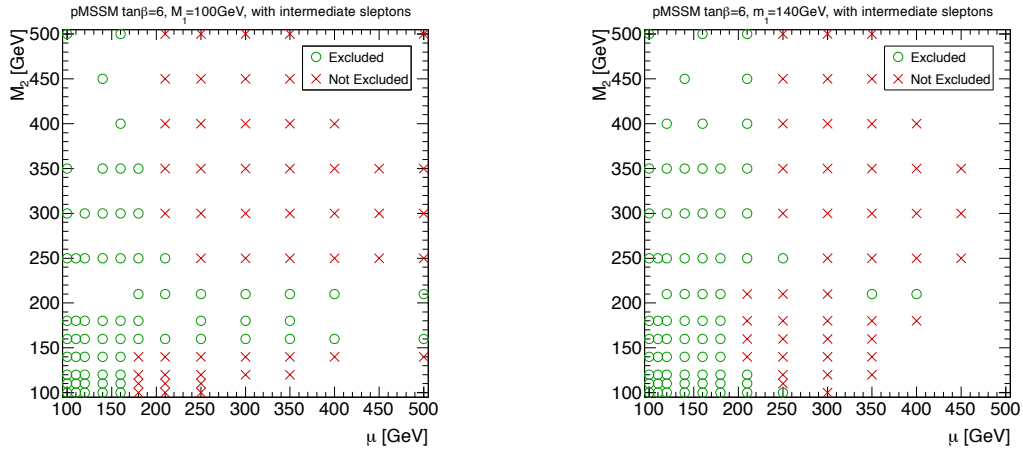


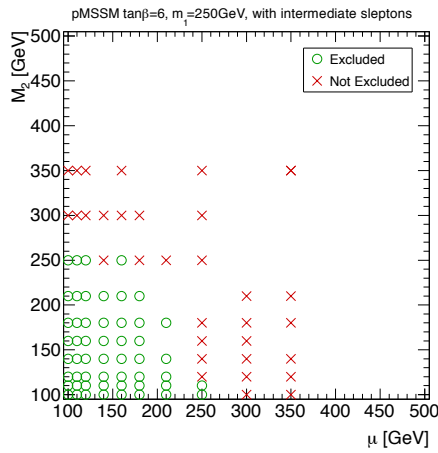
Figure 6.34: 95% exclusion limits in the  $\mu - M_2$  mass planes of the pMSSM for  $M_1 = 250 \text{ GeV}$  (a). The limits are presented in the same format as in Figure 6.21. For each signal point the  $\text{CL}_s$  is that corresponding to the signal region with the best expected sensitivity, which is indicated in (b).

grids are marked with a dot or cross depending on whether they are excluded or not excluded respectively.



(a)

(b)



(c)

Figure 6.35: 2D plots in the  $\mu - M_2$  mass planes of the pMSSM for  $M_1 = 100 \text{ GeV}$  (a),  $M_1 = 140 \text{ GeV}$  (b) and  $M_1 = 250 \text{ GeV}$  (c) showing the positions of the points in the respective signal grids and which points are excluded at 95% confidence level (indicated by the noughts) and which are not (indicated by the crosses).

To investigate this further, Table 6.17 shows the contribution to the signal yield for each of the 32 weak production processes for several points in the  $M_1 = 100 \text{ GeV}$  grid going from  $M_2 = 210 \text{ GeV}$ ,  $\mu = 180 \text{ GeV}$  across to  $M_2 = 210 \text{ GeV}$ ,  $\mu = 400 \text{ GeV}$ . The equivalent table is shown in Table 6.18 for the  $M_1 = 140 \text{ GeV}$  grid.

$(M_1, M_2, \mu)[\text{GeV}]$	(100,210,180)	(100,210,210)	(100,210,250)	(100,210,300)	(100,210,350)	(100,210,400)
Final state	Contribution to SR- $m_{T2}(e^\pm e^\mp, \mu^\pm \mu^\mp \text{ and } e^\pm \mu^\mp \text{ combined})$					
$\tilde{\chi}_1^0 \tilde{\chi}_1^0$	0.0	0.0	0.0	0.0	0.0	0.0
$\tilde{\chi}_1^0 \tilde{\chi}_2^0$	0.38	0.0	0.0	0.0	0.0	0.0
$\tilde{\chi}_1^0 \tilde{\chi}_3^0$	2.94	1.48	0.0	0.0	0.0	0.0
$\tilde{\chi}_1^0 \tilde{\chi}_4^0$	0.0	0.0	0.0	0.0	0.0	0.0
$\tilde{\chi}_1^0 \tilde{\chi}_1^+$	0.0	0.0	0.0	0.0	0.0	0.0
$\tilde{\chi}_1^0 \tilde{\chi}_2^+$	0.0	0.0	0.0	0.0	0.0	0.0
$\tilde{\chi}_1^0 \tilde{\chi}_1^-$	0.0	0.0	0.0	0.0	0.0	0.0
$\tilde{\chi}_1^0 \tilde{\chi}_2^-$	0.0	0.0	0.0	0.0	0.0	0.0
$\tilde{\chi}_2^0 \tilde{\chi}_2^0$	0.0	0.0	0.0	0.0	0.0	0.11
$\tilde{\chi}_2^0 \tilde{\chi}_3^0$	0.56	1.93	0.0	0.0	0.0	0.0
$\tilde{\chi}_2^0 \tilde{\chi}_4^0$	0.0	0.0	0.0	0.0	0.0	0.0
$\tilde{\chi}_2^0 \tilde{\chi}_1^+$	18.54	26.40	40.05	14.43	11.19	9.98
$\tilde{\chi}_2^0 \tilde{\chi}_2^+$	0.0	0.65	0.0	0.0	0.0	0.0
$\tilde{\chi}_2^0 \tilde{\chi}_1^-$	8.88	9.21	8.26	4.71	4.84	5.08
$\tilde{\chi}_2^0 \tilde{\chi}_2^-$	0.0	0.0	0.0	0.0	0.0	0.0
$\tilde{\chi}_3^0 \tilde{\chi}_3^0$	0.0	0.0	0.0	0.0	0.0	0.0
$\tilde{\chi}_3^0 \tilde{\chi}_4^0$	0.0	0.0	2.45	0.0	0.0	0.0
$\tilde{\chi}_3^0 \tilde{\chi}_1^+$	0.98	1.45	0.0	0.0	0.0	0.0
$\tilde{\chi}_3^0 \tilde{\chi}_2^+$	0.0	0.0	0.0	0.0	0.0	0.0
$\tilde{\chi}_3^0 \tilde{\chi}_1^-$	0.63	0.0	0.0	0.0	0.0	0.0
$\tilde{\chi}_3^0 \tilde{\chi}_2^-$	0.0	0.0	0.0	0.0	0.0	0.0
$\tilde{\chi}_4^0 \tilde{\chi}_4^0$	0.0	0.0	0.0	0.0	0.0	0.0
$\tilde{\chi}_4^0 \tilde{\chi}_1^+$	0.0	0.0	0.0	0.0	0.0	0.0
$\tilde{\chi}_4^0 \tilde{\chi}_2^+$	0.28	0.21	0.0	0.65	0.0	0.0
$\tilde{\chi}_4^0 \tilde{\chi}_1^-$	0.0	0.0	0.0	0.0	0.0	0.0
$\tilde{\chi}_4^0 \tilde{\chi}_2^-$	0.49	0.0	0.0	0.0	0.0	0.0
$\tilde{\chi}_1^+ \tilde{\chi}_1^-$	0.0	0.0	0.0	1.33	1.30	0.71
$\tilde{\chi}_1^+ \tilde{\chi}_2^-$	0.0	0.0	0.0	0.0	0.0	0.0
$\tilde{\chi}_2^+ \tilde{\chi}_1^-$	0.27	0.0	0.0	0.0	0.0	0.0
$\tilde{\chi}_2^+ \tilde{\chi}_2^-$	0.0	0.21	0.0	0.0	0.0	0.0
$\tilde{e}_R \tilde{e}_R, \tilde{\mu}_R \tilde{\mu}_R$	0.0	0.0	0.0	0.0	0.0	0.0
$\tilde{\tau}_R \tilde{\tau}_R$	0.0	0.0	0.0	0.0	0.0	0.0
Total	33.95	41.53	50.75	21.13	17.32	15.89

Table 6.17: Contributions to the signal region count in SR- $m_{T2}$  from all the subprocesses in the  $M_1 = 100 \text{ GeV}$  pMSSM grid, for selected points across the line  $M_2 = 210 \text{ GeV}$ . All subprocesses are normalised to  $4.7 \text{ fb}^{-1}$ .

The main contributions to the signal region count for all the models in the tables considered is  $\tilde{\chi}_2^0 \tilde{\chi}_1^\pm$  production. The points in the  $M_1 = 140 \text{ GeV}$  grid that are not excluded have much lower signal counts for these processes. Figure 6.36 shows the cross-section for  $\tilde{\chi}_2^0 \tilde{\chi}_1^\pm$  production for the  $M_1 = 100 \text{ GeV}$  and  $M_1 = 140 \text{ GeV}$  grids. The cross-sections are higher across the  $M_1 = 100 \text{ GeV}$  grid, indicating why the exclusion is stronger in this grid.

The pMSSM grids contain intermediate sleptons (set half-way between the two lightest neutralinos, as in the simplified model grids, though only right-handed sleptons are

$(M_1, M_2, \mu)[\text{GeV}]$	(140,210,180)	(140,210,210)	(140,210,250)	(140,210,300)	(140,210,350)	(140,210,400)
Final state	Contribution to SR- $m_{T2}(e^\pm e^\mp, \mu^\pm \mu^\mp$ and $e^\pm \mu^\mp$ combined)					
$\tilde{\chi}_1^0 \tilde{\chi}_1^0$	0.0	0.0	0.0	0.0	0.0	0.0
$\tilde{\chi}_1^0 \tilde{\chi}_2^0$	0.0	0.0	0.0	0.0	0.0	0.0
$\tilde{\chi}_1^0 \tilde{\chi}_3^0$	4.29	0.67	0.0	0.0	0.0	0.0
$\tilde{\chi}_1^0 \tilde{\chi}_4^0$	0.0	0.0	0.0	0.0	0.0	0.0
$\tilde{\chi}_1^0 \tilde{\chi}_1^+$	0.0	0.0	0.0	0.0	0.0	0.0
$\tilde{\chi}_1^0 \tilde{\chi}_2^+$	0.0	0.0	0.0	0.0	0.0	0.0
$\tilde{\chi}_1^0 \tilde{\chi}_1^-$	0.0	0.0	0.0	0.0	0.0	0.0
$\tilde{\chi}_1^0 \tilde{\chi}_2^-$	0.0	0.0	0.0	0.0	0.0	0.0
$\tilde{\chi}_2^0 \tilde{\chi}_2^0$	0.0	0.0	0.0	0.0	0.03	0.0
$\tilde{\chi}_2^0 \tilde{\chi}_3^0$	0.36	0.0	0.0	0.0	0.25	0.0
$\tilde{\chi}_2^0 \tilde{\chi}_4^0$	0.0	0.0	0.0	0.0	0.0	0.0
$\tilde{\chi}_2^0 \tilde{\chi}_1^+$	4.66	4.37	7.04	6.97	7.74	10.34
$\tilde{\chi}_2^0 \tilde{\chi}_2^+$	0.0	0.0	0.0	0.0	0.08	0.0
$\tilde{\chi}_2^0 \tilde{\chi}_1^-$	1.31	1.53	1.52	1.68	3.53	5.79
$\tilde{\chi}_2^0 \tilde{\chi}_2^-$	0.22	0.0	0.0	0.0	0.0	0.0
$\tilde{\chi}_3^0 \tilde{\chi}_3^0$	0.0	0.0	0.0	0.0	0.0	0.0
$\tilde{\chi}_3^0 \tilde{\chi}_4^0$	0.0	0.0	0.0	0.0	0.0	0.0
$\tilde{\chi}_3^0 \tilde{\chi}_1^+$	3.04	0.42	0.0	0.0	0.0	0.0
$\tilde{\chi}_3^0 \tilde{\chi}_2^+$	0.39	0.0	0.0	0.0	0.0	0.0
$\tilde{\chi}_3^0 \tilde{\chi}_1^-$	1.33	0.44	0.0	0.0	0.0	0.0
$\tilde{\chi}_3^0 \tilde{\chi}_2^-$	0.0	0.0	0.0	0.0	0.0	0.0
$\tilde{\chi}_4^0 \tilde{\chi}_4^0$	0.0	0.0	0.0	0.0	0.0	0.0
$\tilde{\chi}_4^0 \tilde{\chi}_1^+$	0.19	0.0	0.0	0.0	0.0	0.0
$\tilde{\chi}_4^0 \tilde{\chi}_2^+$	0.41	0.0	0.0	0.0	0.0	0.0
$\tilde{\chi}_4^0 \tilde{\chi}_1^-$	0.0	0.23	0.52	0.0	0.0	0.0
$\tilde{\chi}_4^0 \tilde{\chi}_2^-$	0.0	0.0	0.0	0.0	0.0	0.0
$\tilde{\chi}_1^+ \tilde{\chi}_1^-$	0.0	0.0	0.0	0.0	0.0	0.0
$\tilde{\chi}_1^+ \tilde{\chi}_2^-$	0.0	0.0	0.0	0.0	0.0	0.0
$\tilde{\chi}_2^+ \tilde{\chi}_1^-$	0.0	0.0	0.0	0.0	0.0	0.0
$\tilde{\chi}_2^+ \tilde{\chi}_2^-$	0.0	0.45	0.33	0.19	0.0	0.0
$\tilde{e}_R \tilde{e}_R, \tilde{\mu}_R \tilde{\mu}_R$	0.0	0.0	0.0	0.0	0.0	0.0
$\tilde{\tau}_R \tilde{\tau}_R$	0.0	0.0	0.0	0.0	0.0	0.0
Total	16.20	8.11	9.40	8.83	11.64	16.13

Table 6.18: Contributions to the signal region count in SR- $m_{T2}$  from all the subprocesses in the  $M_1 = 140 \text{ GeV}$  pMSSM grid, for selected points across the line  $M_2 = 210 \text{ GeV}$ . All subprocesses are normalised to  $4.7 \text{ fb}^{-1}$ .

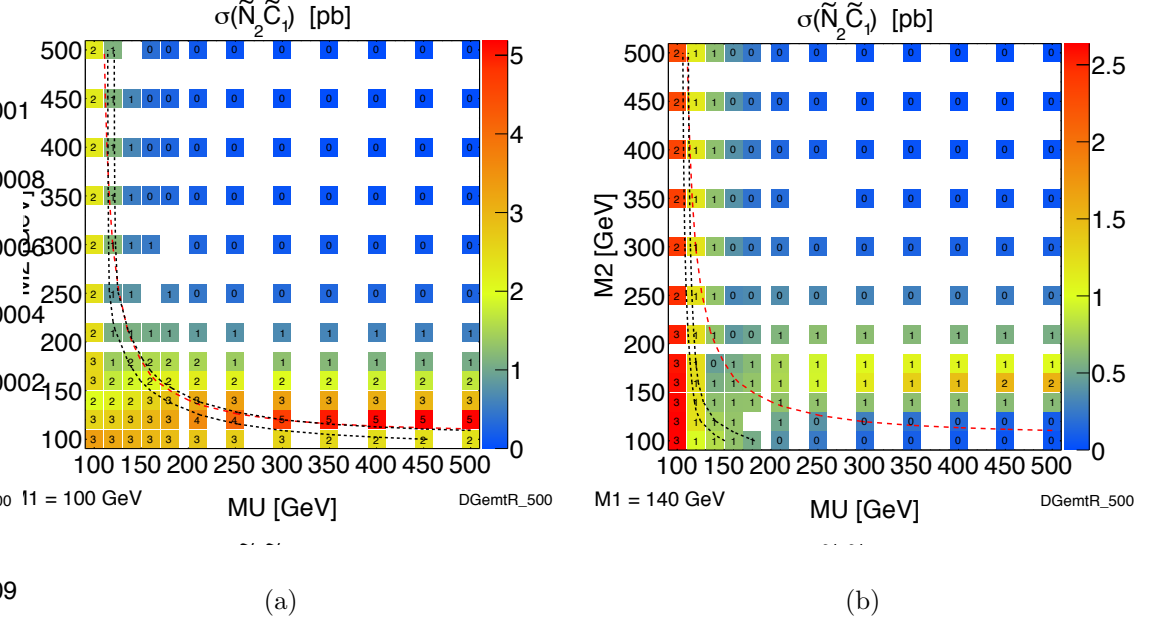


Figure 6.36: Cross-section for  $\tilde{\chi}_2^0 \tilde{\chi}_1^\pm$  for the pMSSM grids with  $M_1 = 100 \text{ GeV}$  (a) and  $M_1 = 140 \text{ GeV}$  (b).

included in the pMSSM grid). Assuming that the sensitivity to the points of interest in Tables 6.17 and 6.18 is driven by  $\tilde{\chi}_2^0 \tilde{\chi}_1^\pm$  production the exclusions (or lack of) can be compared to the exclusion contour in the simplified model  $\tilde{\chi}_2^0 \tilde{\chi}_1^\pm$  grid in Section 6.8.2. The simplified model grid assumes degenerate masses for the  $\tilde{\chi}_1^\pm$  and  $\tilde{\chi}_2^0$ . Figure 6.37 shows the  $\tilde{\chi}_2^0 \tilde{\chi}_1^\pm$  mass-splitting for the two grids under consideration. The points shown in Tables 6.17 and 6.18 have the mass-splittings are of the order of a few GeV, so their results will be compared directly to those in Section 6.8.2.

To enable a comparison, Figure 6.38 shows distributions of the masses of the  $\tilde{\chi}_1^\pm$  and  $\tilde{\chi}_1^0$  sparticles for the two grids. Comparing the two, the point  $(\mu, M_2) = (300, 210)$  is excluded for the  $M_1 = 100 \text{ GeV}$  grid, where it has a mass of 95 GeV for  $\tilde{\chi}_1^0$  and a mass of 180 GeV for the  $\tilde{\chi}_1^\pm$ . In Figure 6.25 this point is on the edge of the excluded region. For the  $M_1 = 140 \text{ GeV}$  grid the same point is not excluded. Here the masses are 180 GeV and 132 GeV respectively for the  $\tilde{\chi}_1^\pm$  and  $\tilde{\chi}_2^0$ , which lies outside of the excluded region Figure 6.25.

The points in Tables 6.17 and 6.18 have very low yields for  $\tilde{\chi}_1^+ \tilde{\chi}_1^-$  production. Figure 6.39 shows the  $\tilde{\chi}_1^\pm \tilde{\chi}_1^0$  mass-splitting for the  $M_1 = 100 \text{ GeV}$  and the  $M_1 = 140 \text{ GeV}$  grids. The  $m_{T2}$  variable is sensitive to the mass-splittings between the heavy pair pro-

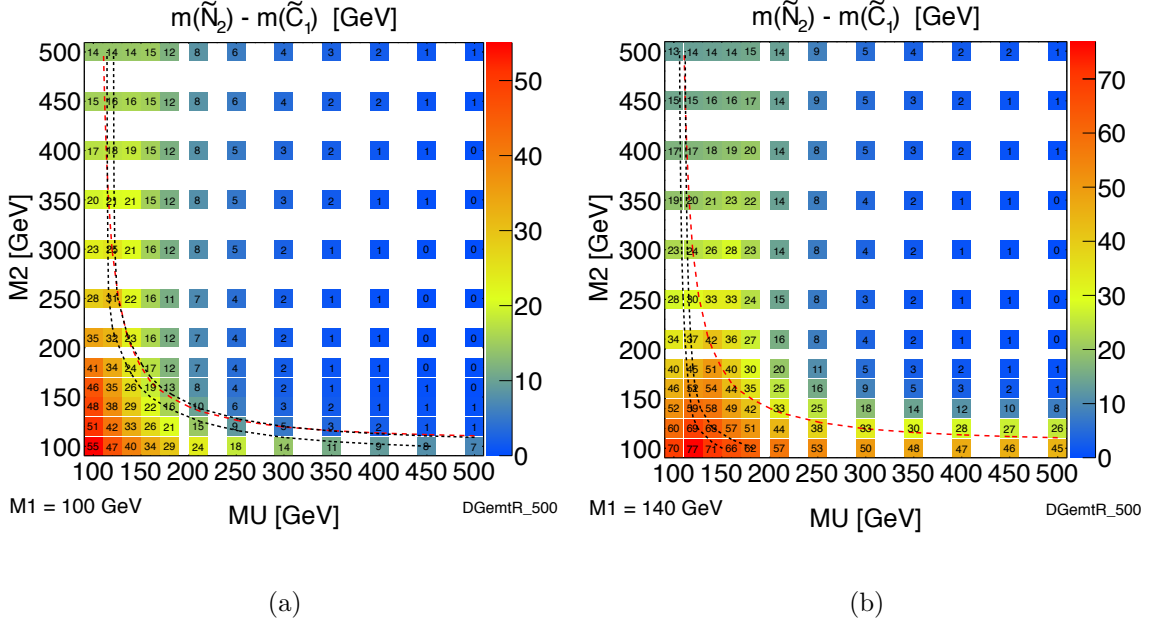


Figure 6.37: Mass-splittings between the  $\tilde{\chi}_2^0$  and  $\tilde{\chi}_1^\pm$  masses for the pMSSM grids with  $M_1 = 100 \text{ GeV}$  (a) and  $M_1 = 140 \text{ GeV}$  (b).

duced particle and the invisible particle that escapes detection (the chargino and LSP in this case). The mass-splittings are small compared to the  $m_{T2}$  cut of 90 GeV for the points in Tables 6.17 and 6.18, which explains why the signal counts are low. Taking the point  $(M_1, M_2, \mu) = (100 \text{ GeV}, 210 \text{ GeV}, 300 \text{ GeV})$  as a reference, which has a chargino mass of 180 GeV and a neutralino mass of 85 GeV, and comparing to Figure 6.21 this point lies outside the excluded region. In the chargino-pair production simplified model grid the signal region contributing to the exclusion limit in this region is actually SR-OSjveto because the smaller mass-splitting leads to a low sensitivity for SR- $m_{T2}$ .

The regions of the grids in the  $M_1 = 100 \text{ GeV}$  grid where the  $\tilde{\chi}_1^\pm \tilde{\chi}_1^0$  mass-splitting is larger, i.e. the top right regions of the grids, will now be considered. Table 6.19 shows the contribution to SR- $m_{T2}$  for a set of points with  $\mu = 400 \text{ GeV}$  in the  $M_1 = 100 \text{ GeV}$  grid. Apart from the  $M_2 = 160 \text{ GeV}$  point, the total signal yields are low so the points are not excluded, but as  $M_2$  increases there are small but non-zero contributions from  $\tilde{\chi}_1^+ \tilde{\chi}_1^-$  production, which by  $M_2 = 400 \text{ GeV}$  are of a comparable level to  $\tilde{\chi}_2^0 \tilde{\chi}_1^\pm$  pair production.

For the higher  $M_2$  values in Table 6.19 direct slepton production provides the largest

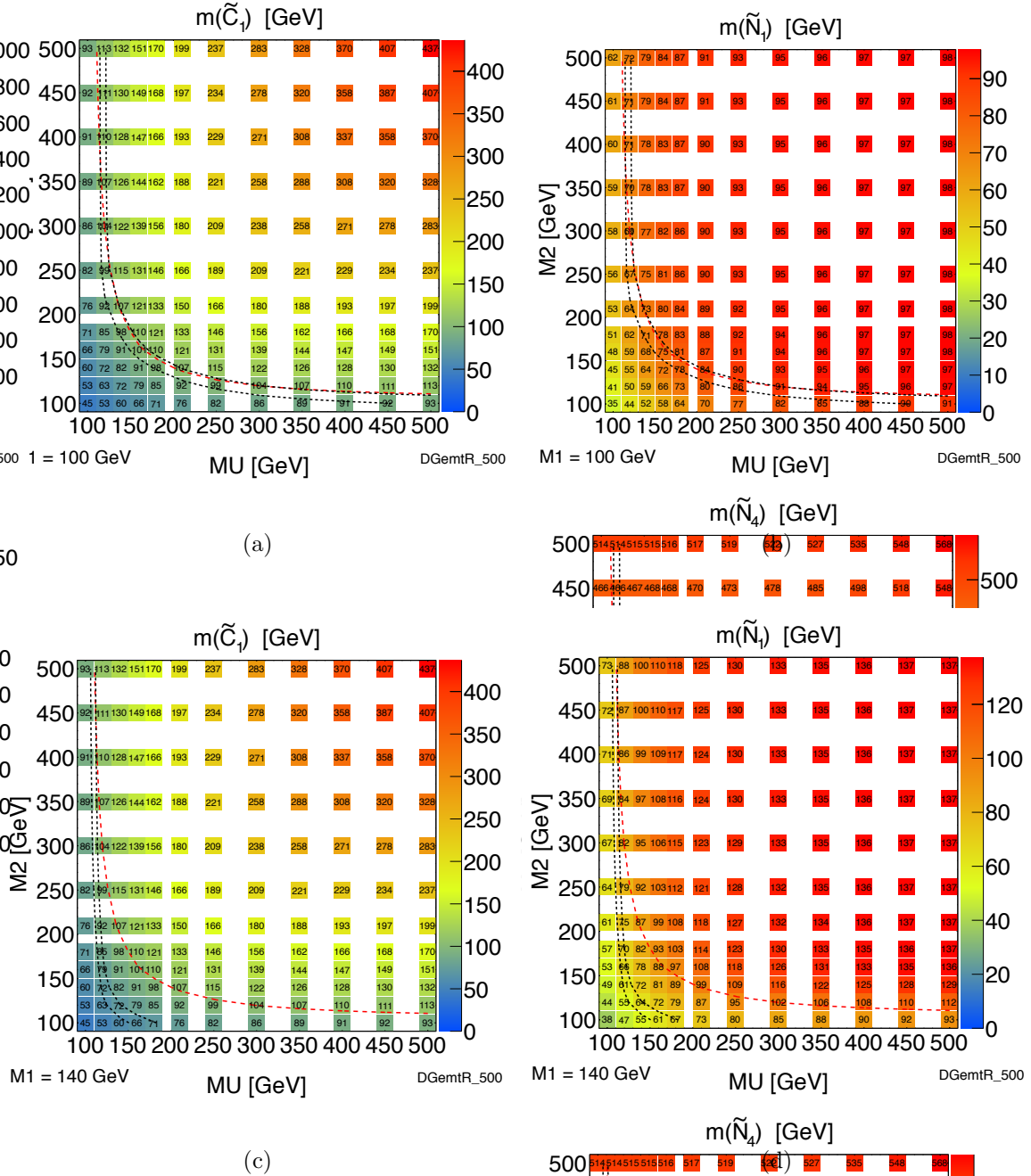


Figure 6.38: Masses of the  $\tilde{\chi}_1^\pm$  (left) and  $\tilde{\chi}_1^0$  (right) gauginos for the pMSSM grids with  $M_1 = 100 \text{ GeV}$  (top) and  $M_1 = 140 \text{ GeV}$  (bottom).

$(M_1, M_2, \mu)[\text{GeV}]$	(100,160,400)	(100,210,400)	(100,250,400)	(100,300,400)	(100,350,400)	(100,400,400)
Final state	Contribution to SR- $m_{T2}(e^\pm e^\mp, \mu^\pm \mu^\mp)$ and $e^\pm \mu^\mp$ combined					
$\tilde{\chi}_1^0 \tilde{\chi}_1^0$	0.0	0.0	0.0	0.0	0.0	0.0
$\tilde{\chi}_1^0 \tilde{\chi}_2^0$	0.0	0.0	0.0	0.0	0.0	0.0
$\tilde{\chi}_1^0 \tilde{\chi}_3^0$	0.0	0.0	0.0	0.0	0.0	0.0
$\tilde{\chi}_1^0 \tilde{\chi}_4^0$	0.0	0.0	0.0	0.0	0.0	0.0
$\tilde{\chi}_1^0 \tilde{\chi}_1^+$	0.0	0.0	0.0	0.0	0.0	0.0
$\tilde{\chi}_1^0 \tilde{\chi}_2^+$	0.0	0.0	0.0	0.0	0.0	0.0
$\tilde{\chi}_1^0 \tilde{\chi}_1^-$	0.0	0.0	0.0	0.0	0.0	0.0
$\tilde{\chi}_1^0 \tilde{\chi}_2^-$	0.0	0.0	0.0	0.0	0.01	0.0
$\tilde{\chi}_2^0 \tilde{\chi}_2^0$	0.0	0.11	0.0	0.0	0.0	0.0
$\tilde{\chi}_2^0 \tilde{\chi}_3^0$	0.0	0.0	0.0	0.05	0.0	0.01
$\tilde{\chi}_2^0 \tilde{\chi}_4^0$	0.0	0.0	0.0	0.0	0.0	0.0
$\tilde{\chi}_2^0 \tilde{\chi}_1^+$	22.14	9.98	3.12	0.90	0.64	0.25
$\tilde{\chi}_2^0 \tilde{\chi}_2^+$	0.0	0.0	0.0	0.026	0.0	0.0
$\tilde{\chi}_2^0 \tilde{\chi}_1^-$	8.09	5.08	1.15	0.33	0.19	0.08
$\tilde{\chi}_2^0 \tilde{\chi}_2^-$	0.0	0.0	0.0	0.0	0.0	0.0
$\tilde{\chi}_3^0 \tilde{\chi}_3^0$	0.0	0.0	0.0	0.0	0.0	0.0
$\tilde{\chi}_3^0 \tilde{\chi}_4^0$	0.0	0.0	0.0	0.0	0.0	0.0
$\tilde{\chi}_3^0 \tilde{\chi}_1^+$	0.0	0.0	0.07	0.0	0.03	0.03
$\tilde{\chi}_3^0 \tilde{\chi}_2^+$	0.0	0.0	0.0	0.0	0.01	0.01
$\tilde{\chi}_3^0 \tilde{\chi}_1^-$	0.0	0.0	0.0	0.0	0.0	0.01
$\tilde{\chi}_3^0 \tilde{\chi}_2^-$	0.0	0.0	0.11	0.0	0.0	0.0
$\tilde{\chi}_4^0 \tilde{\chi}_4^0$	0.0	0.0	0.0	0.0	0.0	0.0
$\tilde{\chi}_4^0 \tilde{\chi}_1^+$	0.0	0.0	0.0	0.0	0.02	0.01
$\tilde{\chi}_4^0 \tilde{\chi}_2^+$	0.0	0.0	0.0	0.0	0.0	0.01
$\tilde{\chi}_4^0 \tilde{\chi}_1^-$	0.0	0.0	0.0	0.0	0.0	0.0
$\tilde{\chi}_4^0 \tilde{\chi}_2^-$	0.0	0.0	0.0	0.0	0.0	0.01
$\tilde{\chi}_1^+ \tilde{\chi}_1^-$	0.0	0.71	1.43	1.06	0.86	0.51
$\tilde{\chi}_1^+ \tilde{\chi}_2^-$	0.0	0.0	0.0	0.0	0.0	0.0
$\tilde{\chi}_2^+ \tilde{\chi}_1^-$	0.0	0.0	0.0	0.02	0.01	0.0
$\tilde{\chi}_2^+ \tilde{\chi}_2^-$	0.0	0.0	0.0	0.0	0.0	0.01
$\tilde{e}_R \tilde{e}_R, \tilde{\mu}_R \tilde{\mu}_R$	0.0	0.0	1.94	3.56	3.13	2.82
$\tilde{\tau}_R \tilde{\tau}_R$	0.0	0.0	0.0	0.0	0.0	0.0
Total	30.22	15.89	7.81	5.94	4.91	3.75

Table 6.19: Contributions to the signal region count in SR- $m_{T2}$  from all the subprocesses in the  $M_1 = 100 \text{ GeV}$  pMSSM grid, for selected points across the line  $\mu = 400 \text{ GeV}$ . All subprocesses are normalised to  $4.7 \text{ fb}^{-1}$ .

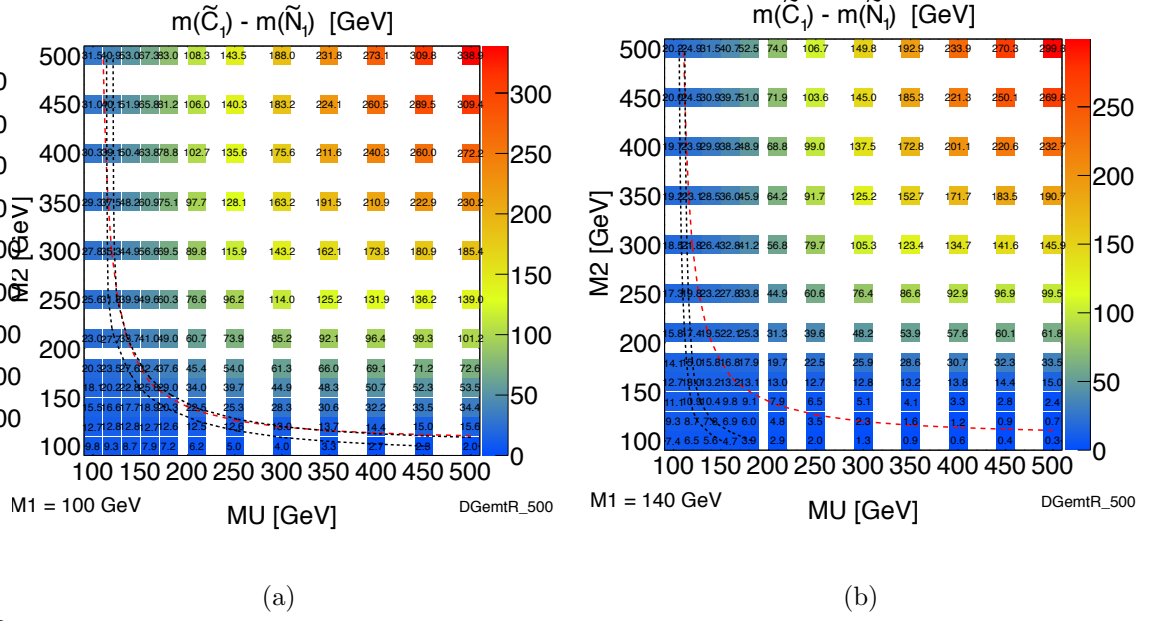


Figure 6.39: Mass-splittings between the  $\tilde{\chi}_1^\pm$  and  $\tilde{\chi}_1^0$  masses for the pMSSM grids with  $M_1 = 100 \text{ GeV}$  (a) and  $M_1 = 140 \text{ GeV}$  (b).

contribution to the signal yield, whereas again there is no contribution from slepton-pair production in the points considered in Tables 6.17 and 6.18. Figure 6.40 shows the  $\tilde{\ell}_R - \tilde{\chi}_1^0$  mass-splitting and the slepton mass for the  $M_1 = 100 \text{ GeV}$  and  $M_1 = 140 \text{ GeV}$  grids. The mass-splittings are larger (and so a higher endpoint for the  $m_{T2}$  distribution is expected) in the top right regions of the grids. For the points in Tables 6.17 and 6.18 although the slepton masses are quite light the mass-splittings are too low for signal events to exceed the  $90 \text{ GeV}$   $m_{T2}$  cut. The direct slepton contributions to the pMSSM grid cannot be directly compared to the direct slepton exclusion results, because only right-handed sleptons are included in the pMSSM grids. The left-handed sleptons are assumed to be out of reach (and so set to  $2 \text{ TeV}$  in mass), whereas the direct slepton simplified model grid contains both left-handed and right-handed sleptons. The production cross-section for right-handed sleptons are lower which again explains the low event counts even for large mass-splittings.

The exclusion in the  $M_1 = 250 \text{ GeV}$  grid is much weaker than in the other two pMSSM grids. Table 6.20 shows a scan across  $\mu$  for  $M_2 = 210 \text{ GeV}$  for the  $M_1 = 250 \text{ GeV}$  grid and Table 6.21 shows a scan across  $M_2$  for  $\mu = 160 \text{ GeV}$ . There are a larger number of subprocesses contributing to the signal region yield compared to in Tables 6.17– 6.19,

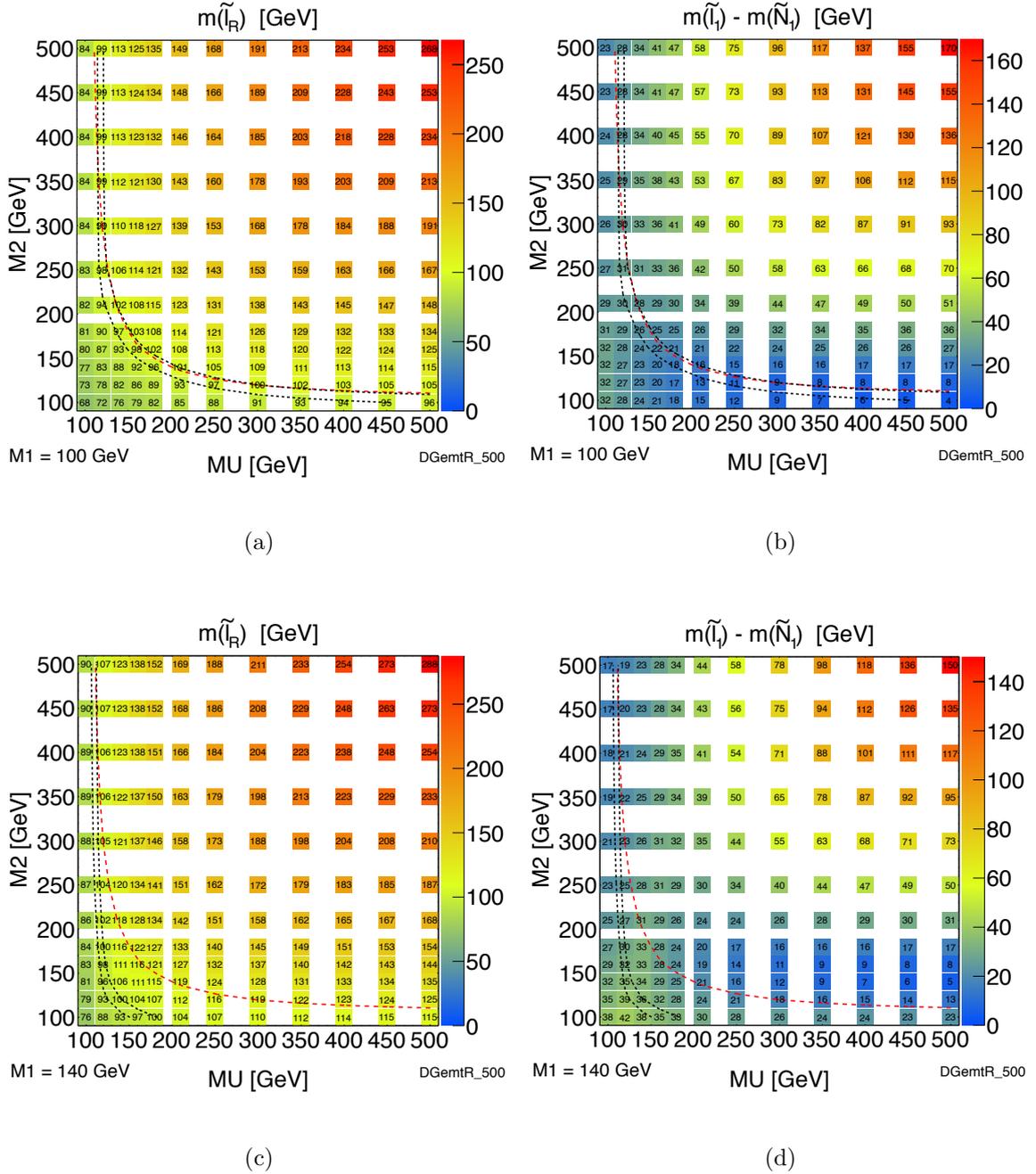


Figure 6.40: Distributions showing the right-handed slepton mass (left) and the mass splittings between the  $\tilde{\ell}_R$  and  $\tilde{\chi}_1^0$  masses (right) and for the pMSSM grids with  $M_1 = 100 \text{ GeV}$  (top) and  $M_1 = 140 \text{ GeV}$  (bottom).

though the counts are small.  $\tilde{\chi}_2^0 \tilde{\chi}_1^\pm$  is still important, but Table 6.21 shows that for low values of  $M_2$  and  $\mu$ ,  $\tilde{\chi}_3^0 \tilde{\chi}_1^\pm$  production is also important.

$(M_1, M_2, \mu)[\text{GeV}]$	(250,210,120)	(250,210,140)	(250,210,160)	(250,210,180)	(250,210,300)	(250,210,350)
Final state	Contribution to $\text{SR-}m_{\text{T2}}(e^\pm e^\mp, \mu^\pm \mu^\mp \text{ and } e^\pm \mu^\mp \text{ combined})$					
$\tilde{\chi}_1^0 \tilde{\chi}_1^0$	0.0	0.0	0.0	0.0	0.0	0.0
$\tilde{\chi}_1^0 \tilde{\chi}_2^0$	12.13	7.88	3.93	2.70	0.0	0.0
$\tilde{\chi}_1^0 \tilde{\chi}_3^0$	0.0	0.21	0.0	0.0	0.0	0.0
$\tilde{\chi}_1^0 \tilde{\chi}_4^0$	0.0	0.0	0.0	0.0	0.0	0.0
$\tilde{\chi}_1^0 \tilde{\chi}_1^+$	0.0	0.0	0.0	0.0	0.0	0.0
$\tilde{\chi}_1^0 \tilde{\chi}_2^+$	0.0	0.0	0.10	0.03	0.0	0.0
$\tilde{\chi}_1^0 \tilde{\chi}_1^-$	0.0	0.0	0.0	0.0	0.0	0.0
$\tilde{\chi}_1^0 \tilde{\chi}_2^-$	0.24	0.0	0.0	0.0	0.0	0.01
$\tilde{\chi}_2^0 \tilde{\chi}_2^0$	0.0	0.0	0.0	0.0	0.0	0.0
$\tilde{\chi}_2^0 \tilde{\chi}_3^0$	0.67	0.0	0.07	0.0	0.0	0.0
$\tilde{\chi}_2^0 \tilde{\chi}_4^0$	1.41	0.0	0.08	0.67	0.0	0.0
$\tilde{\chi}_2^0 \tilde{\chi}_1^+$	7.43	5.61	3.60	3.79	1.75	0.74
$\tilde{\chi}_2^0 \tilde{\chi}_2^+$	0.0	0.17	0.23	0.36	0.06	0.01
$\tilde{\chi}_2^0 \tilde{\chi}_1^-$	1.83	2.79	1.25	1.74	0.78	0.17
$\tilde{\chi}_2^0 \tilde{\chi}_2^-$	0.0	0.0	0.08	0.08	0.05	0.03
$\tilde{\chi}_3^0 \tilde{\chi}_3^0$	0.0	0.0	0.0	0.0	0.0	0.0
$\tilde{\chi}_3^0 \tilde{\chi}_4^0$	0.0	0.0	0.0	0.0	0.15	0.07
$\tilde{\chi}_3^0 \tilde{\chi}_1^+$	1.66	1.76	2.71	3.16	0.01	0.0
$\tilde{\chi}_3^0 \tilde{\chi}_2^+$	1.56	1.58	1.58	1.02	0.0	0.02
$\tilde{\chi}_3^0 \tilde{\chi}_1^-$	0.51	0.60	1.09	1.07	0.0	0.0
$\tilde{\chi}_3^0 \tilde{\chi}_2^-$	0.53	0.77	0.49	0.52	0.02	0.01
$\tilde{\chi}_4^0 \tilde{\chi}_4^0$	0.0	0.0	0.0	0.0	0.0	0.0
$\tilde{\chi}_4^0 \tilde{\chi}_1^+$	0.0	0.16	0.35	0.50	0.15	0.04
$\tilde{\chi}_4^0 \tilde{\chi}_2^+$	0.0	0.71	0.71	1.58	0.26	0.08
$\tilde{\chi}_4^0 \tilde{\chi}_1^-$	0.0	0.17	0.11	0.14	0.06	0.0
$\tilde{\chi}_4^0 \tilde{\chi}_2^-$	0.60	0.18	0.80	0.46	0.02	0.02
$\tilde{\chi}_1^+ \tilde{\chi}_1^-$	0.0	0.0	0.0	0.0	0.0	0.0
$\tilde{\chi}_1^+ \tilde{\chi}_2^-$	0.0	0.0	0.0	0.03	0.01	0.02
$\tilde{\chi}_2^+ \tilde{\chi}_1^-$	0.0	0.0	0.0	0.0	0.0	0.0
$\tilde{\chi}_2^+ \tilde{\chi}_2^-$	0.19	0.54	0.14	0.15	0.02	0.02
$\tilde{e}_R \tilde{e}_R, \tilde{\mu}_R \tilde{\mu}_R$	0.0	0.0	0.0	0.0	0.0	0.0
$\tilde{\tau}_R \tilde{\tau}_R$	0.0	0.0	0.0	0.0	0.0	0.0
Total	28.76	23.12	17.34	17.99	3.36	1.22

Table 6.20: Contributions to the signal region count in  $\text{SR-}m_{\text{T2}}$  from all the subprocesses in the  $M_1 = 250 \text{ GeV}$  pMSSM grid, for selected points across the line  $M_2 = 210 \text{ GeV}$ . All subprocesses are normalised to  $4.7 \text{ fb}^{-1}$ .

$(M_1, M_2, \mu)[\text{GeV}]$	(250,160,160)	(250,180,160)	(250,210,160)	(250,250,160)	(250,300,160)	(250,350,160)
Final state	Contribution to SR- $m_{T2}(e^\pm e^\mp, \mu^\pm \mu^\mp$ and $e^\pm \mu^\mp$ combined)					
$\tilde{\chi}_1^0 \tilde{\chi}_1^0$	0.0	0.0	0.0	0.0	0.0	0.0
$\tilde{\chi}_1^0 \tilde{\chi}_2^0$	5.49	4.91	3.93	3.90	1.39	1.12
$\tilde{\chi}_1^0 \tilde{\chi}_3^0$	0.0	0.0	0.0	0.0	0.0	0.0
$\tilde{\chi}_1^0 \tilde{\chi}_4^0$	0.0	0.0	0.0	0.0	0.0	0.0
$\tilde{\chi}_1^0 \tilde{\chi}_1^+$	0.0	0.0	0.0	0.0	0.0	0.0
$\tilde{\chi}_1^0 \tilde{\chi}_2^+$	0.05	0.07	0.10	0.0	0.0	0.0
$\tilde{\chi}_1^0 \tilde{\chi}_1^-$	0.0	0.0	0.0	0.0	0.0	0.0
$\tilde{\chi}_1^0 \tilde{\chi}_2^-$	0.08	0.0	0.0	0.0	0.0	0.0
$\tilde{\chi}_2^0 \tilde{\chi}_2^0$	0.0	0.0	0.0	0.0	0.0	0.0
$\tilde{\chi}_2^0 \tilde{\chi}_3^0$	0.51	0.57	0.07	0.0	0.21	0.10
$\tilde{\chi}_2^0 \tilde{\chi}_4^0$	0.29	0.16	0.08	0.16	0.0	0.0
$\tilde{\chi}_2^0 \tilde{\chi}_1^+$	5.77	5.94	3.60	2.64	0.32	0.50
$\tilde{\chi}_2^0 \tilde{\chi}_2^+$	0.46	0.41	0.23	0.0	0.0	0.0
$\tilde{\chi}_2^0 \tilde{\chi}_1^-$	2.73	1.87	1.25	1.11	0.23	0.16
$\tilde{\chi}_2^0 \tilde{\chi}_2^-$	0.17	0.23	0.08	0.07	0.0	0.0
$\tilde{\chi}_3^0 \tilde{\chi}_3^0$	0.0	0.0	0.0	0.0	0.0	0.0
$\tilde{\chi}_3^0 \tilde{\chi}_4^0$	0.0	0.0	0.0	0.0	0.0	0.0
$\tilde{\chi}_3^0 \tilde{\chi}_1^+$	5.71	3.18	2.71	0.86	1.67	0.32
$\tilde{\chi}_3^0 \tilde{\chi}_2^+$	2.03	2.06	1.58	0.59	0.09	0.05
$\tilde{\chi}_3^0 \tilde{\chi}_1^-$	2.24	1.69	1.09	0.47	0.31	0.04
$\tilde{\chi}_3^0 \tilde{\chi}_2^-$	0.76	0.87	0.49	0.06	0.0	0.05
$\tilde{\chi}_4^0 \tilde{\chi}_4^0$	0.0	0.0	0.0	0.0	0.0	0.0
$\tilde{\chi}_4^0 \tilde{\chi}_1^+$	0.22	0.40	0.35	0.17	0.10	0.0
$\tilde{\chi}_4^0 \tilde{\chi}_2^+$	0.87	1.15	0.71	0.79	0.31	0.19
$\tilde{\chi}_4^0 \tilde{\chi}_1^-$	0.22	0.24	0.11	0.0	0.0	0.0
$\tilde{\chi}_4^0 \tilde{\chi}_2^-$	0.56	0.32	0.80	0.06	0.11	0.0
$\tilde{\chi}_1^+ \tilde{\chi}_1^-$	0.0	0.0	0.0	0.0	0.0	0.0
$\tilde{\chi}_1^+ \tilde{\chi}_2^-$	0.06	0.07	0.0	0.0	0.0	0.0
$\tilde{\chi}_2^+ \tilde{\chi}_1^-$	0.22	0.0	0.0	0.0	0.0	0.0
$\tilde{\chi}_2^+ \tilde{\chi}_2^-$	0.28	0.23	0.14	0.38	0.20	0.17
$\tilde{e}_R \tilde{e}_R, \tilde{\mu}_R \tilde{\mu}_R$	0.0	0.0	0.0	0.0	0.0	0.0
$\tilde{\tau}_R \tilde{\tau}_R$	0.0	0.0	0.0	0.0	0.0	0.0
Total	28.71	24.36	17.34	11.25	4.94	2.72

Table 6.21: Contributions to the signal region count in SR- $m_{T2}$  from all the subprocesses in the  $M_1 = 250 \text{ GeV}$  pMSSM grid, for selected points across the line  $\mu = 160 \text{ GeV}$ . All subprocesses are normalised to  $4.7 \text{ fb}^{-1}$ .

In summary, this section has presented the exclusion limits across weak production pMSSM grids with intermediate sleptons, and has demonstrated consistency between the exclusions observed for the simplified model grids considered in the analysis and the pMSSM limits. The exclusion contours for the pMSSM grids have been explained by examining the subprocesses contributing to the signal count in SR- $m_{T2}$  (which drives most of the exclusion) in different areas of the grid.

## 6.9 Conclusions

The presented limits provided the first published LHC limits on direct slepton production and chargino-pair production [1] (CMS did not publish exclusions in these scenarios for the 2011 dataset). The  $m_{T2}$  variable proved very effective at background suppression, with the  $m_{T2}$ -based signal region providing most of the sensitivity across all of the signal grids considered.

With it being the first time such an analysis performed at ATLAS, many areas for improvement in future iterations were identified throughout the course of the analysis. Firstly, the statistical interpretation used for the 2011 analysis was fairly simplistic compared to what will be detailed later in Section 7.3, for the analysis on 2012 data. When calculating the  $\text{CL}_s$  values for exclusion contours all lepton flavour channels being considered were treated as a single channel in the fit. That is to say the signal and background counts were summed over all contributing channels (di-electron and di-muon for the direct slepton case, and di-electron, di-muon and electron-muon for all other signal grids), rather than doing a statistical combination of the channels. Also, when multiple signal regions were considered for a particular point, the  $\text{CL}_s$  value was just taken from the signal region with the best expected sensitivity. This was necessary as SR-OSjveto and SR- $m_{T2}$  are not orthogonal so could not be statistically combined. The signal regions were not designed to be orthogonal as they were initially developed independently. If included in future analyses, it was decided that SR-OSjveto should be forced to be orthogonal to SR- $m_{T2}$  by adding an additional requirement of  $m_{T2} < 90 \text{ GeV}$ .

The background estimation techniques that were used for the 2011 analysis reduced the reliance on Monte Carlo simulation for the  $Z + X$  and top backgrounds, however the  $WW$  data-driven method only applied to SR-OSjveto and not to SR- $m_{T2}$ , which meant that Monte Carlo predictions were used for one of the main backgrounds to the most

sensitive signal region. This was identified as an area to improve for future analyses.

In conclusion, this analysis provided a solid starting point for ATLAS searches for weakly produced supersymmetric particles in events with 2 light leptons and missing transverse momentum. The 2012 run saw  $20.3 \text{ fb}^{-1}$  of data at  $\sqrt{s} = 8 \text{ TeV}$  collected. More data meant increased sensitivity to electroweak production processes. However the background compositions changed so re-optimisation was required to deal with the new running environment. The next chapter will discuss the first public ATLAS result on the search for weakly produced SUSY in 2-lepton events using the 2012 dataset.

# Chapter 7

## Extending the reach with 2012 data

### 7.1 Introduction

The end of the 2011 run marked the end of 7 TeV running at the LHC. After a technical stop and period of commissioning, the 2012 run began in March 2012, at a higher centre-of-mass energy of 8 TeV, with the initial aim of delivering  $15 \text{ fb}^{-1}$  to ATLAS and CMS by the end of 2012. It was hoped that, if it did exist, this would be enough data to claim a discovery of the Higgs boson before the first long shutdown, which would start at the end of the run.

2012 was undoubtedly a milestone year for particle physics. On 4th July, the spokespersons of both ATLAS and CMS confirmed that both experiments had  $5\sigma$  observations of a new particle, with a mass around 125 GeV and consistent with the properties of the Standard Model Higgs boson [66, 67]. Assuming this new particle to be the Higgs boson, this discovery had many implications for supersymmetry. Firstly a Higgs mass around 125 GeV provides additional constraints on potential SUSY scenarios [172–176] (they must at least be such that the lightest scalar Higgs particle in the theory is consistent with the new observed particle). Also searches for electroweak production became increasingly relevant as the “Natural SUSY” paradigm [177, 178] states that for supersymmetry to stabilise the weak scale and solve the hierarchy problem, the sparticles that couple strongly to the Higgs boson (the gauginos and third generation sfermions), must be close to or below the TeV scale, and so could be accessible at the LHC.

The higher centre-of-mass energy and luminosity of the 2012 run gave increased sensitivity to many BSM signals. The 2012 running conditions were however more

challenging for performing analyses. This will be discussed further in Section 7.2. The bulk of this chapter focusses on the first 2-lepton analysis of the full 2012 dataset to search for electroweak production in the case that the first and second generation sleptons are light. The analysis was published in an ATLAS “Conference Note” [5] alongside another 2-lepton analysis targeting chargino-pair production in the scenario that intermediate sleptons are not accessible so the decay must proceed via  $W$  bosons. The search for slepton and chargino-pair production used two signal regions based on the  $m_{T2}$  variable. The published analysis will be presented in Section 7.3. The author played an active role in this analysis and unless stated, all the results in this Chapter are the work of the author.

The chapter will then continue in Section 7.4 by considering whether the sensitivity of the  $m_{T2}$ -based search could be extended by exploiting the shape information in  $m_{T2}$  distributions. The chapter will then be concluded with a brief discussion of the “wider picture”, that is to say a summary of the status of all ATLAS searches for supersymmetric particles at the time of writing.

## 7.2 Key developments in 2012

### 7.2.1 Higher centre-of-mass energy

Referring back to Figure 3.3, which shows cross-sections for the pair production of supersymmetric particles at  $\sqrt{s} = 7$  TeV and  $\sqrt{s} = 8$  TeV, production cross-sections increase when the centre-of-mass energy increases. The higher signal cross-sections, along with the higher integrated luminosity of the 2012 run (see next section), increased the sensitivity to SUSY processes that had already been explored, and also allowed the possibility to search for new previously unexplored processes. (As an example, the second analysis in [5], which is not discussed in this thesis, was the first ATLAS search to target chargino-pair production, with decays through gauge bosons.)

### 7.2.2 Higher luminosity

The original LHC plan for the 2012 run was to deliver  $15 \text{ fb}^{-1}$  to ATLAS and CMS by the end of 2012, to give a total of  $20 \text{ fb}^{-1}$  of data from the combined 2011 and 2012 run. The machine performed better than expected and after applying beam, detector

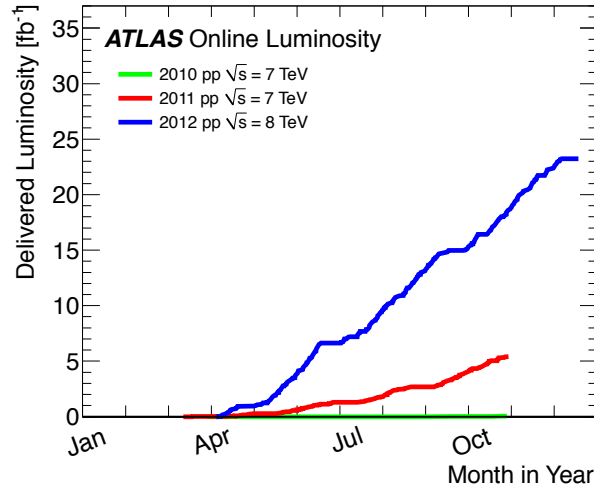


Figure 7.1: Cumulative luminosity versus day delivered to ATLAS during stable beams and for p-p collisions. This is shown for 2010 (green), 2011 (red) and 2012 (blue) running [179].

and data-quality requirements the ATLAS dataset for 2012 corresponds to  $20.3 \text{ fb}^{-1}$ . Figure 7.1 shows the cumulative luminosity versus day delivered to ATLAS during the 2010, 2011, and 2012 runs.

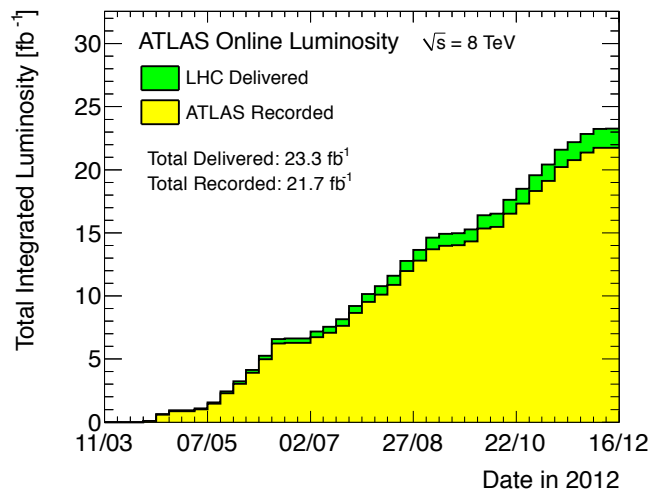


Figure 7.2: Cumulative luminosity versus week delivered to (green), and recorded by ATLAS (yellow) during stable beams and for 8 TeV centre-of-mass energy [179].

The luminosity delivered and recorded by ATLAS during the 2012 run alone is shown in Figure 7.2. This highlights the excellent performance of the ATLAS detector through-

out the run; 87% of the data recorded was suitable for analysis. The peak instantaneous luminosity delivered to ATLAS during stable beams in p-p collisions in 2010, 2011 and the 2012 is shown in Figure 7.3. The instantaneous luminosity in the 2012 run was almost double that in 2011, and this, along with increased pile-up, led to increased trigger rates which had to be managed. In order to keep the thresholds for un-prescaled trigger items low, for, say, inclusive lepton triggers, additional criteria such as isolation requirements had to be optimised.

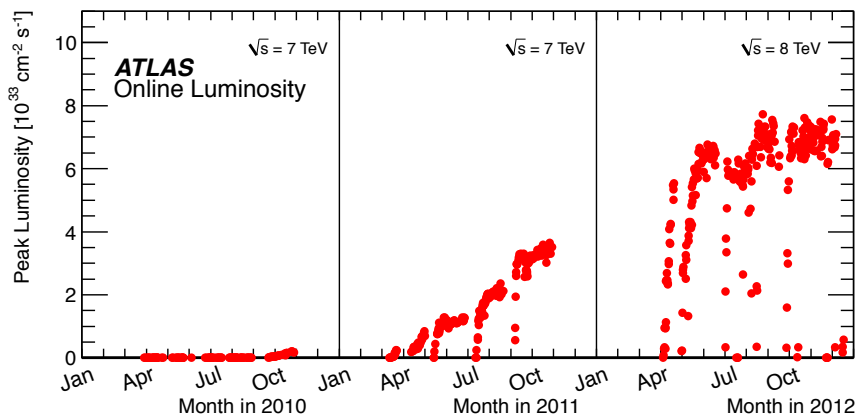


Figure 7.3: The peak instantaneous luminosity delivered to ATLAS per day versus time during the p-p runs of 2010, 2011 and 2012 [179].

### 7.2.3 Higher pile-up

The level of pile-up increased significantly in the 2012 run, providing an increased challenge for object reconstruction and the trigger system. Figure 7.4 shows the luminosity weighted distribution of the mean number of interactions per bunch crossing ( $\langle \mu \rangle$ ) for the 2011 and 2012 datasets. The distribution for the 2012 dataset extends to very high values of  $\langle \mu \rangle$ . As an illustration of the challenges posed by pile-up, Figure 7.5 shows an ATLAS event display for a candidate  $Z$  boson event in the di-muon decay channel with 25 reconstructed vertices. To deal with such challenging environments, reconstruction and identification algorithms for physics objects were optimised to be approximately independent of pile-up and in particular the impact of pile-up on the  $E_T^{\text{miss}}$  (which is essential for most new physics searches) was investigated extensively. Flexibility in the ATLAS computing model made it possible to accommodate the increases in trigger rates and event sizes, as well as increased physics and analysis demands.

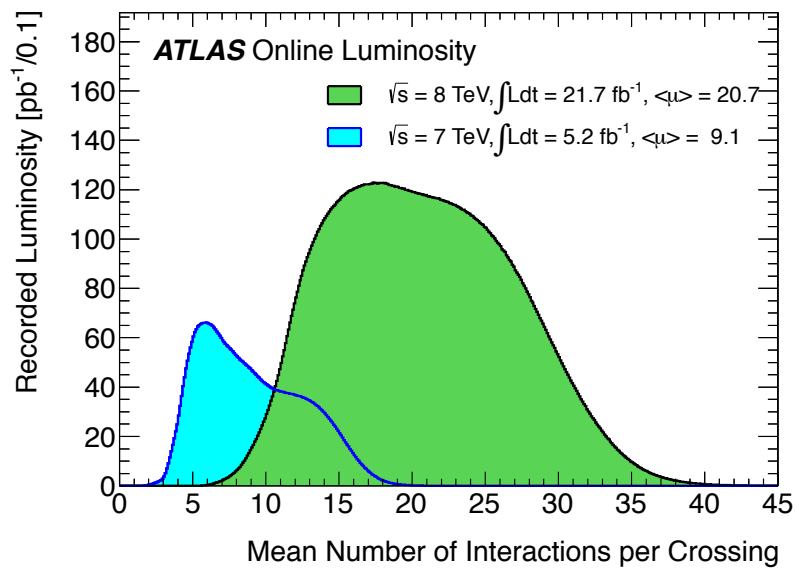


Figure 7.4: The luminosity-weighted distribution of the mean number of interactions per crossing for the 2011 and 2012 data. This shows the full 2011 and 2012  $pp$  runs. The integrated luminosities and the mean  $\mu$  values are given in the figure. The mean number of interactions per crossing corresponds to the mean of the poisson distribution on the number of interactions per crossing calculated for each bunch [179].

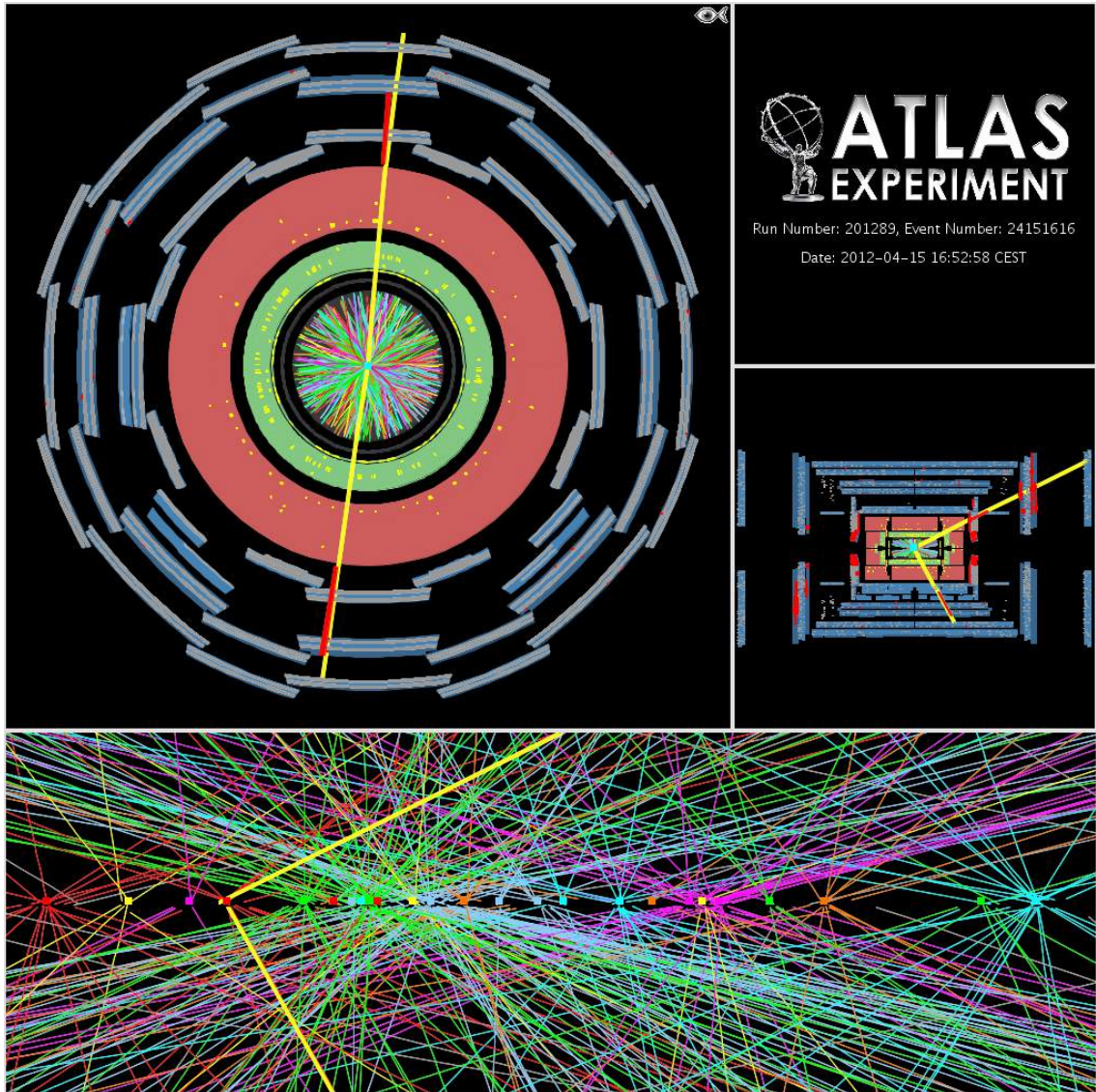


Figure 7.5: A candidate  $Z$  boson event in the di-muon decay channel with 25 reconstructed vertices. This event was recorded on April 15th 2012 and demonstrates the high pile-up environment in 2012 running. For this display the track  $p_T$  threshold is 0.4 GeV and all tracks are required to have at least 3 Pixel and 6 SCT hits [180].

## 7.3 Extending the sensitivity of the $m_{T2}$ -based search

### 7.3.1 Introduction

This section presents the first 2-lepton analysis using the full 2012 dataset to search for electroweak production in the case that sleptons are also light. It was published in [5]. The dataset used corresponded to  $20.3 \text{ fb}^{-1}$  of data at  $\sqrt{s} = 8 \text{ TeV}$ . The analysis was intended to provide an initial quickly available result for the 2012 dataset, which would be followed by a more extensive subsequent analysis including more signal regions and targeting more processes (at time of writing this has yet to be published). It only considered two signal regions, both based on the  $m_{T2}$  variable, and targeted only chargino-pair production and slepton-pair production. The  $m_{T2}$  variable was chosen to define the signal regions as it was the  $m_{T2}$ -based signal region which provided most sensitivity to electroweak processes in the analysis on 2011 data discussed in Chapter 6.

As in the previous chapter, this analysis was a collaborative effort within ATLAS. The author was responsible for the re-optimisation of the signal regions and for performing the final fits for the background expectations and exclusion limits. Unless stated, all results and work presented in this section are the work of the author.

The discussion in this section will focus on the improvements relative to the 2011 analysis and the results obtained. The object definitions used for the 2012 analysis [5] were close to those presented in Section 6.3 but were updated to follow the official ATLAS Supersymmetry group recommendations at the time the analysis was performed, which included any modifications required for using 8 TeV data instead of 7 TeV data. The isolation criteria applied to “signal leptons” were tightened to provide additional discrimination over background events. The trigger strategy was the same as in the 2011 analysis. That is to say trigger re-weighting was performed on Monte Carlo samples whereas signal leptons in data events were required to match the trigger objects. Regions of phase space were again defined to simplify the re-weighting procedure, and in each region either di-lepton or single-lepton triggers were used so as to maximise the signal efficiency. The systematic uncertainties considered in the analysis were also the same as those described in Section 6.6 for the 2011 analysis, so will not be described again in this chapter.

The Monte Carlo samples used for the background samples are also detailed in [5]. Changes with respect to the generators used in the 2011 analysis include the use of

MC@NLO to model the  $t\bar{t}$  background (instead of POWHEG), and POWHEG to model the diboson backgrounds (Herwig and Sherpa were used previously). Additional gluon-gluon contributions to the diboson backgrounds were also included in the 2012 analysis, which were simulated using gg2WW [181] and gg2ZZ [182]. The analysis also considered a Standard Model Higgs with  $m_H = 125$  GeV as part of the Standard Model background. Samples for Standard Model Higgs boson production through gluon fusion, vector-boson fusion and associated Higgs production ( $WH$  and  $ZH$ ) were generated using PYTHIA [149]. The signal grids used to model chargino-pair and slepton-pair production were 8 TeV versions of the grids described in Sections 6.2 and Section 5.4.2 respectively. The signal grids had to be extended to include higher sparticle masses as the sensitivity of searches increased, and in addition the granularity of the simplified model grid for slepton-pair production was increased.

The discussion of the analysis will proceed as follows. Firstly the re-optimisation of the signal regions will be discussed in Section 7.3.2. This will include a discussion of the improved jet veto definition used in 2012, as well as the choice of signal regions. The improved background estimation techniques will be presented in Section 7.3.3, and the results of the analysis will then be presented in Section 7.3.6. The interpretation of the results for slepton-pair and chargino-pair production will then be discussed in Sections 7.3.7 and 7.3.7 respectively.

### 7.3.2 Re-optimisation

Before optimising the signal region(s) for this analysis the definition of the jet veto was revisited. In the 2011 analysis, signal jets were defined as having  $p_T > 30$  GeV and  $|\eta| < 2.5$  as well as  $JVF > 0.75$ . This aimed to suppress the  $t\bar{t}$  background whilst avoiding veto-ing signal events containing pile-up jets. Despite this, as can be seen in Table 6.16 (which gives the results of the background estimates for the 2011 signal regions), the  $t\bar{t}$  background still had a significant contribution in SR- $m_{T2}$ , amounting to 40-60% of the total background, depending on the channel.

In the 2012 analysis additional categories of jets were defined, with the aim of complementing the original veto on “central” jets ( $|\eta| < 2.4$ ) with additional vetoes on “forward” ( $2.4 < |\eta| < 4.5$ ) and  $b$ -tagged jets. The JVf cut value for central jets was also revisited for 2012 data. Based on recommendations from performance groups in ATLAS, and an optimisation study on possible jet veto definitions (which was performed by another analyser) the following jet categories were defined. “Central light-flavour”

jets have  $p_T > 20$  GeV and  $|\eta| < 2.4$ , and do not satisfy the  $b$ -jet identification criteria (the 80% working point of the MV1 algorithm [41] was chosen). If a central light jet has  $20 \text{ GeV} < p_T < 50 \text{ GeV}$ , it must also required satisfy  $|JVF| > 0$ . This is equivalent to requiring that if the jet has charged tracks associated with it, at least one track must originate from the primary vertex. “Central  $b$ -jets” have  $p_T > 20$  GeV,  $|\eta| < 2.4$  and are tagged as  $b$ -jets by the  $b$ -tagging algorithm. Forward jets are defined as having  $p_T > 30$  GeV and  $2.4 < |\eta| < 4.5$ . A higher  $p_T$  cut was used for forward jets as the JVF requirement could not be used in the forward region to reject pile-up jets (it requires tracking information so can only be defined for  $|\eta| < 2.5$ .) The jet veto definition then vetoed events with jets satisfying any of these three categories.

When considering possible signal region selections the  $Z_N$  variable (as introduced in Section 5.4) was used as a measure of expected significance, with the background estimates taken directly from Monte Carlo, assuming a systematic uncertainty on the background estimates of 30% (this was increased relative to the optimisation studies in Section 5.4 to provide a conservative estimate of the sensitivity). Optimisation was performed on the 8 TeV direct slepton simplified model grid. As in Section 5.4 optimisation was performed by requiring two same-flavour opposite-sign leptons ( $e^\pm e^\mp$  or  $\mu^\pm \mu^\mp$ ), applying the jet veto (as defined above), and vetoing events where the di-lepton invariant mass lies inside the  $Z$ -mass window ( $|m_{ll} - m_Z| > 10$  GeV, with  $m_Z = 91.2$  GeV), then scanning through possible values of cuts on  $E_T^{\text{miss,rel}}$  and  $m_{T2}$ .  $Z_N$  distributions for a scan over possible  $m_{T2}$  cuts are shown in Figure 7.6 for a cut on  $E_T^{\text{miss,rel}}$  at 40 GeV, Figure 7.7 for a  $E_T^{\text{miss,rel}}$  cut of 60 GeV and Figure 7.8 for a cut on  $E_T^{\text{miss,rel}}$  of 80 GeV.

As observed in Section 5.4 value of the  $E_T^{\text{miss,rel}}$  cut has little impact on the expected sensitivity, as most of the background rejection comes from the  $m_{T2}$  cut. It was therefore decided to use the 40 GeV cut on  $E_T^{\text{miss,rel}}$  to allow for the possibility that background estimation techniques could be kept the same as in 2011. In the analysis on 2011 data a single  $m_{T2}$  cut was chosen to define SR- $m_{T2}$ , that was chosen to give the best expected sensitivity across the grid. For the 2012 analysis two signal regions were chosen, named “SR- $m_{T2,90}$ ” and “SR- $m_{T2,110}$ ”, with cuts on  $m_{T2}$  at 90 GeV and 110 GeV respectively. When calculating exclusion limits these were combined by taking the  $CL_s$  value for each point from the signal region with the best expected sensitivity (they are not mutually exclusive so cannot be combined statistically). SR- $m_{T2,90}$  had better expected sensitivity for lower mass splittings between the slepton and neutralino masses while SR- $m_{T2,110}$  had more sensitivity to signal points at higher slepton mass.

The hard cuts on  $m_{T2}$  that define the signal regions strongly suppress the Standard

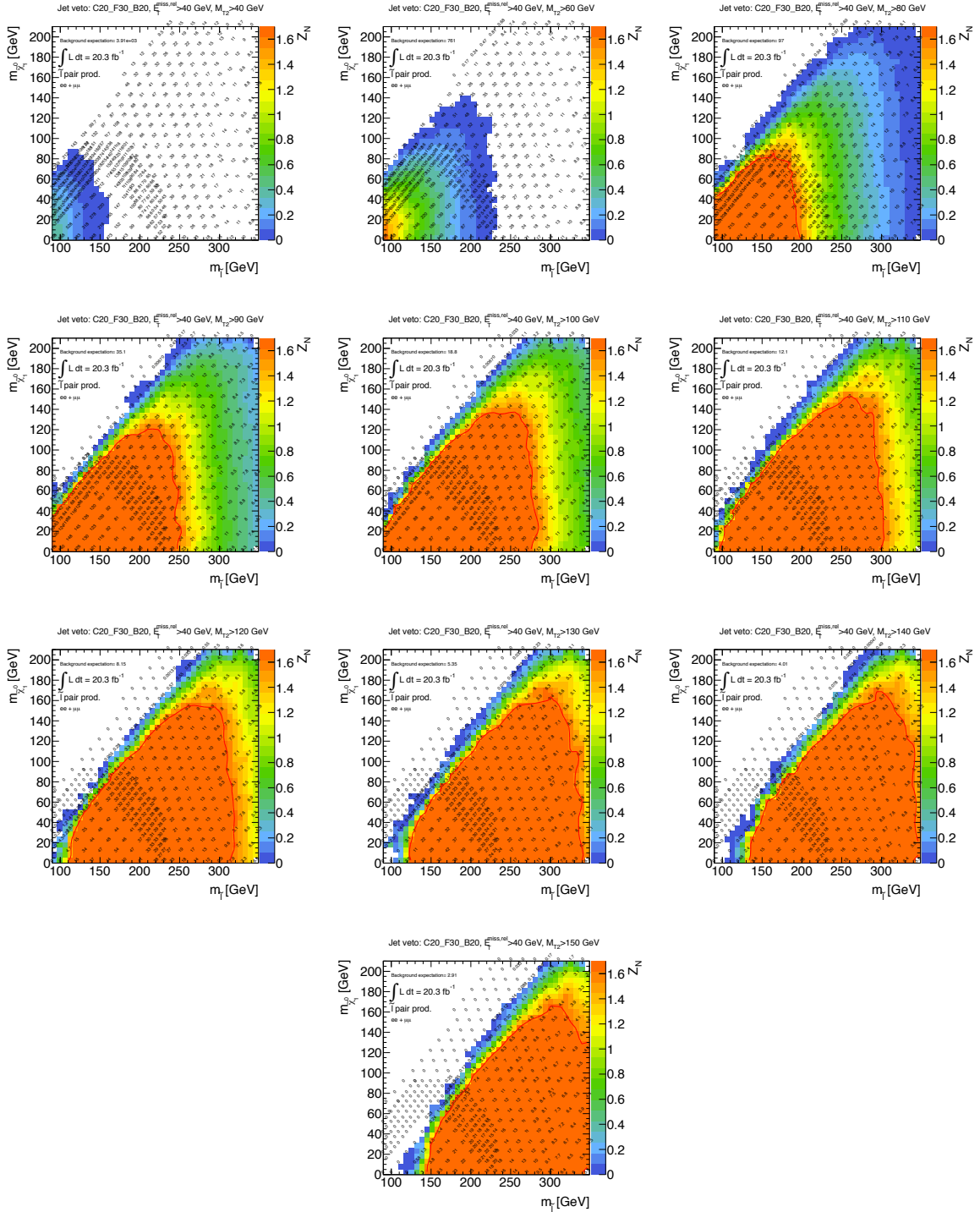


Figure 7.6: Optimisation plots for possible  $m_{T2}$ -based signal regions to target direct slepton production with  $20.3 \text{ fb}^{-1}$  of data at  $\sqrt{s} = 8 \text{ TeV}$ . All signal regions considered have a  $E_T^{\text{miss,rel}}$  cut at 40 GeV. The numbers displayed on the grid points give the signal yields for the cuts considered, normalised to  $20.3 \text{ fb}^{-1}$ . The solid contours indicate the expected 95% CL exclusion, which corresponds to  $Z_N = 1.64$ . The cuts defining each signal region are written above the plots. (C20\_F30\_B20 refers to the jet veto defined by the three categories of jet described in the text.)

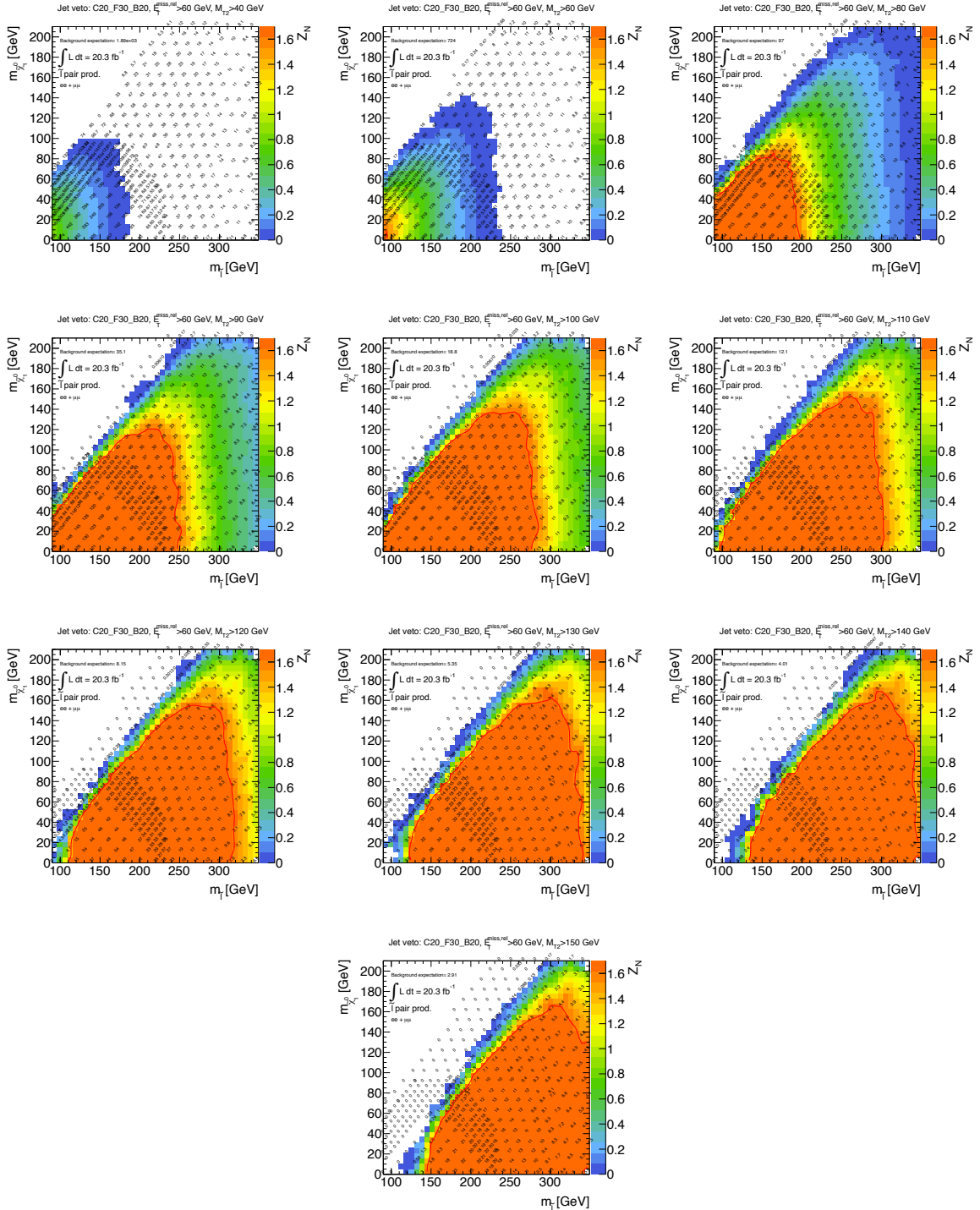


Figure 7.7: Optimisation plots for possible  $m_{T2}$ -based signal regions to target direct slepton production with  $20.3 \text{ fb}^{-1}$  of data at  $\sqrt{s} = 8 \text{ TeV}$ . All signal regions considered have a  $E_T^{\text{miss,rel}}$  cut at 60 GeV. The numbers displayed on the grid points give the signal yields for the cuts considered, normalised to  $20.3 \text{ fb}^{-1}$ . The solid contours indicate the expected 95% CL exclusion, which corresponds to  $Z_N = 1.64$ . The cuts defining each signal region selection are written above the plots. (C20\_F30\_B20 refers to the jet veto defined by the three categories of jet described in the text.)

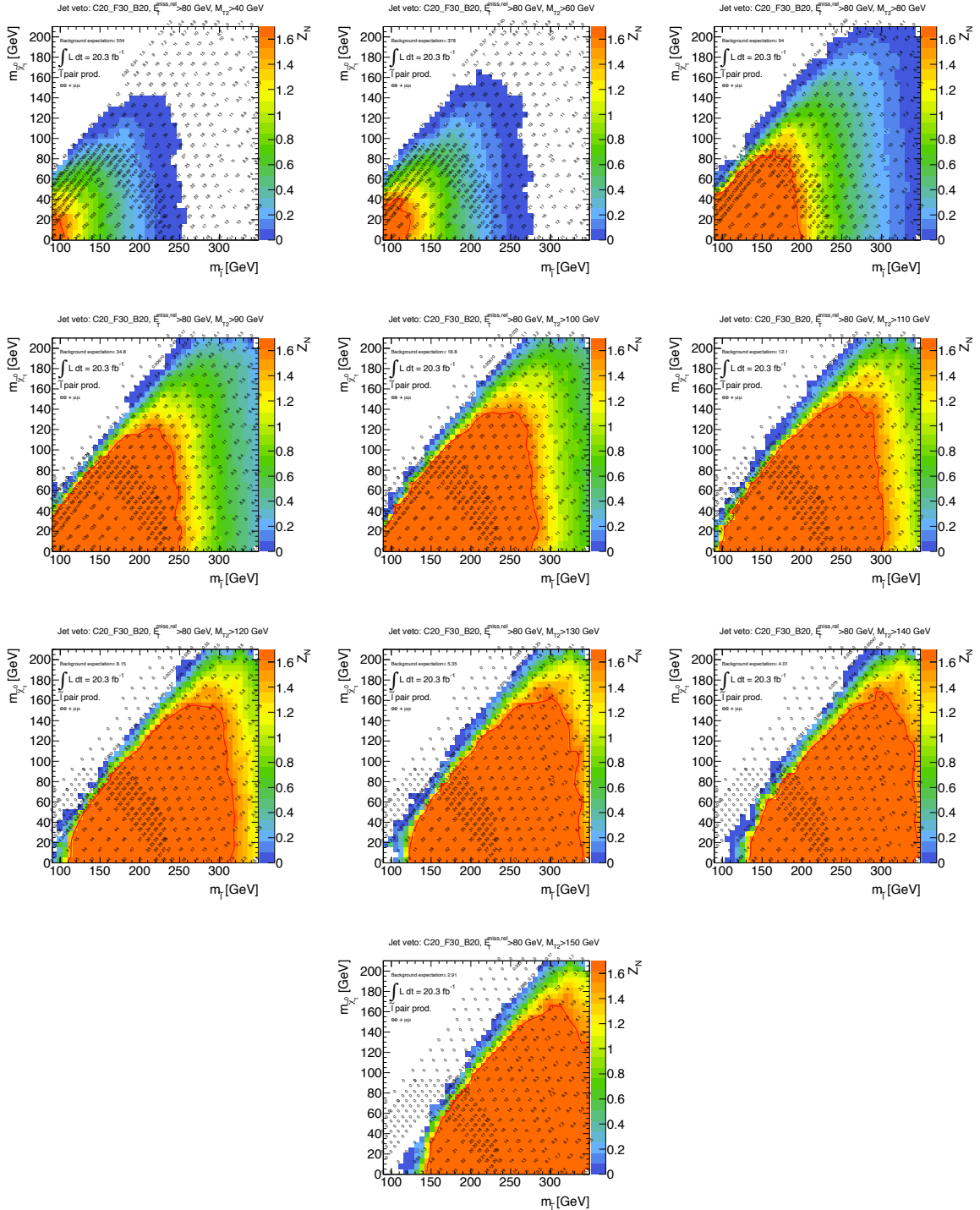


Figure 7.8: Optimisation plots for possible  $m_{T2}$ -based signal regions to target direct slepton production with  $20.3 \text{ fb}^{-1}$  of data at  $\sqrt{s} = 8$  TeV. All signal regions considered have a  $E_T^{\text{miss,rel}}$  cut at 80 GeV. The numbers displayed on the grid points give the signal yields for the cuts considered, normalised to  $20.3 \text{ fb}^{-1}$ . The solid contours indicate the expected 95% CL exclusion, which corresponds to  $Z_N = 1.64$ . The cuts defining each signal region selection are written above the plots. (C20\_F30\_B20 refers to the jet veto defined by the three categories of jet described in the text.)

Model backgrounds, thus allowing sensitivity to models where the signal distribution extends beyond the cut. This is illustrated in Figure 7.9, which shows the  $m_{T2}$  distributions evaluated using Monte Carlo in the previously defined “SR-pre- $m_{T2}$ ” (events must satisfy all cuts in the signal regions but the final  $m_{T2}$  cuts are not applied) for the  $e^\pm e^\mp$  and  $\mu^\pm \mu^\mp$  channels. Several signal points are overlaid. The signal model with a slepton mass of 165 GeV and a neutralino mass of 125 GeV has a small mass splitting and the  $m_{T2}$  distribution falls before the 90 GeV cut. This highlights the limitations of the analysis close to the diagonal.

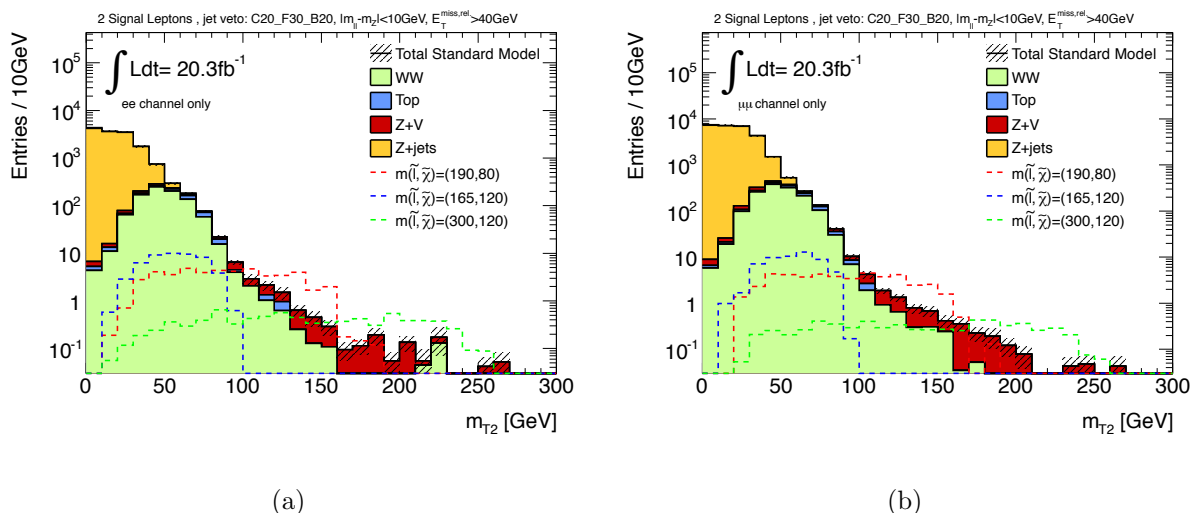


Figure 7.9:  $m_{T2}$  distributions for Monte Carlo events satisfying the “SR-pre- $m_{T2}$ ” selection at  $\sqrt{s} = 8$  TeV, normalised to  $20.3 \text{ fb}^{-1}$ , in (a) the di-electron and (b) the di-muon channel. Several signal points for the direct slepton simplified model grid are overlaid.

### 7.3.3 Background estimation techniques

One main improvement to the analysis on 2012 data relative to the 2011 analysis discussed in Chapter 6 was in the background estimation techniques. This exploited the capability of the likelihood fit to perform simultaneous fits of nuisance parameters across all signal regions and control regions defined in an analysis (as described in Section 4.3.2). For the 2011 analysis the data driven background estimates were calculated explicitly by hand and then input to the `HistFitter` package, that was used to calculate limits. The data driven estimates had to be calculated successively, i.e. the normalisation from the top control region had to be extrapolated to give a data-driven estimate of the top

contamination in the  $WW$  control region, so that the correct normalisation of the  $WW$  background could be extrapolated, and so on. This approach was less sophisticated, and more time consuming, than fitting all backgrounds simultaneously. By including the normalisation of background components as nuisance parameters in the fit, it allowed, for example, the contamination of the  $Z$ +jets background in the  $WW$  control region, to be handled in a consistent way. For the 2012 analysis, the simultaneous fitting technique was used to give the background expectations used for computing the final limits, however data-driven estimates were still calculated explicitly by hand, as in Chapter 6, to provide a cross check.

The groupings of the Standard Model background components were also changed. In the 2011 analysis the Standard Model background components were split into four components: the top background (comprising  $t\bar{t}$  and  $Wt$  single top production), the  $WW$  background, the  $Z+X$  background (comprising  $Z$ +jets,  $WZ$  and  $ZZ$ ) and the fake lepton background. For the  $m_{T2}$ -based signal region, the  $WW$  background was taken from Monte Carlo whilst the other backgrounds were data driven. For the 2012 analysis the  $Z+X$  background was split into two separate components; the “ $ZV$ ” background, where the “ $V$ ” refers to vector boson ( $W$  or  $Z$ ), and the  $Z$ +jets background. This motivation for this can be seen by referring back to Figure 6.13 in Chapter 6. The  $Z+X$  contribution to the  $Z+X$  control region for SR- $m_{T2}$  was dominated by the  $Z$ +jets component, whereas in Figure 6.20 it can be seen that, once the cut on  $m_{T2}$  at 90 GeV was applied, the signal region was dominated by the diboson component, which comprised  $WW$ ,  $WZ$  and  $ZZ$ . To illustrate further, Table 7.1 gives Monte Carlo estimates for the nominal signal region counts for SR- $m_{T2}$  in the 2011 analysis (these are the same as those in Tables 6.9, 6.10 and 6.11 but with the diboson contribution decomposed into separate components). The  $ZZ$  and  $WZ$  components are greater than the  $Z$ +jets contributions.

To summarise, by defining a  $Z+X$  control region for SR- $m_{T2}$  that requires an invariant mass inside the  $Z$ -mass window and  $E_T^{\text{miss,rel}} > 40$  GeV, the control region is dominated by the  $Z$ +jets contribution, however the dominant  $Z+X$  contributions in the signal region come from  $ZZ$  and  $WZ$ . By grouping them together as one background component, if a large scale factor were measured in the control region which is technically only representative of the  $Z$ +jets normalisation, it would then be applied to the  $ZZ$  and  $WZ$  backgrounds in the signal region, which could actually be well modelled by the Monte Carlo. It was therefore decided that for the 2012 analysis, if both background

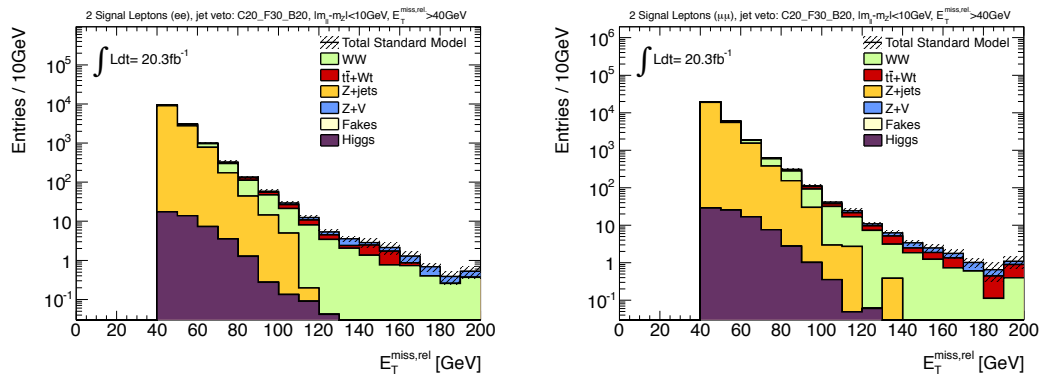
SR- $m_{T2}$	$e^\pm e^\mp$	$\mu^\pm \mu^\mp$	$e^\pm \mu^\mp$
$t\bar{t}$	1.44	3.27	4.12
Single top	0.67	0.68	0.68
$Z$ +jets	0.42	0.90	0.00
$WW$	2.29	3.48	4.84
$WZ$	1.10	1.05	0.22
$ZZ$	1.80	1.82	0.08
Fakes	1.03	0.05	1.14

Table 7.1: Composition of SR- $m_{T2}$  for the  $e^\pm e^\mp$ ,  $\mu^\pm \mu^\mp$  and  $e^\pm \mu^\mp$  channels in the 2011 analysis detailed in Chapter 6 as approximated by Monte Carlo only. Only the nominal counts are presented. The fake estimate is taken from the data-driven method and the “diboson” contributions are separated into  $WW$ ,  $WZ$  and  $ZZ$  components.

components ( $ZV$  and  $Z$ +jets) were to be data-driven then two separate control regions would be required. Apart from the  $Z + X$  background however, the other background groupings are as before.

When constructing the likelihood for the analysis, the main task was to decide which backgrounds to include in the fit and what control regions to use. This was done in collaboration with other analysers, who also provided data-driven estimates calculated explicitly per background component as a cross check. Since the control regions were included in the fit as single binned channels (i.e. shape information was not used), it was also necessary to verify that the shape of the variables defining the signal regions, i.e.  $E_T^{\text{miss,rel}}$  and  $m_{T2}$  were successfully modelled by the Monte Carlo. Distributions showing comparisons between data and Monte Carlo for these variables will be included in this section for each of the control regions discussed. In all distributions presented, the top,  $WW$  and  $ZV$  components of the Standard Model background are scaled by their normalisation factors from the simultaneous fit, and the fake background is evaluated using the matrix method (this was an improved implementation of the method described in Section 6.5, which was provided by another analyser). The only uncertainties included in the error band on the Monte Carlo distributions are statistical errors, and the error bars on the data are statistical poisson errors.

The main criterion when designing the background estimation strategy for the 2012 analysis was that the dominant backgrounds should be estimated using data-driven


 (a) Di-electron  $E_T^{\text{miss,rel}}$  in “SR-pre- $m_{T2}$ ”.

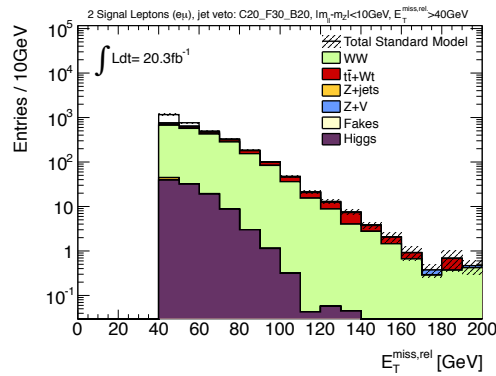
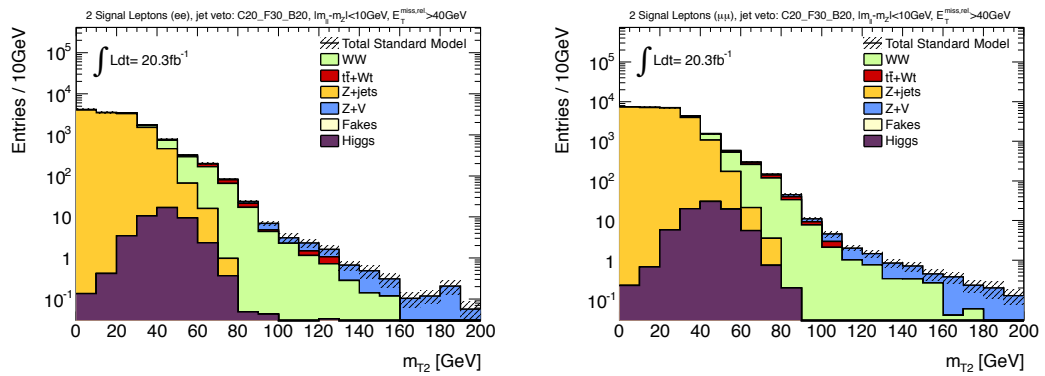
 (b) Di-muon  $E_T^{\text{miss,rel}}$  in “SR-pre- $m_{T2}$ ”.

 (c) Electron-muon  $E_T^{\text{miss,rel}}$  in “SR-pre- $m_{T2}$ ”.

Figure 7.10:  $E_T^{\text{miss,rel}}$  distributions for Monte Carlo events in “SR-pre- $m_{T2}$ ”, which corresponds to events satisfying all cuts in SR- $m_{T2,90}$  and SR- $m_{T2,110}$  but without the final requirements on  $m_{T2}$  applied, in the di-electron (a), di-muon (b) and electron-muon channels (c), normalised to  $20.3 \text{ fb}^{-1}$ .


 (a) Di-electron  $m_{T2}$  in “SR-pre- $m_{T2}$ ”.

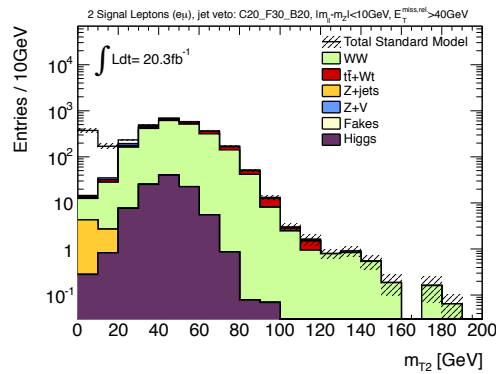
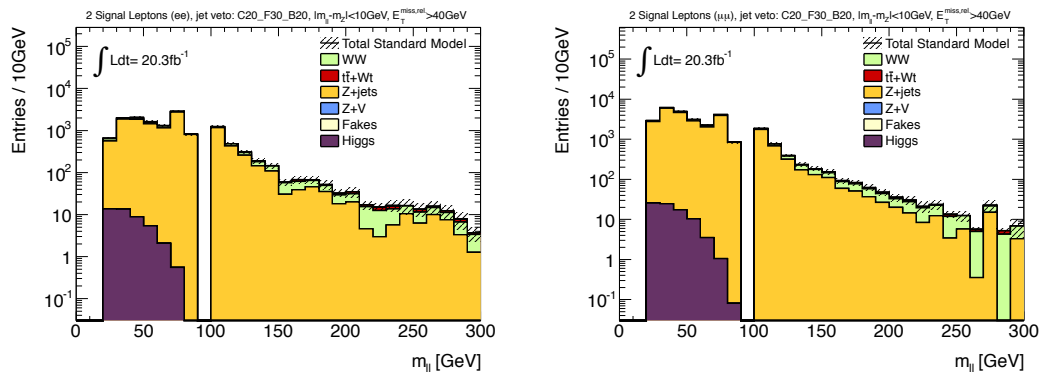
 (b) Di-muon  $m_{T2}$  in “SR-pre- $m_{T2}$ ”.

 (c) Electron-muon  $m_{T2}$  in “SR-pre- $m_{T2}$ ”.

Figure 7.11:  $m_{T2}$  distributions for Monte Carlo events in “SR-pre- $m_{T2}$ ”, which corresponds to events satisfying all cuts in SR- $m_{T2,90}$  and SR- $m_{T2,110}$  but without the final requirements on  $m_{T2}$  applied, in the di-electron (a), di-muon (b) and electron-muon channels (c), normalised to  $20.3 \text{ fb}^{-1}$ .


 (a) Di-electron  $m_{\ell\ell}$  in “SR-pre- $m_{T2}$ ”.

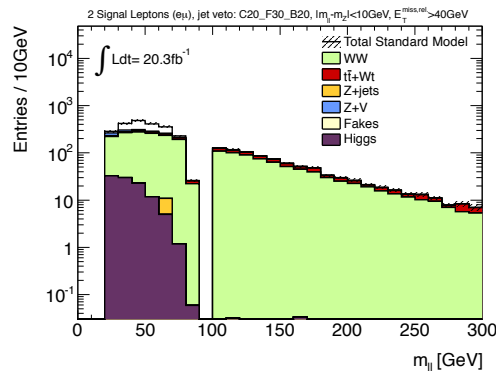
 (b) Di-muon  $m_{\ell\ell}$  in “SR-pre- $m_{T2}$ ”.

 (c) Electron-muon  $m_{\ell\ell}$  in “SR-pre- $m_{T2}$ ”.

Figure 7.12:  $m_{\ell\ell}$  distributions for Monte Carlo events in “SR-pre- $m_{T2}$ ”, which corresponds to events satisfying all cuts in SR- $m_{T2,90}$  and SR- $m_{T2,110}$  but without the final requirements on  $m_{T2}$  applied, in the di-electron (a), di-muon (b) and electron-muon channels (c), normalised to  $20.3 \text{ fb}^{-1}$ .

techniques. Figures 7.10, 7.11 and 7.12 show the  $E_T^{\text{miss,rel}}$ ,  $m_{T2}$  and  $m_{\ell\ell}$  distributions respectively, as evaluated by Monte Carlo, for the di-electron, di-muon and electron muon channels in “SR-pre- $m_{T2}$ ”, which has the same event selection as SR- $m_{T2,90}$  and SR- $m_{T2,110}$  but without the final cuts on  $m_{T2}$ . The  $m_{\ell\ell}$  distribution shows that  $Z$ +jets is the dominant background in SR-pre- $m_{T2}$  in the same flavour channels. Its contribution increased relative to 2011 data due to the increased pile-up, however it can be seen in the  $m_{T2}$  distribution that at high  $m_{T2}$  (as in the signal regions) it is a minor background. The dominant backgrounds at high  $m_{T2}$  come from the  $ZV$ , top, and  $WW$  backgrounds, therefore these backgrounds were evaluated using data-driven methods.

Table 7.2 summarises the background estimation techniques used for each background component. For the data-driven backgrounds, the relevant control regions are defined in Table 7.3. The fake lepton background was again calculated using the matrix method (as mentioned above). The  $Z$ +jets background is small in the signal regions so was taken from Monte Carlo. The  $Z \rightarrow \tau\tau$  background was treated separately to  $Z$ +jets and the  $ZV$  background and was taken directly from Monte Carlo. The “Higgs” background was also included as a Standard Model background, and its impact on the fit will be discussed later in this section. The Monte Carlo samples generated (detailed in [5]) assumed a Standard Model Higgs boson with a mass  $m_H = 125$  GeV. The control regions defined for the top,  $ZV$  and  $WW$  backgrounds will now be discussed in more detail, with an emphasis on the choice of control region, and how they were included in the fit.

Background	$e^\pm e^\mp$ or $\mu^\pm \mu^\mp$		$e^\pm \mu^\mp$	
	Method	CR	Method	CR
$WW$	DD	$WW$ CR	DD Sec	$WW$ CR
$t\bar{t} + Wt$	DD	Top CR	DD	Top CR
$WZ + ZZ$	DD	$ZV$ CRa, $ZV$ CRb	MC	–
$Z$ +jets	MC	–	MC	–
$Z \rightarrow \tau\tau$	MC	–	MC	–
Fake leptons	DD	Matrix method	DD	Matrix method
Higgs	MC	–	MC	–

Table 7.2: Summary of the methods and control regions used to in the analysis on 2012 data to estimate each background source. DD stands for data-driven method.

Signal region	SR- $m_{T2,90}$	SR- $m_{T2,110}$
WW CR lepton flavour $m_{\ell\ell}$ $E_T^{\text{miss,rel}}$ $m_{T2}$	$e^\pm \mu^\mp$ $ m_{\ell\ell} - m_Z  > 10 \text{ GeV}$ $> 40 \text{ GeV}$ 50–90 GeV	
Top CR $b$ -tagged jets signal jets lepton flavour $m_{\ell\ell}$ $E_T^{\text{miss,rel}}$ $m_{T2}$	$\geq 1$ $\geq 2$ $e^\pm e^\mp, \mu^\pm \mu^\mp, e^\pm \mu^\mp$ $ m_{\ell\ell} - m_Z  > 10 \text{ GeV}$ $> 40 \text{ GeV}$ —	
ZV CR lepton flavour $m_{\ell\ell}$ $E_T^{\text{miss,rel}}$ $m_{T2}$	$e^\pm e^\mp, \mu^\pm \mu^\mp$ $ m_{\ell\ell} - m_Z  < 10 \text{ GeV}$ $> 40 \text{ GeV}$	
	$> 90 \text{ GeV}$	$> 110 \text{ GeV}$

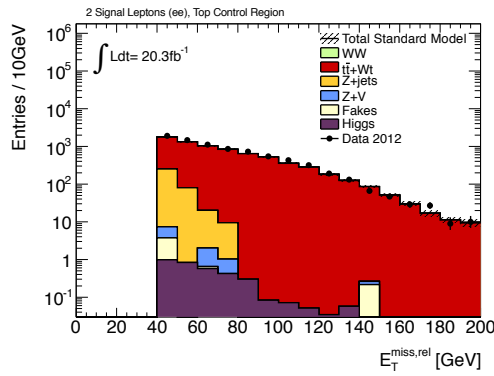
Table 7.3: Control regions defined for the 2012 analysis.

## Top background

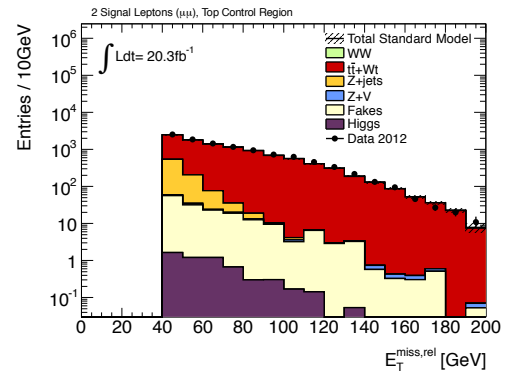
Apart from the updated definitions for “central light”, “central  $b$ -” and “forward-” jets, the top control region for both SR- $m_{T2,90}$  and SR- $m_{T2,110}$  was defined as in the 2011 analysis (see Section 6.5). However when performing the simultaneous fit, only the electron-muon channel was used. This channel contained less contamination from the  $Z$ +jets background, as demonstrated in Table 7.4, which gives the composition of the top control region in all channels, as given by Monte Carlo (except for the fake lepton background which is calculated using the matrix method). It is also visible in Figures 7.13 and 7.14, which give the distributions of  $E_T^{\text{miss,rel}}$  and  $m_{T2}$  respectively, in the top control region, for the three lepton flavour channels. In addition these distributions demonstrate that the shapes of the  $E_T^{\text{miss,rel}}$  and the  $m_{T2}$  distributions were well modelled by the data, which is essential for the method to be valid. As with the 2011 analysis, when explicitly calculating the data driven estimates, the counts in “SR-pre- $m_{T2}$ ” were calculated then the  $m_{T2}$  efficiencies from Monte Carlo applied to give the signal region estimates.

Top CR	$e^\pm e^\mp$	$\mu^\pm \mu^\mp$	$e^\pm \mu^\mp$
Observed events	7905	10715	14578
Total Standard Model	$7361.91 \pm 1765.07$	$10307.51 \pm 2368.29$	$13733.69 \pm 3418.08$
Top	$6923.20 \pm 1760.96$	$9320.67 \pm 2359.17$	$13480.34 \pm 3416.63$
$WW$	$45.17 \pm 8.32$	$59.47 \pm 10.07$	$83.04 \pm 14.29$
$Z$ +jets	$355.39 \pm 98.71$	$725.57 \pm 186.63$	$0.00 \pm 0.00$
$ZV$	$9.83 \pm 2.10$	$11.75 \pm 2.12$	$8.25 \pm 1.42$
$Z \rightarrow \tau\tau$	$24.88 \pm 14.95$	$20.37 \pm 15.43$	$33.81 \pm 14.68$
Higgs	$3.45 \pm 0.62$	$5.79 \pm 0.89$	$8.36 \pm 1.18$
Fakes	$0.00 \pm 0.00$	$163.89 \pm 55.60$	$119.88 \pm 64.47$

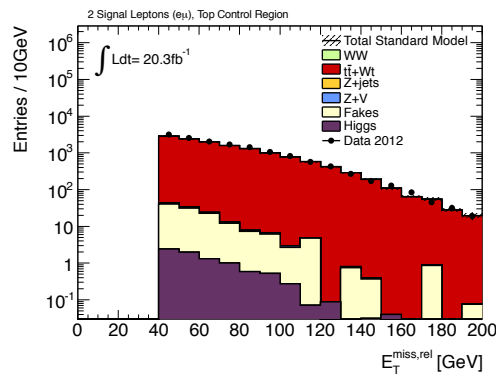
Table 7.4: Nominal Monte Carlo estimates for the top control region used in the 2012 analysis, in the  $e^\pm e^\mp$ ,  $\mu^\pm \mu^\mp$  and  $e^\pm \mu^\mp$  channels, normalised to an integrated luminosity of  $20.3 \text{ fb}^{-1}$ . The errors shown are the statistical plus systematic uncertainties (with the exception of uncertainties related to the choice of Monte Carlo generators used, which were only applied to the signal estimates).



(a) Di-electron OS  $E_T^{\text{miss,rel}}$  in the top control region.

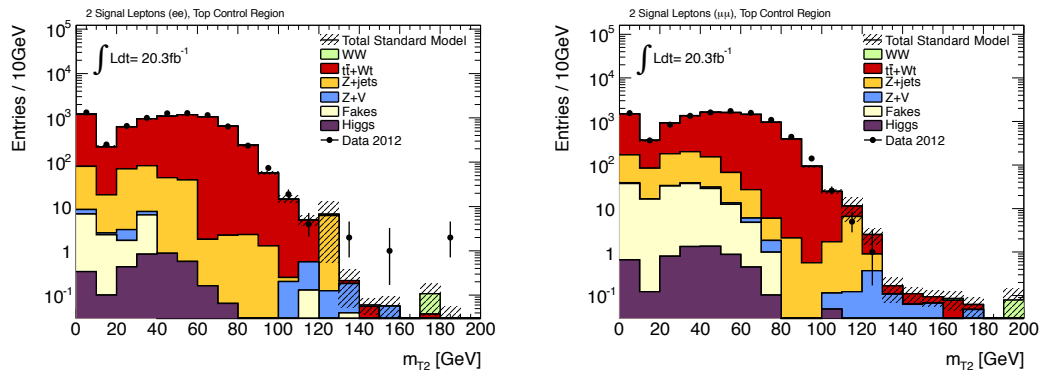


(b) Di-muon OS  $E_T^{\text{miss,rel}}$  in the top control region.



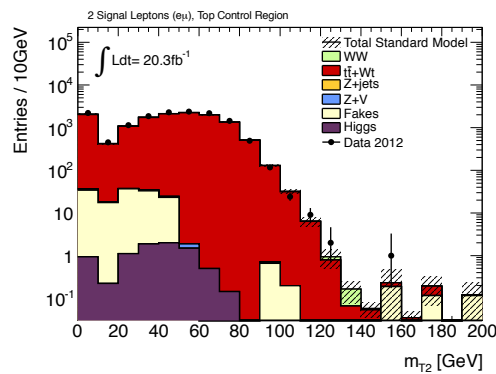
(c) Electron-muon OS  $E_T^{\text{miss,rel}}$  in the top control region.

Figure 7.13: Comparison between data and Monte Carlo for the  $E_T^{\text{miss,rel}}$  distributions of events in the top control region, in the di-electron (a), di-muon (b) and electron-muon channels (c), for  $20.3 \text{ fb}^{-1}$  of data at  $\sqrt{s} = 8 \text{ TeV}$ .



(a) Di-electron OS  $m_{T2}$  in the top control region.

(b) Di-muon OS OS  $m_{T2}$  in the top control region.



(c) Electron-muon OS  $m_{T2}$  in the top control region.

Figure 7.14: Comparison between data and Monte Carlo for the  $m_{T2}$  distributions of events in the top control region, in the di-electron (a), di-muon (b) and electron-muon channels (c), for  $20.3 \text{ fb}^{-1}$  of data at  $\sqrt{s} = 8 \text{ TeV}$ .

### *ZV* background

As can be seen in Figure 7.11, for the same flavour channels the *ZV* contribution is a significant background. The control regions for SR- $m_{T2,90}$  and SR- $m_{T2,110}$  were defined as having the same cuts as the signal regions but with the *Z*-veto reversed. For the explicit data driven calculation, the scale factor was calculated as detailed in Equation (6.3) of Section 6.5 but with the updated control region definition and without including *Z*+jets contribution (except for as a “non-*ZV* contribution”). For the data-driven calculation transfer factors were calculated separately for the di-electron and di-muon channels, however when including the control region in the simultaneous fit both channels were added as separate channels in the fit and the output gave one normalisation factor for the *ZV* background. This is the only case where the simultaneous fit and the data-driven calculation were not in direct correspondence.

<i>ZV</i> CRa	$e^\pm e^\mp$	$\mu^\pm \mu^\mp$
Observed events	44	55
Total Standard Model	$42.96 \pm 6.16$	$50.18 \pm 7.81$
Top	$0.54^{+0.66}_{-0.54}$	$0.06^{+0.08}_{-0.06}$
<i>WW</i>	$1.81 \pm 0.31$	$2.39 \pm 0.45$
<i>Z</i> +jets	$0.00 \pm 0.00$	$0.00 \pm 0.00$
<i>ZV</i>	$40.57 \pm 6.07$	$47.72 \pm 7.67$
<i>Z</i> → $\tau\tau$	$0.00 \pm 0.00$	$0.00 \pm 0.00$
Higgs	$0.04 \pm 0.02$	$0.02^{+0.02}_{-0.02}$
Fakes	$0.00 \pm 0.00$	$0.00 \pm 0.00$

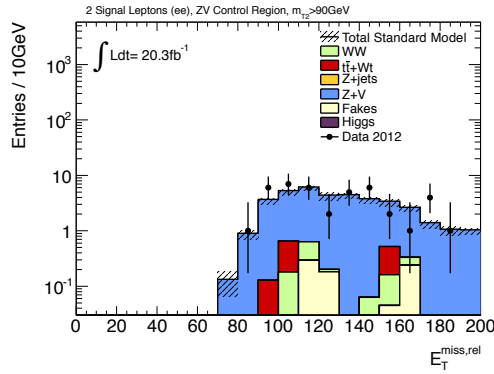
Table 7.5: Nominal Monte Carlo estimates for the *ZV* CRa region used in the 2012 analysis, in the  $e^\pm e^\mp$  and  $\mu^\pm \mu^\mp$  channels, normalised to an luminosity of  $20.3 \text{ fb}^{-1}$ . The errors shown are the statistical plus systematic uncertainties (with the exception of uncertainties related to the choice of Monte Carlo generators used, which were only applied to the signal estimates).

Tables 7.5 and 7.6 show the Monte Carlo estimates for the Standard Model background components for the *ZV* control regions for SR- $m_{T2,90}$  and SR- $m_{T2,110}$  respectively. In both cases, although the statistics in the control regions are low, the *ZV* background is dominant. Figure 7.15 shows the  $E_T^{\text{miss,rel}}$  distribution in the control regions in both

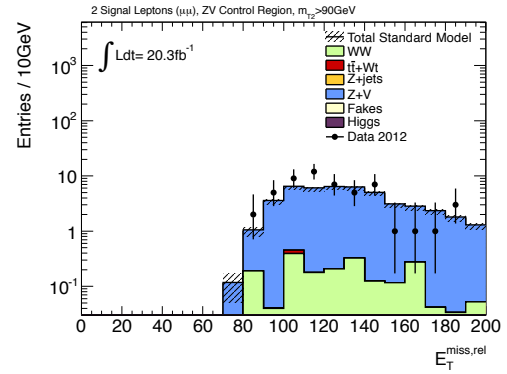
$ZV$ CRb	$e^\pm e^\mp$	$\mu^\pm \mu^\mp$
Observed events	22	28
Total Standard Model	$25.32 \pm 2.31$	$28.04 \pm 3.07$
Top	$0.00 \pm 0.00$	$0.00 \pm 0.00$
$WW$	$0.79 \pm 0.18$	$1.19 \pm 0.24$
$Z$ +jets	$0.00 \pm 0.00$	$0.00 \pm 0.00$
$ZV$	$24.47 \pm 2.24$	$26.84 \pm 2.97$
$Z \rightarrow \tau\tau$	$0.00 \pm 0.00$	$0.00 \pm 0.00$
Higgs	$0.02 \pm 0.01$	$0.01^{+0.01}_{-0.01}$
Fakes	$0.04^{+0.06}_{-0.04}$	$0.00 \pm 0.00$

Table 7.6: Nominal Monte Carlo estimates for the  $ZV$  CRb region used in the 2012 analysis, in the  $e^\pm e^\mp$  and  $\mu^\pm \mu^\mp$  channels, normalised to an luminosity of  $20.3 \text{ fb}^{-1}$ . The errors shown are the statistical plus systematic uncertainties (with the exception of uncertainties related to the choice of Monte Carlo generators used, which were only applied to the signal estimates).

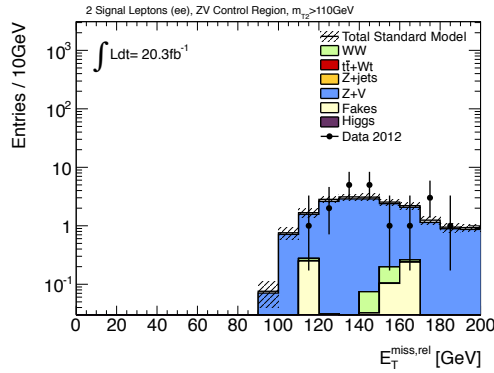
the di-electron and di-muon channels. Although the regions only have a cut on  $E_T^{\text{miss,rel}}$  at 40 GeV, the distributions are pushed towards higher  $E_T^{\text{miss,rel}}$  by the hard cuts on  $m_{T2}$  defining the control regions, as  $m_{T2}$  and  $E_T^{\text{miss,rel}}$  are correlated.



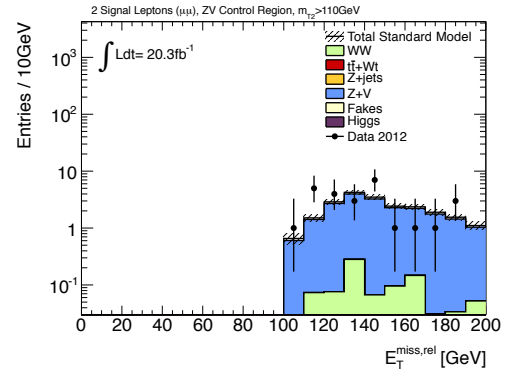
(a) Di-electron  $E_T^{\text{miss,rel}}$  in the  $ZV$  control region for  $\text{SR-}m_{T2,90}$ .



(b) Di-muon  $E_T^{\text{miss,rel}}$  in the  $ZV$  control region for  $\text{SR-}m_{T2,90}$ .



(c) Di-electron  $E_T^{\text{miss,rel}}$  in the  $ZV$  control region for  $\text{SR-}m_{T2,110}$ .



(d) Di-muon  $E_T^{\text{miss,rel}}$  in the  $ZV$  control region for  $\text{SR-}m_{T2,110}$ .

Figure 7.15: Comparison between data and Monte Carlo for the  $E_T^{\text{miss,rel}}$  distributions of events inside the  $Z$  peak ( $|m_{ll} - m_Z| < 10$  GeV) in the  $ZV$  control regions for  $\text{SR-}m_{T2,90}$  (top) and  $\text{SR-}m_{T2,110}$  (bottom), in the di-electron (left) and di-muon channels (right), for  $20.3 \text{ fb}^{-1}$  of data at  $\sqrt{s} = 8$  TeV.

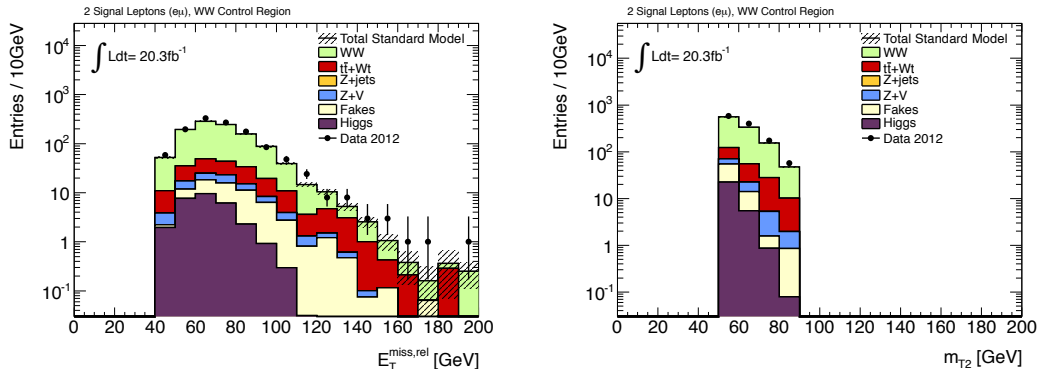
### ***WW* background**

The *WW* control region for both SR- $m_{T2,90}$  and SR- $m_{T2,110}$  had a  $E_T^{\text{miss,rel}}$  cut at 40 GeV and required  $50 \text{ GeV} < m_{T2} < 90 \text{ GeV}$ . Only the  $e^\pm \mu^\mp$  channel was included in the fit, and the data-driven calculation, because it had a lower contamination from the  $Z$ +jets (as can be seen in Figure 7.11). The  $m_{T2}$  range selected was chosen to select a *WW*-enriched sample, which can also be seen in Figure 7.11. The  $E_T^{\text{miss,rel}}$  and  $m_{T2}$  distributions in the *WW* control region are shown in Figure 7.16. Although there is no  $Z$ +jets contamination in the  $e^\pm \mu^\mp$  channel, there are contributions from top and  $ZV$ . The Monte Carlo predictions for the *WW* control region are presented in Table 7.7. Despite contamination from other Standard Model background, an advantage of evaluating the backgrounds using the simultaneous fit is that their respective high statistics control regions will fix the normalisation factor in the fit and so allow the contaminations in the *WW* control region to be evaluated correctly.

<i>WW</i> CR	$e^\pm e^\mp$	$\mu^\pm \mu^\mp$	$e^\pm \mu^\mp$
Observed events	662	1129	1213
Total Standard Model	$610.55 \pm 72.14$	$995.59 \pm 133.52$	$1096.05 \pm 106.30$
Top	$65.31 \pm 21.05$	$81.60 \pm 21.98$	$116.20 \pm 36.35$
<i>WW</i>	$407.61 \pm 29.34$	$662.86 \pm 54.63$	$879.54 \pm 67.10$
$Z$ +jets	$71.57 \pm 48.19$	$172.39 \pm 103.54$	$0.00 \pm 0.00$
$ZV$	$22.36 \pm 2.41$	$47.68 \pm 5.68$	$28.99 \pm 3.02$
$Z \rightarrow \tau\tau$	$0.00 \pm 0.00$	$0.00 \pm 0.00$	$0.00 \pm 0.00$
Higgs	$12.15 \pm 1.33$	$25.80 \pm 2.48$	$28.91 \pm 3.47$
Fakes	$31.56 \pm 10.43$	$5.27 \pm 3.00$	$42.41 \pm 11.49$

Table 7.7: Nominal Monte Carlo estimates for the *WW* control region used in the 2012 analysis, in the  $e^\pm e^\mp$ ,  $\mu^\pm \mu^\mp$  and  $e^\pm \mu^\mp$  channels, normalised to an integrated luminosity of  $20.3 \text{ fb}^{-1}$ . The errors shown are the statistical plus systematic uncertainties (with the exception of uncertainties related to the choice of Monte Carlo generators used, which were only applied to the signal estimates).

It can be seen in Figure 7.16 and Table 7.7 that the Higgs background has a non-negligible contribution to the *WW* control region, making up 1.99%, 2.59% and 2.64% of the total Standard Model background in the  $e^\pm e^\mp$ ,  $\mu^\pm \mu^\mp$  and  $e^\pm \mu^\mp$  channels respectively (note that only the  $e^\pm \mu^\mp$  channel is included in the fit). To quantify its impact,



(a) Electron-muon  $E_T^{\text{miss,rel}}$  in the  $WW$  control region.

(b) Electron-muon  $m_{T2}$  in the  $WW$  control region.

Figure 7.16: Comparison between data and Monte Carlo of the  $E_T^{\text{miss,rel}}$  (a) and  $m_{T2}$  (b) distributions for events in the  $WW$  control region, which is defined using the electron-muon channel only, for  $20.3 \text{ fb}^{-1}$  of data at  $\sqrt{s} = 8 \text{ TeV}$ .

Table 7.8 and Table 7.9 compare the output of the simultaneous fit (which will be described in Section 7.3.5) for the total signal region yields (i.e. the sum of the  $e^\pm e^\mp$ ,  $\mu^\pm \mu^\mp$  and  $e^\pm \mu^\mp$  channels) in  $\text{SR-}m_{T2,90}$  and  $\text{SR-}m_{T2,110}$ , with and without the Higgs background included respectively. Although the Higgs background makes a small contribution to the signal region counts itself (0.33 in  $\text{SR-}m_{T2,90}$  and 0.28 in  $\text{SR-}m_{T2,110}$ ), the  $WW$  contribution decreases by 2.89% in both signal regions when the Higgs contribution is added to the Standard Model background. This can be rationalised by considering the calculations performed to derive the data-driven estimates, as in Equation (6.3) of Section 6.5 (but with a different control region). The Higgs contribution adds to the “non- $WW$ ” component which is subtracted from the data count before calculating the  $WW$  estimate, so when the “non- $WW$ ” component increases the multiplying the transfer factor will decrease.

	SR- $m_{T2,90}$	SR- $m_{T2,110}$
Observed events	53	13
Fitted bkg events	$60.20 \pm 7.18$	$16.84 \pm 6.06$
Top	$8.76 \pm 3.84$	$1.21 \pm 0.96$
$WW$	$37.12 \pm 5.15$	$9.36 \pm 5.04$
$Z$ +jets	$0.00^{+0.01}_{-0.00}$	$0.00 \pm 0.00$
$ZV$	$14.32 \pm 3.09$	$6.26 \pm 3.24$
$Z \rightarrow \tau\tau$	$0.00 \pm 0.00$	$0.00 \pm 0.00$
Fakes	$0.00 \pm 0.00$	$0.00 \pm 0.00$

Table 7.8: Results of the background-only fit for SR- $m_{T2,90}$  and SR- $m_{T2,110}$  (for all lepton flavour channels), for an integrated luminosity of  $20.3 \text{ fb}^{-1}$ , without the Higgs contribution included as the Standard Model background. The errors shown are the statistical plus systematic uncertainties.

	SR- $m_{T2,90}$	SR- $m_{T2,110}$
Observed events	53	13
Total Standard Model	$59.53 \pm 7.03$	$16.81 \pm 5.94$
Top	$8.74 \pm 3.76$	$1.22 \pm 0.96$
$WW$	$36.05 \pm 5.01$	$9.09 \pm 4.90$
$Z$ +jets	$0.00^{+0.01}_{-0.00}$	$0.00 \pm 0.00$
$ZV$	$14.35 \pm 3.10$	$6.28 \pm 3.25$
$Z \rightarrow \tau\tau$	$0.00 \pm 0.00$	$0.00 \pm 0.00$
Higgs	$0.38 \pm 0.08$	$0.22 \pm 0.05$
Fakes	$0.00 \pm 0.00$	$0.00 \pm 0.00$

Table 7.9: Results of the background-only fit for SR- $m_{T2,90}$  and SR- $m_{T2,110}$  (for all lepton flavour channels), for an integrated luminosity of  $20.3 \text{ fb}^{-1}$ , with the Higgs contribution included as a Standard Model background. The errors shown are the statistical plus systematic uncertainties.

### 7.3.4 Results of the background estimation

Tables 7.10 and 7.11 present the background expectations for  $\text{SR-}m_{T2,90}$  and  $\text{SR-}m_{T2,110}$  respectively, based on three different methods. Firstly, background estimates as constrained by the simultaneous fit (which will be outlined in the next section) are presented. The counts based on pure Monte Carlo estimates are provided for comparison. It can be seen that the fit causes  $WW$ ,  $ZV$  and  $\text{top}$ , to be scaled up for  $\text{SR-}m_{T2,90}$ , whereas for  $\text{SR-}m_{T2,110}$  the  $ZV$  background is scaled down, whilst the others still have a scale factor greater than one. Finally, the results of the data driven calculations, that were calculated explicitly as in the 2011 analysis, but using the control regions defined in this section, are also shown. These were intended to provide a cross check for the results of the simultaneous fit. Allowing for uncertainties, the two sets of numbers are consistent. This cross check served as validation of the simultaneous fit technique, the results of which were then used to calculate the model independent limits and exclusion contours which will be presented in Sections 7.3.6 and Section 7.3.7.

Channel	$ee$	$e\mu$	$\mu\mu$	$all$
Observed	15	19	19	53
Simultaneous Fit Results				
$t\bar{t} + Wt$ (fitted)	$0.85^{+1.05}_{-0.85}$	$5.59 \pm 2.11$	$2.47 \pm 1.81$	$8.92 \pm 3.91$
$WW$ (fitted)	$9.33 \pm 1.57$	$14.10 \pm 2.18$	$12.63 \pm 1.94$	$36.06 \pm 5.12$
$ZV$ (fitted)	$6.34 \pm 1.46$	$0.78 \pm 0.25$	$7.25 \pm 1.67$	$14.37 \pm 3.19$
$Z$ +jets (MC-only)	$0.00 \pm 0.00$	$0.00 \pm 0.00$	$0.00^{+0.01}_{-0.00}$	$0.00^{+0.01}_{-0.00}$
$Z \rightarrow \tau\tau$ (MC-only)	$0.00 \pm 0.00$	$0.00 \pm 0.00$	$0.00 \pm 0.00$	$0.00 \pm 0.00$
Higgs (MC-only)	$0.11 \pm 0.04$	$0.19 \pm 0.05$	$0.08 \pm 0.04$	$0.38 \pm 0.08$
Fakes (DD)	$0.00^{+0.18}_{-0.00}$	$0.00^{+0.14}_{-0.00}$	$0.00^{+0.15}_{-0.00}$	$0.00^{+0.28}_{-0.00}$
Total	$16.63 \pm 2.31$	$20.66 \pm 3.23$	$22.44 \pm 3.32$	$59.73 \pm 7.34$
MC-only				
$t\bar{t} + Wt$	$0.80^{+0.98}_{-0.80}$	$5.26 \pm 1.96$	$2.30 \pm 1.68$	$8.35 \pm 3.62$
$WW$	$8.32 \pm 1.50$	$12.54 \pm 2.48$	$11.23 \pm 2.11$	$32.09 \pm 5.68$
$ZV$	$5.98 \pm 1.23$	$0.73 \pm 0.22$	$6.82 \pm 1.56$	$13.53 \pm 2.81$
$Z$ +jets	$0.00 \pm 0.00$	$0.00 \pm 0.00$	$0.00^{+0.01}_{-0.00}$	$0.00^{+0.01}_{-0.00}$
$Z \rightarrow \tau\tau$	$0.00 \pm 0.00$	$0.00 \pm 0.00$	$0.00 \pm 0.00$	$0.00 \pm 0.00$
Higgs	$0.11 \pm 0.04$	$0.19 \pm 0.05$	$0.08 \pm 0.04$	$0.38 \pm 0.08$
Fakes (DD)	$0.00^{+0.18}_{-0.00}$	$0.00^{+0.14}_{-0.00}$	$0.00^{+0.15}_{-0.00}$	$0.00^{+0.28}_{-0.00}$
Total	$15.20 \pm 2.48$	$18.73 \pm 3.58$	$20.43 \pm 4.21$	$54.36 \pm 9.29$
MC-with Scale Factors				
$t\bar{t} + Wt$	$0.85^{+1.04}_{-0.85}$	$5.59 \pm 2.14$	$2.44 \pm 1.82$	$8.88 \pm 3.95$
$WW$	$9.36 \pm 1.56$	$14.11 \pm 2.10$	$12.64 \pm 1.89$	$36.11 \pm 5.94$
$ZV$	$6.49 \pm 1.42$	$0.73 \pm 0.26$	$7.65 \pm 1.91$	$14.87 \pm 3.46$
$Z$ +jets	$0.00 \pm 0.00$	$0.00 \pm 0.00$	$0.00^{+0.01}_{-0.00}$	$0.00^{+0.01}_{-0.00}$
$Z \rightarrow \tau\tau$	$0.00 \pm 0.00$	$0.00 \pm 0.00$	$0.00 \pm 0.00$	$0.00 \pm 0.00$
Higgs	$0.11 \pm 0.04$	$0.19 \pm 0.06$	$0.08 \pm 0.06$	$0.38 \pm 0.11$
Fakes (DD)	$0.00^{+0.18}_{-0.00}$	$0.00^{+0.14}_{-0.00}$	$0.00^{+0.15}_{-0.00}$	$0.00^{+0.28}_{-0.00}$
Total	$16.80 \pm 2.32$	$20.63 \pm 3.19$	$22.81 \pm 3.68$	$60.24 \pm 8.39$

Table 7.10: Comparison of background expectations in SR- $m_{T2,90}$  for  $20.3 \text{ fb}^{-1}$  of data at  $\sqrt{s} = 8 \text{ TeV}$  using the background fit results, the nominal Monte Carlo expectations and the Monte Carlo expectations scaled using the data-driven scale factors. All systematic and statistical uncertainties are included.

Channel	$ee$	$e\mu$	$\mu\mu$	$all$
Observed	4	5	4	13
Simultaneous Fit Results				
$t\bar{t} + Wt$ (fitted)	$0.69 \pm 0.69$	$0.56 \pm 0.42$	$0.00 \pm 0.00$	$1.26 \pm 0.99$
$WW$ (fitted)	$2.67 \pm 1.50$	$3.56 \pm 1.95$	$2.85 \pm 1.58$	$9.08 \pm 4.90$
$ZV$ (fitted)	$2.70 \pm 1.43$	$0.19 \pm 0.12$	$3.39 \pm 1.78$	$6.29 \pm 3.27$
$Z$ +jets (MC-only)	$0.00 \pm 0.00$	$0.00 \pm 0.00$	$0.00 \pm 0.00$	$0.00 \pm 0.00$
$Z \rightarrow \tau\tau$ (MC-only)	$0.00 \pm 0.00$	$0.00 \pm 0.00$	$0.00 \pm 0.00$	$0.00 \pm 0.00$
Higgs (MC-only)	$0.05 \pm 0.03$	$0.12 \pm 0.04$	$0.05 \pm 0.02$	$0.22 \pm 0.05$
Fakes (DD)	$0.00^{+0.09}_{-0.00}$	$0.00^{+0.13}_{-0.00}$	$0.00^{+0.12}_{-0.00}$	$0.00^{+0.28}_{-0.00}$
Total	$6.12 \pm 2.18$	$4.44 \pm 2.00$	$6.29 \pm 2.38$	$16.85 \pm 5.98$
MC-only				
$t\bar{t} + Wt$	$0.64 \pm 0.64$	$0.53 \pm 0.40$	$0.00 \pm 0.00$	$1.17 \pm 0.91$
$WW$	$2.38 \pm 1.35$	$3.16 \pm 1.74$	$2.52 \pm 1.43$	$8.07 \pm 4.40$
$ZV$	$2.92 \pm 1.49$	$0.21 \pm 0.13$	$3.64 \pm 1.87$	$6.76 \pm 3.41$
$Z$ +jets	$0.00 \pm 0.00$	$0.00 \pm 0.00$	$0.00 \pm 0.00$	$0.00 \pm 0.00$
$Z \rightarrow \tau\tau$	$0.00 \pm 0.00$	$0.00 \pm 0.00$	$0.00 \pm 0.00$	$0.00 \pm 0.00$
Higgs	$0.05 \pm 0.03$	$0.12 \pm 0.04$	$0.05 \pm 0.02$	$0.22 \pm 0.05$
Fakes (DD)	$0.00^{+0.09}_{-0.00}$	$0.00^{+0.13}_{-0.00}$	$0.00^{+0.12}_{-0.00}$	$0.00^{+0.28}_{-0.00}$
Total	$5.99 \pm 2.22$	$4.02 \pm 1.80$	$6.21 \pm 2.42$	$16.22 \pm 5.91$
MC-with Scale Factors				
$t\bar{t} + Wt$	$0.68^{+0.68}_{-0.68}$	$0.56 \pm 0.43$	$0.00 \pm 0.00$	$1.24 \pm 0.98$
$WW$	$2.68 \pm 1.50$	$3.56 \pm 1.95$	$2.84 \pm 1.57$	$9.08 \pm 4.89$
$ZV$	$2.56 \pm 1.32$	$0.21 \pm 0.13$	$3.58 \pm 1.88$	$6.35 \pm 3.37$
$Z$ +jets	$0.00 \pm 0.00$	$0.00 \pm 0.00$	$0.00 \pm 0.00$	$0.00 \pm 0.00$
$Z \rightarrow \tau\tau$	$0.00 \pm 0.00$	$0.00 \pm 0.00$	$0.00 \pm 0.00$	$0.00 \pm 0.00$
Higgs	$0.05 \pm 0.03$	$0.12 \pm 0.04$	$0.05 \pm 0.02$	$0.22 \pm 0.05$
Fakes (DD)	$0.00^{+0.09}_{-0.00}$	$0.00^{+0.13}_{-0.00}$	$0.00^{+0.12}_{-0.00}$	$0.00^{+0.10}_{-0.00}$
Total	$5.97 \pm 2.13$	$4.45 \pm 2.00$	$6.46 \pm 2.45$	$16.88 \pm 6.04$

Table 7.11: Comparison of background expectations in  $SR-m_{T2,110}$  for  $20.3 \text{ fb}^{-1}$  of data at  $\sqrt{s} = 8 \text{ TeV}$  using the background fit results, the nominal Monte Carlo expectations and the Monte Carlo expectations scaled using the data-driven scale factors. All systematic and statistical uncertainties are included.

### 7.3.5 Performing the simultaneous fit

This subsection will be devoted to a brief discussion of the simultaneous fitting technique used in the analysis. All limits calculated for the 2012 analysis used the  $CL_s$  prescription, with the profile likelihood ratio as a test statistic. To describe the signal and background in the analysis, a binned probability distribution function (PDF) for the signal regions and control regions was used, as in Equation (4.16) of Section 4.3.3. By including normalisation factors for background components, internally consistent Standard Model background estimates for the signal regions could be obtained by performing a profile likelihood fit to the observed data in the control regions. As discussed in Section 7.3.3, this allowed contaminations from other Standard Model backgrounds in a given control region to be handled correctly, as well as correlations between systematic uncertainties in the signal regions and control regions. Additionally when calculating exclusion  $CL_s$  values for a given signal point, signal contamination in the control regions was also treated correctly.

Background normalisation factors (denoted  $\mathbf{b}$  in Equation (4.16)) were included in the fit for the  $WW$ , top and  $ZV$  backgrounds. All the statistical and systematic uncertainties were included in the PDF as nuisance parameters (these are the  $\theta$  parameters in Equation (4.16)), and were constrained with Gaussian functions taking into account correlations between sample estimates. A full discussion of the implementation of systematic uncertainties for this analysis can be found in Appendix E, which describes in detail the configuration of the fit for this analysis in detail.

When using the fit to estimate the background counts in the signal regions and their associated uncertainties, only the control regions were used to constrain the fit parameters, and possible signal contamination was ignored everywhere. The results for the simultaneous fits shown in Tables 7.10 and 7.11 were obtained in this way. Examples of outputs of the fits performed in this configuration for  $SR-m_{T2,90}$  and  $SR-m_{T2,110}$ , for all of the free parameters included in the PDF, are provided in Appendix E.

For the exclusion contours that will be presented in Section 7.3.7, the signal contributions, as predicted by the model in question, were taken into account in all signal regions and control regions and included in the fit.

When calculating the model independent upper limits on the visible cross-section, and the number of signal events for BSM physics, the signal regions and control regions are included in the fit but the signal contamination is neglected in the control regions,

therefore allowing one single background prediction in each of the signal regions. These predictions are conservative as any signal contamination in the control region is attributed to background only, so gives a possible overestimation of the background. The upper limit is the calculated assuming no systematic uncertainties on the signal events.

### 7.3.6 Results

No significant excesses over the Standard Model background were observed in SR- $m_{T2,90}$  or SR- $m_{T2,110}$ . This can be seen in Figure 7.17, which shows comparisons between data and Monte Carlo for the  $E_T^{\text{miss,rel}}$  and  $m_{T2}$  distributions in “SR-pre- $m_{T2}$ ”, which has the same selections as SR- $m_{T2,90}$  and SR- $m_{T2,110}$  but without the final cut on  $m_{T2}$  applied. The Standard Model backgrounds were taken from Monte Carlo but the  $ZV$ ,  $WW$  and top backgrounds are scaled by their normalisation factors derived from the simultaneous fit. The fake background was evaluated using the matrix method. There is good agreement in the shapes of the variables between data and Monte Carlo. Distributions including full systematic uncertainties, and showing the ratio between data and Monte Carlo, were made by other analysers and can be found in [5].

Table 7.12 presents the observed data and background predictions, calculated using the simultaneous fit detailed in Section 7.3.5, in SR- $m_{T2,90}$  and SR- $m_{T2,110}$ , separated by lepton flavour. As no excess over the Standard Model expectation was observed, limits were set on the visible cross-section for possible non Standard Model processes in each channel,  $\sigma_{\text{vis}}^{95} = \sigma \times \epsilon \times A$ , where  $\epsilon$  and  $A$  are the efficiency and acceptance respectively, as defined in Section 6.8. The number of events observed in data were compared with the Standard Model expectation and upper limits were calculated at 95% CL using the  $\text{CL}_s$  prescription with the profile likelihood ratio as a test statistic, as introduced in Section 4.2. All systematic uncertainties and their correlations were taken into account using nuisance parameters.

Table 7.13 gives more detail on the model independent limits. As well as presenting the observed and expected limits on the visible cross-section in each channel, the observed and expected 95% CL upper limits on the number of signal events (from any non SM process that could contribute to the signal region) is provided. The  $\text{CL}_b$  values indicate the confidence levels observed for the background-only hypothesis.

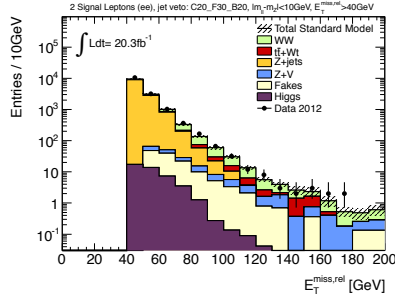
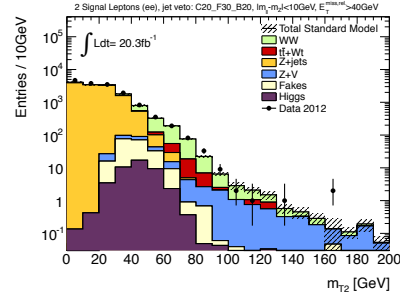
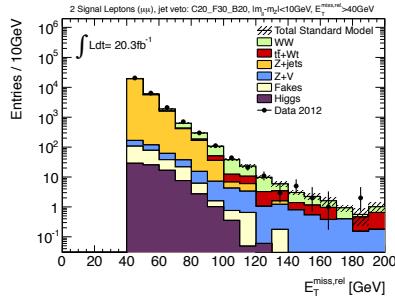
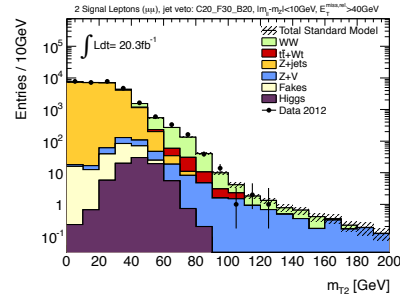
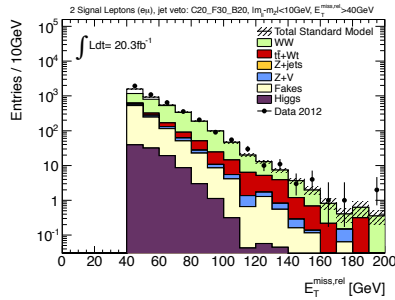
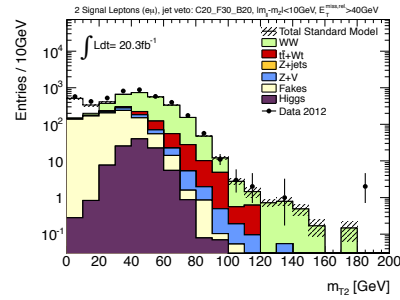

 (a) Di-electron  $E_T^{\text{miss,rel}}$  in “SR-pre- $m_{T2}$ ”.

 (b) Di-electron  $m_{T2}$  in “SR-pre- $m_{T2}$ ”.

 (c) Di-muon  $E_T^{\text{miss,rel}}$  in “SR-pre- $m_{T2}$ ”.

 (d) Di-muon  $m_{T2}$  in “SR-pre- $m_{T2}$ ”.

 (e) Electron-muon  $E_T^{\text{miss,rel}}$  in “SR-pre- $m_{T2}$ ”.

 (f) Electron-muon  $m_{T2}$  in “SR-pre- $m_{T2}$ ”.

Figure 7.17: Comparisons between data and Monte Carlo for distributions of  $E_T^{\text{miss,rel}}$  (left) and  $m_{T2}$  (right) in “SR-pre- $m_{T2}$ ”, in the di-electron (top), di-muon (middle) and electron-muon (bottom) channels, for  $20.3 \text{ fb}^{-1}$  of data at  $\sqrt{s} = 8 \text{ TeV}$ . All components were taken from Monte Carlo except the fake background. The  $ZV$ ,  $WW$  and top backgrounds are scaled by their normalisation factors derived from the simultaneous fit. The dashed uncertainty band represents the statistical uncertainty only.

SR- $m_{T2,90}$	$e^+e^-$	$e^\pm\mu^\mp$	$\mu^+\mu^-$	all
Observed	15	19	19	53
Background total	$16.6 \pm 2.3$	$20.7 \pm 3.2$	$22.4 \pm 3.3$	$59.7 \pm 7.3$
<i>WW</i>	$9.3 \pm 1.6$	$14.1 \pm 2.2$	$12.6 \pm 2.0$	$36.1 \pm 5.1$
<i>ZV</i> ( $V = W$ or $Z$ )	$6.3 \pm 1.5$	$0.8 \pm 0.3$	$7.3 \pm 1.7$	$14.4 \pm 3.2$
Top	$0.9^{+1.1}_{-0.9}$	$5.6 \pm 2.1$	$2.5 \pm 1.8$	$8.9 \pm 3.9$
Higgs	$0.11 \pm 0.04$	$0.19 \pm 0.05$	$0.08 \pm 0.04$	$0.38 \pm 0.08$
Fake	$0.00^{+0.18}_{-0.00}$	$0.00^{+0.14}_{-0.00}$	$0.00^{+0.15}_{-0.00}$	$0.00^{+0.28}_{-0.00}$
Observed $\sigma_{\text{vis}}^{95}$ (fb)	0.44	0.51	0.47	0.81
Expected $\sigma_{\text{vis}}^{95}$ (fb)	$0.50^{+0.22}_{-0.15}$	$0.57^{+0.25}_{-0.17}$	$0.58^{+0.25}_{-0.17}$	$1.00^{+0.41}_{-0.28}$
SR- $m_{T2,110}$	$e^+e^-$	$e^\pm\mu^\mp$	$\mu^+\mu^-$	all
Observed	4	5	4	13
Background total	$6.1 \pm 2.2$	$4.4 \pm 2.0$	$6.3 \pm 2.4$	$16.9 \pm 6.0$
<i>WW</i>	$2.7 \pm 1.5$	$3.6 \pm 2.0$	$2.9 \pm 1.6$	$9.1 \pm 4.9$
<i>ZV</i> ( $V = W$ or $Z$ )	$2.7 \pm 1.4$	$0.2 \pm 0.1$	$3.4 \pm 1.8$	$6.3 \pm 3.3$
Top	$0.7 \pm 0.7$	$0.6 \pm 0.4$	$0.0 \pm 0.0$	$1.3 \pm 1.0$
Higgs	$0.05 \pm 0.03$	$0.12 \pm 0.04$	$0.05 \pm 0.02$	$0.22 \pm 0.05$
Fake	$0.00^{+0.09}_{-0.00}$	$0.00^{+0.13}_{-0.00}$	$0.00^{+0.12}_{-0.00}$	$0.00^{+0.28}_{-0.00}$
Observed $\sigma_{\text{vis}}^{95}$ (fb)	0.27	0.35	0.28	0.54
Expected $\sigma_{\text{vis}}^{95}$ (fb)	$0.33^{+0.16}_{-0.10}$	$0.33^{+0.16}_{-0.09}$	$0.33^{+0.16}_{-0.10}$	$0.62^{+0.23}_{-0.16}$

Table 7.12: Observed and expected numbers of events in SR- $m_{T2,90}$  and SR- $m_{T2,110}$  separated by lepton flavour, for  $20.3 \text{ fb}^{-1}$  of data at  $\sqrt{s} = 8 \text{ TeV}$ . The *WW*, *ZV* and top backgrounds are scaled using the normalisation factors derived from the simultaneous fit, as described in Section 7.3.5. The observed and expected 95% CL upper limits on the visible cross-section,  $\sigma_{\text{vis}}^{95}$ , for non-SM events are also shown.

Signal channel	Observed $\sigma_{\text{vis}}^{95}$ [fb]	$S_{\text{obs}}^{95}$	Expected $\sigma_{\text{vis}}^{95}$ [fb]	$S_{\text{exp}}^{95}$	$CL_B$
SR- $m_{T2,90}$ $ee$	0.44	9.0	$0.50^{+0.22}_{-0.15}$	$10.1^{+4.5}_{-3.0}$	0.37
SR- $m_{T2,90}$ $e\mu$	0.51	10.4	$0.57^{+0.25}_{-0.17}$	$11.5^{+5.0}_{-3.4}$	0.39
SR- $m_{T2,90}$ $\mu\mu$	0.47	9.7	$0.59^{+0.25}_{-0.17}$	$11.9^{+5.1}_{-3.5}$	0.29
SR- $m_{T2,90}$ $ee+\mu\mu$	0.63	12.8	$0.78^{+0.32}_{-0.22}$	$15.8^{+6.6}_{-4.5}$	0.27
SR- $m_{T2,90}$ all	0.81	16.5	$1.00^{+0.41}_{-0.28}$	$20.3^{+8.3}_{-5.6}$	0.26
SR- $m_{T2,110}$ $ee$	0.27	5.5	$0.33^{+0.16}_{-0.10}$	$6.7^{+3.2}_{-2.0}$	0.30
SR- $m_{T2,110}$ $e\mu$	0.35	7.2	$0.33^{+0.16}_{-0.09}$	$6.7^{+3.2}_{-1.9}$	0.57
SR- $m_{T2,110}$ $\mu\mu$	0.28	5.6	$0.33^{+0.16}_{-0.10}$	$6.8^{+3.2}_{-2.0}$	0.30
SR- $m_{T2,110}$ $ee+\mu\mu$	0.39	8.0	$0.48^{+0.20}_{-0.13}$	$9.8^{+4.0}_{-2.6}$	0.27
SR- $m_{T2,110}$ all	0.54	11.0	$0.62^{+0.23}_{-0.16}$	$12.6^{+4.7}_{-3.3}$	0.34

Table 7.13: Breakdown of the model independent limits, for each lepton flavour channel of SR- $m_{T2,90}$  and SR- $m_{T2,110}$ . Going from left to right: 95% CL upper limits on the visible cross section (Observed  $\sigma_{\text{vis}}^{95}$ ) and on the number of signal events ( $S_{\text{obs}}^{95}$ ), the 95% CL expected upper limit on the visible cross section (Expected  $\sigma_{\text{vis}}^{95}$ ), the 95% CL upper limit on the number of signal events, ( $S_{\text{exp}}^{95}$ ) given the expected number (and  $\pm 1\sigma$  excursions on the expectation) of background events, and the  $CL_B$  value, i.e. the confidence level observed for the background-only hypothesis.

### 7.3.7 Interpretation of results

As no significant excesses over the Standard Model expectation were observed, the results of the fit were used to exclude regions of parameter space of the direct slepton and chargino-pair production simplified model grids. Because  $SR-m_{T2,90}$  and  $SR-m_{T2,110}$  are not mutually exclusive, they cannot be statistically combined and so for each model point the signal region with the best expected exclusion sensitivity (i.e. lowest  $CL_s$  value) was chosen to contribute to the limit. Compared to the exclusion limits calculated in Section 6.8, instead of considering signal regions as a sum of the channels being used (i.e. for the slepton limits, the signal region counts were a sum of the di-electron and di-muon channels), the different lepton flavour channels contributing to each signal region were combined statistically when performing the fit. This gave a stronger exclusion than summing the channels. All exclusion limits in this section will be presented in the same format as in Chapter 6. The 95% CL expected and observed  $CL_s$  limits are shown as dashed black and solid red lines respectively. The dashed red lines indicate impact on the observed limit of the  $\pm 1\sigma$  theoretical uncertainty on the signal cross-section, and the solid yellow band indicates the impact of the experimental uncertainties on the expected limit.

#### Limits on direct slepton production

Three sets of exclusions were calculated for the direct slepton signal grid. All cases consider both selectron and smuon production, assuming that the first two generations of sleptons are degenerate, and so use both the di-electron and di-muon channels of  $SR-m_{T2,90}$  and  $SR-m_{T2,110}$ . The exclusion limit in the scenario where left-handed and right-handed sleptons are assumed to have the same mass is shown in Figure 7.18. Right-handed and left-handed sleptons have very different cross-sections for production, with the cross-section for right-handed sleptons much lower. The exclusion limits for right-handed and left-handed slepton production only are shown in Figures 7.19 and 7.20. In all plots the masses of the neutralino and slepton are those after electroweak symmetry breaking (for the 2011 analysis the masses used for the grid were those calculated before electroweak symmetry breaking, however the differences are small). In each case the exclusion contours are displayed on the left, and the signal region contributing to the exclusion limit at each point is indicated on the plots on the right. In all scenarios, as expected from the optimisation in Section 7.3.2,  $SR-m_{T2,90}$  is most sensitive close to the diagonal (where mass-splittings are small) and for small slepton masses, whereas

$SR\text{-}m_{T2,110}$  is more sensitive at higher slepton masses.

For a massless neutralino, slepton masses from 90 GeV to 330 GeV are excluded in the case of combined left-handed and right-handed sleptons, whilst for the case of left-handed sleptons only the exclusion is only from around 100 GeV to 300 GeV. Because of the lower cross-section, the exclusion for right-handed sleptons only is much weaker, with the exclusion going from 100 GeV to 230 GeV in the massless neutralino case.

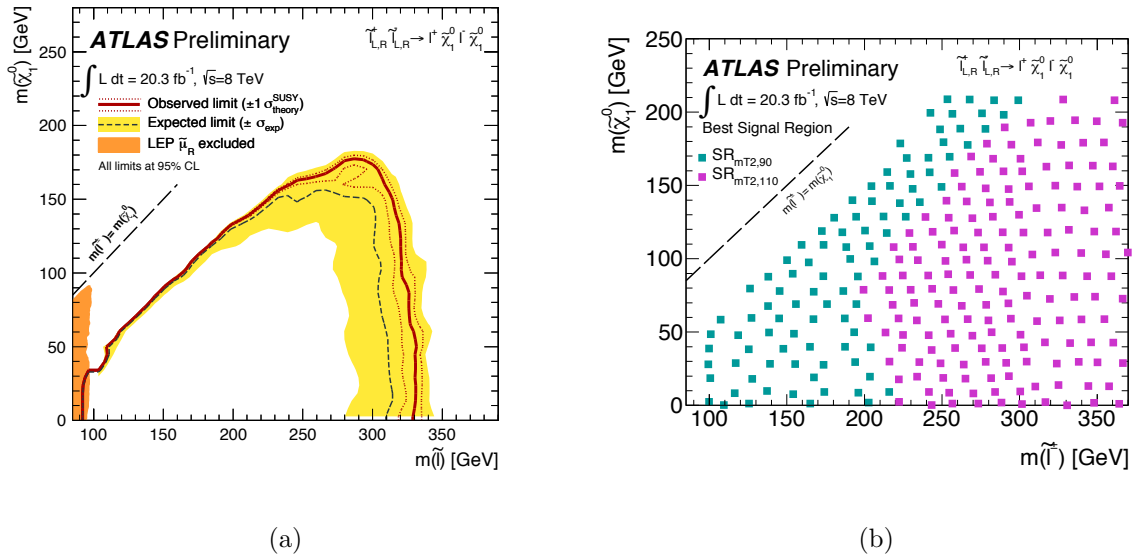


Figure 7.18: 95% exclusion limit in the plane of the slepton mass and the lightest neutralino mass for combined left-handed and right-handed selectrons and smuons (a), for  $20.3 \text{ fb}^{-1}$  of data at  $\sqrt{s} = 8 \text{ TeV}$ . The region excluded by LEP experiments for the right-handed smuon is shown in orange. The limits are presented in the same format as in Figure 6.21. For each signal point the  $CL_s$  is that corresponding to the signal region with the best expected sensitivity. The signal region contributing to the exclusion at each point is indicated in (b).

To further rationalise the shapes of the exclusion contours, Figure 7.21 shows the signal counts in  $SR\text{-}m_{T2,90}$  and  $SR\text{-}m_{T2,110}$  for the three scenarios considered. In all cases the counts drop off close to the diagonal where the mass-splitting between the slepton and the neutralino is small. From Table 7.13 the model independent limits on the number of signal events for the statistical combination of the  $e^\pm e^\mp$  and  $\mu^\pm \mu^\mp$  channels is 12.8 for  $SR\text{-}m_{T2,90}$  and 8.0 for  $SR\text{-}m_{T2,110}$ . These numbers can be used along with the signal counts in Figure 7.21 to check that the exclusion contours are consistent. As an example, for the combine left-handed and right-handed scenario, the excluded contour

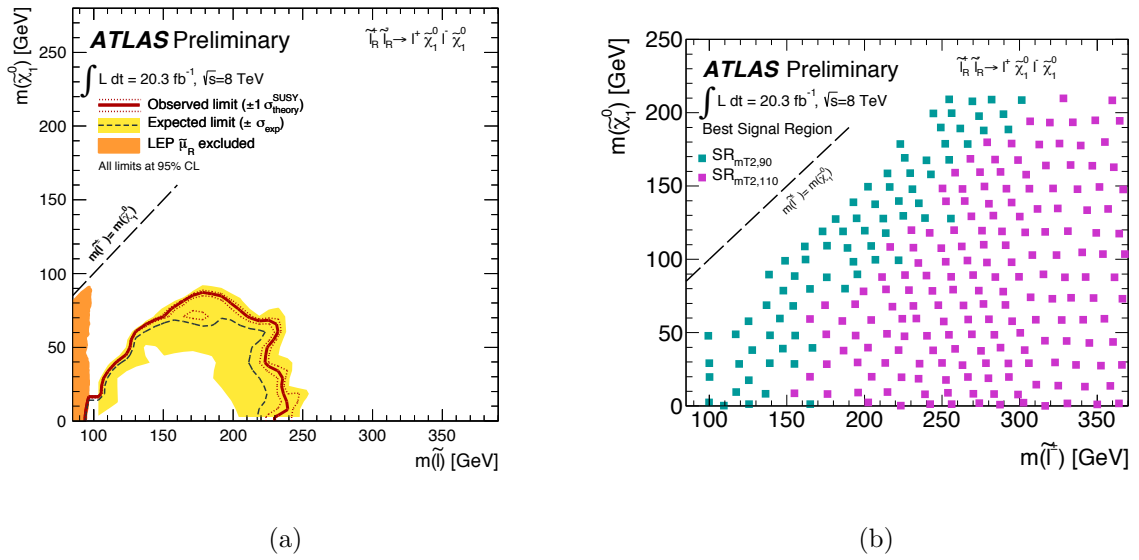


Figure 7.19: 95% exclusion limit in the plane of the slepton mass and the lightest neutralino mass for combined right-handed selectrons and smuons (a), for  $20.3 \text{ fb}^{-1}$  of data at  $\sqrt{s} = 8 \text{ TeV}$ . The region excluded by LEP experiments for the right-handed smuon is shown in orange. The limits are presented in the same format as in Figure 6.21. For each signal point the  $\text{CL}_s$  is that corresponding to the signal region with the best expected sensitivity. The signal region contributing to the exclusion at each point is indicated in (b).

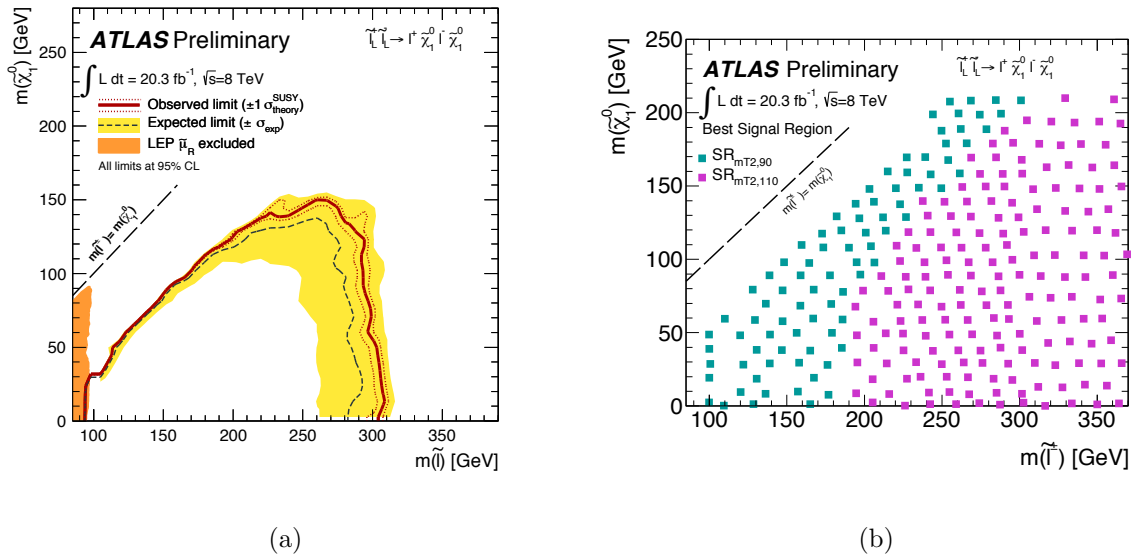


Figure 7.20: 95% exclusion limit in the plane of the slepton mass and the lightest neutralino mass for combined left-handed selectrons and smuons (a), for  $20.3 \text{ fb}^{-1}$  of data at  $\sqrt{s} = 8 \text{ TeV}$ . The region excluded by LEP experiments for the right-handed smuon is shown in orange. The limits are presented in the same format as in Figure 6.21. For each signal point the  $CL_s$  is that corresponding to the signal region with the best expected sensitivity. The signal region contributing to the exclusion at each point is indicated in (b).

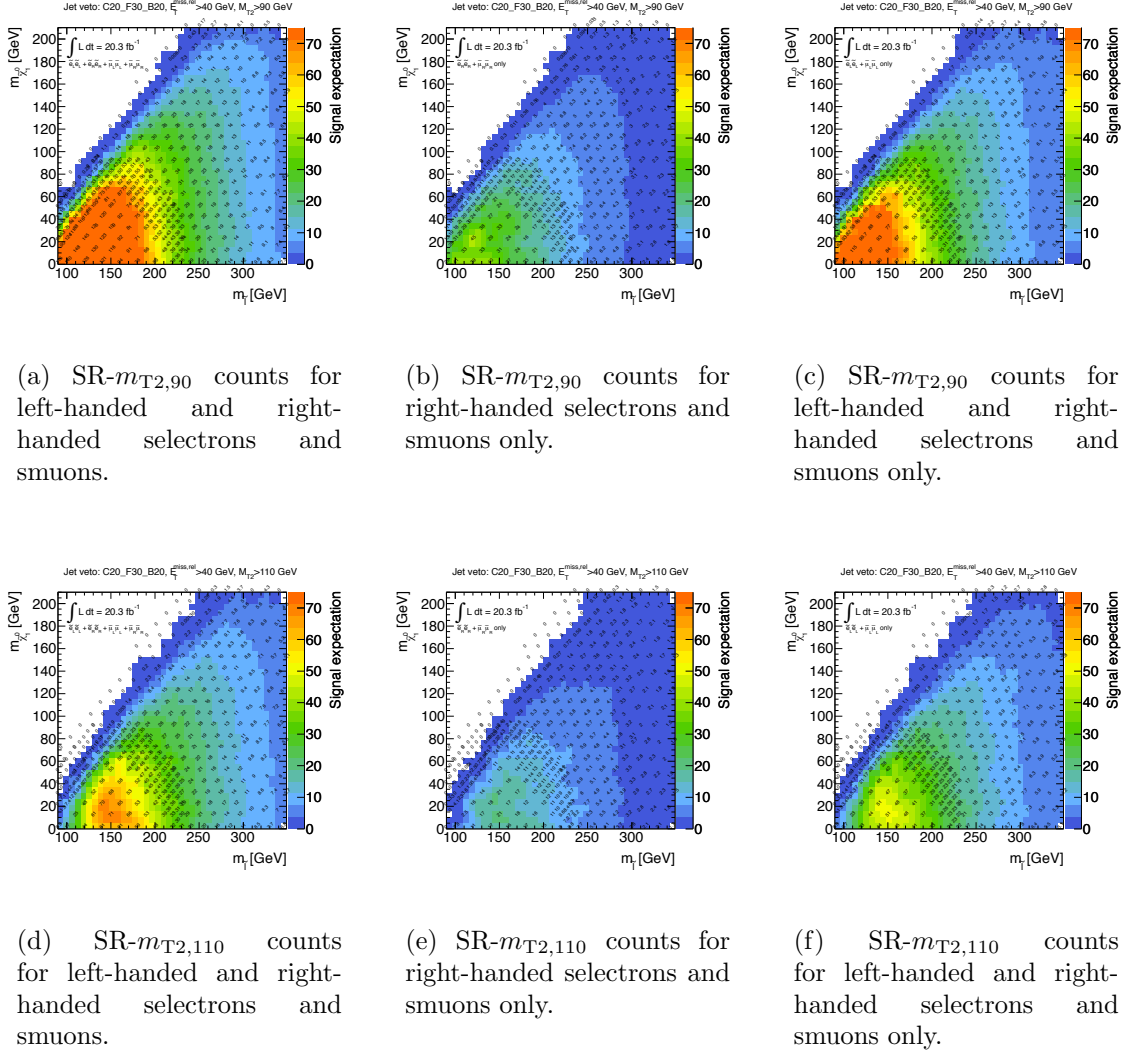


Figure 7.21: Expected signal yields in SR- $m_{T2,90}$  (top) and SR- $m_{T2,110}$  (bottom) for left-handed and right-handed selectrons and smuons (left), right-handed selectrons and smuons only (middle) and left-handed selectrons and smuons only (right), in the direct slepton signal grid, for  $20.3 \text{ fb}^{-1}$  of data at  $\sqrt{s} = 8 \text{ TeV}$ .

extends to 330 GeV for a massless neutralino. For higher slepton masses the exclusion  $CL_s$  values come from SR- $m_{T2,110}$  which is more sensitive. Between 330 GeV and 345 GeV the signal count in SR- $m_{T2,110}$  drops from 8.3 to 7.5, which is consistent with the results in Table 7.13.

### Limits on chargino-pair production

Figure 7.22 shows the 95% exclusion contours for the simplified model grid for chargino-pair production, with intermediate sleptons. The right-hand plot indicates the signal region contributing to the exclusion limit. For a massless neutralino chargino masses between 130 GeV and 460 GeV are excluded at 95% CL. The blue line on the grid corresponds to the 7 TeV exclusion from Figure 6.21.

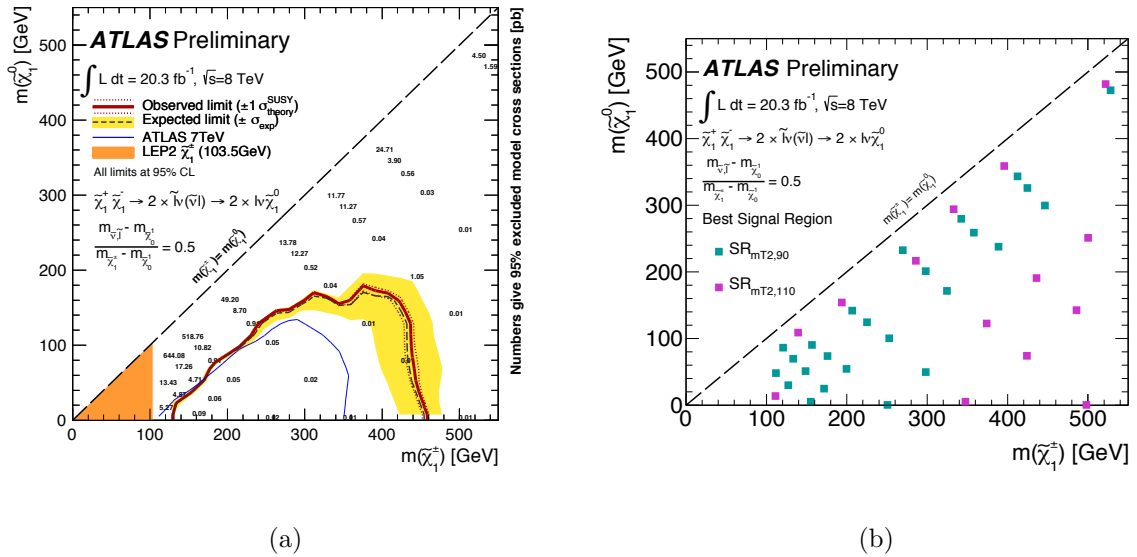


Figure 7.22: 95% exclusion limit in the plane of the chargino mass and the lightest neutralino mass for the chargino-pair production simplified model grid with intermediate sleptons (a), for  $20.3 \text{ fb}^{-1}$  of data at  $\sqrt{s} = 8 \text{ TeV}$ . The region excluded by LEP experiments for the right-handed smuon is shown in orange. The limits are presented in the same format as in Figure 6.21. The numbers displayed on the signal points on the exclusion plot give the 95% CL upper limit on the model cross-section in pb. For each signal point the  $\text{CL}_s$  is that corresponding to the signal region with the best expected sensitivity. The signal region contributing to the exclusion at each point is indicated in (b).

The numbers displayed on the signal points on the exclusion plot give the 95% CL upper limit on the model cross-section in pb. This effectively corresponds to the visible cross-section limit, as given in Table 7.12, divided by the efficiency times acceptance for that model. When all channels were included in the fit, the upper limits on the visible cross-section in  $\text{SR}_{mT2,90}$  and  $\text{SR}_{mT2,110}$  were 0.84 fb and 0.51 fb respectively. The high upper limits on the model cross-sections close to the diagonal reflect the low efficiency-

times-acceptance in that region of the parameter space due to the small mass-splitting between the chargino and neutralino.

### Comparison with CMS limits

It is interesting to compare the limits for slepton- and chargino-pair production with the equivalent limits from the CMS collaboration, to establish whether the searches are competitive (or should be optimised further). As mentioned in Section 6.9, CMS did not publish exclusions for chargino- or slepton-pair production using the 2011 dataset, however searches were performed using the 2012 dataset. Figure 7.23 shows the most recent public CMS limits for slepton-pair and chargino-pair production [183]. For the chargino-pair production intermediate sleptons are accessible and have the same hierarchy with respect to the chargino as the grids considered in the ATLAS analysis, so the results can be directly compared. For the direct slepton scenario, only left-handed sleptons are considered.

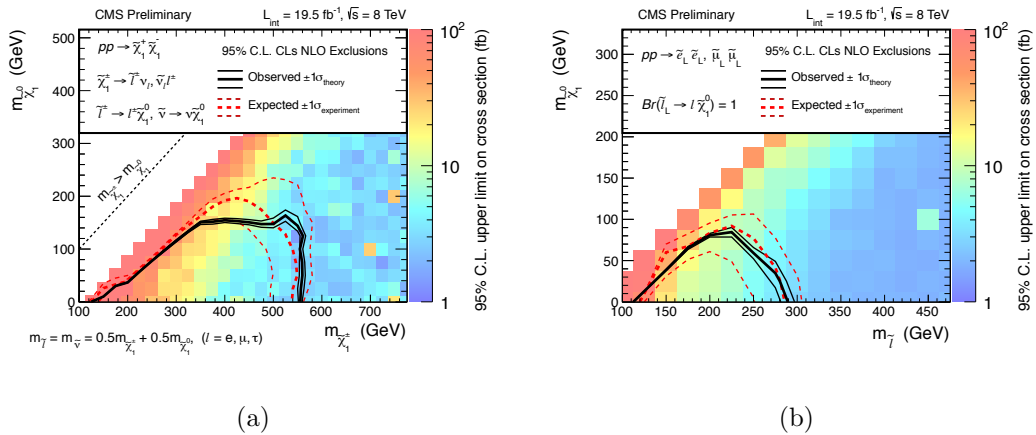


Figure 7.23: Limits on chargino-pair production (a) and slepton-pair production (b) from CMS [183], for the 2012 dataset.

The CMS limits for chargino-pair production are stronger than the ATLAS limits in Figure 7.3.7. Although for a massless neutralino the ATLAS and CMS limits on slepton pair production are similar, the ATLAS limits for left-handed slepton pair production, in Figure 7.20, has more sensitivity to intermediate mass splittings between the slepton and LSP. To illustrate, for a 250 GeV slepton CMS excludes neutralinos below  $\sim 60$  GeV, whereas the ATLAS exclusions extend to  $\sim 130$  GeV in neutralino mass.

The CMS exclusions in these grids were driven by an opposite sign di-lepton channel that used a variable  $m_{CT\perp}$  [184], that is based on the  $m_{CT}$  variable [158, 159]. The search exploits the expected endpoint in  $m_{CT\perp}$  for fully leptonic  $WW$  events at the  $W$ -boson mass. In this sense it is similar to the strategy used in this thesis, which exploits expected endpoints in the  $m_{T2}$  distribution. Further investigation would be required to fully compare the two approaches.

## 7.4 The potential of shape fitting

When calculating the exclusion limits presented in the previous section, all of the signal and control regions were considered as single bins in the fit. This section explores the possibility of using binned signal regions and exploiting shape information, as discussed in Section 4.3.4.

It is natural here to consider performing a shape-fit in  $m_{T2}$ , since for both the processes explored in this chapter the signal distributions can have endpoints depending on the SUSY mass splittings. A shape-fit could therefore provide additional discrimination between signal models. This method relies on the correct Monte Carlo modelling of the  $m_{T2}$  shape, however from Figure 7.11, this appears to be the case.

A comparison is presented here between the exclusion contour obtained by using SR- $m_{T2,90}$  as a single binned channel in the fit, and by fitting the shape  $m_{T2}$  in SR- $m_{T2,90}$ . To constrain the background normalisations of the top,  $ZV$  and  $WW$  backgrounds the same set of control regions as in Section 7.3.3 are used, and as in Section 7.3.3 they are included as single binned channels in the fit. Details of the fit configuration used for this investigation are given in Appendix F.

The results in this section for SR- $m_{T2,90}$  as a single binned channel should not be compared directly to the results in Section 7.3.7, as, in order to consider the diboson generator uncertainties on the shape (rather than just inputting a number for the overall generator uncertainty on the signal region yield), a slightly different set of inputs had to be used for this investigation. This means the Higgs background is not included in the results of this section. The systematics were also treated differently (again see Appendix F).

When performing shape-fitting it is important to consider the Monte Carlo statistics available. For example, if the Monte Carlo statistics ran out before a certain bin, a

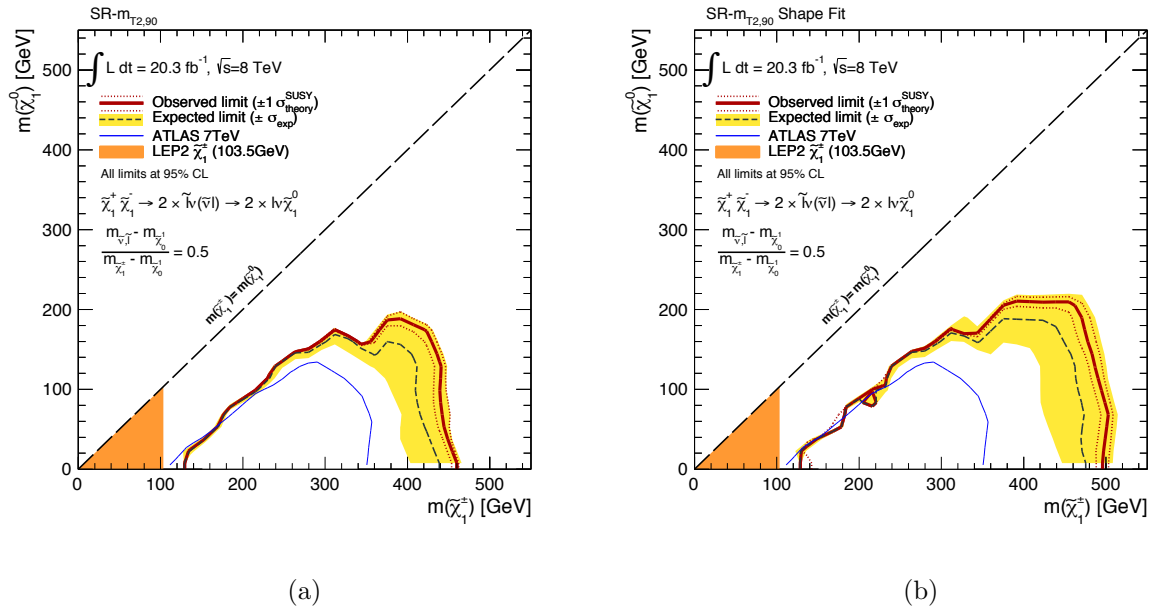


Figure 7.24: 95% exclusion contours for the chargino-pair production simplified model grid using (a) a single binned fit in SR- $m_{T2,90}$ , as in Section 7.3 and (b) a binned fit in  $m_{T2}$  in SR- $m_{T2,90}$ , where two bins are defined between 90 GeV and 130 GeV and the overflow bin is used, for  $20.3 \text{ fb}^{-1}$  of data at  $\sqrt{s} = 8 \text{ TeV}$ . The limits are presented in the same format as in Figure 6.21.

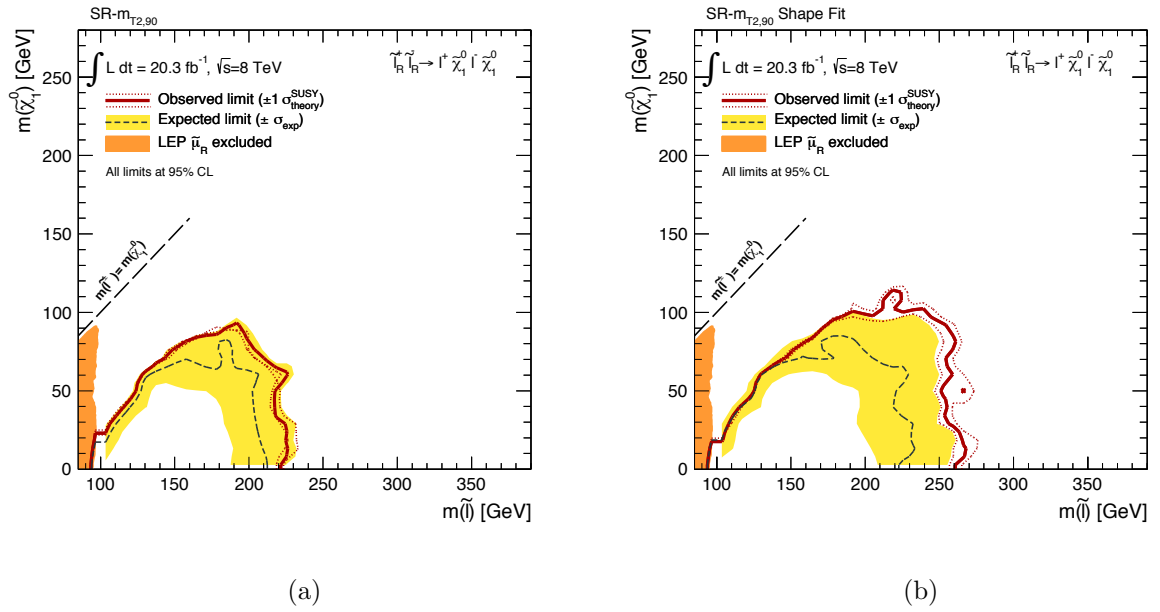


Figure 7.25: 95% exclusion contours for the right-handed selectrons and smuons in the direct slepton simplified model grid using (a) a single binned fit in SR- $m_{T2,90}$ , as in Section 7.3 and (b) a binned fit in  $m_{T2}$  in SR- $m_{T2,90}$ , where two bins are defined between 90 GeV and 130 GeV and the overflow bin is used, for  $20.3 \text{ fb}^{-1}$  of data at  $\sqrt{s} = 8 \text{ TeV}$ . The limits are presented in the same format as in Figure 6.21.

stronger exclusion would be observed because 0 background events would be predicted. To avoid this the binning considered in this section is conservative and intended to provide an initial indication of the potential of the technique rather than the best possible result that could be obtained. Three bins are used, one going from 90 GeV-110 GeV in  $m_{T2}$ , one for 110 GeV-130 GeV in  $m_{T2}$  and an overflow bin for  $m_{T2} > 130$  GeV.

Comparisons between the results of the single binned fit and the shape-fit for SR- $m_{T2,90}$  in the chargino-pair simplified model grid and the direct slepton grid assuming right-handed sleptons only, are provided in Figures 7.24 and 7.25 respectively. The right-handed slepton scenario is chosen for the direct slepton grid as for the other scenarios the exclusions based on the single-binned signal regions are already close to the edge of the grid.

In both scenarios, the exclusion is stronger when shape information is added, thus demonstrating that  $\sim 20 \text{ fb}^{-1}$  of data at  $\sqrt{s} = 8 \text{ TeV}$  is sufficient for shape information in  $m_{T2}$  to be exploited. For the 2011 analysis on  $4.7 \text{ fb}^{-1}$  at  $\sqrt{s} = 7 \text{ TeV}$  the signal region counts for the  $m_{T2}$  region were too low. The conclusion of this section is therefore that sensitivity could be gained by adopting such techniques in future analyses.

## 7.5 The status of ATLAS searches for supersymmetry after the 2012 run

As this thesis has focussed entirely on searches for electroweak production, before concluding this chapter, a brief overview of the status of all searches for SUSY on ATLAS, will be provided. At time of writing, no evidence for SUSY has been observed in any search channel. As a comparison with Figure 5.1, which gave the summary of ATLAS searches for SUSY in the summer of 2011, Figure 7.26 summarises the best ATLAS exclusions on the masses of the SUSY particles, at time of writing.

Inclusive searches for squarks and gluinos have pushed the exclusion limits above a TeV, and searches for third generation squarks (i.e. stops and sbottoms) have excluded large areas of parameter space. Third generation squark searches are also of particular relevance to the Natural SUSY paradigm [177, 178] (along with electroweak production). There are also stronger limits on long-lived and RPV scenarios.

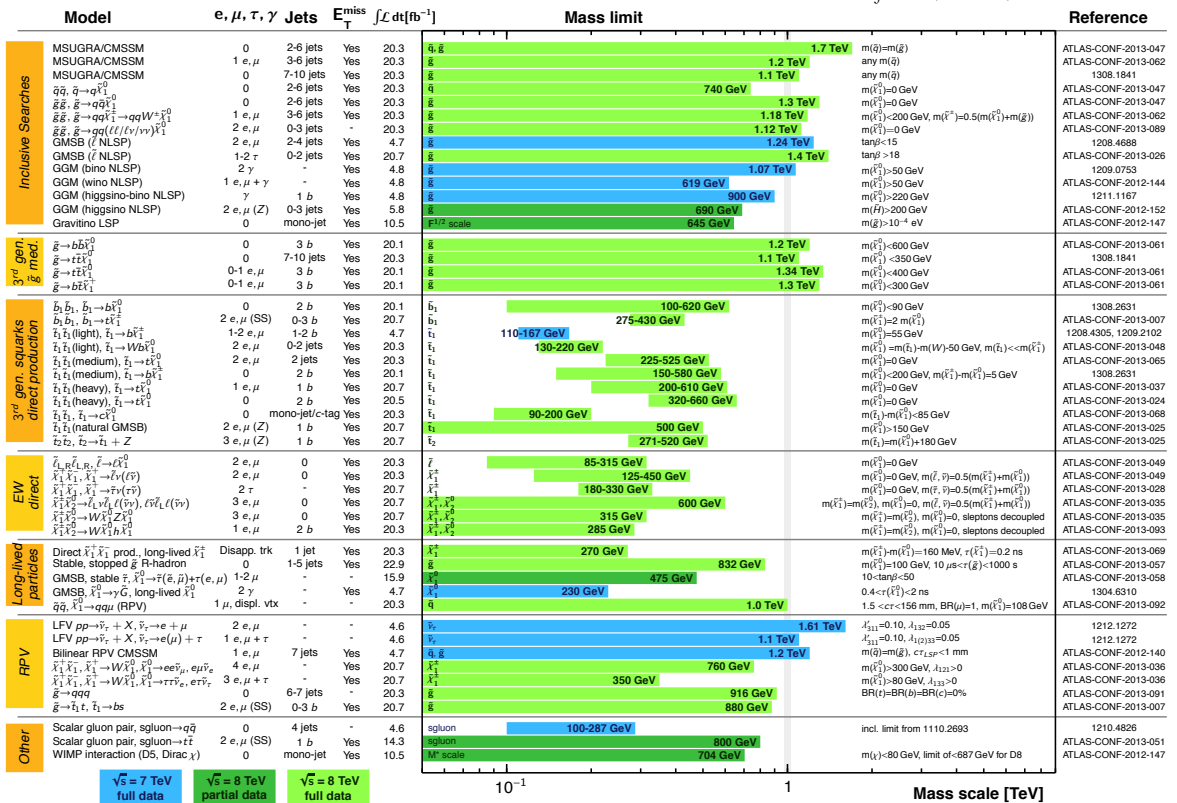
Throughout the first run of the LHC ATLAS (and also CMS, which has not been

ATLAS SUSY Searches\* - 95% CL Lower Limits

Status: SUSY 2013

ATLAS Preliminary

$$\int \mathcal{L} dt = (4.6 - 22.9) \text{ fb}^{-1} \quad \sqrt{s} = 7, 8 \text{ TeV}$$



\*Only a selection of the available mass limits on new states or phenomena is shown. All limits quoted are observed minus 1 $\sigma$  theoretical signal cross section uncertainty.

Figure 7.26: Summary of the best ATLAS exclusions on the masses of the SUSY particles as of August 2013 [185].

discussed in this thesis, but also had an incredibly successful first run of data-taking) has excluded large areas of SUSY parameter space. However there are many channels that are still yet to be explored, and, especially for rarer processes, such as electroweak production and direct stop/sbottom production, there is still a lot to be gained from more data. At the end of the 2013 heavy ion run (which finished in March) the LHC began a two-year shutdown, in order to prepare to run at the full 14 TeV centre-of-mass energy in 2015. The increased centre-of-mass energy will increase SUSY cross-sections, which will again increase the sensitivity of searches. As mentioned previously, for supersymmetry to solve the hierarchy problem and make the weak scale “natural”- we require the stop and gauginos to be fairly light, so perhaps SUSY could be just around the corner.

# Chapter 8

## Concluding Comments

As well as providing overviews of both the ATLAS detector at the LHC, and the Standard Model of particle physics as it is in its current form, this thesis has focussed on results based on the data collected by ATLAS during the 2011 run at  $\sqrt{s} = 7$  TeV (corresponding to an integrated luminosity of  $4.7 \text{ fb}^{-1}$ ) and the 2012 run at  $\sqrt{s} = 8$  TeV (corresponding to  $20.3 \text{ fb}^{-1}$ ). It was a very exciting time to be working at the LHC, with the announcement on July 4th 2012 of a “new scalar particle”, consistent with the properties of the Standard Model Higgs boson. These large datasets also opened up the possibility of sensitivity to many rare new physics scenarios, the electroweak production of supersymmetric particles being one of them.

The searches for various electroweak production scenarios, presented throughout this thesis, have excluded large areas of SUSY parameter space, however the story is far from over, and Chapter 7 explored one way (performing a shape-fit) of improving the sensitivity, based on the 2012 dataset alone. After the long shutdown, which started after the 2012 run and will continue until the end of 2014, the LHC will recommence running at a higher energy, thus enhancing cross-sections for the production of supersymmetric particles. This should further increase sensitivity, though new challenges due to increased pileup, and higher backgrounds will have to be overcome first.

In conclusion, the story is far from over. Although no experimental evidence for supersymmetry has yet been observed, there are still many areas of parameter space left unexplored. Hopefully with more data and improved techniques more challenging scenarios (for example compressed mass spectra) can be targeted. In the case of electroweak production, although the results presented in this thesis have provided initial

---

exclusions, if gauginos and/or sleptons are (relatively) light there is still scope for discovery within the next decade of LHC running. The second run of the LHC, which is due to start in 2015, will give physicists on both ATLAS and CMS the opportunity to probe the SUSY parameter space to higher mass scales, which in the optimistic scenario will lead to discovery, or if not will allow strong constraints to be placed on the possible supersymmetric theories which could exist in nature.

# Appendix A

## Constructing the $m_{T2}$ variable

This appendix provides further details on the “stransverse mass” variable,  $m_{T2}$  [10–12]. As mentioned in Section 5.4, it was designed to be an extension of the transverse mass variable for events involving the pair production of heavy particles, both of which decay semi-invisibly. The transverse mass variable will first be discussed, then  $m_{T2}$  will be motivated and defined.

The transverse mass was first used by the UA1 and UA2 experiments at CERN, which provided the first experimental observations of single  $W$  boson production [133, 134]. Consider the case where a  $W$  boson is produced which then decays leptonically, as shown in Figure A.1.

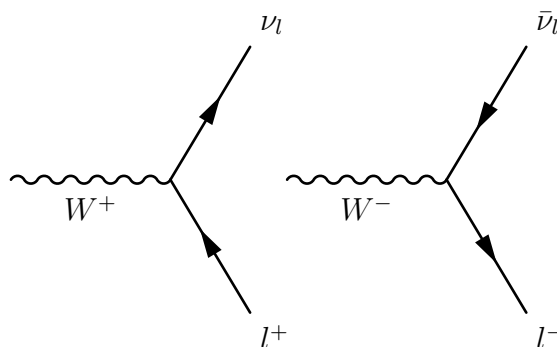


Figure A.1: Feynman diagram for leptonic  $W$  boson decay.

For a given event if the 4-momentum of the neutrino were available the invariant

mass of the  $W$  candidate could be calculated through

$$m_W^2 = (p_l + p_\nu)^2 = m_l^2 + m_\nu^2 + 2[E_T^l E_T^\nu \cosh(\Delta\eta) - \mathbf{p}_T^l \cdot \mathbf{p}_T^\nu], \quad (\text{A.1})$$

where  $E_T^l$  and  $E_T^\nu$  are the transverse energies of the lepton and neutrino respectively,  $\mathbf{p}_T^l$  and  $\mathbf{p}_T^\nu$  are the transverse momentum vectors of the lepton and neutrino respectively, and  $\Delta\eta$  is the pseudorapidity difference between the lepton and the neutrino. If this were calculable on an event-by-event basis the invariant mass distribution would show a peak at the  $W$ -mass. This is how the UA1 and UA2 collaborations detected the  $Z$  boson through its decay to  $e^+e^-$  and  $\mu^+\mu^-$  pairs [186, 187]. However in the case of leptonic  $W$  decays, the final state cannot be fully reconstructed because the neutrino escapes undetected. Its transverse momentum can be inferred from the missing energy in the event, however its longitudinal momentum is unknown. The transverse mass is defined as

$$m_T^2(\mathbf{p}_T^l, \mathbf{p}_T^\nu) = m_l^2 + m_\nu^2 + 2[E_T^l E_T^\nu - \mathbf{p}_T^l \cdot \mathbf{p}_T^\nu]. \quad (\text{A.2})$$

Since  $\cosh(x) > 1$  the transverse mass obeys

$$m_T^2 \leq m_W^2. \quad (\text{A.3})$$

With equality when the lepton and neutrino are produced with the same rapidity. It therefore gives an event-by-event lower bound on the  $W$  mass. The transverse mass distribution for many events can then be used to extract the  $W$  mass in a model independent way. This was first done by the UA1 collaboration in 1983 [133]. In the case of the  $W$  boson mass determination there is one massive particle, which decays to something visible and something invisible. Referring back to Figure 5.6 in Section 5.4, in the case of direct slepton production there are two massive particles produced, each of which decay into something visible and something invisible. As with the case of the  $W$  boson, if the transverse mass were calculable for one leg of the decay the slepton mass would satisfy

$$m_l^2 \geq m_T^2(\mathbf{p}_{T,l}, \mathbf{p}_{T,\tilde{\chi}_1^0}) = m_l^2 + m_{\tilde{\chi}_1^0}^2 + 2[E_{T,l} + E_{T,\tilde{\chi}_1^0} - \mathbf{p}_{T,l} \cdot \mathbf{p}_{T,\tilde{\chi}_1^0}], \quad (\text{A.4})$$

where the subscript  $\tilde{\chi}_1^0$  refers to the neutralino in that leg of the decay. If the momenta

of each of the neutralinos were available, two transverse masses could be calculated and since each gives a lower bound on the mass of the massive particle:

$$m_i^2 \geq \max\{m_T^2(\mathbf{p}_{T,l_a}, \mathbf{p}_{T,\tilde{\chi}_{1,a}^0}), m_T^2(\mathbf{p}_{T,l_b}, \mathbf{p}_{T,\tilde{\chi}_{1,b}^0})\}. \quad (\text{A.5})$$

Where the subscripts  $a$  and  $b$  refer to the two legs of the decay. Unfortunately in this scenario there is no information about the momenta of each of the invisible particles separately. In constructing  $m_{T2}$ , the sum of the neutralino momenta is constrained to equal the missing transverse momentum in the event through

$$\mathbf{p}_T^{\text{miss}} = \mathbf{p}_{T,\tilde{\chi}_{1,a}^0} + \mathbf{p}_{T,\tilde{\chi}_{1,b}^0}. \quad (\text{A.6})$$

By imposing this constraint, and noting that equation (A.5) only holds for the true splitting of the momenta, which is unknown, the only statement that can be made about the slepton mass is

$$m_i^2 \geq m_{T2}^2 = \min_{\mathbf{p}_T^{\text{miss}} = \mathbf{p}_{T,\tilde{\chi}_{1,a}^0} + \mathbf{p}_{T,\tilde{\chi}_{1,b}^0}} [\max\{m_T^2(\mathbf{p}_{T,l_a}, \mathbf{p}_{T,\tilde{\chi}_{1,a}^0}), m_T^2(\mathbf{p}_{T,l_b}, \mathbf{p}_{T,\tilde{\chi}_{1,b}^0})\}]. \quad (\text{A.7})$$

By definition,  $m_{T2}$  is a function of the mass of the invisible particles (which are assumed to have equal mass by construction), and in the case of supersymmetric pair production this is not known. However in the case that direct slepton production was observed at the LHC (or other similar topologies) the  $m_{T2}$  distribution could be used to obtain bounds on the slepton mass in the same way as bounds on the  $W$  mass are extracted from transverse mass distributions.

## Appendix B

### $m_{T2}$ optimisation plots for chargino-pair production

Figures B.1, B.2 and B.3 show the same scan over  $E_T^{\text{miss,rel}}$  and  $m_{T2}$  that was presented for the direct slepton grid in Section 5.4, but using the simplified model grid for chargino-pair production with intermediate sleptons. In these plots all lepton flavour channels ( $e^\pm e^\mp$ ,  $\mu^\pm \mu^\mp$  and  $e^\pm \mu^\mp$ ) were included. By considering the best possible exclusion across the grid the conclusions for the signal region definition are very similar to the results of the optimisation using the direct slepton grid. The expected exclusion for  $m_{T2} > 100$  GeV is slightly better than cutting at 90 GeV, but the signal region that was chosen still provides good sensitivity.

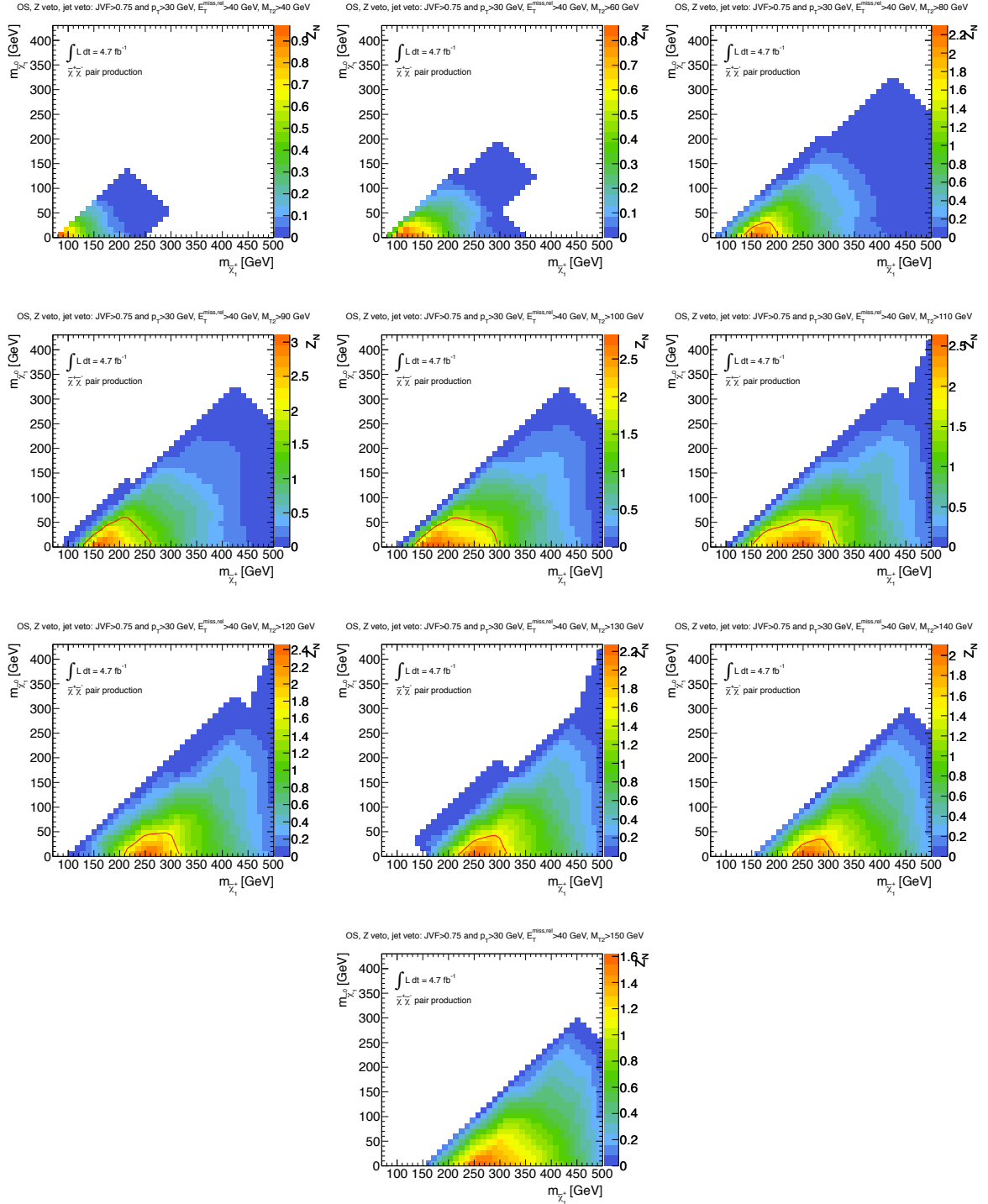


Figure B.1: Optimisation plots, as in Figure 5.9, but for the simplified model grid for chargino-pair production with intermediate sleptons. All signal regions considered have a  $E_T^{\text{miss,rel}}$  cut at 40 GeV. The electron-muon channel is included as well as the same flavour channels. The solid contours indicate the expected 95% CL exclusion, which corresponds to  $Z_N = 1.64$ .

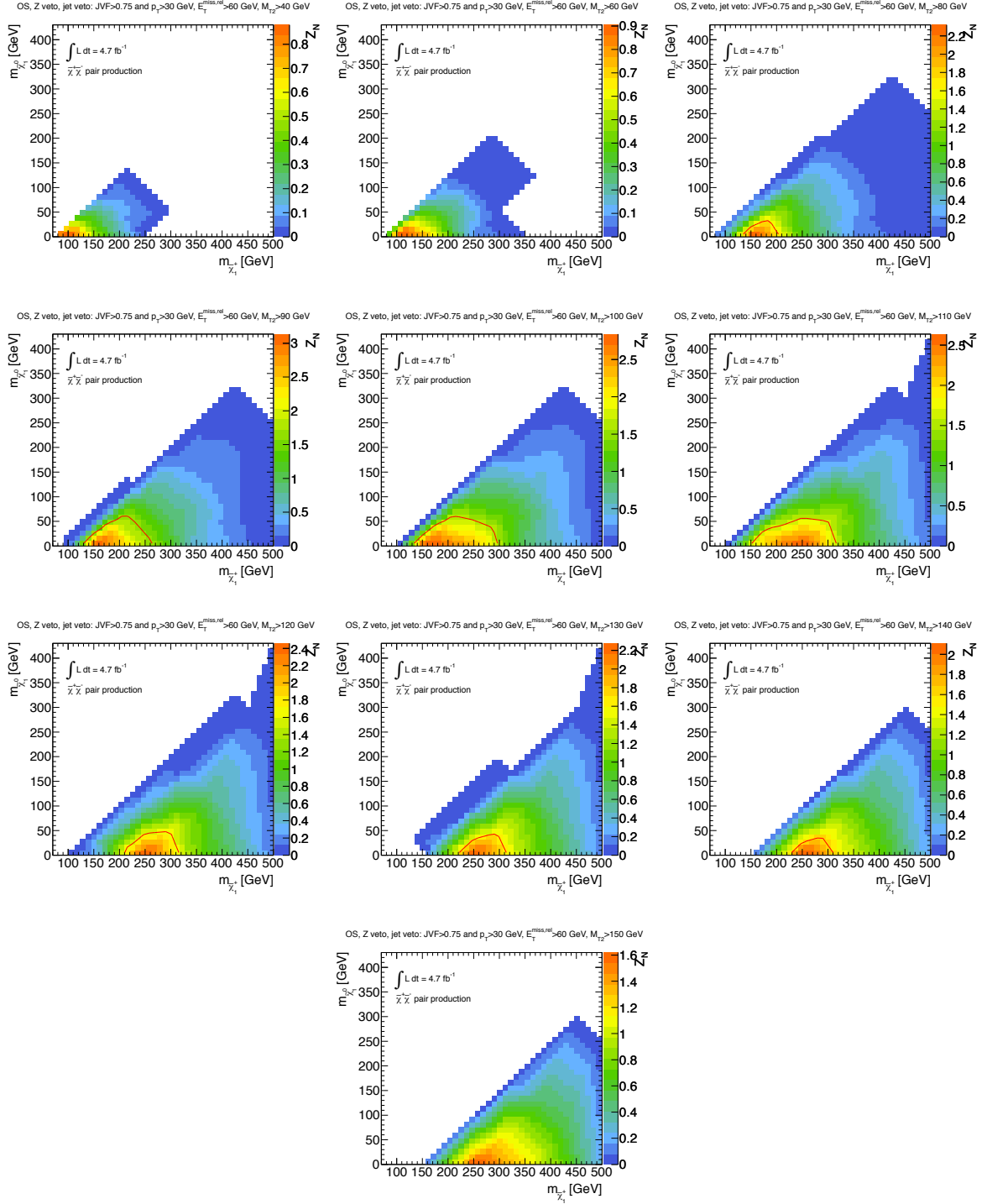


Figure B.2: Optimisation plots, as in Figure 5.10, but for the simplified model grid for chargino-pair production with intermediate sleptons. All signal regions considered have a  $E_T^{\text{miss,rel}}$  cut at 60 GeV. The electron-muon channel is included as well as the same flavour channels.

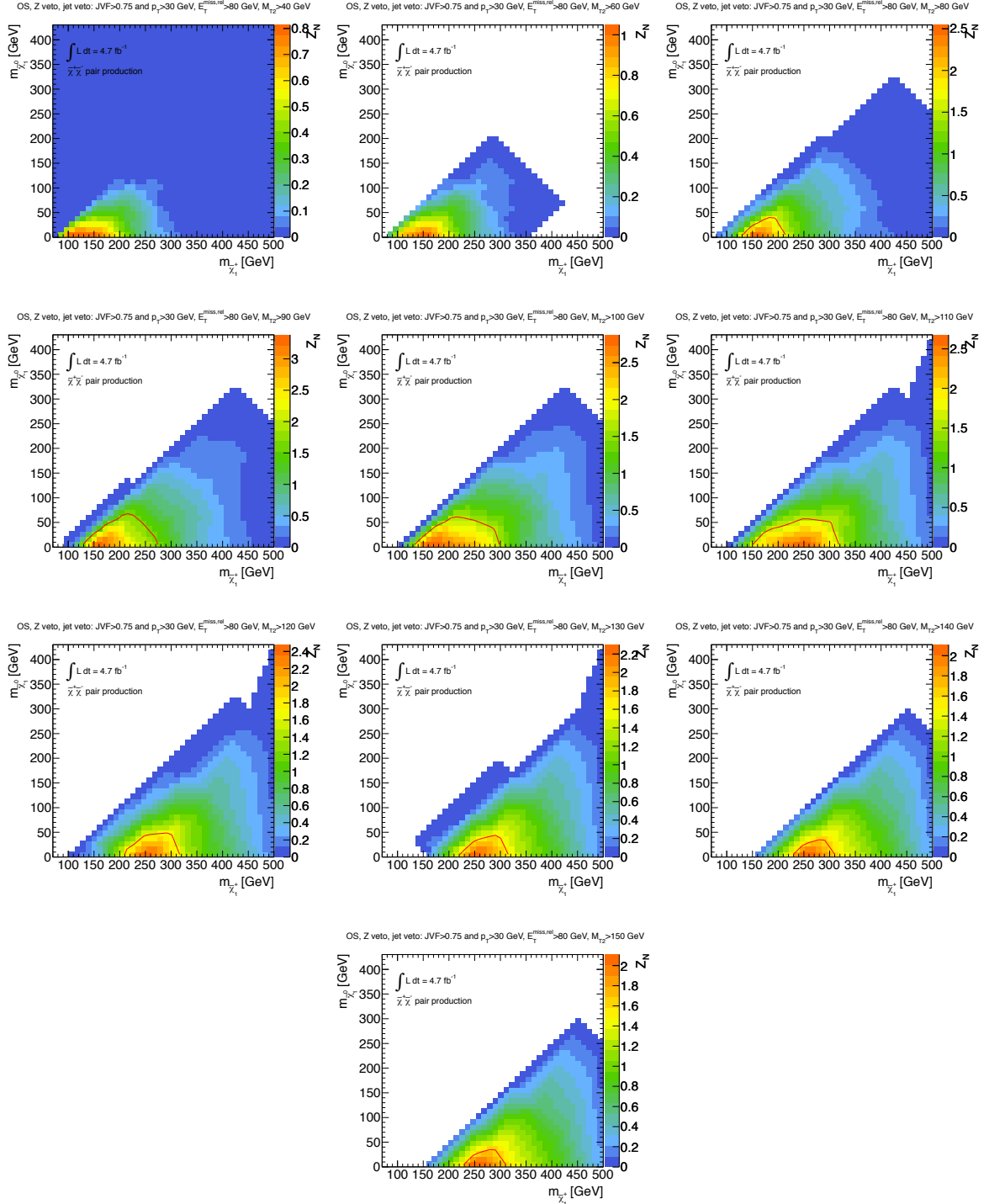


Figure B.3: Optimisation plots, as in Figure 5.11, but for the simplified model grid for chargino-pair production with intermediate sleptons. All signal regions considered have a  $E_T^{\text{miss,rel}}$  cut at 80 GeV. The electron-muon channel is included as well as the same flavour channels.

# Appendix C

## Top-tagging using the $m_{CT}$ variable

This appendix provides more detail on the top-tag veto used in the definition of SR-2jets in 2011 data analysis discussed in Chapter 6. This method uses the “contransverse mass” variable,  $m_{CT}$  [158, 159].  $m_{CT}$  was developed by considering symmetric events where cascade decays of the form in equation (C.1) occur in each leg  $i$  of the chain:

$$\delta \rightarrow \alpha v. \tag{C.1}$$

$\delta_i$  are the initial particles produced in the hard scatter. This scenario can be extended to consider n-step decay chains in each leg consisting of n-1 decays, such that the (n-1)<sup>th</sup> decay produces invisible particles  $\alpha_i$ . The visible products of decays 1 to n-1 in each leg can be considered as single systems,  $v_i$ , of mass  $m(v_i)$  and 4-momentum  $p(v_i)$ . It is assumed that no invisible particles other than  $\alpha_i$  are produced in the chain. It is assumed the particles  $\delta_i$  and  $\alpha_i$  have common masses  $m(\delta)$  and  $m(\alpha)$ .  $m_{CT}$  is then defined as

$$m_{CT}^2(v_1, v_2) = [E_T(v_1) + E_T(v_2)]^2 - [\mathbf{p}_T(v_1) - \mathbf{p}_T(v_2)]^2. \tag{C.2}$$

It can be shown [158] (but not discussed here) that in general  $m_{CT}$  is bounded from above by a quantity dependent on  $m(\alpha)$ ,  $m(\delta)$  and the masses of the visible decay products. If  $m(v_1)=m(v_2)=m(v)$  then the  $m_{CT}$  distribution has an endpoint given by

$$m_{CT}^{max} = \frac{1}{m(\delta)} m^2(v) + \mathcal{M}_0, \tag{C.3}$$

where  $\mathcal{M}_0$  is given by

$$\mathcal{M}_0 = \frac{m^2(\delta) - m^2(\alpha)}{m(\delta)}. \quad (\text{C.4})$$

For di-leptonic  $t\bar{t}$ , the two systems of visible particles  $v_1, v_2$  can be constructed from the leptons, the jets, or from combinations of them. From the Feynman diagram for di-leptonic  $t\bar{t}$  decay shown in Figure 5.7, each leg of the decay proceeds as

$$t \rightarrow bW \rightarrow bl\nu. \quad (\text{C.5})$$

With the two  $bl$  pairs each corresponding to the decay of a different top quark. It is shown in [159] that for the  $t\bar{t}$  system the following set of equations hold (these neglect the mass of the  $b$ -quark, though accounting for  $m(b) \neq 0$  only gives a shift of less than 0.1% in the endpoint positions):

$$m^{\text{max}}(b, l) = \frac{\sqrt{[m^2(t) - m^2(W)][m^2(W) - m^2(\nu)]}}{m(W)} = 152.6 \text{ GeV}, \quad (\text{C.6})$$

$$m_{\text{CT}}^{\text{max}}(b, b') = \frac{m^2(t) - m^2(W)}{m(t)} \equiv 152.6 \text{ GeV}, \quad (\text{C.7})$$

$$m_{\text{CT}}^{\text{max}}(l, l') = \frac{m^2(W) - m^2(\nu)}{m(W)} \equiv 80.4 \text{ GeV}, \quad (\text{C.8})$$

$$m_{\text{CT}}^{\text{max}}([bl], [b'l']) = \frac{m^2(t) - m^2(W)}{m(t)} + m(t) \left( \frac{m^2(W) - m^2(\nu)}{m(W)} \right) \equiv 307.5 \text{ GeV}. \quad (\text{C.9})$$

These equations assume that the  $b$ -quarks and leptons are paired together correctly. For the  $m_{\text{CT}}$  top-tag veto used in SR-2jets, the  $m_{\text{CT}}$  values calculated using combinations of the leptons and/or jets in the event are required to be consistent with these expected bounds. Different pairings of jets and leptons are tried. Firstly the lepton-jet invariant mass values must be consistent with top quark decays, i.e.  $m(j_1 l_1) < 155 \text{ GeV}$  and  $m(j_1 l_2) < 155 \text{ GeV}$ . The  $m_{\text{CT}}$  values calculated based on that pairing must be consistent with the bounds in Equations (C.6)-(C.9). For SR-2jets if at least one combination of lepton-jet pairings satisfied the constraints for a  $t\bar{t}$  event the event was vetoed.

# Appendix D

## Systematics in the 2011 analysis

The tables in this appendix provide a breakdown of the impact of the systematic uncertainties, discussed in Section 6.6, on the Monte Carlo estimates for the various Standard Model background components in the signal regions used in the 2011 analysis. Tables for each signal region are presented separately for each lepton flavour channel (i.e. di-electron, di-muon and electron-muon). Tables D.2-D.5 show the uncertainties in the di-electron channel for SR-OSjveto, SR-SSjveto, SR-2jets and SR- $m_{T2}$ . Tables D.6-D.9 then give the uncertainties in the di-muon channel for SR-OSjveto, SR-SSjveto, SR-2jets and SR- $m_{T2}$ . Finally Tables D.10-D.12 give the uncertainties in the electron-muon channel for SR-OSjveto, SR-SSjveto and SR- $m_{T2}$ . (The electron-muon channel is not used for SR-2jets). The value for each systematic uncertainty is quoted as a percentage deviation from the nominal Monte Carlo prediction. The dominant Monte Carlo uncertainties are the Jet Energy Scale (JES) and Jet Energy Resolution (JER) uncertainties. A summary of the naming convention used in all of the tables is provided in Table D.1.

Systematic name	Description
JES up/down	“up/down” variation of the Jet Energy Scale uncertainty
JER	Jet Energy Resolution Uncertainty
EES up/down	“up/down” variation of the uncertainty on the Electron Energy Scale
EER up/down	“up/down” variation of the uncertainty on the Electron Energy Resolution
MES up/down	“up/down” variation of the uncertainty on the Muon Energy Scale
MS up/down	“up/down” variation of the uncertainty on the muon momentum resolution from the Muon Spectrometer
ID up/down	“up/down” variation of the uncertainty on the muon momentum resolution from the Inner Detector
Cluster up/down	“up/down” variation of the uncertainty related to the CellOut term in the $E_T^{\text{miss}}$
Pileup up/down	“up/down” variation of the uncertainty on the $E_T^{\text{miss}}$ due to pileup
B-tag up/down	“up/down” variation of the uncertainty on the b-tagging weights for b-jets
C-tag up/down	“up/down” variation of the uncertainty on the b-tagging weights for c-jets
Mistag up/down	“up/down” variation of the uncertainty on the b-tagging weights for light flavour jets
e trig up/down	“up/down” variation of the uncertainty on the electron trigger weights
$\mu$ trig up/down	“up/down” variation of the uncertainty on the muon trigger weights
el eff	uncertainty on the electron scale factors applied to correct for differences in efficiency between data/MC
$\mu$ eff	uncertainty on the muon scale factors applied to correct for differences in efficiency between data/MC
Cross-section up/down	“up/down” variation of the uncertainty in the Monte Carlo cross-section(s) for a process
Lumi	uncertainty on the luminosity of the dataset

Table D.1: Explanation of the systematic naming convention used in Tables D.2 to D.12, for Monte Carlo systematic uncertainties considered in the analysis on 2011 data.

ee SR-OSjveto	$t\bar{t}$	Z/ $\gamma^*$ +jets	Single top	W+jets	Dibosons	Total SM
JES up	-7.3%	0%	4.4%	-43%	2.6%	-3.3%
JES down	-8.8%	0%	-5.4%	0%	-0.071%	-4.9%
JER	-7.1%	0%	12%	-43%	1.7%	-2.4%
EES up	-5.1%	-1e+02%	-2.2%	-2.2%	-6.8%	-5.5%
EES down	-0.031%	0%	5.3%	0%	6.1%	2.9%
EER up	-0.1%	0%	-0.11%	0%	1%	0.31%
EER down	-1.6%	-5%	3.5%	-2.2%	-0.18%	-0.38%
MES up	0%	0%	0%	0%	0%	0%
MES down	0%	0%	0%	0%	0%	0%
MS up	0%	0%	0%	0%	0%	0%
MS down	0%	0%	0%	0%	0%	0%
ID up	0%	0%	0%	0%	0%	0%
ID down	0%	0%	0%	0%	0%	0%
Cluster up	-4.7%	0%	11%	0%	7.9%	2.2%
Cluster down	-1.3%	0%	-1.3%	0%	-2.4%	-1.6%
Pileup up	0%	0%	2.1%	0%	3.1%	1.4%
Pileup down	0%	0%	0%	0%	-1.3%	-0.47%
B-tag up	0%	0%	0%	0%	0%	0%
B-tag down	0%	0%	0%	0%	0%	0%
C-tag up	0%	0%	0%	0%	0%	0%
C-tag down	0%	0%	0%	0%	0%	0%
Mistag up	0%	0%	0%	0%	0%	0%
Mistag down	0%	0%	0%	0%	0%	0%
e trig up	2%	1.5%	1.8%	3.3%	2.1%	2%
e trig down	-2%	-1.5%	-1.8%	-3.3%	-2.1%	-2%
$\mu$ trig up	2%	1.5%	1.8%	3.3%	2.1%	2%
$\mu$ trig down	-2%	-1.5%	-1.8%	-3.3%	-2.1%	-2%
el eff	4.9%	3.3%	4.5%	8.4%	3.7%	4.5%
$\mu$ eff	0%	0%	0%	0%	0%	0%
Cross section up	5%	5%	5%	5%	5%	3%
Cross section down	-5%	-5%	-5%	-5%	-5%	3%
Lumi	3.9%	3.9%	3.9%	3.9%	3.9%	3.9%

Table D.2: The impact of all systematic uncertainties considered on the Monte Carlo estimates for di-electron events in SR-OSjveto for the 2011 analysis discussed in Chapter 6. The values are quoted as a percentage deviation from the nominal Monte Carlo prediction.

ee SR-SSjveto	$t\bar{t}$	Z/ $\gamma^*$ +jets	Single top	W+jets	Dibosons	Total SM
JES up	0%	0%	0%	0%	12%	3.3%
JES down	0%	0%	0%	0%	-4.3%	-1.2%
JER	0%	0%	0%	-18%	12%	-6.2%
EES up	0.11%	0%	0%	-18%	2.1%	-9.3%
EES down	0.51%	0%	0.5%	-0.73%	6.3%	1.5%
EER up	0%	0%	0.5%	-0.73%	1.1%	-0.064%
EER down	0.11%	0%	0%	0%	1.9%	0.55%
MES up	0%	0%	0%	0%	0%	0%
MES down	0%	0%	0%	0%	0%	0%
MS up	0%	0%	0%	0%	0%	0%
MS down	0%	0%	0%	0%	0%	0%
ID up	0%	0%	0%	0%	0%	0%
ID down	0%	0%	0%	0%	0%	0%
Cluster up	0%	0%	26%	0%	2.2%	2.3%
Cluster down	0%	0%	0%	-18%	1.9%	-9%
Pileup up	0%	0%	0%	0%	4.4%	1.2%
Pileup down	0%	0%	0%	-18%	1.9%	-9%
B-tag up	0%	0%	0%	0%	0%	0%
B-tag down	0%	0%	0%	0%	0%	0%
C-tag up	0%	0%	0%	0%	0%	0%
C-tag down	0%	0%	0%	0%	0%	0%
Mistag up	0%	0%	0%	0%	0%	0%
Mistag down	0%	0%	0%	0%	0%	0%
e trig up	1.7%	0%	1.7%	1.9%	2.5%	2%
e trig down	-1.7%	0%	-1.7%	-1.9%	-2.5%	-2%
$\mu$ trig up	1.7%	0%	1.7%	1.9%	2.5%	2%
$\mu$ trig down	-1.7%	0%	-1.7%	-1.9%	-2.5%	-2%
el eff	6%	0%	5.2%	6.2%	3.7%	5.4%
$\mu$ eff	0%	0%	0%	0%	0%	0%
Cross section up	5%	0%	5%	5%	5%	3.1%
Cross section down	-5%	0%	-5%	-5%	-5%	3.1%
Lumi	3.9%	0%	3.9%	3.9%	3.9%	3.9%

Table D.3: As in Table D.2, but for di-electron events in SR-SSjveto.

ee SR-2jets	$t\bar{t}$	Z/ $\gamma^*$ +jets	Single top	W+jets	Dibosons	Total SM
JES up	6.1%	9.3%	15%	-0.056%	15%	7.5%
JES down	-5%	-13%	-2.6%	-0.0084%	-14%	-6.7%
JER	1.2%	36%	18%	-0.082%	3.2%	7.2%
EES up	-3.1%	-8.9%	-6.7%	0.88%	-3%	-3.7%
EES down	1%	32%	0.00051%	-0.65%	3.9%	5.7%
EER up	-0.75%	0%	0%	0%	-2.6%	-0.75%
EER down	-3.8%	-0.98%	0%	0%	0.042%	-2.3%
MES up	0%	0%	0%	0%	0%	0%
MES down	0%	0%	0%	0%	0%	0%
MS up	0%	0%	0%	0%	0%	0%
MS down	0%	0%	0%	0%	0%	0%
ID up	0%	0%	0%	0%	0%	0%
ID down	0%	0%	0%	0%	0%	0%
Cluster up	2%	1.8%	-0.22%	0%	2.2%	1.7%
Cluster down	-3%	12%	0%	25%	0.61%	2.4%
Pileup up	0.28%	-6.7%	0%	0%	0.97%	-0.68%
Pileup down	-4.4%	7.2%	0%	0%	0.61%	-1.5%
B-tag up	-17%	0%	-15%	0%	-0.57%	-11%
B-tag down	18%	0%	25%	0%	0.57%	12%
C-tag up	-0.44%	-0.29%	0%	0%	-0.81%	-0.4%
C-tag down	0.44%	0.29%	0%	0%	0.83%	0.4%
Mistag up	-1.4%	-2%	-1.3%	-1.8%	-1.6%	-1.5%
Mistag down	1.4%	2%	1.3%	1.8%	1.6%	1.6%
e trig up	2.3%	2.4%	1.9%	2%	2.2%	2.2%
e trig down	-2.3%	-2.4%	-1.9%	-2%	-2.2%	-2.2%
$\mu$ trig up	2.3%	2.4%	1.9%	2%	2.2%	2.2%
$\mu$ trig down	-2.3%	-2.4%	-1.9%	-2%	-2.2%	-2.2%
el eff	3.9%	3.4%	2.6%	4.7%	3.4%	3.8%
$\mu$ eff	0%	0%	0%	0%	0%	0%
Cross section up	5%	5%	5%	5%	5%	3.1%
Cross section down	-5%	-5%	-5%	-5%	-5%	3.1%
Lumi	3.9%	3.9%	3.9%	3.9%	3.9%	3.9%

Table D.4: As in Table D.2, but for di-electron events in SR-2jets.

ee SR- $m_{T2}$	$t\bar{t}$	Z/ $\gamma^*$ +jets	Single top	W+jets	Dibosons	Total SM
JES up	-18%	-21%	0%	-43%	-3.7%	-12%
JES down	14%	31%	-13%	0%	2.8%	4.5%
JER	8.7%	13%	-13%	-43%	-0.76%	-4.8%
EES up	-30%	-0.44%	-48%	-2.2%	-1.9%	-10%
EES down	12%	31%	0.23%	0%	6.6%	7.3%
EER up	12%	-0.77%	0%	0%	1.5%	2.9%
EER down	-13%	-1.7%	-2.2%	-2.2%	-1.2%	-3.3%
MES up	0%	0%	0%	0%	0%	0%
MES down	0%	0%	0%	0%	0%	0%
MS up	0%	0%	0%	0%	0%	0%
MS down	0%	0%	0%	0%	0%	0%
ID up	0%	0%	0%	0%	0%	0%
ID down	0%	0%	0%	0%	0%	0%
Cluster up	-13%	0%	-30%	0%	-0.77%	-4.8%
Cluster down	13%	0%	0%	0%	-0.54%	1.8%
Pileup up	-13%	0%	0%	0%	-0.6%	-2.4%
Pileup down	13%	0%	0%	0%	0.021%	2.1%
B-tag up	0%	0%	0%	0%	0%	0%
B-tag down	0%	0%	0%	0%	0%	0%
C-tag up	0%	0%	0%	0%	0%	0%
C-tag down	0%	0%	0%	0%	0%	0%
Mistag up	0%	0%	0%	0%	0%	0%
Mistag down	0%	0%	0%	0%	0%	0%
e trig up	2.1%	1.6%	1.9%	3.3%	2%	2.1%
e trig down	-2.1%	-1.6%	-1.9%	-3.3%	-2%	-2.1%
$\mu$ trig up	2.1%	1.6%	1.9%	3.3%	2%	2.1%
$\mu$ trig down	-2.1%	-1.6%	-1.9%	-3.3%	-2%	-2.1%
el eff	2.8%	2.7%	2.8%	8.4%	2.7%	3.4%
$\mu$ eff	0%	0%	0%	0%	0%	0%
Cross section up	5%	5%	5%	5%	5%	3.1%
Cross section down	-5%	-5%	-5%	-5%	-5%	3.1%
Lumi	3.9%	3.9%	3.9%	3.9%	3.9%	3.9%

Table D.5: As in Table D.2, but for di-electron events in SR- $m_{T2}$ .

$\mu\mu$ SR-OSjveto	$t\bar{t}$	Z/ $\gamma^*$ +jets	Single top	W+jets	Dibosons	Total SM
JES up	-15%	0%	-7.6%	0%	1.7%	-7.5%
JES down	1.2%	0%	3.1%	0%	-1.9%	0.25%
JER	-9.9%	0%	-1.1%	-1e+02%	-3%	-7.4%
EES up	0%	0%	0%	0%	0%	0%
EES down	0%	0%	0%	0%	0%	0%
EER up	0%	0%	0%	0%	0%	0%
EER down	0%	0%	0%	0%	0%	0%
MES up	0%	0%	1.8%	0%	0.059%	0.22%
MES down	0%	0%	-1.7%	0%	-0.58%	-0.4%
MS up	0.97%	0%	0%	0%	-0.28%	0.38%
MS down	-0.81%	0%	3.8%	0%	-0.05%	0.016%
ID up	0%	0%	0.094%	0%	-0.11%	-0.029%
ID down	0%	0%	0%	0%	-0.61%	-0.22%
Cluster up	1.6%	0%	2.4%	0%	8.5%	4.2%
Cluster down	-0.39%	0%	-2.6%	0%	-7.4%	-3.2%
Pileup up	1%	0%	0.33%	0%	4.4%	2.2%
Pileup down	-0.59%	0%	0.54%	0%	-3.8%	-1.7%
B-tag up	0%	0%	0%	0%	0%	0%
B-tag down	0%	0%	0%	0%	0%	0%
C-tag up	0%	0%	0%	0%	0%	0%
C-tag down	0%	0%	0%	0%	0%	0%
Mistag up	0%	0%	0%	0%	0%	0%
Mistag down	0%	0%	0%	0%	0%	0%
e trig up	1.9%	5%	2.5%	1.7%	1.9%	2%
e trig down	-1.9%	-5%	-2.5%	-1.7%	-1.9%	-2%
$\mu$ trig up	1.9%	5%	2.5%	1.7%	1.9%	2%
$\mu$ trig down	-1.9%	-5%	-2.5%	-1.7%	-1.9%	-2%
el eff	0%	0%	0%	0%	0%	0%
$\mu$ eff	0.19%	0.16%	0.19%	0.21%	0.19%	0.19%
Cross section up	5%	5%	5%	5%	5%	3.1%
Cross section down	-5%	-5%	-5%	-5%	-5%	3.1%
Lumi	3.9%	3.9%	3.9%	3.9%	3.9%	3.9%

Table D.6: As in Table D.2, but for di-muon events in SR-OSjveto.

$\mu\mu$ SR-SSjveto	$t\bar{t}$	Z/ $\gamma^*$ +jets	Single top	W+jets	Dibosons	Total SM
JES up	0%	0%	0%	0%	13%	7.6%
JES down	0%	0%	9.4%	0.25%	9.8%	23%
JER	0%	0%	0%	0%	14%	8.5%
EES up	0%	0%	0%	0%	0%	0%
EES down	0%	0%	0%	0%	0%	0%
EER up	0%	0%	0%	0%	0%	0%
EER down	0%	0%	0%	0%	0%	0%
MES up	0%	0%	0%	0%	0%	0%
MES down	0%	0%	-90%	0%	0%	-4.8%
MS up	0%	0%	0%	0%	0%	0%
MS down	0%	0%	0%	0%	0%	0%
ID up	0%	0%	0%	0%	0%	0%
ID down	0%	0%	0%	0%	0%	0%
Cluster up	0%	0%	0%	0%	17%	10%
Cluster down	0%	0%	0%	0%	0.48%	0.28%
Pileup up	0%	0%	0%	0%	3.1%	1.8%
Pileup down	0%	0%	0%	0%	0%	0%
B-tag up	0%	0%	0%	0%	0%	0%
B-tag down	0%	0%	0%	0%	0%	0%
C-tag up	0%	0%	0%	0%	0%	0%
C-tag down	0%	0%	0%	0%	0%	0%
Mistag up	0%	0%	0%	0%	0%	0%
Mistag down	0%	0%	0%	0%	0%	0%
e trig up	2.4%	5.7%	2.4%	0%	1.8%	2.3%
e trig down	-2.4%	-5.7%	-2.4%	0%	-1.8%	-2.3%
$\mu$ trig up	2.4%	5.7%	2.4%	0%	1.8%	2.3%
$\mu$ trig down	-2.4%	-5.7%	-2.4%	0%	-1.8%	-2.3%
el eff	0%	0%	0%	0%	0%	0%
$\mu$ eff	0.15%	0.22%	0.21%	0%	0.2%	0.19%
Cross section up	5%	5%	5%	0%	5%	3.3%
Cross section down	-5%	-5%	-5%	0%	-5%	3.3%
Lumi	3.9%	3.9%	3.9%	0%	3.9%	3.9%

Table D.7: As in Table D.2, but for di-muon events in SR-SSjveto.

$\mu\mu$ SR-2jets	$t\bar{t}$	Z/ $\gamma^*$ +jets	Single top	W+jets	Dibosons	Total SM
JES up	2.5%	26%	-3.1%	0.53%	13%	8.6%
JES down	-3.3%	-9.8%	-9.7%	0%	-8.7%	-5.2%
JER	-6.8%	14%	3.9%	0.52%	3.9%	-0.19%
EES up	0%	0%	0%	0%	0%	0%
EES down	0%	0%	0%	0%	0%	0%
EER up	0%	0%	0%	0%	0%	0%
EER down	0%	0%	0%	0%	0%	0%
MES up	-0.00051%	0%	0%	0%	0.77%	0.094%
MES down	-0.00051%	14%	-3.9%	0%	-0.068%	1.8%
MS up	-1.1%	25%	6.4%	0%	-0.024%	3.1%
MS down	-0.00051%	-9.9%	0%	0%	-1.8%	-1.6%
ID up	0%	14%	0%	0%	0.77%	2.1%
ID down	-0.00051%	0%	0%	0%	0%	-0.00035%
Cluster up	-1.7%	0.56%	11%	0%	2.4%	-0.25%
Cluster down	0.33%	1%	0%	0%	-2.8%	0.024%
Pileup up	0%	-4.8%	0%	0%	2.2%	-0.42%
Pileup down	1.2%	-3.7%	0%	0%	-1.1%	0.18%
B-tag up	-23%	-0.3%	-24%	0%	-1.1%	-17%
B-tag down	23%	0.3%	28%	0%	1.1%	18%
C-tag up	-1.1%	-1.6%	-0.28%	0%	-1.2%	-1.1%
C-tag down	1.1%	1.7%	0.28%	0%	1.2%	1.2%
Mistag up	-1.3%	-1.8%	-0.9%	0%	-1.6%	-1.4%
Mistag down	1.3%	1.9%	0.9%	0%	1.6%	1.4%
e trig up	1.8%	1.8%	1.8%	0%	1.7%	1.8%
e trig down	-1.8%	-1.8%	-1.8%	0%	-1.7%	-1.8%
$\mu$ trig up	1.8%	1.8%	1.8%	0%	1.7%	1.8%
$\mu$ trig down	-1.8%	-1.8%	-1.8%	0%	-1.7%	-1.8%
el eff	0%	0%	0%	0%	0%	0%
$\mu$ eff	0.19%	0.18%	0.19%	0%	0.18%	0.19%
Cross section up	5%	5%	5%	0%	5%	3.6%
Cross section down	-5%	-5%	-5%	0%	-5%	3.6%
Lumi	3.9%	3.9%	3.9%	0%	3.9%	3.9%

Table D.8: As in Table D.2, but for di-muon events in SR-2jets.

$\mu\mu$ SR- $m_{T2}$	$t\bar{t}$	Z/ $\gamma^*$ +jets	Single top	W+jets	Dibosons	Total SM
JES up	-33%	-15%	-37%	0%	-3.4%	-15%
JES down	-0.21%	20%	40%	0%	0.82%	4.5%
JER	-24%	31%	-1.1%	0%	-2.7%	-6.3%
EES up	0%	0%	0%	0%	0%	0%
EES down	0%	0%	0%	0%	0%	0%
EER up	0%	0%	0%	0%	0%	0%
EER down	0%	0%	0%	0%	0%	0%
MES up	0%	-15%	0%	0%	-0.0026%	-1.1%
MES down	0%	-15%	0%	0%	-0.0026%	-1.1%
MS up	0%	0%	0.34%	0%	0.51%	0.31%
MS down	0%	-15%	0%	0%	-0.36%	-1.3%
ID up	0%	0%	0%	0%	0%	0%
ID down	0%	-15%	0%	0%	0.5%	-0.86%
Cluster up	0%	0%	14%	0%	3%	2.5%
Cluster down	-7.3%	0%	-18%	0%	-2.2%	-4.5%
Pileup up	0%	0%	14%	0%	0.86%	1.3%
Pileup down	-0.21%	0%	-25%	0%	-0.48%	-1.9%
B-tag up	0%	0%	0%	0%	0%	0%
B-tag down	0%	0%	0%	0%	0%	0%
C-tag up	0%	0%	0%	0%	0%	0%
C-tag down	0%	0%	0%	0%	0%	0%
Mistag up	0%	0%	0%	0%	0%	0%
Mistag down	0%	0%	0%	0%	0%	0%
e trig up	1.6%	1.7%	1.8%	0%	1.7%	1.7%
e trig down	-1.6%	-1.7%	-1.8%	0%	-1.7%	-1.7%
$\mu$ trig up	1.6%	1.7%	1.8%	0%	1.7%	1.7%
$\mu$ trig down	-1.6%	-1.7%	-1.8%	0%	-1.7%	-1.7%
el eff	0%	0%	0%	0%	0%	0%
$\mu$ eff	0.22%	0.21%	0.19%	0%	0.19%	0.2%
Cross section up	5%	5%	5%	0%	5%	3.2%
Cross section down	-5%	-5%	-5%	0%	-5%	3.2%
Lumi	3.9%	3.9%	3.9%	0%	3.9%	3.9%

Table D.9: As in Table D.2, but for di-muon events in SR- $m_{T2}$ .

$e\mu$ SR-OSjveto	$t\bar{t}$	Z/ $\gamma^*$ +jets	Single top	W+jets	Dibosons	Total SM
JES up	-1.2%	0%	-6.7%	0%	5.7%	0.22%
JES down	7.9%	0%	5.8%	0%	-3.6%	3.4%
JER	2.8%	0%	-1.3%	0.17%	-1.9%	0.67%
EES up	-1.4%	-6.3%	-4.3%	4.1%	-4%	-1.7%
EES down	1.7%	0%	4.3%	3.7%	4.1%	2.9%
EER up	0.6%	0%	1.1%	4.1%	0.33%	1.1%
EER down	-0.00071%	0%	3.2%	0.41%	0.17%	0.47%
MES up	-0.00022%	0%	0%	0%	0%	-0.0001%
MES down	-0.62%	0%	0%	0%	-0.15%	-0.33%
MS up	-0.00022%	0%	-0.94%	0%	0.19%	-0.059%
MS down	-0.62%	0%	0%	0%	0%	-0.29%
ID up	0%	0%	0%	0%	0.15%	0.041%
ID down	0%	0%	0%	0%	-0.2%	-0.054%
Cluster up	4.4%	0%	9.2%	0%	7.5%	5.2%
Cluster down	-2.7%	0%	-1.4%	0%	-5.7%	-3%
Pileup up	2.4%	0%	5.5%	0%	3.8%	2.8%
Pileup down	-1.8%	0%	-2.9%	0%	-2.7%	-1.9%
B-tag up	0%	0%	0%	0%	0%	0%
B-tag down	0%	0%	0%	0%	0%	0%
C-tag up	0%	0%	0%	0%	0%	0%
C-tag down	0%	0%	0%	0%	0%	0%
Mistag up	0%	0%	0%	0%	0%	0%
Mistag down	0%	0%	0%	0%	0%	0%
e trig up	1.9%	1.5%	1.9%	4%	2.1%	2.2%
e trig down	-1.9%	-1.5%	-1.9%	-4%	-2.1%	-2.2%
$\mu$ trig up	2%	2.2%	2.1%	4.2%	2.3%	2.4%
$\mu$ trig down	-2%	-2.2%	-2.1%	-4.2%	-2.3%	-2.4%
el eff	1.8%	1.5%	2%	1.1%	1.9%	1.8%
$\mu$ eff	0.094%	0.079%	0.094%	0.11%	0.096%	0.097%
Cross section up	5%	5%	5%	5%	5%	2.9%
Cross section down	-5%	-5%	-5%	-5%	-5%	2.9%
Lumi	3.9%	3.9%	3.9%	3.9%	3.9%	3.9%

Table D.10: As in Table D.2, but for electron-muon events in SR-OSjveto

$e\mu$ SR-SSjveto	$t\bar{t}$	Z/ $\gamma^*$ +jets	Single top	W+jets	Dibosons	Total SM
JES up	0%	0%	0%	0%	1.3%	0.97%
JES down	1e+02%	0%	-4.2%	0%	-13%	-5.6%
JER	0%	0%	23%	0%	-5.2%	1%
EES up	0%	0%	17%	0%	-5.5%	-0.57%
EES down	0%	0%	0.43%	0%	2.5%	2%
EER up	0%	0%	17%	0%	-0.55%	3.1%
EER down	0%	0%	-5.1%	0%	0.041%	-1%
MES up	0%	0%	0%	0%	0%	0%
MES down	0%	0%	0%	0%	0%	0%
MS up	0%	0%	0%	0%	0.00095%	0.0007%
MS down	0%	0%	0%	0%	0%	0%
ID up	0%	0%	0%	0%	0.00095%	0.0007%
ID down	0%	0%	0%	0%	0%	0%
Cluster up	0%	0%	23%	0%	4.9%	8.4%
Cluster down	0%	0%	17%	0%	-2%	2%
Pileup up	0%	0%	0%	0%	-1.4%	-1%
Pileup down	0%	0%	17%	0%	-2%	2%
B-tag up	0%	0%	0%	0%	0%	0%
B-tag down	0%	0%	0%	0%	0%	0%
C-tag up	0%	0%	0%	0%	0%	0%
C-tag down	0%	0%	0%	0%	0%	0%
Mistag up	0%	0%	0%	0%	0%	0%
Mistag down	0%	0%	0%	0%	0%	0%
e trig up	2.3%	0%	3.2%	0%	2.2%	2.4%
e trig down	-2.3%	0%	-3.2%	0%	-2.2%	-2.4%
$\mu$ trig up	2.3%	0%	3.2%	0%	2.4%	2.5%
$\mu$ trig down	-2.3%	0%	-3.2%	0%	-2.4%	-2.5%
el eff	3%	0%	3.2%	0%	1.8%	2.1%
$\mu$ eff	0.11%	0%	0.079%	0%	0.097%	0.094%
Cross section up	5%	0%	5%	0%	5%	3.8%
Cross section down	-5%	0%	-5%	0%	-5%	3.8%
Lumi	3.9%	0%	3.9%	0%	3.9%	3.9%

Table D.11: As in Table D.2, but for electron-muon events in SR-SSjveto.

$e\mu$ SR- $m_{T2}$	$t\bar{t}$	Z/ $\gamma^*$ +jets	Single top	W+jets	Dibosons	Total SM
JES up	-23%	0%	-58%	0%	-1.9%	-15%
JES down	11%	0%	57%	0%	0.22%	8.6%
JER	-3.1%	0%	2.6%	0%	-4.8%	-3.6%
EES up	-6.2%	0%	-29%	0%	-3.2%	-6.2%
EES down	0.057%	0%	16%	0%	1.8%	2.1%
EER up	0.0055%	0%	0.028%	0%	-0.49%	-0.24%
EER down	5.4%	0%	-13%	0%	0.056%	1.4%
MES up	0%	0%	0%	0%	0%	0%
MES down	0%	0%	0%	0%	0%	0%
MS up	0%	0%	0%	0%	0%	0%
MS down	0%	0%	0%	0%	0%	0%
ID up	0%	0%	0%	0%	0%	0%
ID down	0%	0%	0%	0%	0%	0%
Cluster up	0%	0%	-15%	0%	2.3%	0.12%
Cluster down	5.6%	0%	0%	0%	0.21%	2.5%
Pileup up	0%	0%	-13%	0%	0.49%	-0.67%
Pileup down	5.6%	0%	0%	0%	-0.53%	2.1%
B-tag up	0%	0%	0%	0%	0%	0%
B-tag down	0%	0%	0%	0%	0%	0%
C-tag up	0%	0%	0%	0%	0%	0%
C-tag down	0%	0%	0%	0%	0%	0%
Mistag up	0%	0%	0%	0%	0%	0%
Mistag down	0%	0%	0%	0%	0%	0%
e trig up	2.1%	0%	1.7%	0%	1.9%	1.9%
e trig down	-2.1%	0%	-1.7%	0%	-1.9%	-1.9%
$\mu$ trig up	2.3%	0%	1.6%	0%	1.9%	2.1%
$\mu$ trig down	-2.3%	0%	-1.6%	0%	-1.9%	-2.1%
el eff	1.3%	0%	1.3%	0%	1.3%	1.3%
$\mu$ eff	0.1%	0%	0.087%	0%	0.098%	0.098%
Cross section up	5%	0%	5%	0%	5%	3.3%
Cross section down	-5%	0%	-5%	0%	-5%	3.3%
Lumi	3.9%	0%	3.9%	0%	3.9%	3.9%

Table D.12: As in Table D.2, but for electron-muon events in SR- $m_{T2}$ .

## Appendix E

# Fit configuration used for the analysis on 2012 data

This appendix provides further details on the fit configuration used for the statistical interpretation of the results for the analysis on 2012 data [5]. The strategy for the inclusion of the systematic uncertainties as nuisance parameters will be described, and results of the simultaneous fits to the control region data (that were used to extract the signal region estimates) for SR- $m_{T2,90}$  and SR- $m_{T2,110}$  will be provided. All of the results in this appendix were produced by the author using the `HistFitter` package.

As mentioned in Section 7.3.5, a binned probability distribution function (PDF) for the signal regions and control regions was used. In the `HistFitter` package, this is implemented using histograms, where the content of each bin is effectively a counting experiment. For this analysis, histograms corresponding to different components (i.e. signal, or data, or different backgrounds) of the PDF, in each “channel” (in `HistFitter` this refers to the different signal regions and control regions) were built by the software from external inputs. The inputs also provided information to evaluate the impact of systematic uncertainties on these histograms.

A typical PDF contains a number of free parameters. The optimal value and errors of the free parameters can then be fixed simultaneously when the PDF is fitted to the observed data.

For the PDF defined in `HistFitter`, parameters that controlled the normalisation of signal and/or background components were denoted “mu\_XXX”, where XXX defines the corresponding signal or background component. As discussed in Section 7.3.3, for the

analysis under discussion here, the normalisation of the  $WW$ , top and  $ZV$  backgrounds were extracted from the fit, and their normalisations were therefore included in the fit as free parameters, denoted “mu\_WW”, “mu\_Top” and “mu\_ZV” respectively.

All the statistical and systematic uncertainties are included in the PDF as nuisance parameters, and in the notation used by the software denoted “alpha\_XXX”, or “gamma\_XXX” where XXX defines the related uncertainty and also possibly a specific region of phase space or background component.

The `HistFitter` framework allowed systematic uncertainties to be treated in various different ways. For the various systematics that were applied to all Monte Carlo samples used in the fit, two sets of correlated systematic uncertainties were actually defined. For the background components whose normalisations were taken directly from the Monte Carlo predictions (i.e. not constrained by the fit), namely the Higgs,  $Z \rightarrow \tau\tau$  and  $Z$ +jets contributions, a set of nuisance parameters, denoted “alpha\_AR\_MC\_XXX” was defined using a setting called “overallSys”. In `HistFitter`, the “overallSys” systematic adds in a global scaling factor, fully correlated across the histogram bins but not changing its shape. For the background components whose normalisations were constrained by the fit, namely  $ZV$ ,  $WW$  and top, a second set of nuisance parameters were defined, denoted “alpha\_AR\_FIT\_XXX”, which used a setting called “overallNormSys”. For these systematics the uncertainty is normalised to the nominal yield in the control region, thus factoring out the impact of that uncertainty on any scale factor derived from the fit. The aim of this was to try and avoid instabilities in the fit due to strong anti-correlations between fit parameters.

To illustrate how such anti-correlations could occur, the Jet Energy Scale (JES) uncertainty on the top background will be considered. The top background has some JES uncertainty on its Monte Carlo expectation in the signal region. However, the top background normalisation is extracted in the top control region, where there is also a JES uncertainty on the top contribution. When the scale factor for the top background is extracted from the fit, it has an error on it, some of which comes from the JES uncertainty in the control region. This error is then propagated to an uncertainty on the top background in the signal region. In this case there is then the possibility of double counting the JES uncertainty. In principle the correlations should be handled correctly by the fit, however, if JES were a large error, then the “mu\_Top” parameter and the JES nuisance parameter would be strongly anti-correlated. Such anti-correlations could impact upon the stability of the fit. The splitting of the systematic uncertainties into two sets of nuisance parameters, with the “overallNormSys” setting being used for

systematics associated with the fitted backgrounds, was aimed to resolve this issue as in principle all the errors are still propagated to the signal region estimates without generating large anti correlations.

The statistical uncertainties on the background components in each channel were handled using the “shapeStat” setting. This calculates the maximum absolute relative error from the  $\pm 1 \sigma$  histograms for each bin in the fit and applies it as a pure shape systematic without correlations across the bins. The nuisance parameters associated with these systematics are denoted “gamma\_XXX”.

The output of the fits to the control region data, neglecting the signal contamination, for SR- $m_{T2,90}$  and SR- $m_{T2,110}$  are shown in Figures E.1 and E.2 respectively. These show the fitted scale factors and nuisance parameters. It should be noted that the only difference in the fit for SR- $m_{T2,90}$  and SR- $m_{T2,110}$  is the definition of the  $m_{T2}$  cut in the control region for the  $ZV$  backgrounds. A key to the labelling of the fit parameters is provided in Table E.1. The systematic uncertainties applied to Monte Carlo samples were the same as those described for the 2011 analysis in Section 6.6, though for the electron energy scale the different contributions to the uncertainty were considered separately. The parameters denoted “alpha\_AR\_fakes\_XXX” refer to uncertainties arising from the data driven matrix element calculation.

The nuisance parameters included in the fit were modelled initially by a unit gaussian of mean 0. After performing the fit, the final value for the “alpha\_XXX” parameters gives the preferred value of the mean of the gaussian, whereas the error on the parameter represents the preferred gamma-factor of the gaussian (the input value was 1), in units of input sigma. A final error of, say, 0.7, would indicate 30% profiling (without taking into account correlations with other parameters).

From the outputs of the fits in Figures E.1 and E.2, no significant profiling of nuisance parameters was observed. The global correlations between nuisance parameters were also monitored when performing the fit. Figure E.3 and Figure E.4 show the global correlation matrices for SR- $m_{T2,90}$  and SR- $m_{T2,110}$  after performing the fit. Ideally there should be no non-zero off-diagonal elements. Despite the effort to reduce anti-correlations in the fit, there were still strong anti-correlations between both “mu\_2LZV” and “mu\_2LWW” normalisation factors and the “alpha\_AR\_FIT\_JER” nuisance parameter, as well as between the “mu\_2LTop” scale factor and the “alpha\_AR\_FIT\_MC” nuisance parameter. However these anti-correlations did not prevent the fits from converging and were there-

Floating Parameter	InitialValue	FinalValue	(+HiError,-LoError)	GblCorr.
Lumi	1.0000e+00	1.0000e+00	(+2.82e-02,-2.82e-02)	0.068163
alpha_AR_FIT_BT	0.0000e+00	1.1719e-01	(+8.89e-01,-1.12e+00)	0.961894
alpha_AR_FIT_BTC	0.0000e+00	6.5649e-04	(+1.01e+00,-1.01e+00)	0.038111
alpha_AR_FIT_BTL	0.0000e+00	-3.7760e-03	(+1.01e+00,-1.00e+00)	0.336735
alpha_AR_FIT_EER	0.0000e+00	4.7283e-03	(+1.01e+00,-1.00e+00)	0.046210
alpha_AR_FIT_EES_MAT	0.0000e+00	2.9657e-03	(+1.00e+00,-1.00e+00)	0.079138
alpha_AR_FIT_EES_PS	0.0000e+00	-3.8782e-03	(+9.96e-01,-9.94e-01)	0.095755
alpha_AR_FIT_EES_Z	0.0000e+00	2.1736e-02	(+1.01e+00,-1.01e+00)	0.299497
alpha_AR_FIT_ID	0.0000e+00	3.6967e-05	(+1.01e+00,-1.01e+00)	0.005977
alpha_AR_FIT_JER	0.0000e+00	4.0155e-02	(+9.91e-01,-1.00e+00)	0.935103
alpha_AR_FIT_JES	0.0000e+00	1.1279e-02	(+9.94e-01,-1.02e+00)	0.944493
alpha_AR_FIT_MS	0.0000e+00	-3.9204e-03	(+1.00e+00,-1.00e+00)	0.043534
alpha_AR_FIT_RESOST	0.0000e+00	5.7874e-03	(+1.01e+00,-1.00e+00)	0.042895
alpha_AR_FIT_SCALEST	0.0000e+00	1.2589e-02	(+1.01e+00,-1.00e+00)	0.222188
alpha_AR_MC_BT	0.0000e+00	8.5250e-05	(+1.01e+00,-1.01e+00)	0.005096
alpha_AR_MC_BTC	0.0000e+00	1.0324e-04	(+1.01e+00,-1.01e+00)	0.006891
alpha_AR_MC_BTL	0.0000e+00	5.9261e-04	(+1.01e+00,-1.01e+00)	0.030764
alpha_AR_MC_EER	0.0000e+00	-4.2852e-05	(+1.01e+00,-1.01e+00)	0.002612
alpha_AR_MC_EES_MAT	0.0000e+00	8.1793e-05	(+1.01e+00,-1.01e+00)	0.007549
alpha_AR_MC_EES_PS	0.0000e+00	-1.1652e-05	(+1.01e+00,-1.01e+00)	0.000923
alpha_AR_MC_EES_Z	0.0000e+00	-3.3956e-04	(+1.01e+00,-1.01e+00)	0.011100
alpha_AR_MC_ID	0.0000e+00	-5.3696e-07	(+1.01e+00,-1.01e+00)	0.000375
alpha_AR_MC_JER	0.0000e+00	-1.0628e-03	(+1.01e+00,-1.00e+00)	0.092112
alpha_AR_MC_JES	0.0000e+00	6.0144e-04	(+1.01e+00,-1.01e+00)	0.031835
alpha_AR_MC_MS	0.0000e+00	-3.1208e-05	(+1.01e+00,-1.01e+00)	0.000157
alpha_AR_MC_RESOST	0.0000e+00	-8.5660e-05	(+1.01e+00,-1.01e+00)	0.006278
alpha_AR_MC_SCALEST	0.0000e+00	5.7085e-04	(+1.01e+00,-1.01e+00)	0.068254
alpha_AR_fakes_ELFR	0.0000e+00	-4.5026e-05	(+1.01e+00,-1.01e+00)	0.273122
alpha_AR_fakes_ELRE	0.0000e+00	5.4730e-03	(+1.00e+00,-1.01e+00)	0.109334
alpha_AR_fakes_MUFR	0.0000e+00	4.5457e-03	(+1.00e+00,-1.01e+00)	0.139541
alpha_AR_fakes_MURE	0.0000e+00	6.9542e-03	(+9.99e-01,-1.01e+00)	0.035222
gamma_shape_mcstat_Higgs_WWCR1_obs_cuts_bin_0	1.0000e+00	1.0000e+00	(+1.93e-02,-1.93e-02)	0.015836
gamma_shape_mcstat_Higgs_eeZCR4a_obs_cuts_bin_0	1.0000e+00	9.9812e-01	(+4.63e-01,-4.60e-01)	0.001989
gamma_shape_mcstat_Higgs_emuTopCR4_obs_cuts_bin_0	1.0000e+00	1.0000e+00	(+3.69e-02,-3.69e-02)	0.002532
gamma_shape_mcstat_Higgs_mmZCR4a_obs_cuts_bin_0	1.0000e+00	1.0001e+00	(+1.88e-01,-1.88e-01)	0.000328
gamma_shape_mcstat_WW_WWCR1_obs_cuts_bin_0	1.0000e+00	9.9998e-01	(+7.69e-03,-7.65e-03)	0.211496
gamma_shape_mcstat_WW_eeZCR4a_obs_cuts_bin_0	1.0000e+00	9.9870e-01	(+1.46e-01,-1.46e-01)	0.028827
gamma_shape_mcstat_WW_emuTopCR4_obs_cuts_bin_0	1.0000e+00	1.0000e+00	(+2.64e-02,-2.65e-02)	0.020057
gamma_shape_mcstat_WW_mmZCR4a_obs_cuts_bin_0	1.0000e+00	1.0015e+00	(+1.31e-01,-1.32e-01)	0.036500
gamma_shape_mcstat_ZV_WWCR1_obs_cuts_bin_0	1.0000e+00	1.0000e+00	(+3.86e-02,-3.86e-02)	0.033615
gamma_shape_mcstat_ZV_eeZCR4a_obs_cuts_bin_0	1.0000e+00	9.9893e-01	(+2.77e-02,-2.78e-02)	0.121470
gamma_shape_mcstat_ZV_emuTopCR4_obs_cuts_bin_0	1.0000e+00	1.0000e+00	(+7.27e-02,-7.28e-02)	0.005206
gamma_shape_mcstat_ZV_mmZCR4a_obs_cuts_bin_0	1.0000e+00	1.0009e+00	(+2.37e-02,-2.38e-02)	0.121972
gamma_shape_mcstat_Ztt_emuTopCR4_obs_cuts_bin_0	1.0000e+00	9.9933e-01	(+3.47e-01,-3.46e-01)	0.096632
gamma_shape_mcstat_ttst_WWCR1_obs_cuts_bin_0	1.0000e+00	9.9990e-01	(+5.45e-02,-5.43e-02)	0.188240
gamma_shape_mcstat_ttst_eeZCR4a_obs_cuts_bin_0	1.0000e+00	9.3016e-01	(+1.50e+00,-9.30e-01)	0.087095
gamma_shape_mcstat_ttst_emuTopCR4_obs_cuts_bin_0	1.0000e+00	1.0000e+00	(+5.04e-03,-5.11e-03)	0.512790
gamma_shape_mcstat_ttst_mmZCR4a_obs_cuts_bin_0	1.0000e+00	9.9137e-01	(+1.00e+00,-9.82e-01)	0.007756
mu_2LTop	1.0000e+00	1.0582e+00	(+5.40e-02,-3.96e-02)	0.978019
mu_2LWW	1.0000e+00	1.1187e+00	(+1.47e-01,-1.27e-01)	0.927415
mu_2LZV	1.0000e+00	1.0578e+00	(+1.64e-01,-1.40e-01)	0.581163

Figure E.1: Results of the “background-only” fit for SR- $m_{T2,90}$ , for the 2012 analysis [5]. The definitions of the nuisance parameters are provided in Table E.1.

Floating Parameter	InitialValue	FinalValue (+HiError,-LoError)	GblCorr.
Lumi	1.0000e+00	9.9996e-01 (+2.82e-02,-2.81e-02)	0.068140
alpha_AR_FIT_BT	0.0000e+00	1.1692e-01 (+8.89e-01,-1.12e+00)	0.961881
alpha_AR_FIT_BTC	0.0000e+00	3.1250e-04 (+1.01e+00,-1.01e+00)	0.037804
alpha_AR_FIT_BTL	0.0000e+00	-1.1003e-02 (+1.02e+00,-9.95e-01)	0.336595
alpha_AR_FIT_EER	0.0000e+00	-1.5584e-03 (+1.01e+00,-1.01e+00)	0.042631
alpha_AR_FIT_EES_MAT	0.0000e+00	1.3772e-02 (+1.01e+00,-1.00e+00)	0.085855
alpha_AR_FIT_EES_PS	0.0000e+00	-1.0245e-03 +/- 9.84e-01	0.095824
alpha_AR_FIT_EES_Z	0.0000e+00	2.8762e-02 (+1.00e+00,-1.01e+00)	0.295596
alpha_AR_FIT_ID	0.0000e+00	-2.6133e-05 (+1.01e+00,-1.01e+00)	0.005400
alpha_AR_FIT_JER	0.0000e+00	4.2974e-02 (+9.98e-01,-9.98e-01)	0.934489
alpha_AR_FIT_JES	0.0000e+00	1.5665e-02 (+9.92e-01,-1.02e+00)	0.945054
alpha_AR_FIT_MS	0.0000e+00	-4.2437e-03 (+1.01e+00,-1.01e+00)	0.040312
alpha_AR_FIT_RESOST	0.0000e+00	1.3268e-02 (+1.01e+00,-1.01e+00)	0.053843
alpha_AR_FIT_SCALEST	0.0000e+00	1.3540e-02 (+1.01e+00,-1.01e+00)	0.217566
alpha_AR_MC_BT	0.0000e+00	4.0051e-05 (+1.01e+00,-1.01e+00)	0.005094
alpha_AR_MC_BTC	0.0000e+00	5.8660e-05 (+1.01e+00,-1.01e+00)	0.006888
alpha_AR_MC_BTL	0.0000e+00	-2.3196e-04 (+1.01e+00,-1.01e+00)	0.030752
alpha_AR_MC_EER	0.0000e+00	-4.6137e-05 (+1.01e+00,-1.01e+00)	0.002610
alpha_AR_MC_EES_MAT	0.0000e+00	-6.7647e-05 (+1.01e+00,-1.01e+00)	0.007549
alpha_AR_MC_EES_PS	0.0000e+00	9.6076e-06 (+1.01e+00,-1.01e+00)	0.000922
alpha_AR_MC_EES_Z	0.0000e+00	4.5881e-04 (+1.01e+00,-1.01e+00)	0.011075
alpha_AR_MC_ID	0.0000e+00	2.3458e-06 (+1.01e+00,-1.01e+00)	0.000375
alpha_AR_MC_JER	0.0000e+00	1.8248e-03 (+1.01e+00,-1.01e+00)	0.092085
alpha_AR_MC_JES	0.0000e+00	-2.0505e-04 (+1.01e+00,-1.01e+00)	0.031821
alpha_AR_MC_MS	0.0000e+00	4.9439e-06 (+1.01e+00,-1.01e+00)	0.000118
alpha_AR_MC_RESOST	0.0000e+00	-1.3261e-04 (+1.01e+00,-1.01e+00)	0.006276
alpha_AR_MC_SCALEST	0.0000e+00	-1.9227e-03 (+1.01e+00,-1.00e+00)	0.068072
alpha_AR_fakes_ELF	0.0000e+00	-5.3083e-03 (+1.01e+00,-1.00e+00)	0.275264
alpha_AR_fakes_ELF	0.0000e+00	5.2836e-03 (+9.96e-01,-1.02e+00)	0.109606
alpha_AR_fakes_MUFR	0.0000e+00	5.3191e-03 (+1.00e+00,-1.01e+00)	0.139534
alpha_AR_fakes_MURE	0.0000e+00	6.9341e-03 (+9.99e-01,-1.01e+00)	0.034974
gamma_shape_mcstat_Higgs_WWCR1_obs_cuts_bin_0	1.0000e+00	1.0000e+00 (+1.93e-02,-1.93e-02)	0.015840
gamma_shape_mcstat_Higgs_eeZCR4b_obs_cuts_bin_0	1.0000e+00	9.9502e-01 (+6.90e-01,-6.81e-01)	0.001809
gamma_shape_mcstat_Higgs_emuTopCR4_obs_cuts_bin_0	1.0000e+00	1.0000e+00 (+3.69e-02,-3.69e-02)	0.002532
gamma_shape_mcstat_Higgs_mmZCR4b_obs_cuts_bin_0	1.0000e+00	9.9984e-01 (+2.59e-01,-2.59e-01)	0.000364
gamma_shape_mcstat_WW_WWCR1_obs_cuts_bin_0	1.0000e+00	9.9997e-01 (+7.70e-03,-7.64e-03)	0.212256
gamma_shape_mcstat_WW_eeZCR4b_obs_cuts_bin_0	1.0000e+00	9.9780e-01 (+1.92e-01,-1.92e-01)	0.022192
gamma_shape_mcstat_WW_emuTopCR4_obs_cuts_bin_0	1.0000e+00	1.0000e+00 (+2.64e-02,-2.65e-02)	0.020108
gamma_shape_mcstat_WW_mmZCR4b_obs_cuts_bin_0	1.0000e+00	1.0023e+00 (+1.66e-01,-1.66e-01)	0.032694
gamma_shape_mcstat_ZV_WWCR1_obs_cuts_bin_0	1.0000e+00	9.9998e-01 (+3.86e-02,-3.86e-02)	0.029470
gamma_shape_mcstat_ZV_eeZCR4b_obs_cuts_bin_0	1.0000e+00	9.9804e-01 (+3.55e-02,-3.55e-02)	0.116097
gamma_shape_mcstat_ZV_emuTopCR4_obs_cuts_bin_0	1.0000e+00	1.0000e+00 (+7.27e-02,-7.28e-02)	0.004561
gamma_shape_mcstat_ZV_mmZCR4b_obs_cuts_bin_0	1.0000e+00	1.0015e+00 (+3.12e-02,-3.11e-02)	0.109810
gamma_shape_mcstat_Ztt_emuTopCR4_obs_cuts_bin_0	1.0000e+00	9.9964e-01 (+3.47e-01,-3.46e-01)	0.096549
gamma_shape_mcstat_ttst_WWCR1_obs_cuts_bin_0	1.0000e+00	9.9977e-01 (+5.46e-02,-5.42e-02)	0.188400
gamma_shape_mcstat_ttst_emuTopCR4_obs_cuts_bin_0	1.0000e+00	1.0000e+00 (+5.05e-03,-5.10e-03)	0.512786
mu_2LTop	1.0000e+00	1.0581e+00 (+5.43e-02,-3.94e-02)	0.978118
mu_2LWW	1.0000e+00	1.1228e+00 (+1.46e-01,-1.29e-01)	0.930282
mu_2LZV	1.0000e+00	9.2706e-01 (+1.71e-01,-1.47e-01)	0.430297

Figure E.2: Results of the “background-only” fit for SR- $m_{T2,110}$ , for the 2012 analysis [5]. The definitions of the nuisance parameters are provided in Table E.1.

Fit parameter	Explanation
Lumi	Luminosity uncertainty, taken to be 2.8% for the $20.3fb^{-1}$ dataset
alpha_AR_FIT_BTBTB	Uncertainties in the b-tagging weights for b-jets, c-jets and light flavour jets. Applied to all "fitted" backgrounds
alpha_AR_FIT_BTCTC	
alpha_AR_FIT_BTTLT	
alpha_AR_FIT_EER	Uncertainty in electron energy resolution, applied to all "fitted" backgrounds
alpha_AR_FIT_EES_MAT	Electron energy scale uncertainties, arising from uncertainties due to Material, "PS" (need to find out what this is) and the Z $\rightarrow$ ee scale (which is a combination of uncertainties due to the method, statistics and choice of generator). Applied to all "fitted" backgrounds
alpha_AR_FIT_EES_PS	
alpha_AR_FIT_EES_Z	
alpha_AR_FIT_ID	Muon ID resolution uncertainty, applied to all "fitted" backgrounds
alpha_AR_FIT_JER	Jet energy resolution uncertainty, applied to all "fitted" backgrounds
alpha_AR_FIT_JES	Jet energy scale uncertainty, applied to all "fitted" backgrounds
alpha_AR_FIT_MS	Muon MS resolution uncertainty, applied to all "fitted" backgrounds
alpha_AR_FIT_RESOST	Uncertainty in resolution of the MET soft term, applied to all "fitted" backgrounds
alpha_AR_FIT_SCALEST	Uncertainty in the scale of the MET soft term, applied to all "fitted" backgrounds
alpha_AR_MC_BTBTB	Uncertainties in the b-tagging weights for b-jets, c-jets and light flavour jets. Applied to all "non-fitted" backgrounds
alpha_AR_MC_BTCTC	
alpha_AR_MC_BTTLT	
alpha_AR_MC_EER	Uncertainty in electron energy resolution, applied to all "fitted" backgrounds
alpha_AR_MC_EES_MAT	Electron energy scale uncertainties, arising from uncertainties due to Material, "PS" (need to find out what this is) and the Z $\rightarrow$ ee scale (which is a combination of uncertainties due to the method, statistics and choice of generator). Applied to all "non-fitted" backgrounds
alpha_AR_MC_EES_PS	
alpha_AR_MC_EES_Z	
alpha_AR_MC_ID	Muon ID resolution uncertainty, applied to all "non-fitted" backgrounds
alpha_AR_MC_JER	Jet energy resolution uncertainty, applied to all "non-fitted" backgrounds
alpha_AR_MC_JES	Jet energy scale uncertainty, applied to all "non-fitted" backgrounds
alpha_AR_MC_MS	Muon MS resolution uncertainty, applied to all "non-fitted" backgrounds
alpha_AR_MC_RESOST	Uncertainty in resolution of the MET soft term, applied to all "non-fitted" backgrounds
alpha_AR_MC_SCALEST	Uncertainty in the scale of the MET soft term, applied to all "non-fitted" backgrounds
alpha_AR_fakes_ELFR	Uncertainty in the fake electron fake-rate
alpha_AR_fakes_ELRE	Uncertainty in the fake electron real efficiency
alpha_AR_fakes_MUFR	Uncertainty in the fake muon fake-rate
alpha_AR_fakes_MURE	Uncertainty in the fake muon real efficiencies
gamma_shape_mcstat_XXX	Uncorrelated nuisance parameters representing the statistical uncertainties of each background component in all of the channels included in the Simultaneous fit. For a given channel, a background component is only included if it has a non-zero count in that region, so not all background components feature in every channel. If they don't, a nuisance parameter is not assigned for the statistical uncertainty of that background
mu_2LTop	Normalisation scaling factor for the top background
mu_2LWW	Normalisation scaling factor for the WW background
mu_2LZV	Normalisation scaling factor for the ZV background

Table E.1: Descriptions of the fit parameters included in the simultaneous fit used for the analysis on the 2012 dataset [5].

fore not investigated further.

Breakdowns of the impacts of systematic uncertainties on the background estimates in the signal regions are provided in Tables E.2 to E.6. The uncertainties giving the largest deviation from the total background count are listed at the top. The contribution due to each source of uncertainty is given as the absolute error as well as the relative percentage error (which is given in square brackets). The generator uncertainty on the diboson production was calculated by taking the relative difference between two different Monte Carlo generators (*Sherpa* and *POWHEG*) which was the agreed method within the ATLAS SUSY working group. For the analysis this was calculated explicitly rather than including the information in the fit, and was applied to the signal region expectations only. These are the nuisance parameters “alpha\_SR4a\_WW\_hackGen” etc. The reason for including a single number by hand for the generator uncertainties in all channels was that by averaging over the  $e^\pm e^\mp$ ,  $\mu^\pm \mu^\mp$  and  $e^\pm \mu^\mp$  channels, the impact of limited Monte Carlo statistics on the diboson generator uncertainty was reduced. A similar method was used to apply a single number for the theory uncertainty on the top background; this is the nuisance parameter “alpha\_ALLSR4\_TopTheory”. These numbers were calculated by other analysers so details will not be discussed here. It should be noted that the uncertainties may not add in quadrature to give the total uncertainty due to correlations. Only the backgrounds that contribute to each channel are included in the tables.





SR- $m_{T2,90} e^\pm e^\mp$	Total	Top	WW	Z + V
Total background expectation	16.63	0.85	9.33	6.34
Total statistical	$\pm 1.29$	$\pm 0.86$	$\pm 0.81$	$\pm 0.48$
Total background systematic	$\pm 2.31$ [13.89%]	$\pm 1.05$ [122.94%]	$\pm 1.57$ [16.81%]	$\pm 1.46$ [23.01%]
alpha_AR_FIT_JER	$\pm 1.58$ [9.5%]	$\pm 0.45$ [52.4%]	$\pm 0.74$ [8.0%]	$\pm 0.39$ [6.1%]
alpha_SR4a_ZV_hackGen	$\pm 1.14$ [6.9%]	$\pm 0.00$ [0.00%]	$\pm 0.00$ [0.00%]	$\pm 1.14$ [18.0%]
mu_2LWW	$\pm 1.14$ [6.9%]	$\pm 0.00$ [0.00%]	$\pm 1.14$ [12.2%]	$\pm 0.00$ [0.00%]
alpha_SR4a_WW_hackGen	$\pm 1.12$ [6.7%]	$\pm 0.00$ [0.00%]	$\pm 1.12$ [12.0%]	$\pm 0.00$ [0.00%]
mu_2LZV	$\pm 0.91$ [5.5%]	$\pm 0.00$ [0.00%]	$\pm 0.00$ [0.00%]	$\pm 0.91$ [14.4%]
gamma_shape_mcstat_top_eeSR4a	$\pm 0.86$ [5.2%]	$\pm 0.86$ [101.0%]	$\pm 0.00$ [0.00%]	$\pm 0.00$ [0.00%]
gamma_shape_mcstat_WW_eeSR4a	$\pm 0.81$ [4.8%]	$\pm 0.00$ [0.00%]	$\pm 0.81$ [8.6%]	$\pm 0.00$ [0.00%]
alpha_AR_FIT_EES_Z	$\pm 0.64$ [3.9%]	$\pm 0.00$ [0.07%]	$\pm 0.57$ [6.1%]	$\pm 0.07$ [1.1%]
gamma_shape_mcstat_ZV_eeSR4a	$\pm 0.48$ [2.9%]	$\pm 0.00$ [0.00%]	$\pm 0.00$ [0.00%]	$\pm 0.48$ [7.6%]
alpha_AR_FIT_RESOST	$\pm 0.27$ [1.6%]	$\pm 0.32$ [37.8%]	$\pm 0.06$ [0.60%]	$\pm 0.00$ [0.06%]
alpha_ALLSR4_Top_Theory	$\pm 0.21$ [1.3%]	$\pm 0.21$ [25.0%]	$\pm 0.00$ [0.00%]	$\pm 0.00$ [0.00%]
alpha_AR_FIT_SCALEST	$\pm 0.16$ [0.95%]	$\pm 0.00$ [0.00%]	$\pm 0.13$ [1.4%]	$\pm 0.03$ [0.43%]
alpha_eeSR4a_Fake_Stat	$\pm 0.14$ [0.87%]	$\pm 0.00$ [0.00%]	$\pm 0.00$ [0.00%]	$\pm 0.00$ [0.00%]
alpha_AR_FIT_EES_MAT	$\pm 0.13$ [0.81%]	$\pm 0.00$ [0.00%]	$\pm 0.10$ [1.1%]	$\pm 0.03$ [0.52%]
alpha_eeSR4a_Fake_Syst	$\pm 0.10$ [0.63%]	$\pm 0.00$ [0.00%]	$\pm 0.00$ [0.00%]	$\pm 0.00$ [0.00%]
alpha_AR_FIT_JES	$\pm 0.06$ [0.39%]	$\pm 0.00$ [0.00%]	$\pm 0.06$ [0.69%]	$\pm 0.00$ [0.00%]
gamma_shape_mcstat_Higgs_eeSR4a	$\pm 0.04$ [0.23%]	$\pm 0.00$ [0.00%]	$\pm 0.00$ [0.00%]	$\pm 0.00$ [0.00%]
alpha_AR_FIT_BTL	$\pm 0.04$ [0.23%]	$\pm 0.00$ [0.48%]	$\pm 0.02$ [0.26%]	$\pm 0.01$ [0.16%]
mu_2LTop	$\pm 0.04$ [0.23%]	$\pm 0.04$ [4.4%]	$\pm 0.00$ [0.00%]	$\pm 0.00$ [0.00%]
alpha_AR_FIT_EER	$\pm 0.01$ [0.06%]	$\pm 0.03$ [3.7%]	$\pm 0.01$ [0.16%]	$\pm 0.03$ [0.42%]
alpha_AR_MC_JER	$\pm 0.01$ [0.05%]	$\pm 0.00$ [0.00%]	$\pm 0.00$ [0.00%]	$\pm 0.00$ [0.00%]
Lumi	$\pm 0.00$ [0.02%]	$\pm 0.00$ [0.00%]	$\pm 0.00$ [0.00%]	$\pm 0.00$ [0.00%]
alpha_AR_FIT_EES_PS	$\pm 0.00$ [0.02%]	$\pm 0.00$ [0.00%]	$\pm 0.00$ [0.00%]	$\pm 0.00$ [0.04%]
alpha_AR_FIT_BTC	$\pm 0.00$ [0.00%]	$\pm 0.00$ [0.00%]	$\pm 0.00$ [0.00%]	$\pm 0.00$ [0.01%]
alpha_AR_MC_EES_Z	$\pm 0.00$ [0.00%]	$\pm 0.00$ [0.00%]	$\pm 0.00$ [0.00%]	$\pm 0.00$ [0.00%]
alpha_AR_MC_EES_MAT	$\pm 0.00$ [0.00%]	$\pm 0.00$ [0.00%]	$\pm 0.00$ [0.00%]	$\pm 0.00$ [0.00%]
alpha_AR_MC_EER	$\pm 0.00$ [0.00%]	$\pm 0.00$ [0.00%]	$\pm 0.00$ [0.00%]	$\pm 0.00$ [0.00%]
alpha_AR_MC_RESOST	$\pm 0.00$ [0.00%]	$\pm 0.00$ [0.00%]	$\pm 0.00$ [0.00%]	$\pm 0.00$ [0.00%]
alpha_AR_MC_SCALEST	$\pm 0.00$ [0.00%]	$\pm 0.00$ [0.00%]	$\pm 0.00$ [0.00%]	$\pm 0.00$ [0.00%]
alpha_AR_MC_EES_PS	$\pm 0.00$ [0.00%]	$\pm 0.00$ [0.00%]	$\pm 0.00$ [0.00%]	$\pm 0.00$ [0.00%]
alpha_AR_MC_BTL	$\pm 0.00$ [0.00%]	$\pm 0.00$ [0.00%]	$\pm 0.00$ [0.00%]	$\pm 0.00$ [0.00%]
alpha_AR_fakes_MURE	$\pm 0.00$ [0.00%]	$\pm 0.00$ [0.00%]	$\pm 0.00$ [0.00%]	$\pm 0.00$ [0.00%]
gamma_shape_mcstat_WW_mmZXCR4a	$\pm 0.00$ [0.00%]	$\pm 0.00$ [0.00%]	$\pm 0.00$ [0.00%]	$\pm 0.00$ [0.00%]
gamma_shape_mcstat_Higgs_eeZXCR4a	$\pm 0.00$ [0.00%]	$\pm 0.00$ [0.00%]	$\pm 0.00$ [0.00%]	$\pm 0.00$ [0.00%]
alpha_AR_MC_BTC	$\pm 0.00$ [0.00%]	$\pm 0.00$ [0.00%]	$\pm 0.00$ [0.00%]	$\pm 0.00$ [0.00%]
alpha_AR_MC_BT	$\pm 0.00$ [0.00%]	$\pm 0.00$ [0.00%]	$\pm 0.00$ [0.00%]	$\pm 0.00$ [0.00%]
alpha_AR_MC_ID	$\pm 0.00$ [0.00%]	$\pm 0.00$ [0.00%]	$\pm 0.00$ [0.00%]	$\pm 0.00$ [0.00%]
alpha_AR_FIT_BT	$\pm 0.00$ [0.00%]	$\pm 0.00$ [0.00%]	$\pm 0.00$ [0.00%]	$\pm 0.00$ [0.00%]
alpha_AR_FIT_ID	$\pm 0.00$ [0.00%]	$\pm 0.00$ [0.00%]	$\pm 0.00$ [0.00%]	$\pm 0.00$ [0.00%]
gamma_shape_mcstat_Higgs_mmZXCR4a	$\pm 0.00$ [0.00%]	$\pm 0.00$ [0.00%]	$\pm 0.00$ [0.00%]	$\pm 0.00$ [0.00%]
gamma_shape_mcstat_WW_emuTopCR4	$\pm 0.00$ [0.00%]	$\pm 0.00$ [0.00%]	$\pm 0.00$ [0.00%]	$\pm 0.00$ [0.00%]
alpha_AR_fakes_MUFR	$\pm 0.00$ [0.00%]	$\pm 0.00$ [0.00%]	$\pm 0.00$ [0.00%]	$\pm 0.00$ [0.00%]
gamma_shape_mcstat_top_WWCR1	$\pm 0.00$ [0.00%]	$\pm 0.00$ [0.00%]	$\pm 0.00$ [0.00%]	$\pm 0.00$ [0.00%]
alpha_AR_MC_JES	$\pm 0.00$ [0.00%]	$\pm 0.00$ [0.00%]	$\pm 0.00$ [0.00%]	$\pm 0.00$ [0.00%]
alpha_AR_FIT_MS	$\pm 0.00$ [0.00%]	$\pm 0.00$ [0.00%]	$\pm 0.00$ [0.00%]	$\pm 0.00$ [0.00%]
alpha_AR_fakes_ELRE	$\pm 0.00$ [0.00%]	$\pm 0.00$ [0.00%]	$\pm 0.00$ [0.00%]	$\pm 0.00$ [0.00%]
gamma_shape_mcstat_ZV_mmZXCR4a	$\pm 0.00$ [0.00%]	$\pm 0.00$ [0.00%]	$\pm 0.00$ [0.00%]	$\pm 0.00$ [0.00%]
gamma_shape_mcstat_ZV_WWCR1	$\pm 0.00$ [0.00%]	$\pm 0.00$ [0.00%]	$\pm 0.00$ [0.00%]	$\pm 0.00$ [0.00%]
alpha_AR_fakes_ELFR	$\pm 0.00$ [0.00%]	$\pm 0.00$ [0.00%]	$\pm 0.00$ [0.00%]	$\pm 0.00$ [0.00%]
gamma_shape_mcstat_top_mmZXCR4a	$\pm 0.00$ [0.00%]	$\pm 0.00$ [0.00%]	$\pm 0.00$ [0.00%]	$\pm 0.00$ [0.00%]
gamma_shape_mcstat_Higgs_WWCR1	$\pm 0.00$ [0.00%]	$\pm 0.00$ [0.00%]	$\pm 0.00$ [0.00%]	$\pm 0.00$ [0.00%]
gamma_shape_mcstat_Ztt_emuTopCR4	$\pm 0.00$ [0.00%]	$\pm 0.00$ [0.00%]	$\pm 0.00$ [0.00%]	$\pm 0.00$ [0.00%]
gamma_shape_mcstat_ZV_eeZXCR4a	$\pm 0.00$ [0.00%]	$\pm 0.00$ [0.00%]	$\pm 0.00$ [0.00%]	$\pm 0.00$ [0.00%]
gamma_shape_mcstat_WW_WWCR1	$\pm 0.00$ [0.00%]	$\pm 0.00$ [0.00%]	$\pm 0.00$ [0.00%]	$\pm 0.00$ [0.00%]
gamma_shape_mcstat_top_eeZXCR4a	$\pm 0.00$ [0.00%]	$\pm 0.00$ [0.00%]	$\pm 0.00$ [0.00%]	$\pm 0.00$ [0.00%]
gamma_shape_mcstat_Higgs_emuTopCR4	$\pm 0.00$ [0.00%]	$\pm 0.00$ [0.00%]	$\pm 0.00$ [0.00%]	$\pm 0.00$ [0.00%]
gamma_shape_mcstat_WW_eeZXCR4a	$\pm 0.00$ [0.00%]	$\pm 0.00$ [0.00%]	$\pm 0.00$ [0.00%]	$\pm 0.00$ [0.00%]
alpha_AR_MC_MS	$\pm 0.00$ [0.00%]	$\pm 0.00$ [0.00%]	$\pm 0.00$ [0.00%]	$\pm 0.00$ [0.00%]
gamma_shape_mcstat_top_emuTopCR4	$\pm 0.00$ [0.00%]	$\pm 0.00$ [0.00%]	$\pm 0.00$ [0.00%]	$\pm 0.00$ [0.00%]
gamma_shape_mcstat_ZV_emuTopCR4	$\pm 0.00$ [0.00%]	$\pm 0.00$ [0.00%]	$\pm 0.00$ [0.00%]	$\pm 0.00$ [0.00%]

Table E.2: Breakdown of the systematic uncertainties on the background estimates in the  $e^\pm e^\mp$  channel of SR- $m_{T2,90}$ , for the analysis on 2012 data [5]. The percentages show the size of the uncertainty relative to the total expected background.

$SR\text{-}m_{T2,90} e^\pm \mu^\mp$	Total	Top	WW	Z + V
Total background expectation	20.66	5.59	14.10	0.78
Total statistical	$\pm 1.56$	$\pm 1.28$	$\pm 0.85$	$\pm 0.18$
Total background systematic	$\pm 3.23$ [15.63%]	$\pm 2.11$ [37.70%]	$\pm 2.18$ [15.47%]	$\pm 0.25$ [32.32%]
alpha_AR_FIT_JER	$\pm 2.39$ [11.6%]	$\pm 0.53$ [9.5%]	$\pm 1.83$ [13.0%]	$\pm 0.02$ [3.1%]
mu_2LWW	$\pm 1.73$ [8.4%]	$\pm 0.00$ [0.00%]	$\pm 1.73$ [12.2%]	$\pm 0.00$ [0.00%]
alpha_SR4a_WW_hackGen	$\pm 1.69$ [8.2%]	$\pm 0.00$ [0.00%]	$\pm 1.69$ [12.0%]	$\pm 0.00$ [0.00%]
alpha_ALLSR4_Top_Theory	$\pm 1.40$ [6.8%]	$\pm 1.40$ [25.0%]	$\pm 0.00$ [0.00%]	$\pm 0.00$ [0.00%]
gamma_shape_mcstat_top_emuSR4a	$\pm 1.28$ [6.2%]	$\pm 1.28$ [22.8%]	$\pm 0.00$ [0.00%]	$\pm 0.00$ [0.00%]
alpha_AR_FIT_SCALEST	$\pm 1.22$ [5.9%]	$\pm 0.46$ [8.3%]	$\pm 0.72$ [5.1%]	$\pm 0.04$ [4.6%]
alpha_AR_FIT_EES_Z	$\pm 0.92$ [4.4%]	$\pm 0.33$ [5.9%]	$\pm 0.55$ [3.9%]	$\pm 0.03$ [3.9%]
gamma_shape_mcstat_WW_emuSR4a	$\pm 0.85$ [4.1%]	$\pm 0.00$ [0.00%]	$\pm 0.85$ [6.0%]	$\pm 0.00$ [0.00%]
alpha_AR_FIT_MS	$\pm 0.38$ [1.9%]	$\pm 0.33$ [5.9%]	$\pm 0.05$ [0.37%]	$\pm 0.00$ [0.62%]
mu_2LTop	$\pm 0.25$ [1.2%]	$\pm 0.25$ [4.4%]	$\pm 0.00$ [0.00%]	$\pm 0.00$ [0.00%]
alpha_AR_FIT_RESOST	$\pm 0.23$ [1.1%]	$\pm 0.23$ [4.2%]	$\pm 0.01$ [0.6%]	$\pm 0.01$ [0.78%]
gamma_shape_mcstat_ZV_emuSR4a	$\pm 0.18$ [0.85%]	$\pm 0.00$ [0.00%]	$\pm 0.00$ [0.00%]	$\pm 0.18$ [22.7%]
alpha_SR4a_ZV_hackGen	$\pm 0.14$ [0.68%]	$\pm 0.00$ [0.00%]	$\pm 0.00$ [0.00%]	$\pm 0.14$ [18.0%]
alpha_emSR4a_Fake_Stat	$\pm 0.11$ [0.56%]	$\pm 0.00$ [0.00%]	$\pm 0.00$ [0.00%]	$\pm 0.00$ [0.00%]
mu_2LZV	$\pm 0.11$ [0.54%]	$\pm 0.00$ [0.00%]	$\pm 0.00$ [0.00%]	$\pm 0.11$ [14.4%]
alpha_emSR4a_Fake_Syst	$\pm 0.07$ [0.36%]	$\pm 0.00$ [0.00%]	$\pm 0.00$ [0.00%]	$\pm 0.00$ [0.00%]
alpha_AR_FIT_EES_MAT	$\pm 0.07$ [0.35%]	$\pm 0.00$ [0.02%]	$\pm 0.09$ [0.62%]	$\pm 0.01$ [1.9%]
alpha_AR_FIT_ID	$\pm 0.07$ [0.34%]	$\pm 0.02$ [0.31%]	$\pm 0.07$ [0.53%]	$\pm 0.01$ [1.7%]
gamma_shape_mcstat_Higgs_emuSR4a	$\pm 0.05$ [0.23%]	$\pm 0.00$ [0.00%]	$\pm 0.00$ [0.00%]	$\pm 0.00$ [0.00%]
alpha_AR_FIT_BTL	$\pm 0.04$ [0.21%]	$\pm 0.01$ [0.10%]	$\pm 0.04$ [0.25%]	$\pm 0.00$ [0.20%]
alpha_AR_FIT_JES	$\pm 0.03$ [0.16%]	$\pm 0.00$ [0.00%]	$\pm 0.03$ [0.24%]	$\pm 0.00$ [0.00%]
alpha_AR_FIT_EER	$\pm 0.03$ [0.13%]	$\pm 0.02$ [0.31%]	$\pm 0.03$ [0.18%]	$\pm 0.02$ [2.4%]
alpha_AR_MC_SCALEST	$\pm 0.01$ [0.06%]	$\pm 0.00$ [0.00%]	$\pm 0.00$ [0.00%]	$\pm 0.00$ [0.00%]
alpha_AR_MC_ID	$\pm 0.01$ [0.06%]	$\pm 0.00$ [0.00%]	$\pm 0.00$ [0.00%]	$\pm 0.00$ [0.00%]
alpha_AR_MC_EES_Z	$\pm 0.01$ [0.04%]	$\pm 0.00$ [0.00%]	$\pm 0.00$ [0.00%]	$\pm 0.00$ [0.00%]
Lumi	$\pm 0.01$ [0.03%]	$\pm 0.00$ [0.00%]	$\pm 0.00$ [0.00%]	$\pm 0.00$ [0.00%]
alpha_AR_MC_JER	$\pm 0.00$ [0.00%]	$\pm 0.00$ [0.00%]	$\pm 0.00$ [0.00%]	$\pm 0.00$ [0.00%]
alpha_AR_FIT_BTC	$\pm 0.00$ [0.00%]	$\pm 0.00$ [0.00%]	$\pm 0.00$ [0.00%]	$\pm 0.00$ [0.00%]
alpha_AR_FIT_EES_PS	$\pm 0.00$ [0.00%]	$\pm 0.00$ [0.02%]	$\pm 0.00$ [0.01%]	$\pm 0.00$ [0.02%]
alpha_AR_MC_BTL	$\pm 0.00$ [0.00%]	$\pm 0.00$ [0.00%]	$\pm 0.00$ [0.00%]	$\pm 0.00$ [0.00%]
alpha_AR_MC_EER	$\pm 0.00$ [0.00%]	$\pm 0.00$ [0.00%]	$\pm 0.00$ [0.00%]	$\pm 0.00$ [0.00%]
alpha_AR_MC_EES_MAT	$\pm 0.00$ [0.00%]	$\pm 0.00$ [0.00%]	$\pm 0.00$ [0.00%]	$\pm 0.00$ [0.00%]
alpha_AR_MC_EES_PS	$\pm 0.00$ [0.00%]	$\pm 0.00$ [0.00%]	$\pm 0.00$ [0.00%]	$\pm 0.00$ [0.00%]
alpha_AR_fakes_MURE	$\pm 0.00$ [0.00%]	$\pm 0.00$ [0.00%]	$\pm 0.00$ [0.00%]	$\pm 0.00$ [0.00%]
gamma_shape_mcstat_WW_mmZXCR4a	$\pm 0.00$ [0.00%]	$\pm 0.00$ [0.00%]	$\pm 0.00$ [0.00%]	$\pm 0.00$ [0.00%]
gamma_shape_mcstat_Higgs_eeZXCR4a	$\pm 0.00$ [0.00%]	$\pm 0.00$ [0.00%]	$\pm 0.00$ [0.00%]	$\pm 0.00$ [0.00%]
alpha_AR_MC_BTC	$\pm 0.00$ [0.00%]	$\pm 0.00$ [0.00%]	$\pm 0.00$ [0.00%]	$\pm 0.00$ [0.00%]
alpha_AR_MC_BTB	$\pm 0.00$ [0.00%]	$\pm 0.00$ [0.00%]	$\pm 0.00$ [0.00%]	$\pm 0.00$ [0.00%]
alpha_AR_FIT_BTB	$\pm 0.00$ [0.00%]	$\pm 0.00$ [0.00%]	$\pm 0.00$ [0.00%]	$\pm 0.00$ [0.00%]
gamma_shape_mcstat_Higgs_mmZXCR4a	$\pm 0.00$ [0.00%]	$\pm 0.00$ [0.00%]	$\pm 0.00$ [0.00%]	$\pm 0.00$ [0.00%]
gamma_shape_mcstat_WW_emuTopCR4	$\pm 0.00$ [0.00%]	$\pm 0.00$ [0.00%]	$\pm 0.00$ [0.00%]	$\pm 0.00$ [0.00%]
alpha_AR_fakes_MUFR	$\pm 0.00$ [0.00%]	$\pm 0.00$ [0.00%]	$\pm 0.00$ [0.00%]	$\pm 0.00$ [0.00%]
gamma_shape_mcstat_top_WWCR1	$\pm 0.00$ [0.00%]	$\pm 0.00$ [0.00%]	$\pm 0.00$ [0.00%]	$\pm 0.00$ [0.00%]
alpha_AR_MC_JES	$\pm 0.00$ [0.00%]	$\pm 0.00$ [0.00%]	$\pm 0.00$ [0.00%]	$\pm 0.00$ [0.00%]
alpha_AR_fakes_ELRE	$\pm 0.00$ [0.00%]	$\pm 0.00$ [0.00%]	$\pm 0.00$ [0.00%]	$\pm 0.00$ [0.00%]
gamma_shape_mcstat_ZV_mmZXCR4a	$\pm 0.00$ [0.00%]	$\pm 0.00$ [0.00%]	$\pm 0.00$ [0.00%]	$\pm 0.00$ [0.00%]
alpha_AR_MC_RESOST	$\pm 0.00$ [0.00%]	$\pm 0.00$ [0.00%]	$\pm 0.00$ [0.00%]	$\pm 0.00$ [0.00%]
gamma_shape_mcstat_ZV_WWCR1	$\pm 0.00$ [0.00%]	$\pm 0.00$ [0.00%]	$\pm 0.00$ [0.00%]	$\pm 0.00$ [0.00%]
alpha_AR_fakes_ELF	$\pm 0.00$ [0.00%]	$\pm 0.00$ [0.00%]	$\pm 0.00$ [0.00%]	$\pm 0.00$ [0.00%]
gamma_shape_mcstat_top_mmZXCR4a	$\pm 0.00$ [0.00%]	$\pm 0.00$ [0.00%]	$\pm 0.00$ [0.00%]	$\pm 0.00$ [0.00%]
gamma_shape_mcstat_Higgs_WWCR1	$\pm 0.00$ [0.00%]	$\pm 0.00$ [0.00%]	$\pm 0.00$ [0.00%]	$\pm 0.00$ [0.00%]
gamma_shape_mcstat_Ztt_emuTopCR4	$\pm 0.00$ [0.00%]	$\pm 0.00$ [0.00%]	$\pm 0.00$ [0.00%]	$\pm 0.00$ [0.00%]
gamma_shape_mcstat_WW_eeZXCR4a	$\pm 0.00$ [0.00%]	$\pm 0.00$ [0.00%]	$\pm 0.00$ [0.00%]	$\pm 0.00$ [0.00%]
gamma_shape_mcstat_WW_WWCR1	$\pm 0.00$ [0.00%]	$\pm 0.00$ [0.00%]	$\pm 0.00$ [0.00%]	$\pm 0.00$ [0.00%]
gamma_shape_mcstat_top_eeZXCR4a	$\pm 0.00$ [0.00%]	$\pm 0.00$ [0.00%]	$\pm 0.00$ [0.00%]	$\pm 0.00$ [0.00%]
gamma_shape_mcstat_Higgs_emuTopCR4	$\pm 0.00$ [0.00%]	$\pm 0.00$ [0.00%]	$\pm 0.00$ [0.00%]	$\pm 0.00$ [0.00%]
gamma_shape_mcstat_WW_eeZXCR4a	$\pm 0.00$ [0.00%]	$\pm 0.00$ [0.00%]	$\pm 0.00$ [0.00%]	$\pm 0.00$ [0.00%]
alpha_AR_MC_MS	$\pm 0.00$ [0.00%]	$\pm 0.00$ [0.00%]	$\pm 0.00$ [0.00%]	$\pm 0.00$ [0.00%]
gamma_shape_mcstat_top_emuTopCR4	$\pm 0.00$ [0.00%]	$\pm 0.00$ [0.00%]	$\pm 0.00$ [0.00%]	$\pm 0.00$ [0.00%]
gamma_shape_mcstat_ZV_emuTopCR4	$\pm 0.00$ [0.00%]	$\pm 0.00$ [0.00%]	$\pm 0.00$ [0.00%]	$\pm 0.00$ [0.00%]

Table E.3: As in Table E.2, but for the  $e^\pm \mu^\mp$  channel of  $SR\text{-}m_{T2,90}$ .

$SR-m_{T2,90}\mu^\pm\mu^\mp$	Total	Top	WW	Z + V	Z+jets
Total background expectation	22.44	2.47	12.63	7.25	0.00
Total statistical	$\pm 1.38$	$\pm 0.93$	$\pm 0.90$	$\pm 0.45$	$\pm 0.00$
Total background systematic	$\pm 3.32$ [14.80%]	$\pm 1.81$ [73.28%]	$\pm 1.94$ [15.36%]	$\pm 1.67$ [23.05%]	$\pm 0.01$ [122.11%]
alpha_AR_FIT_JER	$\pm 3.77$ [16.8%]	$\pm 1.39$ [56.2%]	$\pm 1.48$ [11.7%]	$\pm 0.90$ [12.3%]	$\pm 0.00$ [0.00%]
mu_2LWW	$\pm 1.55$ [6.9%]	$\pm 0.00$ [0.00%]	$\pm 1.55$ [12.2%]	$\pm 0.00$ [0.00%]	$\pm 0.00$ [0.00%]
alpha_SR4a_WW_hackGen	$\pm 1.52$ [6.8%]	$\pm 0.00$ [0.00%]	$\pm 1.52$ [12.0%]	$\pm 0.00$ [0.00%]	$\pm 0.00$ [0.00%]
alpha_SR4a_ZV_hackGen	$\pm 1.31$ [5.8%]	$\pm 0.00$ [0.00%]	$\pm 0.00$ [0.00%]	$\pm 1.31$ [18.0%]	$\pm 0.00$ [0.00%]
mu_2LZV	$\pm 1.04$ [4.6%]	$\pm 0.00$ [0.00%]	$\pm 0.00$ [0.00%]	$\pm 1.04$ [14.4%]	$\pm 0.00$ [0.00%]
gamma_shape_mcstat_top_mmSR4a	$\pm 0.93$ [4.2%]	$\pm 0.93$ [37.7%]	$\pm 0.00$ [0.00%]	$\pm 0.00$ [0.00%]	$\pm 0.00$ [0.00%]
gamma_shape_mcstat_WW_mmSR4a	$\pm 0.90$ [4.0%]	$\pm 0.00$ [0.00%]	$\pm 0.90$ [7.1%]	$\pm 0.00$ [0.00%]	$\pm 0.00$ [0.00%]
alpha_AR_FIT_SCALEST	$\pm 0.71$ [3.2%]	$\pm 0.08$ [3.4%]	$\pm 0.53$ [4.2%]	$\pm 0.09$ [1.3%]	$\pm 0.00$ [0.00%]
alpha_ALLSR4_Top_Theory	$\pm 0.62$ [2.8%]	$\pm 0.62$ [25.0%]	$\pm 0.00$ [0.00%]	$\pm 0.00$ [0.00%]	$\pm 0.00$ [0.00%]
gamma_shape_mcstat_ZV_mmSR4a	$\pm 0.45$ [2.0%]	$\pm 0.00$ [0.00%]	$\pm 0.00$ [0.00%]	$\pm 0.45$ [6.2%]	$\pm 0.00$ [0.00%]
alpha_mmSR4a_Fake_Stat	$\pm 0.12$ [0.53%]	$\pm 0.00$ [0.00%]	$\pm 0.00$ [0.00%]	$\pm 0.00$ [0.00%]	$\pm 0.00$ [0.00%]
alpha_AR_FIT_MS	$\pm 0.12$ [0.52%]	$\pm 0.08$ [3.4%]	$\pm 0.07$ [0.53%]	$\pm 0.10$ [1.4%]	$\pm 0.00$ [0.00%]
mu_2LTop	$\pm 0.11$ [0.49%]	$\pm 0.11$ [4.4%]	$\pm 0.00$ [0.00%]	$\pm 0.00$ [0.00%]	$\pm 0.00$ [0.00%]
alpha_mmSR4a_Fake_Syst	$\pm 0.09$ [0.40%]	$\pm 0.00$ [0.00%]	$\pm 0.00$ [0.00%]	$\pm 0.00$ [0.00%]	$\pm 0.00$ [0.00%]
alpha_AR_FIT_RESOST	$\pm 0.05$ [0.24%]	$\pm 0.17$ [7.0%]	$\pm 0.03$ [0.25%]	$\pm 0.09$ [1.2%]	$\pm 0.00$ [0.00%]
alpha_AR_FIT_BTL	$\pm 0.04$ [0.19%]	$\pm 0.00$ [0.04%]	$\pm 0.03$ [0.25%]	$\pm 0.01$ [0.16%]	$\pm 0.00$ [0.00%]
gamma_shape_mcstat_Higgs_mmSR4a	$\pm 0.03$ [0.14%]	$\pm 0.00$ [0.00%]	$\pm 0.00$ [0.00%]	$\pm 0.00$ [0.00%]	$\pm 0.00$ [0.00%]
alpha_AR_MC_JER	$\pm 0.03$ [0.12%]	$\pm 0.00$ [0.00%]	$\pm 0.00$ [0.00%]	$\pm 0.00$ [0.00%]	$\pm 0.00$ [0.00%]
alpha_AR_FIT_JES	$\pm 0.01$ [0.04%]	$\pm 0.00$ [0.00%]	$\pm 0.01$ [0.07%]	$\pm 0.00$ [0.00%]	$\pm 0.00$ [0.00%]
gamma_shape_mcstat_Zjets_mmSR4a	$\pm 0.00$ [0.02%]	$\pm 0.00$ [0.00%]	$\pm 0.00$ [0.00%]	$\pm 0.00$ [0.00%]	$\pm 0.00$ [100.0%]
alpha_AR_MC_RESOST	$\pm 0.00$ [0.01%]	$\pm 0.00$ [0.00%]	$\pm 0.00$ [0.00%]	$\pm 0.00$ [0.00%]	$\pm 0.00$ [49.5%]
alpha_AR_MC_SCALEST	$\pm 0.00$ [0.01%]	$\pm 0.00$ [0.00%]	$\pm 0.00$ [0.00%]	$\pm 0.00$ [0.00%]	$\pm 0.00$ [49.5%]
Lumi	$\pm 0.00$ [0.01%]	$\pm 0.00$ [0.00%]	$\pm 0.00$ [0.00%]	$\pm 0.00$ [0.00%]	$\pm 0.00$ [2.8%]
alpha_AR_FIT_BTC	$\pm 0.00$ [0.01%]	$\pm 0.00$ [0.00%]	$\pm 0.00$ [0.00%]	$\pm 0.00$ [0.02%]	$\pm 0.00$ [0.00%]
alpha_AR_MC_BTC	$\pm 0.00$ [0.00%]				
alpha_AR_FIT_ID	$\pm 0.00$ [0.00%]	$\pm 0.00$ [0.00%]	$\pm 0.01$ [0.09%]	$\pm 0.01$ [0.15%]	$\pm 0.00$ [0.00%]
alpha_AR_MC_BTL	$\pm 0.00$ [0.00%]				
alpha_AR_FIT_BT	$\pm 0.00$ [0.00%]				
alpha_AR_fakes_MURE	$\pm 0.00$ [0.00%]				
gamma_shape_mcstat_WW_mmZXCR4a	$\pm 0.00$ [0.00%]				
gamma_shape_mcstat_Higgs_eeZXCR4a	$\pm 0.00$ [0.00%]				
alpha_AR_MC_BT	$\pm 0.00$ [0.00%]				
alpha_AR_MC_ID	$\pm 0.00$ [0.00%]				
alpha_AR_MC_EES_MAT	$\pm 0.00$ [0.00%]				
alpha_AR_MC_EES_Z	$\pm 0.00$ [0.00%]				
gamma_shape_mcstat_Higgs_mmZXCR4a	$\pm 0.00$ [0.00%]				
gamma_shape_mcstat_WW_emuTopCR4	$\pm 0.00$ [0.00%]				
alpha_AR_fakes_MUFR	$\pm 0.00$ [0.00%]				
alpha_AR_FIT_EER	$\pm 0.00$ [0.00%]				
gamma_shape_mcstat_top_WWCR1	$\pm 0.00$ [0.00%]				
alpha_AR_MC_JES	$\pm 0.00$ [0.00%]				
alpha_AR_fakes_ELRE	$\pm 0.00$ [0.00%]				
gamma_shape_mcstat_ZV_mmZXCR4a	$\pm 0.00$ [0.00%]				
alpha_AR_FIT_EES_PS	$\pm 0.00$ [0.00%]				
alpha_AR_FIT_EES_MAT	$\pm 0.00$ [0.00%]				
gamma_shape_mcstat_ZV_WWCR1	$\pm 0.00$ [0.00%]				
alpha_AR_fakes_ELFR	$\pm 0.00$ [0.00%]				
gamma_shape_mcstat_top_mmZXCR4a	$\pm 0.00$ [0.00%]				
gamma_shape_mcstat_Higgs_WWCR1	$\pm 0.00$ [0.00%]				
gamma_shape_mcstat_Ztt_emuTopCR4	$\pm 0.00$ [0.00%]				
gamma_shape_mcstat_ZV_eeZXCR4a	$\pm 0.00$ [0.00%]				
gamma_shape_mcstat_WW_WWCR1	$\pm 0.00$ [0.00%]				
gamma_shape_mcstat_top_eeZXCR4a	$\pm 0.00$ [0.00%]				
gamma_shape_mcstat_Higgs_emuTopCR4	$\pm 0.00$ [0.00%]				
gamma_shape_mcstat_WW_eeZXCR4a	$\pm 0.00$ [0.00%]				
alpha_AR_MC_MS	$\pm 0.00$ [0.00%]				
alpha_AR_MC_EER	$\pm 0.00$ [0.00%]				
gamma_shape_mcstat_top_emuTopCR4	$\pm 0.00$ [0.00%]				
alpha_AR_FIT_EES_Z	$\pm 0.00$ [0.00%]				
gamma_shape_mcstat_ZV_emuTopCR4	$\pm 0.00$ [0.00%]				
alpha_AR_MC_EES_PS	$\pm 0.00$ [0.00%]				

Table E.4: As in Table E.2, but for the  $\mu^\pm\mu^\mp$  channel of  $SR-m_{T2,90}$ .

$SR\text{-}m_{T2,110}e^\pm e^\mp$	Total	Top	WW	Z + V
Total background expectation	6.12	0.69	2.67	2.70
Total statistical	$\pm 0.72$	$\pm 0.49$	$\pm 0.44$	$\pm 0.28$
Total background systematic	$\pm 2.18$ [35.67%]	$\pm 0.69$ [99.84%]	$\pm 1.50$ [56.19%]	$\pm 1.43$ [53.06%]
alpha_SR4b_WW_hackGen	$\pm 1.42$ [23.2%]	$\pm 0.00$ [0.00%]	$\pm 1.42$ [53.0%]	$\pm 0.00$ [0.00%]
alpha_SR4b_ZV_hackGen	$\pm 1.32$ [21.6%]	$\pm 0.00$ [0.00%]	$\pm 0.00$ [0.00%]	$\pm 1.32$ [49.0%]
alpha_AR_FIT_JER	$\pm 0.85$ [13.9%]	$\pm 0.45$ [65.1%]	$\pm 0.22$ [8.1%]	$\pm 0.19$ [6.9%]
gamma_shape_mcstat_top_eeSR4b	$\pm 0.49$ [8.0%]	$\pm 0.49$ [70.7%]	$\pm 0.00$ [0.00%]	$\pm 0.00$ [0.00%]
mu_2LZV	$\pm 0.46$ [7.6%]	$\pm 0.00$ [0.00%]	$\pm 0.00$ [0.00%]	$\pm 0.46$ [17.1%]
gamma_shape_mcstat_WW_eeSR4b	$\pm 0.44$ [7.2%]	$\pm 0.00$ [0.00%]	$\pm 0.44$ [16.4%]	$\pm 0.00$ [0.00%]
mu_2LWW	$\pm 0.33$ [5.4%]	$\pm 0.00$ [0.00%]	$\pm 0.33$ [12.3%]	$\pm 0.00$ [0.00%]
alpha_AR_FIT_EES_Z	$\pm 0.28$ [4.7%]	$\pm 0.00$ [0.00%]	$\pm 0.13$ [4.9%]	$\pm 0.15$ [5.6%]
gamma_shape_mcstat_ZV_eeSR4b	$\pm 0.28$ [4.6%]	$\pm 0.00$ [0.00%]	$\pm 0.00$ [0.00%]	$\pm 0.28$ [10.3%]
alpha_ALLSR4_Top_Theory	$\pm 0.17$ [2.8%]	$\pm 0.17$ [25.0%]	$\pm 0.00$ [0.00%]	$\pm 0.00$ [0.00%]
alpha_AR_FIT_EES_MAT	$\pm 0.15$ [2.5%]	$\pm 0.00$ [0.00%]	$\pm 0.10$ [3.6%]	$\pm 0.05$ [2.0%]
alpha_AR_FIT_RESOST	$\pm 0.14$ [2.4%]	$\pm 0.00$ [0.00%]	$\pm 0.00$ [0.01%]	$\pm 0.14$ [5.4%]
alpha_AR_FIT_SCALEST	$\pm 0.12$ [2.0%]	$\pm 0.00$ [0.00%]	$\pm 0.07$ [2.5%]	$\pm 0.06$ [2.1%]
alpha_eeSR4b_Fake_Stat	$\pm 0.08$ [1.3%]	$\pm 0.00$ [0.00%]	$\pm 0.00$ [0.00%]	$\pm 0.00$ [0.00%]
alpha_AR_FIT_JES	$\pm 0.08$ [1.2%]	$\pm 0.00$ [0.00%]	$\pm 0.08$ [2.9%]	$\pm 0.00$ [0.00%]
alpha_AR_FIT_EER	$\pm 0.04$ [0.72%]	$\pm 0.00$ [0.00%]	$\pm 0.01$ [0.27%]	$\pm 0.05$ [1.9%]
alpha_eeSR4b_Fake_Syst	$\pm 0.04$ [0.65%]	$\pm 0.00$ [0.00%]	$\pm 0.00$ [0.00%]	$\pm 0.00$ [0.00%]
mu_2LTop	$\pm 0.03$ [0.50%]	$\pm 0.03$ [4.4%]	$\pm 0.00$ [0.00%]	$\pm 0.00$ [0.00%]
gamma_shape_mcstat_Higgs_eeSR4b	$\pm 0.03$ [0.44%]	$\pm 0.00$ [0.00%]	$\pm 0.00$ [0.00%]	$\pm 0.00$ [0.00%]
alpha_AR_FIT_EES_PS	$\pm 0.02$ [0.25%]	$\pm 0.00$ [0.00%]	$\pm 0.00$ [0.03%]	$\pm 0.01$ [0.54%]
alpha_AR_MC_JER	$\pm 0.01$ [0.13%]	$\pm 0.00$ [0.00%]	$\pm 0.00$ [0.00%]	$\pm 0.00$ [0.00%]
alpha_AR_FIT_BTL	$\pm 0.01$ [0.12%]	$\pm 0.00$ [0.00%]	$\pm 0.00$ [0.11%]	$\pm 0.00$ [0.16%]
Lumi	$\pm 0.00$ [0.02%]	$\pm 0.00$ [0.00%]	$\pm 0.00$ [0.00%]	$\pm 0.00$ [0.00%]
alpha_AR_FIT_BTC	$\pm 0.00$ [0.00%]	$\pm 0.00$ [0.00%]	$\pm 0.00$ [0.00%]	$\pm 0.00$ [0.01%]
alpha_AR_MC_EER	$\pm 0.00$ [0.00%]	$\pm 0.00$ [0.00%]	$\pm 0.00$ [0.00%]	$\pm 0.00$ [0.00%]
alpha_AR_MC_EES_PS	$\pm 0.00$ [0.00%]	$\pm 0.00$ [0.00%]	$\pm 0.00$ [0.00%]	$\pm 0.00$ [0.00%]
alpha_AR_MC_EES_Z	$\pm 0.00$ [0.00%]	$\pm 0.00$ [0.00%]	$\pm 0.00$ [0.00%]	$\pm 0.00$ [0.00%]
alpha_AR_MC_EES_MAT	$\pm 0.00$ [0.00%]	$\pm 0.00$ [0.00%]	$\pm 0.00$ [0.00%]	$\pm 0.00$ [0.00%]
alpha_AR_MC_BTL	$\pm 0.00$ [0.00%]	$\pm 0.00$ [0.00%]	$\pm 0.00$ [0.00%]	$\pm 0.00$ [0.00%]
alpha_AR_fakes_MURE	$\pm 0.00$ [0.00%]	$\pm 0.00$ [0.00%]	$\pm 0.00$ [0.00%]	$\pm 0.00$ [0.00%]
alpha_AR_MC_BTC	$\pm 0.00$ [0.00%]	$\pm 0.00$ [0.00%]	$\pm 0.00$ [0.00%]	$\pm 0.00$ [0.00%]
alpha_AR_MC_BTBT	$\pm 0.00$ [0.00%]	$\pm 0.00$ [0.00%]	$\pm 0.00$ [0.00%]	$\pm 0.00$ [0.00%]
gamma_shape_mcstat_ZV_mmZXCR4b	$\pm 0.00$ [0.00%]	$\pm 0.00$ [0.00%]	$\pm 0.00$ [0.00%]	$\pm 0.00$ [0.00%]
alpha_AR_MC_ID	$\pm 0.00$ [0.00%]	$\pm 0.00$ [0.00%]	$\pm 0.00$ [0.00%]	$\pm 0.00$ [0.00%]
alpha_AR_FIT_BTBT	$\pm 0.00$ [0.00%]	$\pm 0.00$ [0.00%]	$\pm 0.00$ [0.00%]	$\pm 0.00$ [0.00%]
alpha_AR_FIT_ID	$\pm 0.00$ [0.00%]	$\pm 0.00$ [0.00%]	$\pm 0.00$ [0.00%]	$\pm 0.00$ [0.00%]
gamma_shape_mcstat_WW_eeZXCR4b	$\pm 0.00$ [0.00%]	$\pm 0.00$ [0.00%]	$\pm 0.00$ [0.00%]	$\pm 0.00$ [0.00%]
gamma_shape_mcstat_Higgs_eeZXCR4b	$\pm 0.00$ [0.00%]	$\pm 0.00$ [0.00%]	$\pm 0.00$ [0.00%]	$\pm 0.00$ [0.00%]
gamma_shape_mcstat_WW_emuTopCR4	$\pm 0.00$ [0.00%]	$\pm 0.00$ [0.00%]	$\pm 0.00$ [0.00%]	$\pm 0.00$ [0.00%]
alpha_AR_fakes_MUFR	$\pm 0.00$ [0.00%]	$\pm 0.00$ [0.00%]	$\pm 0.00$ [0.00%]	$\pm 0.00$ [0.00%]
gamma_shape_mcstat_top_WWCR1	$\pm 0.00$ [0.00%]	$\pm 0.00$ [0.00%]	$\pm 0.00$ [0.00%]	$\pm 0.00$ [0.00%]
alpha_AR_MC_JES	$\pm 0.00$ [0.00%]	$\pm 0.00$ [0.00%]	$\pm 0.00$ [0.00%]	$\pm 0.00$ [0.00%]
alpha_AR_FIT_MS	$\pm 0.00$ [0.00%]	$\pm 0.00$ [0.00%]	$\pm 0.00$ [0.00%]	$\pm 0.00$ [0.00%]
alpha_AR_fakes_ELRE	$\pm 0.00$ [0.00%]	$\pm 0.00$ [0.00%]	$\pm 0.00$ [0.00%]	$\pm 0.00$ [0.00%]
alpha_AR_MC_RESOST	$\pm 0.00$ [0.00%]	$\pm 0.00$ [0.00%]	$\pm 0.00$ [0.00%]	$\pm 0.00$ [0.00%]
gamma_shape_mcstat_ZV_WWCR1	$\pm 0.00$ [0.00%]	$\pm 0.00$ [0.00%]	$\pm 0.00$ [0.00%]	$\pm 0.00$ [0.00%]
gamma_shape_mcstat_ZV_eeZXCR4b	$\pm 0.00$ [0.00%]	$\pm 0.00$ [0.00%]	$\pm 0.00$ [0.00%]	$\pm 0.00$ [0.00%]
gamma_shape_mcstat_WW_mmZXCR4b	$\pm 0.00$ [0.00%]	$\pm 0.00$ [0.00%]	$\pm 0.00$ [0.00%]	$\pm 0.00$ [0.00%]
alpha_AR_fakes_ELFR	$\pm 0.00$ [0.00%]	$\pm 0.00$ [0.00%]	$\pm 0.00$ [0.00%]	$\pm 0.00$ [0.00%]
gamma_shape_mcstat_Higgs_WWCR1	$\pm 0.00$ [0.00%]	$\pm 0.00$ [0.00%]	$\pm 0.00$ [0.00%]	$\pm 0.00$ [0.00%]
gamma_shape_mcstat_Ztt_emuTopCR4	$\pm 0.00$ [0.00%]	$\pm 0.00$ [0.00%]	$\pm 0.00$ [0.00%]	$\pm 0.00$ [0.00%]
gamma_shape_mcstat_WW_WWCR1	$\pm 0.00$ [0.00%]	$\pm 0.00$ [0.00%]	$\pm 0.00$ [0.00%]	$\pm 0.00$ [0.00%]
gamma_shape_mcstat_Higgs_emuTopCR4	$\pm 0.00$ [0.00%]	$\pm 0.00$ [0.00%]	$\pm 0.00$ [0.00%]	$\pm 0.00$ [0.00%]
alpha_AR_MC_SCALEST	$\pm 0.00$ [0.00%]	$\pm 0.00$ [0.00%]	$\pm 0.00$ [0.00%]	$\pm 0.00$ [0.00%]
alpha_AR_MC_MS	$\pm 0.00$ [0.00%]	$\pm 0.00$ [0.00%]	$\pm 0.00$ [0.00%]	$\pm 0.00$ [0.00%]
gamma_shape_mcstat_top_emuTopCR4	$\pm 0.00$ [0.00%]	$\pm 0.00$ [0.00%]	$\pm 0.00$ [0.00%]	$\pm 0.00$ [0.00%]
gamma_shape_mcstat_Higgs_mmZXCR4b	$\pm 0.00$ [0.00%]	$\pm 0.00$ [0.00%]	$\pm 0.00$ [0.00%]	$\pm 0.00$ [0.00%]
gamma_shape_mcstat_ZV_emuTopCR4	$\pm 0.00$ [0.00%]	$\pm 0.00$ [0.00%]	$\pm 0.00$ [0.00%]	$\pm 0.00$ [0.00%]

Table E.5: As in Table E.2, but for the  $e^\pm e^\mp$  channel of  $SR\text{-}m_{T2,110}$ .

$SR-m_{T2,110}e^\pm\mu^\mp$	Total	Top	WW	Z + V
Total background expectation	4.44	0.56	3.56	0.19
Total statistical	$\pm 0.61$	$\pm 0.40$	$\pm 0.43$	$\pm 0.08$
Total background systematic	$\pm 2.00$ [45.09%]	$\pm 0.42$ [75.96%]	$\pm 1.95$ [54.65%]	$\pm 0.12$ [64.83%]
alpha_SR4b_WW_hackGen	$\pm 1.89$ [42.6%]	$\pm 0.00$ [0.00%]	$\pm 1.89$ [53.0%]	$\pm 0.00$ [0.00%]
mu_2LWW	$\pm 0.44$ [9.8%]	$\pm 0.00$ [0.00%]	$\pm 0.44$ [12.3%]	$\pm 0.00$ [0.00%]
gamma_shape_mcstat_WW_emuSR4b	$\pm 0.43$ [9.7%]	$\pm 0.00$ [0.00%]	$\pm 0.43$ [12.0%]	$\pm 0.00$ [0.00%]
gamma_shape_mcstat_top_emuSR4b	$\pm 0.40$ [9.0%]	$\pm 0.40$ [71.6%]	$\pm 0.00$ [0.00%]	$\pm 0.00$ [0.00%]
alpha_AR_FIT_JER	$\pm 0.30$ [6.9%]	$\pm 0.00$ [0.00%]	$\pm 0.30$ [8.4%]	$\pm 0.01$ [3.2%]
alpha_ALLSR4_Top_Theory	$\pm 0.14$ [3.1%]	$\pm 0.14$ [25.0%]	$\pm 0.00$ [0.00%]	$\pm 0.00$ [0.00%]
alpha_emSR4b_Fake_Stat	$\pm 0.13$ [2.9%]	$\pm 0.00$ [0.00%]	$\pm 0.00$ [0.00%]	$\pm 0.00$ [0.00%]
alpha_SR4b_ZV_hackGen	$\pm 0.09$ [2.1%]	$\pm 0.00$ [0.00%]	$\pm 0.00$ [0.00%]	$\pm 0.09$ [49.0%]
gamma_shape_mcstat_ZV_emuSR4b	$\pm 0.08$ [1.7%]	$\pm 0.00$ [0.00%]	$\pm 0.00$ [0.00%]	$\pm 0.08$ [39.1%]
alpha_AR_FIT_EES_Z	$\pm 0.05$ [1.2%]	$\pm 0.00$ [0.00%]	$\pm 0.05$ [1.5%]	$\pm 0.00$ [0.40%]
gamma_shape_mcstat_Higgs_emuSR4b	$\pm 0.04$ [0.87%]	$\pm 0.00$ [0.00%]	$\pm 0.00$ [0.00%]	$\pm 0.00$ [0.00%]
alpha_AR_FIT_SCALEST	$\pm 0.03$ [0.75%]	$\pm 0.00$ [0.00%]	$\pm 0.03$ [0.97%]	$\pm 0.00$ [0.59%]
mu_2LZV	$\pm 0.03$ [0.74%]	$\pm 0.00$ [0.00%]	$\pm 0.00$ [0.00%]	$\pm 0.03$ [17.1%]
alpha_emSR4b_Fake_Syst	$\pm 0.02$ [0.56%]	$\pm 0.00$ [0.00%]	$\pm 0.00$ [0.00%]	$\pm 0.00$ [0.00%]
mu_2LTop	$\pm 0.02$ [0.56%]	$\pm 0.02$ [4.4%]	$\pm 0.00$ [0.00%]	$\pm 0.00$ [0.00%]
alpha_AR_FIT_EER	$\pm 0.02$ [0.36%]	$\pm 0.00$ [0.00%]	$\pm 0.01$ [0.41%]	$\pm 0.00$ [0.59%]
alpha_AR_FIT_BTL	$\pm 0.01$ [0.27%]	$\pm 0.00$ [0.21%]	$\pm 0.01$ [0.30%]	$\pm 0.00$ [0.08%]
alpha_AR_FIT_EES_MAT	$\pm 0.01$ [0.18%]	$\pm 0.00$ [0.00%]	$\pm 0.00$ [0.02%]	$\pm 0.01$ [3.7%]
Lumi	$\pm 0.00$ [0.08%]	$\pm 0.00$ [0.00%]	$\pm 0.00$ [0.00%]	$\pm 0.00$ [0.00%]
alpha_AR_FIT_RESOST	$\pm 0.00$ [0.06%]	$\pm 0.00$ [0.00%]	$\pm 0.00$ [0.09%]	$\pm 0.00$ [0.09%]
alpha_AR_MC_JER	$\pm 0.00$ [0.00%]	$\pm 0.00$ [0.00%]	$\pm 0.00$ [0.00%]	$\pm 0.00$ [0.00%]
alpha_AR_MC_EES_Z	$\pm 0.00$ [0.00%]	$\pm 0.00$ [0.00%]	$\pm 0.00$ [0.00%]	$\pm 0.00$ [0.00%]
alpha_AR_FIT_EES_PS	$\pm 0.00$ [0.00%]	$\pm 0.00$ [0.00%]	$\pm 0.00$ [0.00%]	$\pm 0.00$ [0.00%]
alpha_AR_MC_BTL	$\pm 0.00$ [0.00%]	$\pm 0.00$ [0.00%]	$\pm 0.00$ [0.00%]	$\pm 0.00$ [0.00%]
alpha_AR_FIT_BTC	$\pm 0.00$ [0.00%]	$\pm 0.00$ [0.00%]	$\pm 0.00$ [0.00%]	$\pm 0.00$ [0.00%]
alpha_AR_fakes_MURE	$\pm 0.00$ [0.00%]	$\pm 0.00$ [0.00%]	$\pm 0.00$ [0.00%]	$\pm 0.00$ [0.00%]
alpha_AR_MC_BTC	$\pm 0.00$ [0.00%]	$\pm 0.00$ [0.00%]	$\pm 0.00$ [0.00%]	$\pm 0.00$ [0.00%]
alpha_AR_MC_BTb	$\pm 0.00$ [0.00%]	$\pm 0.00$ [0.00%]	$\pm 0.00$ [0.00%]	$\pm 0.00$ [0.00%]
gamma_shape_mcstat_ZV_mmZXCR4b	$\pm 0.00$ [0.00%]	$\pm 0.00$ [0.00%]	$\pm 0.00$ [0.00%]	$\pm 0.00$ [0.00%]
alpha_AR_MC_ID	$\pm 0.00$ [0.00%]	$\pm 0.00$ [0.00%]	$\pm 0.00$ [0.00%]	$\pm 0.00$ [0.00%]
alpha_AR_FIT_BTb	$\pm 0.00$ [0.00%]	$\pm 0.00$ [0.00%]	$\pm 0.00$ [0.00%]	$\pm 0.00$ [0.00%]
alpha_AR_FIT_ID	$\pm 0.00$ [0.00%]	$\pm 0.00$ [0.00%]	$\pm 0.00$ [0.00%]	$\pm 0.00$ [0.00%]
gamma_shape_mcstat_WW_eeZXCR4b	$\pm 0.00$ [0.00%]	$\pm 0.00$ [0.00%]	$\pm 0.00$ [0.00%]	$\pm 0.00$ [0.00%]
alpha_AR_MC_EES_MAT	$\pm 0.00$ [0.00%]	$\pm 0.00$ [0.00%]	$\pm 0.00$ [0.00%]	$\pm 0.00$ [0.00%]
gamma_shape_mcstat_Higgs_eeZXCR4b	$\pm 0.00$ [0.00%]	$\pm 0.00$ [0.00%]	$\pm 0.00$ [0.00%]	$\pm 0.00$ [0.00%]
gamma_shape_mcstat_WW_emuTopCR4	$\pm 0.00$ [0.00%]	$\pm 0.00$ [0.00%]	$\pm 0.00$ [0.00%]	$\pm 0.00$ [0.00%]
alpha_AR_fakes_MUFR	$\pm 0.00$ [0.00%]	$\pm 0.00$ [0.00%]	$\pm 0.00$ [0.00%]	$\pm 0.00$ [0.00%]
gamma_shape_mcstat_top_WWCR1	$\pm 0.00$ [0.00%]	$\pm 0.00$ [0.00%]	$\pm 0.00$ [0.00%]	$\pm 0.00$ [0.00%]
alpha_AR_MC_JES	$\pm 0.00$ [0.00%]	$\pm 0.00$ [0.00%]	$\pm 0.00$ [0.00%]	$\pm 0.00$ [0.00%]
alpha_AR_FIT_MS	$\pm 0.00$ [0.00%]	$\pm 0.00$ [0.00%]	$\pm 0.00$ [0.00%]	$\pm 0.00$ [0.00%]
alpha_AR_fakes_ELRE	$\pm 0.00$ [0.00%]	$\pm 0.00$ [0.00%]	$\pm 0.00$ [0.00%]	$\pm 0.00$ [0.00%]
alpha_AR_MC_RESOST	$\pm 0.00$ [0.00%]	$\pm 0.00$ [0.00%]	$\pm 0.00$ [0.00%]	$\pm 0.00$ [0.00%]
gamma_shape_mcstat_ZV_WWCR1	$\pm 0.00$ [0.00%]	$\pm 0.00$ [0.00%]	$\pm 0.00$ [0.00%]	$\pm 0.00$ [0.00%]
gamma_shape_mcstat_ZV_eeZXCR4b	$\pm 0.00$ [0.00%]	$\pm 0.00$ [0.00%]	$\pm 0.00$ [0.00%]	$\pm 0.00$ [0.00%]
gamma_shape_mcstat_WW_mmZXCR4b	$\pm 0.00$ [0.00%]	$\pm 0.00$ [0.00%]	$\pm 0.00$ [0.00%]	$\pm 0.00$ [0.00%]
alpha_AR_fakes_ELFR	$\pm 0.00$ [0.00%]	$\pm 0.00$ [0.00%]	$\pm 0.00$ [0.00%]	$\pm 0.00$ [0.00%]
gamma_shape_mcstat_Higgs_WWCR1	$\pm 0.00$ [0.00%]	$\pm 0.00$ [0.00%]	$\pm 0.00$ [0.00%]	$\pm 0.00$ [0.00%]
alpha_AR_FIT_JES	$\pm 0.00$ [0.00%]	$\pm 0.00$ [0.00%]	$\pm 0.00$ [0.00%]	$\pm 0.00$ [0.00%]
gamma_shape_mcstat_Ztt_emuTopCR4	$\pm 0.00$ [0.00%]	$\pm 0.00$ [0.00%]	$\pm 0.00$ [0.00%]	$\pm 0.00$ [0.00%]
gamma_shape_mcstat_WW_WWCR1	$\pm 0.00$ [0.00%]	$\pm 0.00$ [0.00%]	$\pm 0.00$ [0.00%]	$\pm 0.00$ [0.00%]
gamma_shape_mcstat_Higgs_emuTopCR4	$\pm 0.00$ [0.00%]	$\pm 0.00$ [0.00%]	$\pm 0.00$ [0.00%]	$\pm 0.00$ [0.00%]
alpha_AR_MC_SCALEST	$\pm 0.00$ [0.00%]	$\pm 0.00$ [0.00%]	$\pm 0.00$ [0.00%]	$\pm 0.00$ [0.00%]
alpha_AR_MC_MS	$\pm 0.00$ [0.00%]	$\pm 0.00$ [0.00%]	$\pm 0.00$ [0.00%]	$\pm 0.00$ [0.00%]
alpha_AR_MC_EER	$\pm 0.00$ [0.00%]	$\pm 0.00$ [0.00%]	$\pm 0.00$ [0.00%]	$\pm 0.00$ [0.00%]
gamma_shape_mcstat_top_emuTopCR4	$\pm 0.00$ [0.00%]	$\pm 0.00$ [0.00%]	$\pm 0.00$ [0.00%]	$\pm 0.00$ [0.00%]
gamma_shape_mcstat_Higgs_mmZXCR4b	$\pm 0.00$ [0.00%]	$\pm 0.00$ [0.00%]	$\pm 0.00$ [0.00%]	$\pm 0.00$ [0.00%]
gamma_shape_mcstat_ZV_emuTopCR4	$\pm 0.00$ [0.00%]	$\pm 0.00$ [0.00%]	$\pm 0.00$ [0.00%]	$\pm 0.00$ [0.00%]
alpha_AR_MC_EES_PS	$\pm 0.00$ [0.00%]	$\pm 0.00$ [0.00%]	$\pm 0.00$ [0.00%]	$\pm 0.00$ [0.00%]

Table E.6: As in Table E.2, but for the  $e^\pm\mu^\mp$  channel of  $SR-m_{T2,110}$ .

$SR-m_{T2,110\mu^\pm\mu^\mp}$	Total	WW	Z + V
Total background expectation	6.29	2.85	3.39
Total statistical	$\pm 0.53$	$\pm 0.44$	$\pm 0.27$
Total background systematic	$\pm 2.38$ [37.94%]	$\pm 1.58$ [55.53%]	$\pm 1.78$ [52.53%]
alpha_SR4b_ZV_hackGen	$\pm 1.66$ [26.5%]	$\pm 0.00$ [0.00%]	$\pm 1.66$ [49.0%]
alpha_SR4b_WW_hackGen	$\pm 1.51$ [24.0%]	$\pm 1.51$ [53.0%]	$\pm 0.00$ [0.00%]
alpha_AR_FIT_JER	$\pm 0.79$ [12.5%]	$\pm 0.37$ [12.8%]	$\pm 0.42$ [12.4%]
mu_2LZV	$\pm 0.58$ [9.3%]	$\pm 0.00$ [0.00%]	$\pm 0.58$ [17.1%]
gamma_shape_mcstat_WW_mmSR4b	$\pm 0.44$ [7.0%]	$\pm 0.44$ [15.5%]	$\pm 0.00$ [0.00%]
mu_2LWW	$\pm 0.35$ [5.5%]	$\pm 0.35$ [12.3%]	$\pm 0.00$ [0.00%]
gamma_shape_mcstat_ZV_mmSR4b	$\pm 0.27$ [4.3%]	$\pm 0.00$ [0.00%]	$\pm 0.27$ [8.0%]
alpha_mmSR4b_Fake_Stat	$\pm 0.12$ [1.9%]	$\pm 0.00$ [0.00%]	$\pm 0.00$ [0.00%]
alpha_AR_FIT_RESOST	$\pm 0.05$ [0.73%]	$\pm 0.03$ [0.91%]	$\pm 0.07$ [2.1%]
alpha_AR_FIT_SCALEST	$\pm 0.04$ [0.68%]	$\pm 0.05$ [1.8%]	$\pm 0.01$ [0.22%]
alpha_AR_FIT_JES	$\pm 0.04$ [0.63%]	$\pm 0.03$ [0.89%]	$\pm 0.01$ [0.42%]
alpha_AR_FIT_MS	$\pm 0.03$ [0.55%]	$\pm 0.01$ [0.20%]	$\pm 0.04$ [1.2%]
gamma_shape_mcstat_Higgs_mmSR4b	$\pm 0.02$ [0.37%]	$\pm 0.00$ [0.00%]	$\pm 0.00$ [0.00%]
alpha_AR_FIT_BTL	$\pm 0.02$ [0.27%]	$\pm 0.01$ [0.40%]	$\pm 0.01$ [0.16%]
alpha_mmSR4b_Fake_Syst	$\pm 0.00$ [0.08%]	$\pm 0.00$ [0.00%]	$\pm 0.00$ [0.00%]
alpha_AR_FIT_ID	$\pm 0.00$ [0.03%]	$\pm 0.00$ [0.00%]	$\pm 0.00$ [0.06%]
alpha_AR_FIT_BTC	$\pm 0.00$ [0.02%]	$\pm 0.00$ [0.00%]	$\pm 0.00$ [0.04%]
Lumi	$\pm 0.00$ [0.02%]	$\pm 0.00$ [0.00%]	$\pm 0.00$ [0.00%]
alpha_AR_MC_JER	$\pm 0.00$ [0.01%]	$\pm 0.00$ [0.00%]	$\pm 0.00$ [0.00%]
alpha_AR_MC_BTL	$\pm 0.00$ [0.00%]	$\pm 0.00$ [0.00%]	$\pm 0.00$ [0.00%]
alpha_AR_fakes_MURE	$\pm 0.00$ [0.00%]	$\pm 0.00$ [0.00%]	$\pm 0.00$ [0.00%]
alpha_AR_MC_BTC	$\pm 0.00$ [0.00%]	$\pm 0.00$ [0.00%]	$\pm 0.00$ [0.00%]
alpha_AR_MC_BTBT	$\pm 0.00$ [0.00%]	$\pm 0.00$ [0.00%]	$\pm 0.00$ [0.00%]
gamma_shape_mcstat_ZV_mmZXCR4b	$\pm 0.00$ [0.00%]	$\pm 0.00$ [0.00%]	$\pm 0.00$ [0.00%]
alpha_AR_MC_ID	$\pm 0.00$ [0.00%]	$\pm 0.00$ [0.00%]	$\pm 0.00$ [0.00%]
alpha_AR_FIT_BTBT	$\pm 0.00$ [0.00%]	$\pm 0.00$ [0.00%]	$\pm 0.00$ [0.00%]
gamma_shape_mcstat_WW_eeZXCR4b	$\pm 0.00$ [0.00%]	$\pm 0.00$ [0.00%]	$\pm 0.00$ [0.00%]
alpha_AR_MC_EES_MAT	$\pm 0.00$ [0.00%]	$\pm 0.00$ [0.00%]	$\pm 0.00$ [0.00%]
alpha_AR_MC_EES_Z	$\pm 0.00$ [0.00%]	$\pm 0.00$ [0.00%]	$\pm 0.00$ [0.00%]
gamma_shape_mcstat_Higgs_eeZXCR4b	$\pm 0.00$ [0.00%]	$\pm 0.00$ [0.00%]	$\pm 0.00$ [0.00%]
gamma_shape_mcstat_WW_emuTopCR4	$\pm 0.00$ [0.00%]	$\pm 0.00$ [0.00%]	$\pm 0.00$ [0.00%]
alpha_AR_fakes_MUFR	$\pm 0.00$ [0.00%]	$\pm 0.00$ [0.00%]	$\pm 0.00$ [0.00%]
alpha_AR_FIT_EER	$\pm 0.00$ [0.00%]	$\pm 0.00$ [0.00%]	$\pm 0.00$ [0.00%]
gamma_shape_mcstat_ttst_WWCR1	$\pm 0.00$ [0.00%]	$\pm 0.00$ [0.00%]	$\pm 0.00$ [0.00%]
alpha_AR_MC_JES	$\pm 0.00$ [0.00%]	$\pm 0.00$ [0.00%]	$\pm 0.00$ [0.00%]
alpha_AR_fakes_ELRE	$\pm 0.00$ [0.00%]	$\pm 0.00$ [0.00%]	$\pm 0.00$ [0.00%]
alpha_AR_FIT_EES_PS	$\pm 0.00$ [0.00%]	$\pm 0.00$ [0.00%]	$\pm 0.00$ [0.00%]
alpha_AR_MC_RESOST	$\pm 0.00$ [0.00%]	$\pm 0.00$ [0.00%]	$\pm 0.00$ [0.00%]
mu_2LTop	$\pm 0.00$ [0.00%]	$\pm 0.00$ [0.00%]	$\pm 0.00$ [0.00%]
alpha_AR_FIT_EES_MAT	$\pm 0.00$ [0.00%]	$\pm 0.00$ [0.00%]	$\pm 0.00$ [0.00%]
gamma_shape_mcstat_ZV_WWCR1	$\pm 0.00$ [0.00%]	$\pm 0.00$ [0.00%]	$\pm 0.00$ [0.00%]
gamma_shape_mcstat_ZV_eeZXCR4b	$\pm 0.00$ [0.00%]	$\pm 0.00$ [0.00%]	$\pm 0.00$ [0.00%]
gamma_shape_mcstat_WW_mmZXCR4b	$\pm 0.00$ [0.00%]	$\pm 0.00$ [0.00%]	$\pm 0.00$ [0.00%]
alpha_AR_fakes_ELFR	$\pm 0.00$ [0.00%]	$\pm 0.00$ [0.00%]	$\pm 0.00$ [0.00%]
gamma_shape_mcstat_Higgs_WWCR1	$\pm 0.00$ [0.00%]	$\pm 0.00$ [0.00%]	$\pm 0.00$ [0.00%]
gamma_shape_mcstat_Ztt_emuTopCR4	$\pm 0.00$ [0.00%]	$\pm 0.00$ [0.00%]	$\pm 0.00$ [0.00%]
gamma_shape_mcstat_WW_WWCR1	$\pm 0.00$ [0.00%]	$\pm 0.00$ [0.00%]	$\pm 0.00$ [0.00%]
gamma_shape_mcstat_Higgs_emuTopCR4	$\pm 0.00$ [0.00%]	$\pm 0.00$ [0.00%]	$\pm 0.00$ [0.00%]
alpha_AR_MC_SCALEST	$\pm 0.00$ [0.00%]	$\pm 0.00$ [0.00%]	$\pm 0.00$ [0.00%]
alpha_AR_MC_MS	$\pm 0.00$ [0.00%]	$\pm 0.00$ [0.00%]	$\pm 0.00$ [0.00%]
alpha_AR_MC_EER	$\pm 0.00$ [0.00%]	$\pm 0.00$ [0.00%]	$\pm 0.00$ [0.00%]
gamma_shape_mcstat_ttst_emuTopCR4	$\pm 0.00$ [0.00%]	$\pm 0.00$ [0.00%]	$\pm 0.00$ [0.00%]
alpha_AR_FIT_EES_Z	$\pm 0.00$ [0.00%]	$\pm 0.00$ [0.00%]	$\pm 0.00$ [0.00%]
gamma_shape_mcstat_Higgs_mmZXCR4b	$\pm 0.00$ [0.00%]	$\pm 0.00$ [0.00%]	$\pm 0.00$ [0.00%]
gamma_shape_mcstat_ZV_emuTopCR4	$\pm 0.00$ [0.00%]	$\pm 0.00$ [0.00%]	$\pm 0.00$ [0.00%]
alpha_AR_MC_EES_PS	$\pm 0.00$ [0.00%]	$\pm 0.00$ [0.00%]	$\pm 0.00$ [0.00%]

Table E.7: As in Table E.2, but for the  $\mu^\pm\mu^\mp$  channel of SR- $m_{T2,110}$ .

# Appendix F

## Fit configuration used for the shape fit investigation

This appendix gives a description of the configuration used for the simultaneous fits in the shape-fitting investigation discussed in Section 7.4. Differences with respect to the configuration used for the public results [5], which is detailed in Appendix E are highlighted.

When performing a shape-fit it is important to allow for the possibility of systematic uncertainties affecting the shape of a distribution rather than just its overall normalisation. For all the exclusion plots in the shape-fitting investigation, the systematics affecting Monte Carlo samples (e.g. JES) were based on the “histoSys” systematic in `HistFitter`. For binned channels in the fit, this applies an uncertainty as a shape uncertainty, correlated across the bins of the histogram. This allows both the shape and normalisation of the histogram to be changed according to the fit parameters. For the case of single binned channels, the only difference between “histoSys” and “overallSys” (discussed in Appendix E) is in the interpolation and extrapolation methods used to predict expectation values in a given bin as a function of nuisance parameter. For the “histoSys” option linear interpolation is used whereas in “overallSys” exponential interpolation is used.

The strategy for the final fit configuration will now be described. To speed up the computational time, the fit was performed by defining only one set of nuisance parameters (all using the “histoSys” option) and applying them to all Monte Carlo samples. The correlation matrices for  $SR-m_{T2,90}$  and  $SR-m_{T2,110}$  are shown in Figures F.1

and F.2 respectively. Especially in SR- $m_{T2,90}$ , there are a significant number of non-zero off diagonal elements indicating correlations between nuisance parameters.

To investigate this further, Figures F.3 and F.4 show the correlation matrices when the nuisance parameters are split into two sets as in the previous section. One set, defined here as “normHistoSys” is applied to the samples being fitted (i.e.  $WW$ ,  $ZV$  and top), and another set, defined as “histoSys” are applied to the backgrounds taken purely from Monte Carlo. The correlation matrices in this case are consistent with those in the previous section, and the correlations between nuisance parameters seem better behaved. However as the correlations observed using one set of nuisance parameters did not appear to affect the stability of the fit the shape-fitting investigation the splitting of nuisance parameters was not performed.

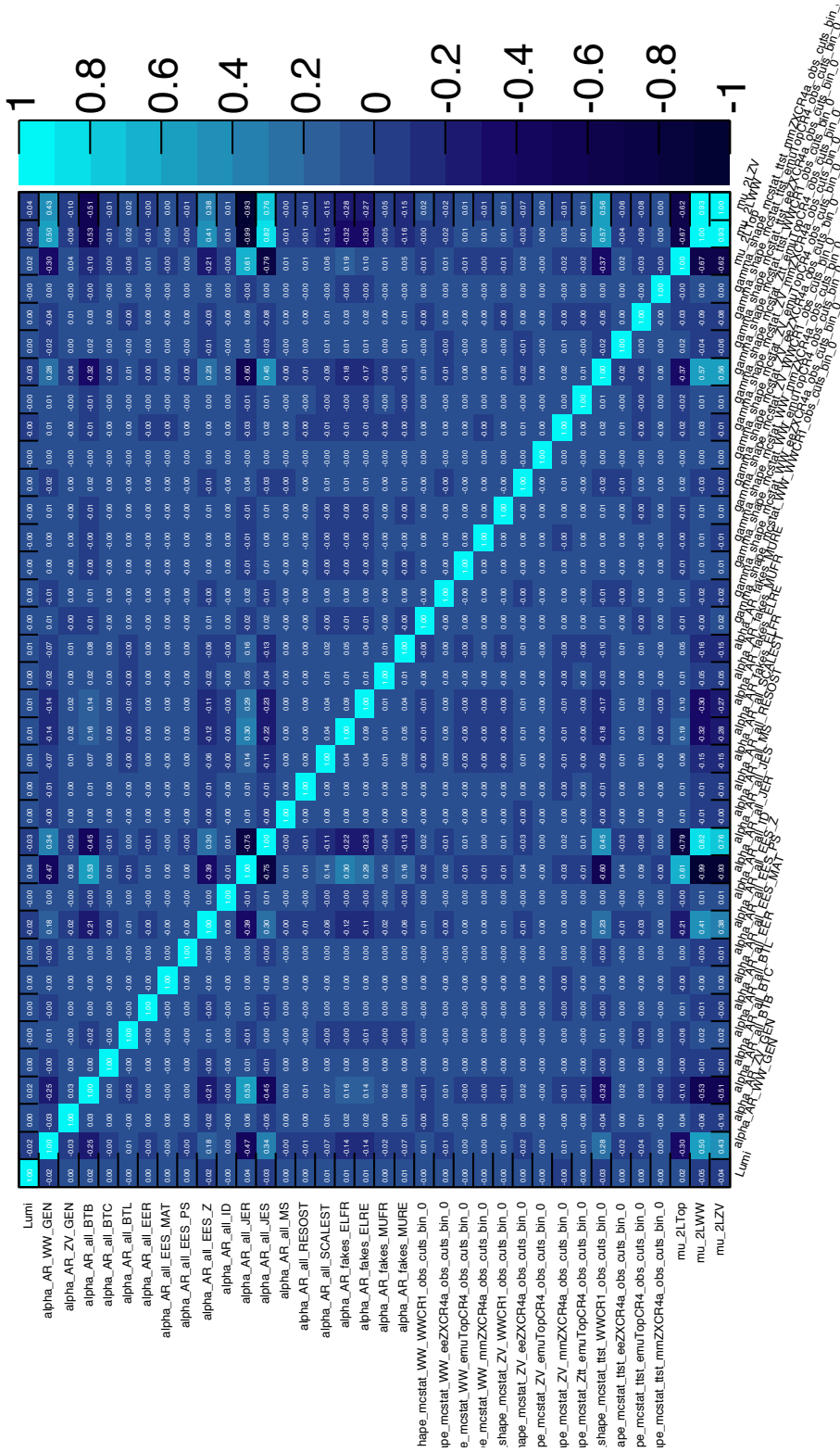


Figure F.1: The correlation matrix for the background-only fit for SR- $m_{T,90}$  when one set nuisance parameters for the systematic uncertainties corresponding to Monte Carlo samples is applied to all samples using the “histoSys” option. The labelling is as in Table E.1 but with one set of nuisance parameters applied to all Monte Carlo samples.

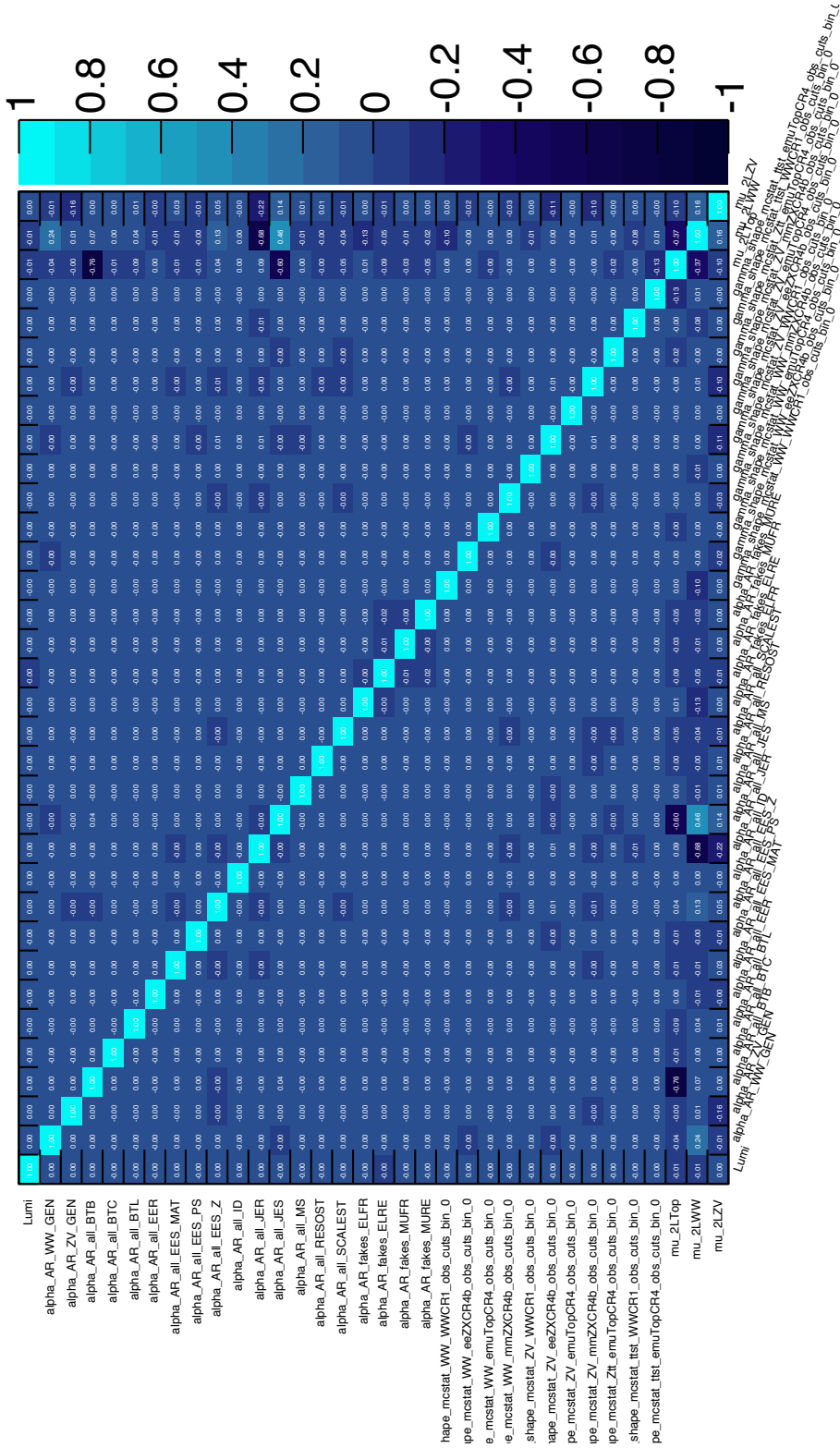


Figure F.2: The correlation matrix for the background-only fit for SR- $m_{T2,110}$  when one set nuisance parameters for the systematic uncertainties corresponding to Monte Carlo samples is applied to all samples using the “histoSys” option. The labelling is as in Table E.1 but with one set of nuisance parameters applied to all Monte Carlo samples.

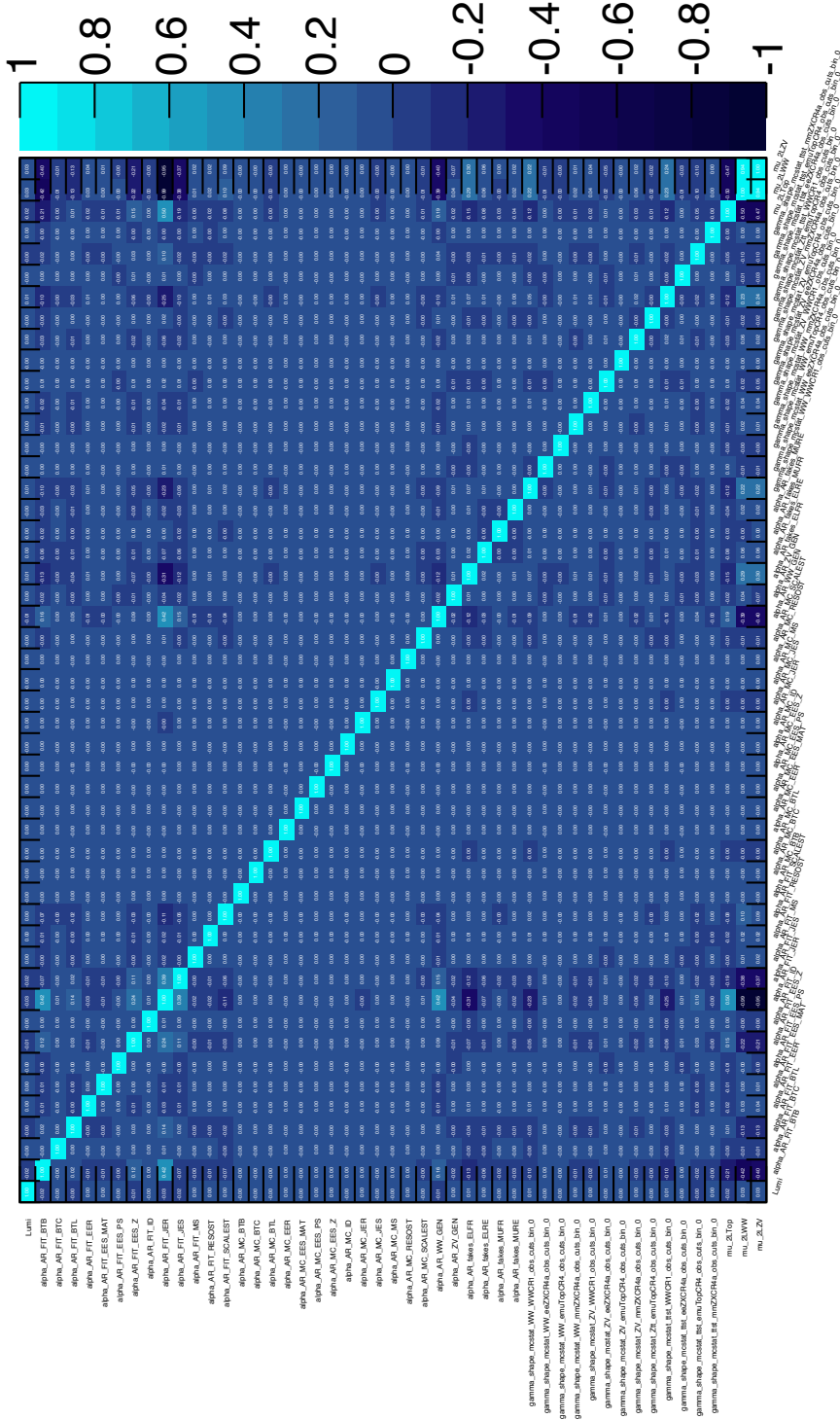


Figure F.3: The correlation matrix for the background-only fit for  $SR-m_{T2,90}$  when two sets of nuisance parameters are defined. The set for the fitted samples use the “normHistoSys” setting whereas the other uses “histoSys”. The labelling of nuisance parameters is as in Table E.1.



# Colophon

This thesis was made in L<sup>A</sup>T<sub>E</sub>X 2<sub>ε</sub> using the “hepthesis” class [188].

# Bibliography

- [1] Georges Aad et al. Search for direct slepton and gaugino production in final states with two leptons and missing transverse momentum with the ATLAS detector in  $pp$  collisions at  $\sqrt{s} = 7$  TeV. *Phys.Lett.*, B718:879–901, 2013, 1208.2884.
- [2] R. Brun and F. Rademakers. ROOT: An object oriented data analysis framework. *Nucl.Instrum.Meth.*, A389:81–86, 1997.
- [3] A L Read. Presentation of search results: the  $cl_s$  technique. *Journal of Physics G: Nuclear and Particle Physics*, 28(10):2693, 2002.
- [4] Lorenzo Moneta, Kevin Belasco, Kyle S. Cranmer, S. Kreiss, Alfio Lazzaro, et al. The RooStats Project. *PoS*, ACAT2010:057, 2010, 1009.1003.
- [5] Search for direct-slepton and direct-chargino production in final states with two opposite-sign leptons, missing transverse momentum and no jets in 20/fb of  $pp$  collisions at  $\sqrt{s} = 8$  tev with the atlas detector. Technical Report ATLAS-CONF-2013-049, CERN, Geneva, May 2013.
- [6] S. Weinberg. Implications of Dynamical Symmetry Breaking. *Phys. Rev.*, D13:974–996, 1976.
- [7] E. Gildener. Gauge Symmetry Hierarchies. *Phys. Rev.*, D14:1667, 1976.
- [8] S. Weinberg. Implications of Dynamical Symmetry Breaking: An Addendum. *Phys. Rev.*, D19:1277–1280, 1979.
- [9] L. Susskind. Dynamics of Spontaneous Symmetry Breaking in the Weinberg-Salam Theory. *Phys. Rev.*, D20:2619–2625, 1979.
- [10] C.G. Lester and D.J. Summers. Measuring masses of semi-invisibly decaying particles pair produced at hadron colliders. *Phys.Lett.*, B463:99–103, 1999, hep-ph/9906349.
- [11] Alan Barr, Christopher Lester, and P. Stephens.  $m(T_2)$ : The Truth behind the glamour. *J.Phys.*, G29:2343–2363, 2003, hep-ph/0304226.

- 
- [12] Alan J. Barr, Ben Gripaios, and Christopher G. Lester. Weighing Wimps with Kinks at Colliders: Invisible Particle Mass Measurements from Endpoints. *JHEP*, 0802:014, 2008, 0711.4008.
- [13] Lyndon Evans and Philip Bryant. LHC Machine. *JINST*, 3:S08001, 2008.
- [14] CERN TE-EPC group. Cern accelerator complex diagram. <http://te-dep-epc.web.cern.ch/te-dep-epc/machines/general.stm>.
- [15] J. Beringer et al. Review of Particle Physics (RPP). *Phys.Rev.*, D86:010001, 2012.
- [16] Antonio Riotto. Theories of baryogenesis. pages 326–436, 1998, hep-ph/9807454.
- [17] The ATLAS collaboration. Atlas detector photos. <http://atlas.ch/photos/>.
- [18] *ATLAS detector and physics performance: Technical Design Report, 1*. Technical Design Report ATLAS. CERN, Geneva, 1999. Electronic version not available.
- [19] *ATLAS detector and physics performance: Technical Design Report, 2*. Technical Design Report ATLAS. CERN, Geneva, 1999. Electronic version not available.
- [20] G. Aad et al. The ATLAS Experiment at the CERN Large Hadron Collider. *JINST*, 3:S08003, 2008.
- [21] *ATLAS inner detector: Technical Design Report, 1*. Technical Design Report ATLAS. CERN, Geneva, 1997.
- [22] S Haywood, L Rossi, R Nickerson, and A Romaniouk. *ATLAS inner detector: Technical Design Report, 2*. Technical Design Report ATLAS. CERN, Geneva, 1997.
- [23] Norbert Wermes and G Hallewel. *ATLAS pixel detector: Technical Design Report*. Technical Design Report ATLAS. CERN, Geneva, 1998.
- [24] G. Aad et al. Atlas pixel detector electronics and sensors. *J. Instrum.*, 3:P07007, 2008.
- [25] J N Jackson. The atlas semiconductor tracker (sct). *Nucl. Instrum. Methods Phys. Res., A*, 541:89–95, 2005.
- [26] T Cornelissen, M Elsing, I Gavrilenko, W Liebig, E Moyse, and A Salzburger. The new atlas track reconstruction (newt). *Journal of Physics: Conference Series*, 119(3):032014, 2008.
- [27] G. Aad et al. Expected Performance of the ATLAS Experiment - Detector, Trigger and Physics. 2009, 0901.0512.

- 
- [28] T.G. Cornelissen, N Van Eldik, M. Elsing, W. Liebig, E. Moyse, et al. Updates of the ATLAS Tracking Event Data Model (Release 13). 2007.
- [29] W. Lampl, S. Laplace, D. Lelas, P. Loch, H. Ma, et al. Calorimeter clustering algorithms: Description and performance. 2008.
- [30] *ATLAS muon spectrometer: Technical Design Report*. Technical Design Report ATLAS. CERN, Geneva, 1997. distribution.
- [31] *ATLAS magnet system: Technical Design Report, 1*. Technical Design Report ATLAS. CERN, Geneva, 1997.
- [32] The ATLAS collaboration. Atlas magnet system. <http://atlas-ma.web.cern.ch/atlas-ma/>.
- [33] *Atlas Computing: technical design report*. CERN, Geneva, 2005.
- [34] R Jones and D Barberis. The atlas computing model. *Journal of Physics: Conference Series*, 119(7):072020, 2008.
- [35] G. Aad et al. The ATLAS Simulation Infrastructure. *European Physical Journal C*, 70:823–874, December 2010, 1005.4568.
- [36] J T Boyd, M J Costa, A Tonoyan, and the Atlas Collaboration. Commissioning of the atlas reconstruction software with first data. *Journal of Physics: Conference Series*, 219(3):032059, 2010.
- [37] G. Barrand, I. Belyaev, P. Binko, M. Cattaneo, R. Chytracek, et al. GAUDI - A software architecture and framework for building HEP data processing applications. *Comput.Phys.Commun.*, 140:45–55, 2001.
- [38] ATLAS Collaboration. Electron performance measurements with the ATLAS detector using the 2010 LHC proton-proton collision data. 2011, 1110.3174.
- [39] R. Nicolaidou, L. Chevalier, S. Hassani, J.F. Laporte, E. Le Menedeu, et al. Muon identification procedure for the ATLAS detector at the LHC using Muonboy reconstruction package and tests of its performance using cosmic rays and single beam data. *J.Phys.Conf.Ser.*, 219:032052, 2010.
- [40] Matteo Cacciari, Gavin P. Salam, and Gregory Soyez. The Anti-k(t) jet clustering algorithm. *JHEP*, 0804:063, 2008, 0802.1189.
- [41] Commissioning of the atlas high-performance b-tagging algorithms in the 7 tev collision data. Technical Report ATLAS-CONF-2011-102, CERN, Geneva, Jul 2011.

- [42] Matt Dobbs and Jorgen Beck Hansen. The HepMC C++ Monte Carlo event record for High Energy Physics. *Comput.Phys.Commun.*, 134:41–46, 2001.
- [43] S. Agostinelli et al. GEANT4: A Simulation toolkit. *Nucl.Instrum.Meth.*, A506:250–303, 2003.
- [44] Elzbieta Richter-Was, D. Froidevaux, and Luc Poggioli. ATLFast 2.0 a fast simulation package for ATLAS. 1998.
- [45] W Lukas. Fast simulation for atlas: Atlfast-ii and isf. Technical Report ATL-SOFT-PROC-2012-065, CERN, Geneva, Jun 2012.
- [46] Mark Thomson. *Modern Particle Physics*. Cambridge University Press, 2013.
- [47] Michael E. Peskin and Daniel V. Schroeder. *An Introduction to Quantum Field Theory*. Perseus Books, Cambridge, Massachusetts, 1995.
- [48] E. Noether. Invariante variationsprobleme. *Nachrichten von der Gesellschaft der Wissenschaften zu Gttingen, Mathematisch-Physikalische Klasse*, 1918:235–257, 1918.
- [49] David Griffiths. *Introduction to Elementary Particles*. John Wiley and Sons, 1987.
- [50] S.L. Glashow. Partial Symmetries of Weak Interactions. *Nucl.Phys.*, 22:579–588, 1961.
- [51] Steven Weinberg. A Model of Leptons. *Phys.Rev.Lett.*, 19:1264–1266, 1967.
- [52] Abdus Salam. Weak and Electromagnetic Interactions. *Conf.Proc.*, C680519:367–377, 1968.
- [53] Peter W. Higgs. Broken Symmetries and the Masses of Gauge Bosons. *Phys.Rev.Lett.*, 13:508–509, 1964.
- [54] F. Englert and R. Brout. Broken Symmetry and the Mass of Gauge Vector Mesons. *Phys.Rev.Lett.*, 13:321–323, 1964.
- [55] F.J. Hasert et al. Observation of Neutrino Like Interactions Without Muon Or Electron in the Gargamelle Neutrino Experiment. *Phys.Lett.*, B46:138–140, 1973.
- [56] Nicola Cabibbo. Unitary Symmetry and Leptonic Decays. *Phys.Rev.Lett.*, 10:531–533, 1963.
- [57] Makoto Kobayashi and Toshihide Maskawa. CP Violation in the Renormalizable Theory of Weak Interaction. *Prog.Theor.Phys.*, 49:652–657, 1973.
- [58] Murray Gell-Mann. A Schematic Model of Baryons and Mesons. *Phys.Lett.*, 8:214–215, 1964.

- [59] G. Zweig. An SU(3) model for strong interaction symmetry and its breaking. Pt. 1. 1964.
- [60] V.E. Barnes, P.L. Connolly, D.J. Crennell, B.B. Culwick, W.C. Delaney, et al. Observation of a Hyperon with Strangeness -3. *Phys.Rev.Lett.*, 12:204–206, 1964.
- [61] Fyodor Tkachov. A Contribution to the history of quarks: Boris Struminsky’s 1965 JINR publication. 2009, 0904.0343.
- [62] M.Y. Han and Yoichiro Nambu. Three Triplet Model with Double SU(3) Symmetry. *Phys.Rev.*, 139:B1006–B1010, 1965.
- [63] H. Fritzsch, Murray Gell-Mann, and H. Leutwyler. Advantages of the Color Octet Gluon Picture. *Phys.Lett.*, B47:365–368, 1973.
- [64] J. Goldstone. Field Theories with Superconductor Solutions. *Nuovo Cim.*, 19:154–164, 1961.
- [65] Jeffrey Goldstone, Abdus Salam, and Steven Weinberg. Broken symmetries. *Phys. Rev.*, 127:965–970, Aug 1962.
- [66] Georges Aad et al. Observation of a new particle in the search for the Standard Model Higgs boson with the ATLAS detector at the LHC. *Phys.Lett.*, B716:1–29, 2012, 1207.7214.
- [67] Serguei Chatrchyan et al. Observation of a new boson at a mass of 125 GeV with the CMS experiment at the LHC. *Phys.Lett.*, B716:30–61, 2012, 1207.7235.
- [68] K. Abe et al. Solar neutrino results in Super-Kamiokande-III. *Phys.Rev.*, D83:052010, 2011, 1010.0118.
- [69] Y. Fukuda et al. Evidence for oscillation of atmospheric neutrinos. *Phys.Rev.Lett.*, 81:1562–1567, 1998, hep-ex/9807003.
- [70] P. Adamson et al. Measurements of atmospheric neutrinos and antineutrinos in the MINOS Far Detector. *Phys.Rev.*, D86:052007, 2012, 1208.2915.
- [71] Stephen P. Martin. A Supersymmetry primer. 1997, hep-ph/9709356.
- [72] Aaron Pierce. Implications of the Higgs Boson and the LHC for the MSSM. 2013, 1303.1142.
- [73] H. Miyazawa. Baryon Number Changing Currents. *Prog. Theor. Phys.*, 36 (6):1266–1276, 1966.
- [74] P. Ramond. Dual Theory for Free Fermions. *Phys. Rev.*, D3:2415–2418, 1971.

- [75] Yu. A. Gol'fand and E. P. Likhtman. Extension of the Algebra of Poincare Group Generators and Violation of p Invariance. *JETP Lett.*, 13:323–326, 1971. [Pisma Zh.Eksp.Teor.Fiz.13:452-455,1971].
- [76] A. Neveu and J. H. Schwarz. Factorizable dual model of pions. *Nucl. Phys.*, B31:86–112, 1971.
- [77] A. Neveu and J. H. Schwarz. Quark Model of Dual Pions. *Phys. Rev.*, D4:1109–1111, 1971.
- [78] J.L. Gervais and B. Sakita. Field theory interpretation of supergauge in dual models. *Nucl. Phys.*, B34:632–639, 1971.
- [79] D. V. Volkov and V. P. Akulov. Is the Neutrino a Goldstone Particle? *Phys. Lett.*, B46:109–110, 1973.
- [80] J. Wess and B. Zumino. A Lagrangian Model Invariant Under Supergauge Transformations. *Phys. Lett.*, B49:52, 1974.
- [81] J. Wess and B. Zumino. Supergauge Transformations in Four-Dimensions. *Nucl. Phys.*, B70:39–50, 1974.
- [82] S. Dimopoulos, S. Raby, and Frank Wilczek. Supersymmetry and the Scale of Unification. *Phys. Rev.*, D24:1681–1683, 1981.
- [83] N. Sakai. Naturalness in Supersymmetric Guts. *Zeit. Phys.*, C11:153, 1981.
- [84] Luis E. Ibanez and Graham G. Ross. Low-Energy Predictions in Supersymmetric Grand Unified Theories. *Phys. Lett.*, B105:439, 1981.
- [85] M. B. Einhorn and D. R. T. Jones. The Weak Mixing Angle and Unification Mass in Supersymmetric SU(5). *Nucl. Phys.*, B196:475, 1982.
- [86] William J. Marciano and Goran Senjanovic. Predictions of Supersymmetric Grand Unified Theories. *Phys. Rev.*, D25:3092, 1982.
- [87] C. Giunti, C. W. Kim, and U.W. Lee. Running coupling constants and grand unification models. *Mod. Phys. Lett.*, A6:1745–1755, 1991.
- [88] J.R. Ellis, S. Kelley, and D.V. Nanopoulos. Probing the desert using gauge coupling unification. *Phys. Lett.*, B260:131–137, 1991.
- [89] U. Amaldi, W. de Boer, and H. Furstenau. Comparison of grand unified theories with electroweak and strong coupling constants measured at LEP. *Phys. Lett.*, B260:447–455, 1991.

- [90] P. Langacker and M.-X. Luo. Implications of precision electroweak experiments for  $M(t)$ ,  $\rho(0)$ ,  $\sin^2\theta(W)$  and grand unification. *Phys. Rev.*, D44:817–822, 1991.
- [91] H. Goldberg. Constraint on the photino mass from cosmology. *Phys. Rev. Lett.*, 50:1419, 1983.
- [92] J.R. Ellis, J.S. Hagelin, D.V. Nanopoulos, K.A. Olive, and M. Srednicki. Supersymmetric relics from the big bang. *Nucl. Phys.*, B238:453–476, 1984.
- [93] S. Dimopoulos and H. Georgi. Softly Broken Supersymmetry and SU(5). *Nucl. Phys.*, B193:150, 1981.
- [94] E. Witten. Dynamical Breaking of Supersymmetry. *Nucl. Phys.*, B188:513, 1981.
- [95] M. Dine, W. Fischler, and M. Srednicki. Supersymmetric Technicolor. *Nucl. Phys.*, B189:575–593, 1981.
- [96] S. Dimopoulos and S. Raby. Supercolor. *Nucl. Phys.*, B192:353, 1981.
- [97] Romesh K. Kaul and Parthasarathi Majumdar. Cancellation of Quadratically Divergent Mass Corrections in Globally Supersymmetric Spontaneously Broken Gauge Theories. *Nucl.Phys.*, B199:36, 1982.
- [98] Howard E. Haber and Gordon L. Kane. The Search for Supersymmetry: Probing Physics Beyond the Standard Model. *Phys.Rept.*, 117:75–263, 1985.
- [99] University of Zurich Physics Department. Feynman diagram library (fdl). <http://www.physik.uzh.ch/~che/FeynDiag/index.php>.
- [100] P. Fayet. Supersymmetry and Weak, Electromagnetic and Strong Interactions. *Phys. Lett.*, B64:159, 1976.
- [101] P. Fayet. Spontaneously Broken Supersymmetric Theories of Weak, Electromagnetic and Strong Interactions. *Phys. Lett.*, B69:489, 1977.
- [102] G. R. Farrar and P. Fayet. Phenomenology of the Production, Decay, and Detection of New Hadronic States Associated with Supersymmetry. *Phys. Lett.*, B76:575–579, 1978.
- [103] P. Fayet. Relations Between the Masses of the Superpartners of Leptons and Quarks, the Goldstino Couplings and the Neutral Currents. *Phys. Lett.*, B84:416, 1979.
- [104] E. Cremmer, P. Fayet, and L. Girardello. Gravity-induced supersymmetry breaking and low energy mass spectrum. *Physics Letters B*, 122(1):41 – 48, 1983.

- 
- [105] Lawrence J. Hall, Joseph D. Lykken, and Steven Weinberg. Supergravity as the Messenger of Supersymmetry Breaking. *Phys.Rev.*, D27:2359–2378, 1983.
- [106] G.F. Giudice and R. Rattazzi. Theories with gauge mediated supersymmetry breaking. *Phys.Rept.*, 322:419–499, 1999, hep-ph/9801271.
- [107] Michael Dine, Ann E. Nelson, Yosef Nir, and Yuri Shirman. New tools for low energy dynamical supersymmetry breaking. *Phys. Rev. D*, 53:2658–2669, Mar 1996.
- [108] Markus Luty and Raman Sundrum. Anomaly mediated supersymmetry breaking in four-dimensions, naturally. *Phys.Rev.*, D67:045007, 2003, hep-th/0111231.
- [109] John A. Conley, James S. Gainer, JoAnne L. Hewett, My Phuong Le, and Thomas G. Rizzo. Supersymmetry Without Prejudice at the LHC. *Eur.Phys.J.*, C71:1697, 2011, 1009.2539.
- [110] Carola F. Berger, James S. Gainer, JoAnne L. Hewett, and Thomas G. Rizzo. Supersymmetry Without Prejudice. *JHEP*, 0902:023, 2009, 0812.0980.
- [111] Daniele Alves et al. Simplified Models for LHC New Physics Searches. *J.Phys.*, G39:105005, 2012, 1105.2838.
- [112] Georges Aad et al. Search for direct chargino production in anomaly-mediated supersymmetry breaking models based on a disappearing-track signature in  $pp$  collisions at  $\sqrt{s} = 7$  TeV with the ATLAS detector. *JHEP*, 1301:131, 2013, 1210.2852.
- [113] W. Beenakker, R. Hopker, and M. Spira. PROSPINO: A Program for the production of supersymmetric particles in next-to-leading order QCD. 1996, hep-ph/9611232.
- [114] Bernhard Mistlberger and Falko Dulat. Limit setting procedures and theoretical uncertainties in Higgs boson searches. 2012, 1204.3851.
- [115] Glen Cowan, Kyle Cranmer, Eilam Gross, and Ofer Vitells. Asymptotic formulae for likelihood-based tests of new physics. *Eur.Phys.J.*, C71:1554, 2011, 1007.1727.
- [116] J. Neyman and E. S. Pearson. On the problem of the most efficient tests of statistical hypotheses. *Philosophical Transactions of the Royal Society of London. Series A, Containing Papers of a Mathematical or Physical Character*, 231:pp. 289–337, 1933.
- [117] W. Buttinger. Asymptotic Formula for a General Double-Bounded Custom-Sided Likelihood Based Test Statistic. *ArXiv e-prints*, February 2013, 1302.2799.
- [118] Abraham Wald. Tests of statistical hypotheses concerning several parameters when the number of observations is large. *Transactions of the American Mathematical Society*, 54(3):pp. 426–482, 1943.

- [119] R. Barate et al. Search for the standard model Higgs boson at LEP. *Phys.Lett.*, B565:61–75, 2003, hep-ex/0306033.
- [120] Gordon L. Kane, Christopher F. Kolda, Leszek Roszkowski, and James D. Wells. Study of constrained minimal supersymmetry. *Phys.Rev.*, D49:6173–6210, 1994, hep-ph/9312272.
- [121] W. de Boer. The Constrained MSSM revisited. 1996, hep-ph/9611394.
- [122] A Hoecker. Mass reach of atlas searches for new phenomena. Technical Report ATLCOM-PHYS-2011-973, CERN, Geneva, Jul 2011.
- [123] ATLAS SUSY working group. Feynman diagrams. <https://twiki.cern.ch/twiki/bin/view/AtlasProtected/SUSYFeynmanDiagrams>.
- [124] Search for electroweak production of supersymmetric particles in final states with at least two hadronically decaying taus and missing transverse momentum with the atlas detector in proton-proton collisions at  $\sqrt{s} = 8$  tev. Technical Report ATLAS-CONF-2013-028, CERN, Geneva, Mar 2013.
- [125] LEP SUSY Working Group (ALEPH, DELPHI, L3, OPAL), Notes LEPSUSYWG/01-03.1 and 04-01.1, <http://lepsusy.web.cern.ch/lepsusy/Welcome.html>.
- [126] A. Heister et al. Search for scalar leptons in  $e^+e^-$  collisions at center-of-mass energies up to 209-GeV. *Phys.Lett.*, B526:206–220, 2002, hep-ex/0112011.
- [127] J. Abdallah et al. Searches for supersymmetric particles in  $e^+e^-$  collisions up to 208-GeV and interpretation of the results within the MSSM. *Eur.Phys.J.*, C31:421–479, 2003, hep-ex/0311019.
- [128] P. Achard et al. Search for scalar leptons and scalar quarks at LEP. *Phys.Lett.*, B580:37–49, 2004, hep-ex/0310007.
- [129] G. Abbiendi et al. Search for anomalous production of dilepton events with missing transverse momentum in  $e^+e^-$  collisions at  $\sqrt{s} = 183$ -GeV to 209-GeV. *Eur.Phys.J.*, C32:453–473, 2004, hep-ex/0309014.
- [130] A. Heister et al. Absolute mass lower limit for the lightest neutralino of the MSSM from  $e^+e^-$  data at  $\sqrt{s}$  up to 209 GeV. *Phys.Lett.*, B583:247–263, 2004.
- [131] M. Acciarri et al. Search for charginos and neutralinos in  $e^+e^-$  collisions at  $\sqrt{S} = 189$ -GeV. *Phys.Lett.*, B472:420–433, 2000, hep-ex/9910007.
- [132] G. Abbiendi et al. Search for chargino and neutralino production at  $\sqrt{s} = 192$ -GeV to 209 GeV at LEP. *Eur.Phys.J.*, C35:1–20, 2004, hep-ex/0401026.

- 
- [133] G. Arnison et al. Experimental Observation of Isolated Large Transverse Energy Electrons with Associated Missing Energy at  $\sqrt{s} = 540$  GeV. *Phys.Lett.*, B122:103–116, 1983.
- [134] M. Banner et al. Observation of Single Isolated Electrons of High Transverse Momentum in Events with Missing Transverse Energy at the CERN anti-p p Collider. *Phys.Lett.*, B122:476–485, 1983.
- [135] S.S. AbdusSalam, B.C. Allanach, H.K. Dreiner, J. Ellis, U. Ellwanger, et al. Benchmark Models, Planes, Lines and Points for Future SUSY Searches at the LHC. *Eur.Phys.J.*, C71:1835, 2011, 1109.3859.
- [136] G. Corcella, I.G. Knowles, G. Marchesini, S. Moretti, K. Odagiri, et al. HERWIG 6: An Event generator for hadron emission reactions with interfering gluons (including supersymmetric processes). *JHEP*, 0101:010, 2001, hep-ph/0011363.
- [137] Georges Aad et al. Measurement of the  $WW$  cross section in  $\sqrt{s} = 7$  TeV  $pp$  collisions with ATLAS. *Phys.Rev.Lett.*, 107:041802, 2011, 1104.5225.
- [138] Georges Aad et al. Search for supersymmetric particles in events with lepton pairs and large missing transverse momentum in  $\sqrt{s} = 7$  TeV proton-proton collisions with the ATLAS experiment. *Eur.Phys.J.*, C71:1682, 2011, 1103.6214.
- [139] Georges Aad et al. Search for an excess of events with an identical flavour lepton pair and significant missing transverse momentum in  $\sqrt{s} = 7$  TeV proton-proton collisions with the ATLAS detector. *Eur.Phys.J.*, C71:1647, 2011, 1103.6208.
- [140] Search for supersymmetric particles in events with lepton pairs and large missing transverse momentum in  $\sqrt{s} = 7$  TeV proton-proton collisions with the ATLAS experiment. *Eur.Phys.J.*, C71:1682, 2011, 1103.6214.
- [141] Georges Aad et al. Search for direct production of charginos and neutralinos in events with three leptons and missing transverse momentum in  $\sqrt{s} = 7$  TeV  $pp$  collisions with the ATLAS detector. *Phys.Lett.*, B718:841–859, 2013, 1208.3144.
- [142] Stefano Frixione, Paolo Nason, and Carlo Oleari. Matching NLO QCD computations with Parton Shower simulations: the POWHEG method. *JHEP*, 0711:070, 2007, 0709.2092.
- [143] Stefano Frixione and Bryan R. Webber. The MC@NLO event generator. 2002, hep-ph/0207182.
- [144] Stefano Frixione, Paolo Nason, and Bryan R. Webber. Matching NLO QCD and parton showers in heavy flavor production. *JHEP*, 0308:007, 2003, hep-ph/0305252.

- [145] Stefano Frixione, Eric Laenen, Patrick Motylinski, and Bryan R. Webber. Single-top production in MC@NLO. *JHEP*, 0603:092, 2006, hep-ph/0512250.
- [146] Michelangelo L. Mangano, Mauro Moretti, Fulvio Piccinini, Roberto Pittau, and Antonio D. Polosa. ALPGEN, a generator for hard multiparton processes in hadronic collisions. *JHEP*, 0307:001, 2003, hep-ph/0206293.
- [147] T. Gleisberg, Stefan. Hoeche, F. Krauss, M. Schonherr, S. Schumann, et al. Event generation with SHERPA 1.1. *JHEP*, 0902:007, 2009, 0811.4622.
- [148] J.M. Butterworth, Jeffrey R. Forshaw, and M.H. Seymour. Multiparton interactions in photoproduction at HERA. *Z.Phys.*, C72:637–646, 1996, hep-ph/9601371.
- [149] Torbjorn Sjostrand, Stephen Mrenna, and Peter Z. Skands. PYTHIA 6.4 Physics and Manual. *JHEP*, 0605:026, 2006, hep-ph/0603175.
- [150] M. Aliev, H. Lacker, U. Langenfeld, S. Moch, P. Uwer, et al. HATHOR: HAdronic Top and Heavy quarks crOss section calculator. *Comput.Phys.Commun.*, 182:1034–1046, 2011, 1007.1327.
- [151] John M. Campbell and R. Keith Ellis. An Update on vector boson pair production at hadron colliders. *Phys.Rev.*, D60:113006, 1999, hep-ph/9905386.
- [152] John M. Campbell, R. Keith Ellis, and Ciaran Williams. Vector boson pair production at the LHC. *JHEP*, 1107:018, 2011, 1105.0020.
- [153] Ryan Gavin, Ye Li, Frank Petriello, and Seth Quackenbush. FEWZ 2.0: A code for hadronic Z production at next-to-next-to-leading order. *Comput.Phys.Commun.*, 182:2388–2403, 2011, 1011.3540.
- [154] M. Bahr, S. Gieseke, M.A. Gigg, D. Grellscheid, K. Hamilton, et al. Herwig++ Physics and Manual. *Eur.Phys.J.*, C58:639–707, 2008, 0803.0883.
- [155] G. Aad et al. Measurement of the  $W \rightarrow \ell\nu$  and  $Z/\gamma^* \rightarrow \ell\ell$  production cross sections in proton-proton collisions at  $\sqrt{s} = 7$  TeV with the ATLAS detector. *JHEP*, 1012:060, 2010, 1010.2130.
- [156] Georges Aad et al. Jet energy measurement with the ATLAS detector in proton-proton collisions at  $\sqrt{s} = 7$  TeV. *Eur.Phys.J.*, C73:2304, 2013, 1112.6426.
- [157] I Santoyo Castillo, C Clement, G Conti, J Firmino da Costa, J Dietrich, A Floderus, S Fratina, ST French, B Gjelsten, E Gramstad, M Hamer, C Hensel, E Hines, B Jackson, T Kono, F Legger, C Lester, M Medinnis, B Meirose, A S Mete, H Okawa, F Ould-Saada, M Pedersen, F Salvatore, A Taffard, E Thomson, B Toggerson, R Ueno, S Williams, and

- J Wittkowski. Searching for direct gaugino production and direct slepton production with two leptons and missing transverse momentum at  $s = 7$  tev (supporting int note). Technical Report ATL-COM-PHYS-2011-1721, CERN, Geneva, Dec 2011.
- [158] D.R. Tovey. On measuring the masses of pair-produced semi-invisibly decaying particles at hadron colliders. *JHEP*, 0804:034, 2008.
- [159] Giacomo Polesello and Daniel R. Tovey. Supersymmetric particle mass measurement with the boost-corrected contranverse mass. *JHEP*, 1003:030, 2010, 0910.0174.
- [160] Georges Aad et al. Luminosity Determination in  $pp$  Collisions at  $\sqrt{s} = 7$  TeV Using the ATLAS Detector at the LHC. *Eur.Phys.J.*, C71:1630, 2011, 1101.2185.
- [161] Luminosity determination in  $pp$  collisions at  $\sqrt{s} = 7$  tev using the atlas detector in 2011. Technical Report ATLAS-CONF-2011-116, CERN, Geneva, Aug 2011.
- [162] Jet energy scale and its systematic uncertainty in proton-proton collisions at  $\sqrt{s}=7$  TeV in ATLAS 2010 data. 2011.
- [163] Georges Aad et al. Jet energy resolution in proton-proton collisions at  $\sqrt{s} = 7$  TeV recorded in 2010 with the ATLAS detector. *Eur.Phys.J.*, C73:2306, 2013, 1210.6210.
- [164] b-jet tagging efficiency calibration using the system8 method. Technical Report ATLAS-CONF-2011-143, CERN, Geneva, Oct 2011.
- [165] Muon reconstruction efficiency in reprocessed 2010 lhc proton-proton collision data recorded with the atlas detector. Technical Report ATLAS-CONF-2011-063, CERN, Geneva, Apr 2011.
- [166] A measurement of the atlas muon reconstruction and trigger efficiency using  $j/\psi$  decays. Technical Report ATLAS-CONF-2011-021, CERN, Geneva, Mar 2011.
- [167] Georges Aad et al. Measurement of the top quark pair production cross section in  $pp$  collisions at  $\sqrt{s} = 7$  TeV in dilepton final states with ATLAS. *Phys.Lett.*, B707:459–477, 2012, 1108.3699.
- [168] Michael Kramer, Anna Kulesza, Robin van der Leeuw, Michelangelo Mangano, Sanjay Padhi, et al. Supersymmetry production cross sections in  $pp$  collisions at  $\sqrt{s} = 7$  TeV. 2012, 1206.2892.
- [169] T. Aaltonen et al. Search for Supersymmetry in  $p\bar{p}$  Collisions at  $\sqrt{s} = 1.96$ -TeV Using the Trilepton Signature of Chargino-Neutralino Production. *Phys.Rev.Lett.*, 101:251801, 2008, 0808.2446.

- [170] V.M. Abazov et al. Search for associated production of charginos and neutralinos in the trilepton final state using  $2.3 \text{ fb}^{-1}$  of data. *Phys.Lett.*, B680:34–43, 2009, 0901.0646.
- [171] Georges Aad et al. Search for supersymmetry in events with three leptons and missing transverse momentum in  $\sqrt{s} = 7 \text{ TeV}$   $pp$  collisions with the ATLAS detector. *Phys.Rev.Lett.*, 108:261804, 2012, 1204.5638.
- [172] A. Arbey, M. Battaglia, A. Djouadi, F. Mahmoudi, and J. Quevillon. Implications of a 125 GeV Higgs for supersymmetric models. *Phys.Lett.*, B708:162–169, 2012, 1112.3028.
- [173] S. Scopel, N. Fornengo, and A. Bottino. Embedding the 125 GeV Higgs boson measured at the LHC in an effective MSSM: possible implications for neutralino dark matter. *Phys.Rev.*, D88:023506, 2013, 1304.5353.
- [174] Patrick Draper, Patrick Meade, Matthew Reece, and David Shih. Implications of a 125 GeV Higgs for the MSSM and Low-Scale SUSY Breaking. *Phys.Rev.*, D85:095007, 2012, 1112.3068.
- [175] Andrew Fowlie, Malgorzata Kazana, Kamila Kowalska, Shoaib Munir, Leszek Roszkowski, et al. The CMSSM Favoring New Territories: The Impact of New LHC Limits and a 125 GeV Higgs. *Phys.Rev.*, D86:075010, 2012, 1206.0264.
- [176] Sujeet Akula, Pran Nath, and Gregory Peim. Implications of the Higgs Boson Discovery for mSUGRA. *Phys.Lett.*, B717:188–192, 2012, 1207.1839.
- [177] Riccardo Barbieri and G.F. Giudice. Upper Bounds on Supersymmetric Particle Masses. *Nucl.Phys.*, B306:63, 1988.
- [178] B. de Carlos and J.A. Casas. One loop analysis of the electroweak breaking in supersymmetric models and the fine tuning problem. *Phys.Lett.*, B309:320–328, 1993, hep-ph/9303291.
- [179] The ATLAS collaboration. Atlas public results on luminosity measurements. <https://twiki.cern.ch/twiki/bin/view/AtlasPublic/LuminosityPublicResults>.
- [180] The ATLAS collaboration. Atlas public event displays. <https://twiki.cern.ch/twiki/bin/view/AtlasPublic/EventDisplayPublicResults>.
- [181] T. Binoth, M. Ciccolini, N. Kauer, and M. Kramer. Gluon-induced W-boson pair production at the LHC. *JHEP*, 0612:046, 2006, hep-ph/0611170.
- [182] T. Binoth, N. Kauer, and P. Mertsch. Gluon-induced QCD corrections to  $pp \rightarrow ZZ \rightarrow \ell\bar{\ell}\ell'\bar{\ell}'$ . page 142, 2008, 0807.0024.

- 
- [183] Search for electroweak production of charginos, neutralinos, and sleptons using leptonic final states in pp collisions at 8 tev. Technical Report CMS-PAS-SUS-13-006, CERN, Geneva, 2013.
- [184] Konstantin T. Matchev and Myeonghun Park. A General method for determining the masses of semi-invisibly decaying particles at hadron colliders. *Phys.Rev.Lett.*, 107:061801, 2011, 0910.1584.
- [185] ATLAS SUSY working group. Public results. <https://twiki.cern.ch/twiki/bin/view/AtlasPublic/SupersymmetryPublicResults>.
- [186] G. Arnison et al. Experimental Observation of Lepton Pairs of Invariant Mass Around 95-GeV/c<sup>2</sup> at the CERN SPS Collider. *Phys.Lett.*, B126:398–410, 1983.
- [187] P. Bagnaia et al. Evidence for  $Z_0 \rightarrow e^+e^-$  at the CERN anti-p p Collider. *Phys.Lett.*, B129:130–140, 1983.
- [188] A. Buckley. hepthesis- a LaTeX document class for academic theses. <http://www.ctan.org/tex-archive/help/Catalogue/entries/hepthesis.html>.

# List of Figures

2.1	The CERN accelerator complex. . . . .	4
2.2	Locations of the four main LHC experiments around the ring. . . . .	6
2.3	Computer generated image of the ATLAS detector . . . . .	8
2.4	Structural elements traversed by a charged particle in the ID . . . . .	11
2.5	Computer generated image of the ATLAS Inner Detector. . . . .	12
2.6	Schematic view of the ATLAS pixel detector. . . . .	13
2.7	Layout of the ATLAS SCT. . . . .	14
2.8	Track parameter definitions with respect to the perigee. . . . .	16
2.9	Computer generated view of the ATLAS calorimeters. . . . .	18
2.10	The accordion structure of the ATLAS electromagnetic calorimeter . . . . .	19
2.11	Quarter-section of the ATLAS Muon Spectrometer. . . . .	21
2.12	Cut-away view of the ATLAS Muon Spectrometer . . . . .	22
2.13	Expected contributions to the muon momentum resolution as a function of $p_T$ . . . . .	23
2.14	Geometry of the windings in the ATLAS magnet system. . . . .	24
2.15	The ATLAS central solenoid. . . . .	25
2.16	The ATLAS barrel toroid. . . . .	25
2.17	The ATLAS end-cap toroids. . . . .	26
2.18	Block diagram of the ATLAS Level 1 trigger. . . . .	27
2.19	Block diagram of the ATLAS TDAQ system. . . . .	28

2.20	Flowchart of data through the ATLAS computing model. . . . .	30
2.21	Full chain for Monte Carlo production in ATLAS. . . . .	34
3.1	Loop correction to the Higgs boson mass from a top quark loop. . . . .	47
3.2	Loop contributions to the Higgs boson mass in supersymmetry. . . . .	49
3.3	Cross-sections for supersymmetric particle production at 7 TeV and 8 TeV. . .	53
4.1	Probability density functions for the test statistic in the LEP Higgs combination.	61
5.1	Summary of ATLAS SUSY exclusions in July 2011. . . . .	69
5.2	Three possible weak production processes at the LHC. . . . .	70
5.3	Possible decays of pair-produced electroweak sparticles at the LHC. . . . .	72
5.4	Previous limits on direct slepton production from LEP. . . . .	73
5.5	LEP limit on the mass of the lightest neutralino. . . . .	74
5.6	Slepton-pair production at the LHC. . . . .	75
5.7	Fully leptonic $WW$ and $t\bar{t}$ decays. . . . .	77
5.8	Cross-sections for points in the direct slepton signal grid . . . . .	78
5.9	$m_{T2}$ optimisation plots for slepton-pair production with $E_T^{\text{miss,rel}} > 40$ GeV, for 4.7 fb <sup>-1</sup> . . . . .	81
5.10	$m_{T2}$ optimisation plots for slepton-pair production with $E_T^{\text{miss,rel}} > 60$ GeV, for 4.7 fb <sup>-1</sup> . . . . .	82
5.11	$m_{T2}$ optimisation plots for slepton-pair production with $E_T^{\text{miss,rel}} > 80$ GeV, for 4.7 fb <sup>-1</sup> . . . . .	83
5.12	Theoretical endpoints of the $m_{T2}$ distributions for slepton-pair production. . .	84
6.1	Phase-space regions defining the 2011 trigger strategy. . . . .	97
6.2	$E_T^{\text{miss,rel}}$ distributions for opposite-sign di-lepton events. . . . .	99
6.3	$E_T^{\text{miss,rel}}$ distributions for same-sign di-lepton events. . . . .	100
6.4	$m_{\ell\ell}$ for opposite-sign di-lepton events, with $E_T^{\text{miss,rel}} > 40$ GeV. . . . .	101

6.5	Signal jet multiplicity for opposite-sign di-lepton events, with $E_T^{\text{miss,rel}} > 40$ GeV.	102
6.6	Leading lepton $p_T$ for opposite-sign di-lepton events, with $E_T^{\text{miss,rel}} > 40$ GeV.	103
6.7	Cross-sections for direct gaugino production modes in the “pure wino” scenario	105
6.8	$\tilde{\chi}_1^+ \tilde{\chi}_1^-$ pair production with decays to two leptons.	106
6.9	$\tilde{\chi}_2^0 \tilde{\chi}_1^\pm$ pair production with a same-sign lepton signature.	107
6.10	$\tilde{\chi}_2^0 \tilde{\chi}_1^\pm$ pair production with two leptons and two jets in the final state.	107
6.11	$m_{ll}$ distributions in the $Z + X$ control region for SR-OSjveto.	121
6.12	$m_{ll}$ distributions in the $Z + X$ control region for SR-2jets.	122
6.13	$m_{ll}$ distributions in the $Z + X$ control region for SR- $m_{T2}$ .	122
6.14	$E_T^{\text{miss,rel}}$ distributions in the $Z + X$ control region for SR-OSjveto.	123
6.15	$E_T^{\text{miss,rel}}$ distributions in the $Z + X$ control region for SR-2jets.	123
6.16	$E_T^{\text{miss,rel}}$ distributions in the $Z + X$ control region for SR- $m_{T2}$ .	124
6.17	$m_{T2}$ distributions in the $Z + X$ control region for SR- $m_{T2}$ in the 2011 analysis.	124
6.18	$E_T^{\text{miss,rel}}$ distributions in the top control region for SR- $m_{T2}$ in the 2011 analysis	125
6.19	$m_{T2}$ distributions in the top control region for SR- $m_{T2}$ in the 2011 analysis	126
6.20	Distributions of $E_T^{\text{miss,rel}}$ and $m_{T2}$ in the 2011 signal regions.	129
6.21	95% CL exclusion limits for $\tilde{\chi}_1^+ \tilde{\chi}_1^-$ production using the 2011 dataset	132
6.22	Efficiency-times-acceptance, acceptance and efficiency for $\tilde{\chi}_1^+ \tilde{\chi}_1^-$ production in SR- $m_{T2}$ .	133
6.23	Efficiency-times-acceptance, acceptance and efficiency for $\tilde{\chi}_1^+ \tilde{\chi}_1^-$ production in SR-OSjveto.	134
6.24	Cross-sections for the $\tilde{\chi}_1^\pm \tilde{\chi}_1^\mp$ simplified model grid	135
6.25	95% CL exclusion limits for $\tilde{\chi}_1^\pm \tilde{\chi}_2^0$ production using the 2011 dataset	136
6.26	Efficiency-times-acceptance, acceptance and efficiency for $\tilde{\chi}_1^\pm \tilde{\chi}_2^0$ production in SR- $m_{T2}$ .	137
6.27	Efficiency-times-acceptance, acceptance and efficiency for $\tilde{\chi}^\pm \tilde{\chi}_2^0$ production in SR-OSjveto.	138

6.28	Efficiency-times-acceptance, acceptance and efficiency for $\tilde{\chi}^\pm \tilde{\chi}_2^0$ production in SR-SSjveto. . . . .	139
6.29	95% CL exclusion limits for $\tilde{\ell}^\pm$ pair production using the 2011 dataset with a flavour-blind signal region. . . . .	141
6.30	Efficiency-times-acceptance, acceptance and efficiency for $\tilde{\ell}^\pm$ pair production in SR- $m_{T2}$ , for a flavour blind signal region. . . . .	142
6.31	95% CL exclusion limits for $\tilde{\ell}^\pm$ pair production using the 2011 dataset. . . . .	143
6.32	95% CL exclusion limits in the $M_1 = 100$ GeV pMSSM grid using the 2011 dataset	144
6.33	95% CL exclusion limits in the $M_1 = 140$ GeV pMSSM grid using the 2011 dataset	145
6.34	95% CL exclusion limits in the $M_1 = 250$ GeV pMSSM grid using the 2011 dataset	146
6.35	Excluded points in the weak production pMSSM grids. . . . .	147
6.36	$\tilde{\chi}_2^0 \tilde{\chi}_1^\pm$ production cross-sections in the $M_1 = 100$ GeV and $M_1 = 140$ GeV pMSSM grids. . . . .	150
6.37	$\tilde{\chi}_2^0 \tilde{\chi}_1^\pm$ mass-splitting for the $M_1 = 100$ GeV and $M_1 = 140$ GeV pMSSM grids.	151
6.38	$\tilde{\chi}_1^\pm$ and $\tilde{\chi}_1^0$ masses in the $M_1 = 100$ GeV and $M_1 = 140$ GeV pMSSM grids. . .	152
6.39	$\tilde{\chi}_1^\pm - \tilde{\chi}_1^0$ mass-splittings in the $M_1 = 100$ GeV and $M_1 = 140$ GeV pMSSM grids.	154
6.40	$\tilde{\ell}_R$ and $\tilde{\chi}_1^0$ masses in the $M_1 = 100$ GeV and $M_1 = 140$ GeV pMSSM grids. . .	155
7.1	Cumulative luminosity delivered to ATLAS throughout 2010, 2011 and 2012. . .	162
7.2	Cumulative Luminosity delivered to ATLAS throughout 2012. . . . .	162
7.3	Peak instantaneous luminosity delivered to ATLAS in 2010, 2011 and 2012. . .	163
7.4	$\langle \mu \rangle$ distributions in 2011 and 2012. . . . .	164
7.5	ATLAS event display for a high pile-up $Z \rightarrow \mu\mu$ event. . . . .	165
7.6	$m_{T2}$ optimisation plots for slepton-pair production with $E_T^{\text{miss,rel}} > 40$ GeV, for $20.3 \text{ fb}^{-1}$ . . . . .	169
7.7	$m_{T2}$ optimisation plots for slepton-pair production with $E_T^{\text{miss,rel}} > 60$ GeV, for $20.3 \text{ fb}^{-1}$ . . . . .	170
7.8	$m_{T2}$ optimisation plots for slepton-pair production with $E_T^{\text{miss,rel}} > 80$ GeV, for $20.3 \text{ fb}^{-1}$ . . . . .	171

7.9	$m_{T2}$ distributions in SR-pre- $m_{T2}$ , with direct slepton signal points overlaid. . .	172
7.10	$E_T^{\text{miss,rel}}$ distribution for Monte Carlo events in SR-pre- $m_{T2}$ . . . . .	175
7.11	$m_{T2}$ distribution for Monte Carlo events in SR-pre- $m_{T2}$ . . . . .	176
7.12	$m_{\ell\ell}$ distribution for Monte Carlo events in SR-pre- $m_{T2}$ . . . . .	177
7.13	$E_T^{\text{miss,rel}}$ distributions in the top control region for the 2012 analysis. . . . .	181
7.14	$m_{T2}$ distributions in the top control region for the 2012 analysis. . . . .	182
7.15	$E_T^{\text{miss,rel}}$ distributions in the $ZV$ control regions for the 2012 analysis. . . . .	185
7.16	$m_{T2}$ distributions in the $WW$ control region for the 2012 analysis. . . . .	187
7.17	$E_T^{\text{miss,rel}}$ and $m_{T2}$ distributions in SR-pre- $m_{T2}$ in the 2012 analysis. . . . .	194
7.18	95% CL exclusion limits for $\tilde{\ell}_{L,R}^+ \tilde{\ell}_{L,R}^-$ pair production using the 2012 dataset . .	198
7.19	95% CL exclusion limits for $\tilde{\ell}_R^+ \tilde{\ell}_R^-$ pair production using the 2012 dataset . . . .	199
7.20	95% CL exclusion limits for $\tilde{\ell}_L^+ \tilde{\ell}_L^-$ pair production using the 2012 dataset . . . .	200
7.21	Signal counts for slepton-pair production in SR- $m_{T2,90}$ and SR- $m_{T2,110}$ for $20.3 \text{ fb}^{-1}$ .	201
7.22	95% CL exclusion limits for $\tilde{\chi}_1^+ \tilde{\chi}_1^-$ production using the 2012 dataset . . . . .	202
7.23	CMS limits on slepton- and chargino-pair production. . . . .	203
7.24	95% CL exclusion limits for $\tilde{\chi}_1^+ \tilde{\chi}_1^-$ production using a shape-fit in $m_{T2}$ . . . . .	205
7.25	95% CL exclusion limits for $\tilde{\ell}_R^+ \tilde{\ell}_R^-$ production using a shape-fit in $m_{T2}$ . . . . .	206
7.26	Summary of ATLAS SUSY exclusions in August 2013. . . . .	208
A.1	Feynman diagram for leptonic $W$ boson decay. . . . .	212
B.1	$m_{T2}$ optimisation plots for chargino-pair production with $E_T^{\text{miss,rel}} > 40 \text{ GeV}$ , for $4.7 \text{ fb}^{-1}$ . . . . .	216
B.2	$m_{T2}$ optimisation plots for chargino-pair production with $E_T^{\text{miss,rel}} > 60 \text{ GeV}$ , for $4.7 \text{ fb}^{-1}$ . . . . .	217
B.3	$m_{T2}$ optimisation plots for chargino-pair production with $E_T^{\text{miss,rel}} > 80 \text{ GeV}$ , for $4.7 \text{ fb}^{-1}$ . . . . .	218

---

E.1	Simultaneous fit results for $\text{SR-}m_{T2,90}$ . . . . .	237
E.2	Simultaneous fit results for $\text{SR-}m_{T2,110}$ . . . . .	238
E.3	Correlation matrix for the simultaneous fit results for $\text{SR-}m_{T2,90}$ . . . . .	241
E.4	Correlation matrix for the simultaneous fit results for $\text{SR-}m_{T2,110}$ . . . . .	242
F.1	Correlation matrix for the simultaneous fit results for $\text{SR-}m_{T2,90}$ in the shape fit investigation using one set of nuisance parameters for the fitted and non-fitted backgrounds. . . . .	251
F.2	Correlation matrix for the simultaneous fit results for $\text{SR-}m_{T2,110}$ in the shape fit investigation using one set of nuisance parameters for the fitted and non-fitted backgrounds. . . . .	252
F.3	Correlation matrix for the simultaneous fit results for $\text{SR-}m_{T2,90}$ in the shape fit investigation using two sets of nuisance parameters for the fitted and non-fitted backgrounds. . . . .	253
F.4	Correlation matrix for the simultaneous fit results for $\text{SR-}m_{T2,110}$ in the shape fit investigation using two sets of nuisance parameters for the fitted and non-fitted backgrounds. . . . .	254

# List of Tables

2.1	General performance requirements of the ATLAS detector. . . . .	9
3.1	The three generations of Standard Model fermions. . . . .	40
3.2	Electroweak quantum numbers of the Standard Model fermions. . . . .	41
6.1	Possible final states arising from electroweak production processes. . . . .	87
6.2	Object selection criteria in the 2011 analysis. . . . .	91
6.3	Event quality criteria for the 2011 analysis. . . . .	94
6.4	Single- and double-electron triggers used in the 2011 analysis. . . . .	95
6.5	Single- and double-muon triggers used in the 2011 analysis. . . . .	95
6.6	Electron-muon trigger used in the 2011 analysis. . . . .	96
6.7	Trigger strategy for different phase space regions in the 2011 analysis. . . . .	97
6.8	Signal region definitions for the 2011 analysis. . . . .	104
6.9	Monte-Carlo estimates for the 2011 signal regions in the di-electron channel. . .	109
6.10	Monte-Carlo estimates for the 2011 signal regions in the di-muon channel. . . .	110
6.11	Monte-Carlo estimates for the 2011 signal regions in the electron-muon channel.	111
6.12	Groupings of background processes in the 2011 analysis. . . . .	112
6.13	Summary of background estimation techniques in the 2011 analysis. . . . .	114
6.14	Top control region definitions for the 2011 analysis. . . . .	115
6.15	$Z + X$ control region definitions for the 2011 analysis. . . . .	115

---

6.16	Results for data and predicted background in the 2011 signal regions. . . . .	130
6.17	Breakdown of SR- $m_{T2}$ signal counts for selected points with $M_1 = 100$ GeV and $M_2 = 210$ GeV. . . . .	148
6.18	Breakdown of SR- $m_{T2}$ signal counts for selected points with $M_1 = 140$ GeV and $M_2 = 210$ GeV. . . . .	149
6.19	Breakdown of SR- $m_{T2}$ signal counts for selected points with $M_1 = 100$ GeV and $\mu = 400$ GeV. . . . .	153
6.20	Breakdown of SR- $m_{T2}$ signal counts for selected points with $M_1 = 250$ GeV and $M_2 = 210$ GeV. . . . .	156
6.21	Breakdown of SR- $m_{T2}$ signal counts for selected points with $M_1 = 250$ GeV and $\mu = 160$ GeV. . . . .	157
7.1	Monte Carlo compositions for SR- $m_{T2}$ in the 2011 analysis. . . . .	174
7.2	Background estimation techniques used in the 2012 analysis. . . . .	178
7.3	Control regions for the 2012 analysis . . . . .	179
7.4	Monte Carlo estimates for the top control region, normalised to $20.3 \text{ fb}^{-1}$ . . . . .	180
7.5	Monte Carlo estimates for the $ZV$ control region for SR- $m_{T2,90}$ , normalised to $20.3 \text{ fb}^{-1}$ . . . . .	183
7.6	Monte Carlo estimates for the $ZV$ control region for SR- $m_{T2,110}$ , normalised to $20.3 \text{ fb}^{-1}$ . . . . .	184
7.7	Monte Carlo estimates for the $WW$ control region, normalised to $20.3 \text{ fb}^{-1}$ . . . . .	186
7.8	Simultaneous fit results without the Higgs background included. . . . .	188
7.9	Simultaneous fit results with the Higgs background included. . . . .	188
7.10	Background estimates for SR- $m_{T2,90}$ in the 2012 analysis. . . . .	190
7.11	Background estimates for SR- $m_{T2,110}$ in the 2012 analysis. . . . .	191
7.12	Results in SR- $m_{T2,90}$ and SR- $m_{T2,110}$ for $20.3 \text{ fb}^{-1}$ . . . . .	195
7.13	Breakdown of model independent limits for SR- $m_{T2,90}$ and SR- $m_{T2,110}$ . . . . .	196
D.1	Naming convention for systematic errors in the 2011 analysis. . . . .	222

---

D.2	Monte Carlo systematic uncertainties for SR-OSjveto in the $ee$ channel. . . . .	223
D.3	Monte Carlo systematic uncertainties for SR-SSjveto in the $ee$ channel. . . . .	224
D.4	Monte Carlo systematic uncertainties for SR-2jets in the $ee$ channel. . . . .	225
D.5	Monte Carlo systematic uncertainties for SR- $m_{T2}$ in the $ee$ channel. . . . .	226
D.6	Monte Carlo systematic uncertainties for SR-OSjveto in the $\mu\mu$ channel. . . . .	227
D.7	Monte Carlo systematic uncertainties for SR-SSjveto in the $\mu\mu$ channel. . . . .	228
D.8	Monte Carlo systematic uncertainties for SR-2jets in the $\mu\mu$ channel. . . . .	229
D.9	Monte Carlo systematic uncertainties for SR- $m_{T2}$ in the $\mu\mu$ channel. . . . .	230
D.10	Monte Carlo systematic uncertainties for SR-OSjveto in the $e\mu$ channel. . . . .	231
D.11	Monte Carlo systematic uncertainties for SR-SSjveto in the $e\mu$ channel. . . . .	232
D.12	Monte Carlo systematic uncertainties for SR- $m_{T2}$ in the $e\mu$ channel. . . . .	233
E.1	Fit parameter definitions in the 2012 analysis. . . . .	239
E.2	Breakdown of systematic uncertainties in the $e^\pm e^\mp$ channel of SR- $m_{T2,90}$ . . . . .	243
E.3	Breakdown of systematic uncertainties in the $e^\pm \mu^\mp$ channel of SR- $m_{T2,90}$ . . . . .	244
E.4	Breakdown of systematic uncertainties in the $\mu^\pm \mu^\mp$ channel of SR- $m_{T2,90}$ . . . . .	245
E.5	Breakdown of systematic uncertainties in the $e^\pm e^\mp$ channel of SR- $m_{T2,110}$ . . . . .	246
E.6	Breakdown of systematic uncertainties in the $e^\pm \mu^\mp$ channel of SR- $m_{T2,110}$ . . . . .	247
E.7	Breakdown of systematic uncertainties in the $\mu^\pm \mu^\mp$ channel of SR- $m_{T2,110}$ . . . . .	248